Effects and Applications of Capillary Condensation in Ultrathin Nanoparticle Assemblies

by

ZEKERIYYA GEMICI

Bachelor of Arts in Chemistry and Biological Sciences
Cornell University, Ithaca, New York, 2005

SUBMITTED TO THE DEPARTMENT OF CHEMICAL ENGINEERING IN PARTIAL FULFILLMENT OF THE REQUIREMENTS FOR THE DEGREE OF

DOCTOR OF PHILOSOPHY IN CHEMICAL ENGINEERING PRACTICE

at the

MASSACHUSETTS INSTITUTE OF TECHNOLOGY

JUNE 2010

Signature of Author_____
Department of Chemical Engineering
March 1st, 2010

Certified by_____
Robert E. Cohen
St. Laurent Professor of Chemical Engineering
Thesis Advisor

Certified by_____
Michael F. Rubner
TDK Professor of Materials Science and Engineering
Thesis Advisor

Accepted by _____
William M. Deen
Professor of Chemical Engineering
Chairman, Committee for Graduate Students

Effects and Applications of Capillary Condensation in Ultrathin Nanoparticle Assemblies

by

Zekeriyya Gemici

Submitted to the Department of Chemical Engineering

on February 24th, 2008 in Partial Fulfillment of the

Requirements for the Degree of Doctor of Philosophy in

Chemical Engineering Practice

Abstract

The electrostatic layer-by-layer (LbL) assembly technique can be used to make uniform, conformal multi-stack nanoparticle thin films from aqueous solution, with precise thickness and roughness control over each stack. Much of the effort in this area has focused on the assembly and characterization of novel nanostructures. However, there is a scarcity of studies addressing critical barriers to commercialization of LbL technology, such as the lack of mechanical durability and the difficulty of incorporating a diverse set of functional organic molecules into aqueous solution-based nanoparticle assemblies. The versatility of existing chemical functionalization methods are limited by requirements for particular substrate surface chemistries, compatible solvents, and concerns over uncontrolled nanoparticle deposition. Here we describe the advantageous use of capillary condensation, a well-known natural phenomenon in nanoporous materials, as a more universal functionalization strategy. Capillary condensation of solvent molecules into nanoporous LbL films was shown to bridge neighboring nanoparticles via a dissolution-redeposition mechanism to impart mechanical durability to otherwise delicate films. *In situ* crosslinking ability of photosensitive capillary-condensates was demonstrated. Particle size-dependence of the capillary condensation process was studied theoretically and utilized experimentally to modulate refractive index over coating thickness to achieve broadband antireflection (AR) functionality. Multi-stack AR coatings with alternating high- and low-index stacks were also made, and the influence of inter-stack and surface roughness on film transparency were studied quantitatively. The equivalent-stack approximation was utilized and presented as an enabling design tool for fabricating sophisticated solution-based optical coatings. Surface wettability could also be modified using capillary condensation – either by condensation of adventitious vapors during an ageing process leading to a loss of optimized film properties, or by advantageous condensation of carefully chosen hydrophobic or hydrophilic molecules to tune wettability. Finally, preliminary Young's moduli measurements of all-nanoparticle and polymer-nanoparticle composite films were made using strain induced elastic buckling instabilities for mechanical measurements (SIEBIMM).

Thesis advisors: Prof. Robert E. Cohen, St. Laurent Professor of Chemical Engineering

Prof. Michael F. Rubner, TDK Professor of Materials Science and Engineering

Acknowledgements

Advisors. I am deeply grateful to my thesis advisors, Prof. Cohen and Prof. Rubner, for the academic and personal guidance they provided during my stay here at MIT. I will proudly carry for the rest of my life the traces of their wonderful personalities which have rubbed onto me.

Thesis Committee. Prof. George Stephanopoulos and Prof. Paula Hammond have substantially contributed to the quality of this thesis. I am grateful to my committee for their friendly yet rigorous advice and guidance, as well as their support with letters of recommendation.

Other Faculty. Many thanks to Prof. Kristen van Vliet, Prof. Gareth McKinley, Prof. Francesco Stellacci, Prof. Alan Hatton, Prof. Daniel Blankschtein, Prof. Mehmet Bayindir, and Prof. Jeff Tester for their great advice and for making their laboratories available for collaborative work. I also thank Prof. Robert Pindyck from the MIT Sloan School of Management for reviewing my capstone chapter (Chapter 8).

Lab Members. I would like to thank all the members of the Cohen and Rubner labs for their endless personal and academic support throughout my PhD experience. In particular, I would like to thank Dr. Daeyeon Lee, Dr. Adam Nolte, Dr. Solar Olugebefola, Jonathan Daley, Erik Williamson, Shreerang Chhatre, Al Swiston, Dr. Pinar Kurt, and Dr. Ayse Asatekin.

Department of Chemical Engineering. I am grateful to the department for the first-year fellowship support, the first-year office space, the qualifying exam experience, the well-established set of policies for graduate students, the student lounge, the regular Friday seminars, the wonderful Thanksgiving dinners, and many other services which made my stay at MIT so pleasant.

> **The Practice School.** I thank the Department of Chemical Engineering Practice School for administering the PhD in Chemical Engineering Practice (PhD CEP) program. If it was not for the PhD CEP program, I would have never considered pursuing a doctoral degree. I also thank Cabot Corporation and Novartis AG for hosting Practice School stations.

Sponsors and Collaborators. Thanks to JSR Corporation, Essilor International SA, Agiltron Corporation, as well as other industrial collaborators for enriching my PhD experience. In particular, I would like to thank Hiroomi Shimomura, Patrick Schwachulla and Dr. Haipeng Zheng. I also thank KAUST and Applied Materials Inc. for fellowship support.

Student Groups. Both the MIT Turkish Student Association and the MIT Muslim Students' Association have provided great learning and socializing opportunities in my free time, and I am grateful to the founders and members of both student groups for a wonderful experience.

Friends. I am forever indebted to Yasin Ozcan, Emre Aciksoz, Tural Badirkhanli, Ibrahim Kanan, Omair Saadat, Baris Polat, Mehmet Yunt, Selcuk Bayraktar, Dr. Aykut Firat, Sukru Cinar, Nizameddin Ordulu, Halil Tekin, Umit Demirbas, Dr. Yildiray Yildiz, Abdullah Kaya, Ali Muhammed, Dr. Alp Simsek, Erbay Dokmeci, Dr. Hasan Arslan, Igor Ganichev, Dr. Mehmet Ali Sanlikol, Yusuf Erkul, Dr. Ozge Akbulut and Emil Guluzade.

Family. Mom – thank you VERY much for your constant love, help and prayers! Without your boundless support, I could have never even graduated from college, let alone completing a PhD thesis. In addition, I thank my dad, sister, brother, brother-in-law, as well as my nieces and nephews for making my life meaningful. Last but not least, very special thanks to a very special person, my fiancée, Hilal Elmas.

Dedication

This thesis is dedicated to my sister, Zeynep Sena Uslucan, and everyone denied access to their civil right of a formal education due to discrimination based on religion, ethnicity, sex, and financial resources.

"A free people [claim] their rights as derived from the laws of nature, and not as the gift of their chief magistrate." - *Thomas Jefferson*

Table of Contents

List of Figures

List of Tables

Chapter 1
Introduction

1.1 Nanoparticle Thin Films

Friction, wettability, biocompatibility, susceptibility to bacterial attachment or soiling, adhesiveness, and glossiness are examples of critical material properties determined almost solely by surface physics and chemistry. Hence, there is ever-growing interest in coatings which can impart desired surface characteristics to any bulk material of choice in an *ad hoc* manner. Coatings can be roughly divided into three categories: solution-based coatings, vacuum-deposited coatings, and powder coatings. This thesis concentrates on overcoming the shortcomings of solution-based coatings for optical applications and for modification of surface wettability.

Nanoparticles are indispensable ingredients of solution-based optical, dielectric, and catalytic thin films. Solution-based techniques of making nanoparticle thin films can also be categorized as (i) nanoparticle deposition techniques, whereby a nanoparticle sol is deposited onto a surface and subsequently allowed to gel, and (ii) nanoparticle assembly techniques, whereby secondary interactions (e.g., electrostatic, van der Waals, hydrogen bonding interactions, etc.) drive the spontaneous assembly of nanoparticles onto a surface.

While solution-based methods are promising low-cost alternatives to vacuum methods, they can have significant limitations. Coating uniformity, thickness control, and roughness control are difficulties encountered in nanoparticle deposition methods. Lack of mechanical durability and incorporation of a diverse set of functional organic molecules into nanoparticle thin films are major challenges for nanoparticle assembly methods.

1.2 Layer-by-Layer Assembly of Nanoparticle Thin Films

Electrostatic LbL assembly is illustrated in Figure 1.1[1]. The process begins when an electrostatically charged substrate (e.g., a glass slide cleaned with NaOH, a plasma-treated polycarbonate slide, etc.) is dipped into a dilute aqueous solution of oppositely charged polyelectrolyte or nanoparticle. The solution constituents electrostatically adsorb on the substrate until the surface charge is not only neutralized, but also reversed. Thus, the adsorption process is a self-limiting equilibrium process, and

this autoinhibitory nature of the LbL assembly process provides excellent thickness control. The physisorbed material on the substrate is then thoroughly rinsed off, and the substrate is dipped into a dilute aqueous solution of another oppositely charged polyelectrolyte or nanoparticle. The same charge reversal process ensues once more, and at this point a "bilayer" of material is deposited on the surface. Film thickness can be controlled by varying the number of bilayers to be assembled. Film composition can be controlled by varying the solution composition, and the film morphology is a function of the nanoparticle or polyelectrolyte charge density.

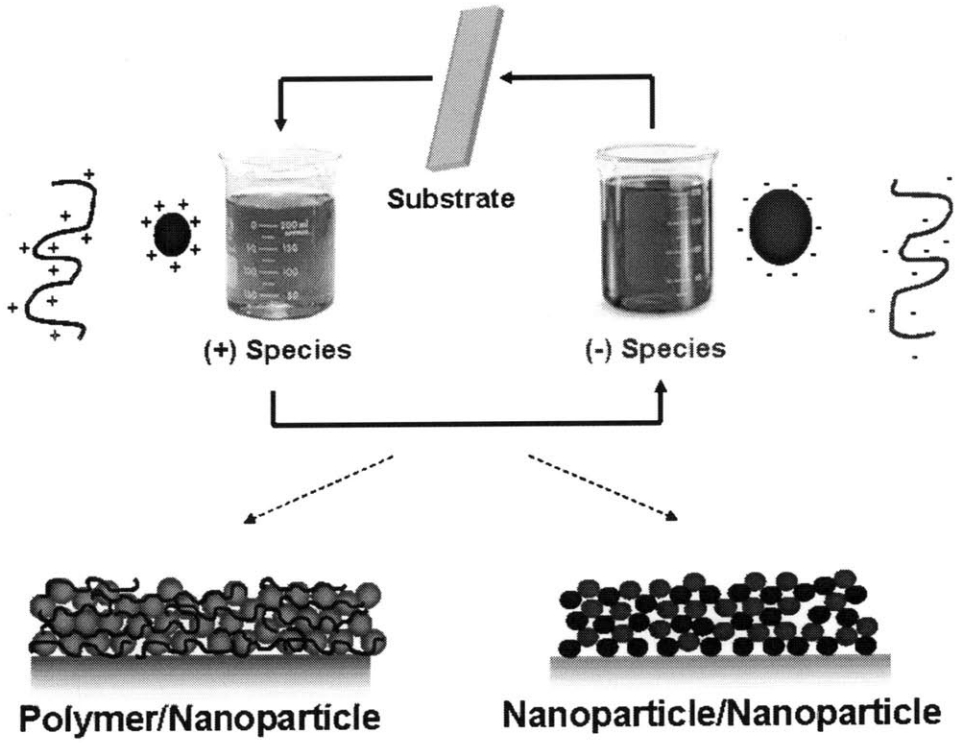

Figure 1.1. Illustration of the layer-by-layer (LbL) assembly technique. Figure modified from work of Lee et al.[1]

Polymer-nanoparticle and all-nanoparticle LbL films can both be prepared. While polymer-nanoparticle films have been studied extensively in the last decade, all-nanoparticle LbL films (first reported by Iler[2] in 1966) have been largely overlooked until Lee et al.[1, 3, 4] recently published several reports on their growth mechanism and potential applications. All-nanoparticle films grow from nuclei that form in the first few bilayers. The ratio of the charge densitites on positively- and negatively-charged nanoparticles determines the nucleation density, which in turn determines film topography (e.g., roughness). Interestingly, positively charged nanoparticles occupy a much smaller

volume fraction in both polymer-nanoparticle and all-nanoparticle LbL films than their negatively charged analogues. As a result, positively charged nanoparticle-polyanion LbL films are much less porous than negatively charged nanoparticle-polycation LbL films.

LbL technology has matured to a point where it is possible to tune film thickness, roughness, and porosity as necessary. LbL nanoparticle thin films assemble on substrates in a highly conformal and uniform manner, and are easily scalable to accommodate very small or very large substrates. Moreover, the coating process is solvent-free, energy-efficient, and coats both sides of the substrate simultaneously. However, lack of sufficient mechanical durability for commercial applications and the difficulty of incorporating functional organic groups into the film present major challenges.

1.3 Thermodynamics of Nanoparticle Thin Films

Porous nanoparticle thin films consist of many loosely-packed nanoparticles in contact with each other. A significant part of this thesis is dedicated to understanding and exploiting the thermodynamic habitat in the pores of nanoparticle thin films for chemical and physical functionalization of the thin films. Specifically, advantageous use of capillary condensation in nanopores as a universal functionalization strategy is of interest. For background information on the physics of capillary condensation, consider the case of two neighboring nanoparticles, with a liquid "bridge" around their point of contact (Figure 1.2). This liquid bridge represents the capillary-condensate.

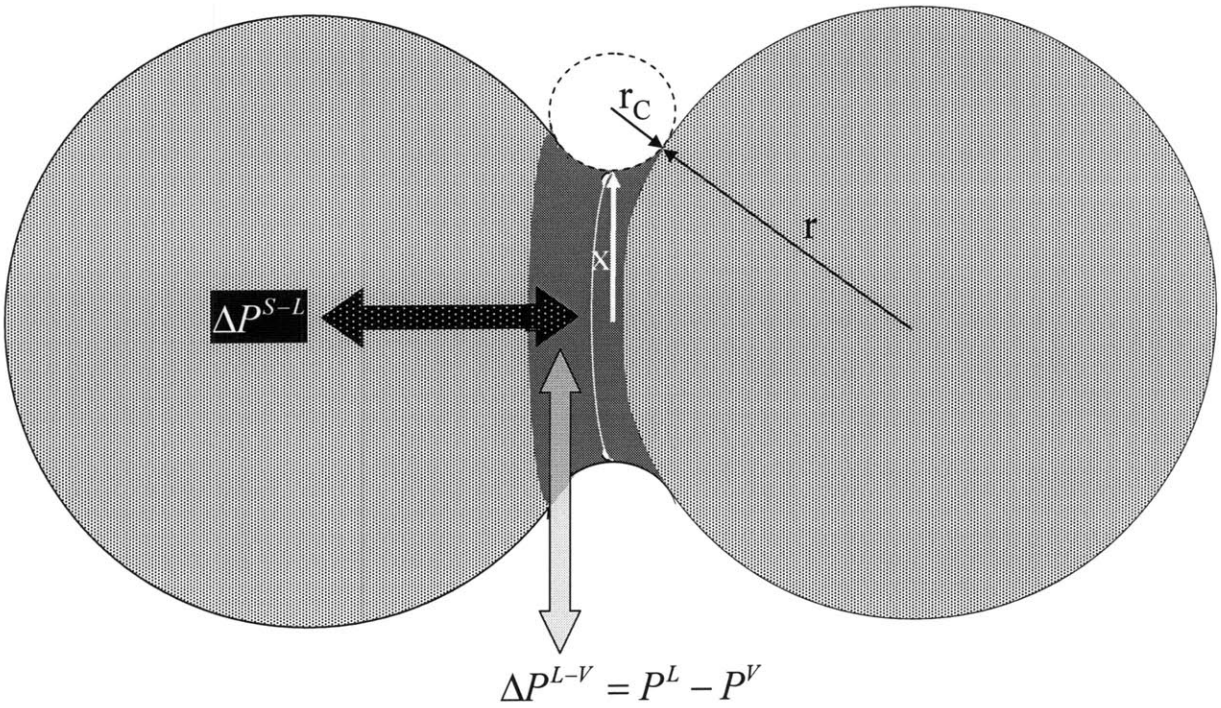

Figure 1.2. Capillary-condensate (blue) between two spherical nanoparticles (gray). A pressure difference exists across both the S-L and the L-V interfaces, due to interfacial curvature.

There are two curved interfaces of interest: the liquid – vapor (L-V) interface, and the solid – liquid (S-L) interface. Assuming assumes a 0° contact angle between the condensate and the nanoparticle surface, the L-V interface is a saddle surface which has two principle radii (x and r_C; see Figure 1.2) with opposite contributions to the pressure difference, ΔP^{L-V}:

$$\Delta P^{L-V} = \gamma^{L-V}\left(\frac{1}{x} - \frac{1}{r_C}\right), \tag{1.1}$$

where γ^{L-V} is the surface tension of the liquid condensate. x and r_C are related by the Pythagorean Theorem:

$$(r + r_C)^2 = r^2 + (x + r_C)^2 \tag{1.2}$$

Solving for r_C and substituting into Equation (1.1), we obtain:

$$\Delta P^{L-V} = \gamma^{L-V}\frac{1}{x}\left(3 - \frac{2r}{x}\right) \tag{1.3}$$

Now consider vapor phase molecules in a dry interparticle capillary. If the molecules condense, $x \to 0^+$ initially, and $\lim_{x\to 0^+} \Delta P^{L-V} = -\infty$. Since $dG = V_m dP$ at constant temperature, where G and V_m are the molar free energy and molar volume of the condensate, respectively, the condensing molecules are welcomed with a large discount in their molar Gibbs free energies. A pressure difference, ΔP, across a curved interface necessitates a Poynting correction to the free energy term[5]. Approximating chemical activity with vapor pressure, the modified energy term predicts a depressed vapor pressure ($P_0^{Capillary}$) for the capillary-condensate liquid[6]:

$$RT \ln\left(\frac{P_0^{Capillary}}{P_0}\right) = \gamma^{L-V} V_m \left(\frac{1}{x} - \frac{1}{r_C}\right), \tag{1.4}$$

where P_0, R and T are the standard vapor pressure of the capillary-condensate, the universal gas constant and the absolute temperature, respectively. The highly curved interfaces found in nanopores promote condensation of surrounding chemical vapors even in sub-saturated conditions. Thus, it is possible to target functional chemical vapors to nanoparticle junctions without grossly altering film morphology. Any two touching spheres are capable of inducing *some* capillary condensation. However, capillary condensation cannot take place once $x = r_C$. $\Delta P^{L-V} = 0$ when $x = r_C = 2r/3$ (Equations 1.2 and 1.4), which marks the theoretical maximum extent of capillary condensation at full saturation. In practice, the extent of capillary condensation is somewhere in between the two limits, depending on the level of vapor saturation. For a given extent of capillary condensation, the volume fraction of the capillary-condensate in a nanoparticle thin film depends on the particle size distribution. These two process parameters will be elaborated on in Chapter 3.

Unlike the L-V interface discussed in the introduction, the S-L interface is a convex spherical dome such that:

$$\Delta P^{S-L} = \gamma^{S-L}\left(\frac{2}{r}\right), \tag{1.5}$$

where r is the nanoparticle radius. Thus, the pressure inside the solid nanoparticle is always greater by ΔP^{S-L} than the pressure in the liquid capillary-condensate. The pressure difference across the

solid-liquid interface elevates the molar Gibbs free energy (and the solubility) of the nanoparticle form (S^{NP}) of a certain chemical species over that of its bulk (i.e., flat interface) form (S^{Bulk})[5]:

$$S^{NP} \simeq S^{Bulk} \exp\left(\frac{2\gamma^{S-L}V_m^{S}}{RTr}\right), \tag{1.6}$$

where V_m^S is the solid-phase molar volume of the nanoparticle material. If S^{Bulk} is appreciable, the condensate can be used to physically join neighboring nanoparticles via a dissolution-redeposition mechanism. This strategy to improve mechanical durability and wear-resistance of nanoparticle thin films will be further explained in Chapter 2.

1.4 Antireflection (AR) films

Light is reflected from any interface between two transparent materials (e.g., glass and air) of different refractive indices. Unwanted reflections reduce the transparency and precision of optical components. For example, ghost images in mirrors and more sophisticated imaging devices composed of multiple lenses in tandem are caused by reflections[7-9].

Antireflection (AR) coatings are key optical components which eliminate unwanted reflections by modulating the refractive index change incident light experiences at interfaces. The simplest type of AR coating is a thin film with a homogenous refractive index in between those of the two transparent media at the interface of which reflections are to be eliminated. Incidentally, the optimal refractive index, n, for such a single-stack thin film is[9]:

$$n = \sqrt{n_1 n_2}\,, \tag{1.7}$$

where n_1 and n_2 are the refractive indices of the two transparent media in between which the single-stack AR film is to be sandwiched. A single-stack film operates by internally reflecting the incident light beam many times within the AR film. These many reflections cause phase shifts in the light wave, and reflecting waves destructively interfere with each other. The phase shift is a function of film thickness (d), and the optical thickness of the AR film ($n \cdot d$) determines which wavelength of incident light (λ) the AR film is optimized for[9]:

$$\frac{\lambda}{4} = n \cdot d \tag{1.8}$$

Thus, a single-stack AR coating does not eliminate reflections at all wavelengths with equal efficiency. A transparent substrate coated with a single-stack AR coating has a single minimum in its reflectance profile and is therefore distinctly colored. Broadband AR coatings operate at much wider wavelength ranges. A broadband AR coating can be (i) a graded-index film[10] whose refractive index varies gradually between those of its neighboring media in order to modulate the otherwise abrupt change in refractive index across the interface, or (ii) a multi-stack film[9] composed of alternating high- and low-index stacks. Different sections of multi-stack films target different wavelengths. Thus, multiple reflectance minima are present in the reflectance profiles of multi-stack broadband AR-coated substrates. Coating performance improves with number of stacks. In contrast, the performance of a graded-index film is limited by how closely the refractive indices at interfaces are matched. For example, the performance of a graded-index AR coating at a glass-air interface is often limited by the lowest index that can be achieved on the air side of the AR coating, since air has an index of approximately unity.

1.5 Thesis Outline

In Chapter 2, hydrothermal treatment is presented as a special instance of capillary condensation (i.e., capillary condensation of saturated steam), where the condensate dissolves and subsequently re-precipitates parts of neighboring nanoparticles to fuse them together and to impart mechanical durability to the entire film assembly. This was, to the best of our knowledge, the first application of hydrothermal treatment on self-assembled nanoparticle thin films for mechanical durability enhancement. The wear-resistances of nanoporous all-nanoparticle and polymer-nanoparticle LbL films (80-150 nm thick) on both glass and polycarbonate substrates were greatly enhanced at relatively low temperatures (124-134°C).

The advantageous use of capillary condensation of chemical vapors into nanoparticle thin films as a more universal functionalization strategy is presented in Chapter 3. The wide array of materials that can be capillary-condensed and the possibility of translating a gradient in particle size (and capillary radius) distribution into a gradient in chemical or physical properties are emphasized. Novel graded-index optical films were prepared as proof of concept. Such films are expected to have a significant

impact on micro-optics applications due to a unique combination of favorable optical and mechanical properties. In situ crosslinking of polymerizable condensates is also demonstrated, and the potential for 3-D patterning is brought to the reader's attention.

A method we developed to utilize stress-induced elastic buckling instabilities for mechanical measurements (SIEBIMM) on colloidal assemblies is discussed next in Chapter 4. Although SIEBIMM and nanoindentation experiments provide essentially identical mechanical property information (i.e., Young's modulus), substrate influences, experimental noise, and concerns of irregular thin film topography are minimized using SIEBIMM. Thin films of interest are assembled on soft elastic substrates (e.g., PDMS rubber) for SIEBIMM studies. Interestingly, the thermodynamic effects which drive capillary condensation of vapor-phase materials into nanoparticle thin films also drive the capillary suction of free and mobile PDMS chains from the underlying elastic substrate into the overlying porous nanoparticle thin film. Cracking and coating delamination are additional problems that plague SIEBIMM studies on colloidal systems. We present a robust experimental procedure which involves a pre-treatment of the PDMS substrate and selection of an appropriate barrier layer between the substrate and the nanoparticle thin film. Youngs moduli of all-nanoparticle and polymer-nanoparticle assemblies are studied as a function of humidity.

Wetting properties of nanoparticle thin films are studied and presented in Chapter 5. A standard wetting diagram analysis is performed on anti-fogging films by Cebeci et al[11] and superhydrophobic films by Bravo et al[12]. While topographic characterization by atomic force microscopy (AFM) did not reveal any differences between films with drastically different wetting behaviors, a wetting diagram analysis reveals structural trends with increasing film thickness. The influence of capillary effects on wetting properties and film ageing are also touched upon.

LbL multi-stack broadband AR coating design and synthesis are presented in Chapter 6 as a cheap, aqueous solution-based alternative to vacuum deposition of multi-stack AR coatings. An old, often overlooked and underappreciated optical thin film design method for broadband AR coatings is presented and utilized. The method we employed can perform significantly better than some widespread commercial optical film design algorithms (e.g., the Needle algorithm), particularly when the permissible number of stacks or film thickness are limited. The effects of inter-stack and surface roughness on optical properties of these constructs (e.g., haze and spectral response) have been studied quantitatively using a combination of Fourier-transform methods and AFM measurements.

Finally, conclusions from the thesis work and suggestions for future research are presented in Chapter 7.

Chapter 2

Capillary Condensation of Saturated Steam via Hydrothermal Treatment for Enhanced Mechanical Durability

2.1 Introduction

Thin films functionalized with nanoparticles show great promise in applications for optics[13, 14], display technology[15], photonics[16], and catalysis[17] to name a few. Much of the effort in this area has focused on the assembly and characterization of novel nanostructures. However, there have been relatively few reports addressing the mechanical durability (or robustness) of nanoparticle thin films, particularly from the perspective of challenges consumer products are expected to face in everyday use. Even in specialty applications where films are isolated from the outside world, some durability is required to complete manufacturing processes defect-free.

While nanoindentation[18] and scanning force microscopy[19-21] (SFM) studies have elucidated strong secondary interactions between nanoparticles and between nanoparticles and flat surfaces, a covalently linked, fused structure may be necessary to impart durability to the entire film. Similarly, the reinforcing effect of nanoparticles in elastomers improves with increasing particle-matrix interactions[22]. Many nanoparticle deposition techniques (e.g., sol-gel chemistry[23], dip coating, spin coating) allow incorporation of crosslinking agents and monomers into the coating formulation, albeit with limited control over the resulting nanostructure. Subsequent curing steps lead to extensive interconnectivity and mechanical robustness. Nanoparticle assembly techniques (e.g., layer-by-layer[2], Langmuir-Blodgett[24, 25], *in situ* nanoparticle synthesis within polymer matrices[26]) allow precise control and rational design of both physical (e.g., thickness, refractive index, optical transparency) and chemical (e.g., functionality, surface energy) properties. Assembly is often driven by van der Waals, electrostatic, hydrogen bonding, and other secondary interactions[27]. Secondary interactions are relatively weak over macroscopic length scales and therefore do not impart sufficient mechanical durability to the entire film. Auxiliary components (e.g., crosslinking agents) may not be compatible with the assembly technique. Instead, infiltration of polymerizable species into pre-assembled structures has been attempted. Rouse et al.[28], for example, have investigated infiltration of sol-gel

precursors into polymer/silicate sheet composites and the subsequent gelation of the precursors. Infiltration techniques, however, inevitably alter surface functionality, porosity, become auto-inhibitory as coating thickness increases, and may not be compatible with multilayer coatings. Miguez et al.[29] used chemical vapor deposition (CVD) to adsorb and hydrolyze $SiCl_4$ monolayers on stacks of silica microspheres. Several adsorption/hydrolysis cycles were sufficient to strengthen the nanoparticle construct. However, surface functionality (e.g., catalytic) may be annulled by encapsulation within inert SiO_2 shells. The requirement of a perfectly anhydrous environment and the extreme reactivity of $SiCl_4$ further complicate CVD processing.

An alternative, brute-force solution to the robustness problem is calcinating a nanoparticle assembly at high temperatures. Porous silica nanoparticle films on soda lime glass, in the absence of reactive or polymerizable species, require heating at ~550°C[11], a temperature close to the annealing temperature of soda lime glass. Cross-sectional scanning electron microscope (SEM) micrographs of calcinated silica nanoparticle films on glass show sintering among nanoparticles, as well as melting and fusion at the substrate-film interface (see Figure B.1). 550°C is not sufficient for silica nanoparticle films on silicon wafers, quartz, or sapphire substrates, all of which have higher annealing temperatures. Such high-temperature processes are not possible on plastic substrates. In addition to limiting substrate choice, high temperatures destroy organic components. Organic-inorganic nanocomposites, however, have been shown to synergistically improve mechanical properties[28].

In his landmark book, *The Chemistry of Silica*, Iler[30] discusses hot water and hydrothermal (i.e., steam) treatments for mechanical reinforcement of silica gels, such as catalyst supports or highly structured silicas. The discussed techniques are based on fusion of neighboring, nanoscale features into smoother necks. The necking process has the same thermodynamic basis as Ostwald ripening: nanoparticles have enhanced solubilities, and dissolved species minimize their free energies by precipitating onto larger particles with sufficiently large radii of curvature[5]. In nanoparticle assemblies, convex regions with negative radii of curvature are available in between neighboring nanoparticles, where dissolved material deposits and forms necks. A more detailed thermodynamic discussion can be found in Section 1.3. A few studies[31, 32] of accelerated crystallization and porosity control in spin-coated sol-gel titania films mention the reinforcement effect of hot water and

hydrothermal treatments. However, hydrothermal reinforcement of delicate nanoparticle thin film assemblies remains largely unexplored.

The LbL assembly of oppositely charged polyelectrolytes[33] has attracted much attention in recent years. Charged nanoparticles have also been integrated into LbL films[1, 3, 11, 12, 21, 34-58]. A great virtue of the LbL assembly technique is its capability to produce uniform, conformal thin film coatings of virtually any charged polymer or nanoparticle species, with morphological and compositional control over the resultant multilayer assembly[59]. Despite the fact that many commercially attractive functionalities have been demonstrated, most nanoparticle-containing LbL films are easily damaged with gentle rubbing. This clearly has limited practical application and impeded large-scale technological development.

In this chapter, we explore the use of hydrothermal treatments to enhance the mechanical durability of LbL-assembled polymer-nanoparticle and all-nanoparticle multilayer thin films. We demonstrate that significant improvements in mechanical durability can indeed be realized. To our knowledge, this is the first report of the successful mechanical reinforcement of LbL nanoparticle assemblies by hydrothermal treatment, and we anticipate that this approach can be extended readily to delicate structures created using other assembly techniques.

2.2 Results and Discussion

As a vehicle for exploring mechanical durability, we focused on the AR properties of nanoparticle containing multilayer films. Without an antireflection coating, a typical glass substrate ($n \sim 1.52$) in air ($n \sim 1$) transmits ~92% of incident light, due to ~4% reflective losses at each interface[7, 8]. Single-layer antireflection coatings are created by depositing a thin film with quarter-wavelength optical thickness and intermediate refractive index (between that of air and the substrate). A particularly challenging problem is the construction of low-index coatings with acceptable mechanical properties. MgF_2 is a common low-index component ($n \sim 1.38$) in antireflection coatings[8]; the dense structure of MgF_2 coatings contributes to its good mechanical properties. However, lower refractive index coatings (indices as low as 1.23) are required for optimal single-layer antireflection coatings on substrates such as glass and polycarbonate (PC, $n \sim 1.52$-1.59). The low (and readily tunable) refractive index possible with specific nanoporous thin film coatings containing randomly packed nanoparticles provides a means to achieve this requirement. With such coatings, the response to a

mechanical challenge can be ascertained by measurements of light transmittance and/or reflectance before and after testing, thereby providing a technologically relevant performance metric.

Low refractive index, nanoporous thin film coatings were fabricated from both polymer-nanoparticle[57] and all-nanoparticle[1] LbL assemblies (see Section 2.4.2). In the case of the polymer-nanoparticle thin films, 15 nm negatively charged silica nanoparticles were assembled with a positively charged polymer (poly(diallyldimethylammonium chloride), PDAC). For the all-nanoparticle thin films, negatively charged silica nanoparticles (15 nm) and positively charged 3-aminopropylsilane-modified silica nanoparticles (15 nm), or silica and titania (5 nm) nanoparticles were assembled into all-silica[3] or silica-titania[1] nanoparticle thin films. The refractive indices of the PDAC-silica and all-silica nanoparticle films were n ~ 1.25-1.26, whereas the refractive indices of silica-titania nanoparticle thin films were n ~ 1.31. In all cases, mechanical durability was examined on films with thicknesses in the range of 80-150 nm. Over this range, durability was essentially independent of film thickness.

The mechanical durability of the resultant thin film coatings was assessed both qualitatively and quantitatively. The qualitative test involved rigorous rubbing with KimWipes®. In the more quantitative abrasion test, two different normal stresses (25 kPa and 100 kPa) were applied with rotational shear (150 rpm for 1 hour) in an automatic metal polisher (see Section 2.4.6 for more details). It should be noted that the standard industrial test applies a 25 kPa normal stress. Samples were examined for mechanical damage by visual observation and optical and scanning electron microscope (SEM) measurements. As noted above, transmittance/reflectance measurements were used to determine changes in AR performance. Since only one side of a coated substrate is abraded, the maximum possible loss in peak transmittance is ~4%[7, 60].

Two technologically important substrates for anti-reflection coatings were evaluated: soda lime glass and polycarbonate. The results obtained with glass substrates are presented first, as the use of glass makes it possible to compare the results of hydrothermal treatments directly with those obtained by well-established high temperature treatments. For all of the multilayer systems evaluated, on both glass and polycarbonate, as-assembled films were easily removed and/or severely damaged by gentle rubbing. This underscores the importance of identifying a process that can make these coatings more mechanically robust.

2.2.1 Films on Soda Lime Glass Substrate

Figures 2.1, 2.2, and B.2 display SEM images of various multilayer thin film coatings on soda lime glass before and after either thermal or hydrothermal treatment. As-assembled, all-silica nanoparticle films consist of discrete spherical silica particles (Figure 2.1a). Both negatively- and positively-charged silica particles are of approximately the same size (15 nm) and therefore cannot be distinguished visually. High-temperature calcination somewhat densifies the film and hence increases the refractive index slightly (from n ~ 1.26 to n ~ 1.28), but does not appear to significantly alter surface morphology (Figure 2.1b); the particles do not lose their granularities. Hydrothermally treated silica particles, on the other hand, begin forming significantly fused structures at 134°C (Figures 2.1c and 2.1d). Particles fuse via a dissolution/redeposition mechanism, the thermodynamic basis of which has been described earlier[5, 30]. In hydrothermal environments, silica nanoparticles release soluble silicates which then re-deposit in confined convex regions (e.g., between neighboring nanoparticles). It should be noted that extensive particle fusion as observed by SEM is not necessary for mechanical robustness. For example, calcinated films on soda lime glass are mechanically durable, but appear almost identical to as-assembled films in plane-view SEM micrographs.

PDAC-silica (Figure 2.2a) and all-silica (Figure 2.1a) nanoparticle films, in their as-assembled states, are both composed of discrete nanoparticles. However, PDAC-silica nanoparticle films on soda lime glass require less heat than all-silica nanoparticle films to form noticeably fused structures upon autoclaving. While the PDAC-silica nanoparticle film becomes an interconnected organic-inorganic composite at only 124°C (Figure 2.2c), extensive particle fusion is not noticeable in all-silica nanoparticle films autoclaved below 134°C (Figure 2.1c). Whether the polymer component promotes interparticle necking by chemical or physical (e.g., by altering structure, or by providing a scaffold for redeposition) means is not clear and deserves further investigation.

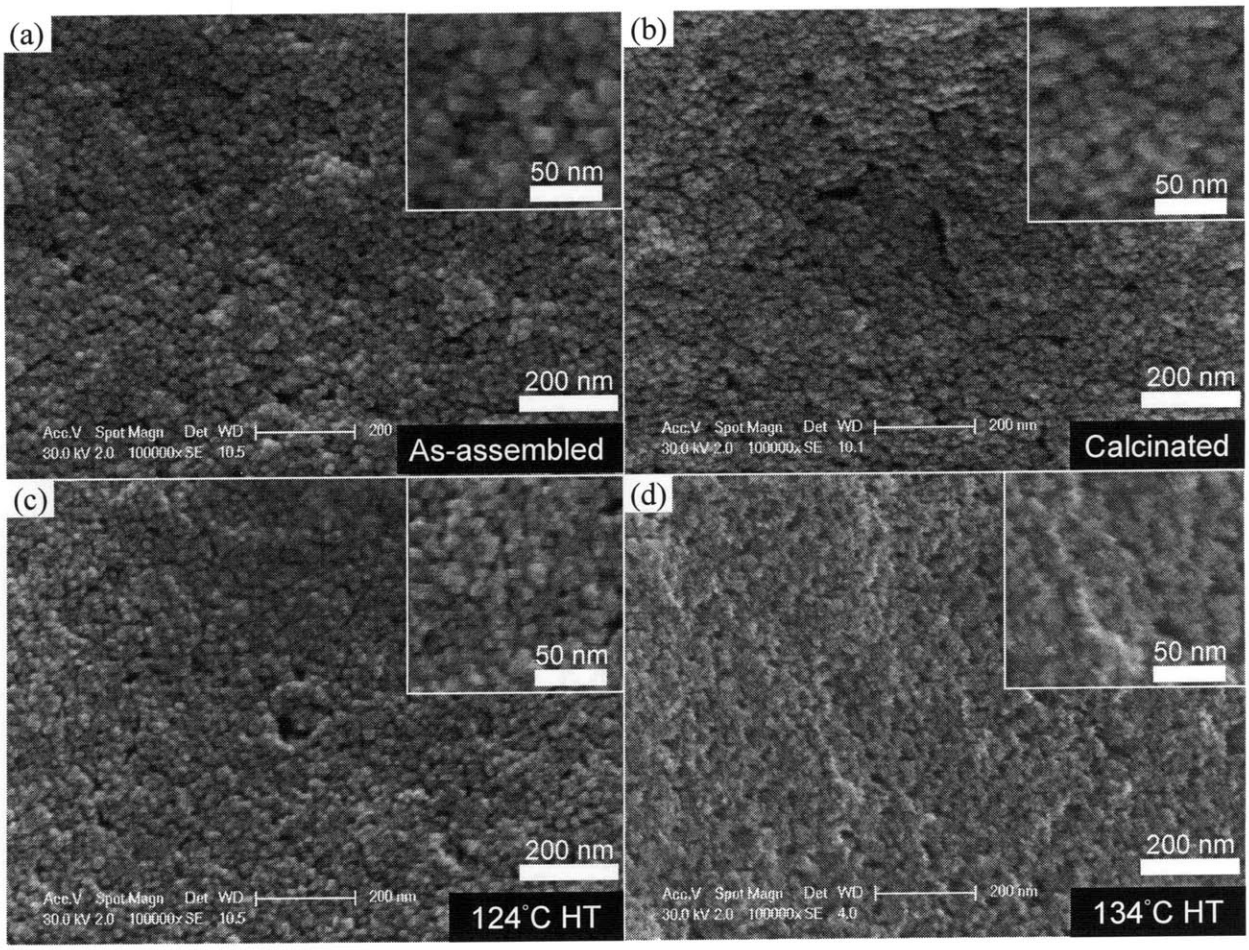

Figure 2.1. (a) An as-assembled all-silica nanoparticle film with no mechanical durability, (b) a calcinated, durable all-silica nanoparticle film, (c,d) durable all-silica nanoparticle films autoclaved for 1 hour at 124°C and 134°C, respectively. HT stands for hydrothermal treatment. Each micrograph has been digitally magnified in its corresponding inset.

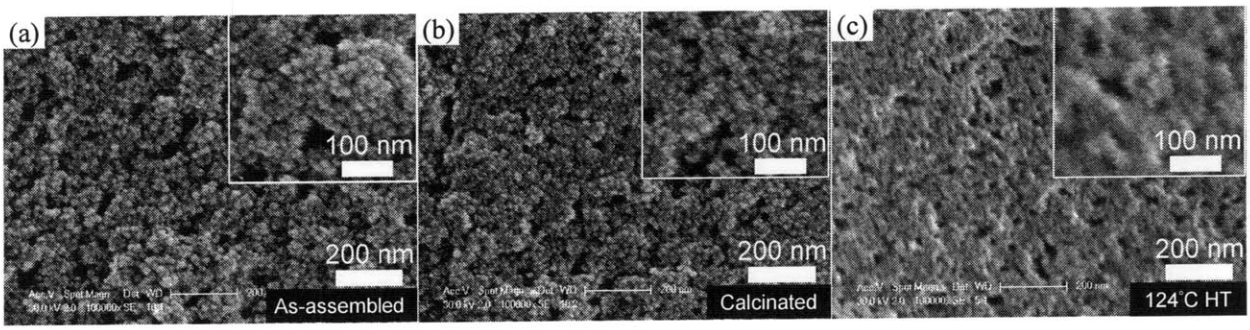

Figure 2.2. (a) An as-assembled PDAC-silica nanoparticle film with no mechanical durability, (b) a calcinated, durable PDAC-silica nanoparticle film, (c) a durable PDAC-silica nanoparticle film autoclaved for 1 hour at 124°C. HT stands for hydrothermal treatment. Each micrograph has been digitally magnified in its corresponding inset.

In parallel to their more extensively fused structures, autoclaved PDAC-silica nanoparticle films are more durable than all-silica nanoparticle films in the quantitative abrasion test. As explained earlier, all tested films have low refractive indices and act as single-layer antireflection coatings, with optimal performance at a single wavelength. The various autoclaved, calcinated, and as-assembled films enable >99% transmittance on glass at their optimal wavelength. In the case of all as-assembled films, mild manual rubbing results in a ~4% decrease in transmittance at the optimal wavelength due to complete removal of the film from one side of the underlying glass substrate. Under a 25 kPa normal stress – an industry standard – all-silica nanoparticle films autoclaved at 124°C for 1 hour showed minimal changes in transmittance. Therefore, a higher normal stress of 100 kPa was adopted as the standard testing condition in order to resolve differences in durability among various films. A representative pair of transmittance curves (before/after testing) of an all-silica nanoparticle film autoclaved at 124°C for 1 hour is shown in Figure 2.3a. The various films have been ranked from 1 (most durable, less than 0.2% decrease in transmittance) to 3 (least durable, more than 0.6% decrease in transmittance) in Table 2.1, and individual data points are graphed in Figure 2.3b. The autoclaved PDAC-silica nanoparticle film performed best and ranked first. The autoclaved all-silica nanoparticle film ranked second, along with autoclaved silica-titania, calcinated silica-titania, and calcinated PDAC-silica nanoparticle films. The calcinated all-silica nanoparticle film ranked third.

Differences in film durability inferred from transmittance measurements can be observed directly in SEM micrographs. Autoclaved all-silica nanoparticle films on soda lime glass are shown in

Figures 2.4a and 2.4b before and after abrasion testing, respectively. The most pronounced scratches observed in Figure 2.4b are macroscopically visible and several microns wide. Autoclaved and tested PDAC-silica nanoparticle films are shown in Figure 2.5. No macroscopic damage is apparent in PDAC-silica nanoparticle films. The possibility of damage at the outer edge of a PDAC-silica nanoparticle film (which travels the longest distance during rotational motion) was suggested by darker bands of color (Figure 2.5c). Damage was confirmed by the observation of shallow, microscopic scratches visible at higher magnification (Figure 2.5d). Such scratches contribute to the ~0.1% loss in transmittance of abraded PDAC-silica nanoparticle films, as antireflection functionality is extremely sensitive to film thickness.

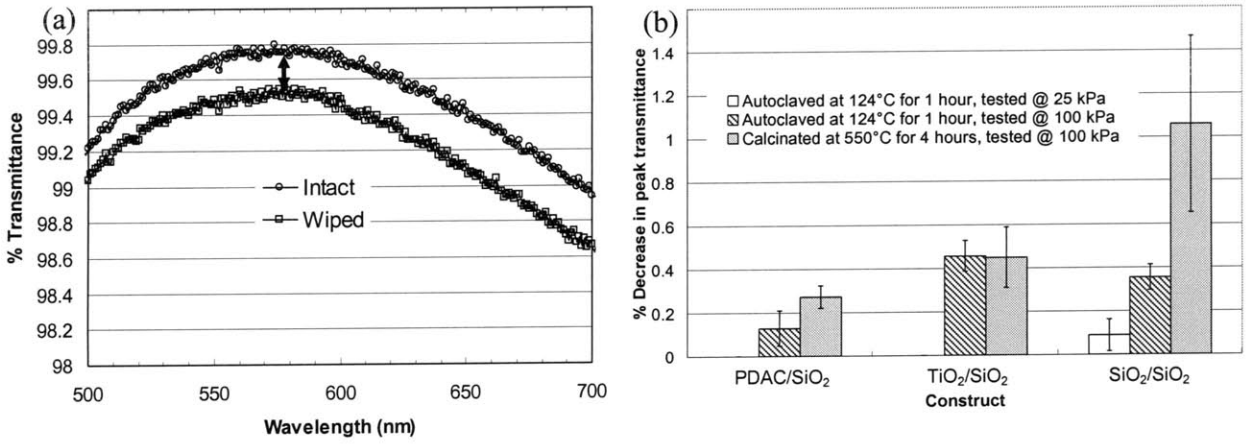

Figure 2.3. (a) A representative pair of transmittance curves before and after quantitative abrasion testing of an autoclaved (124°C, 1 hour) all-silica nanoparticle film under a 100 kPa normal stress, and (b) the difference between peak transmittance levels (as shown with an arrow in (a)) averaged and plotted for various film constructs.

Table 2.1. A ranking of various films on soda lime glass in terms of their abrasion resistance under a 100 kPa normal stress. Films have been ranked from 1 (most durable, less than 0.2% decrease in transmittance) to 3 (least durable, more than 0.6% decrease in transmittance). As-assembled films show no durability and at least a 4% decrease in transmittance[60]. HT stands for hydrothermal treatment.

System	Film	Quantitative Testing Rank	
		124°C HT	550°C Calc.
All-nanoparticle	All-silica	2	3
	Silica-titania	2	2
Polymer-nanoparticle	PDAC-silica	1	2

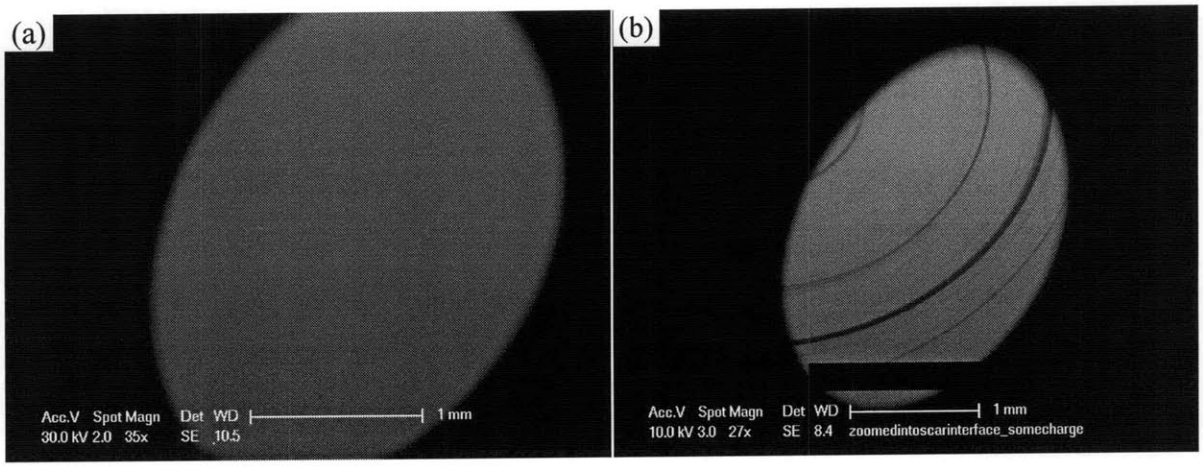

Figure 2.4. (a) An autoclaved (124°C, 1-hour) all-silica nanoparticle film (b) after abrasion testing under a 100 kPa normal stress. Dark regions in (b) are scratched and worn regions.

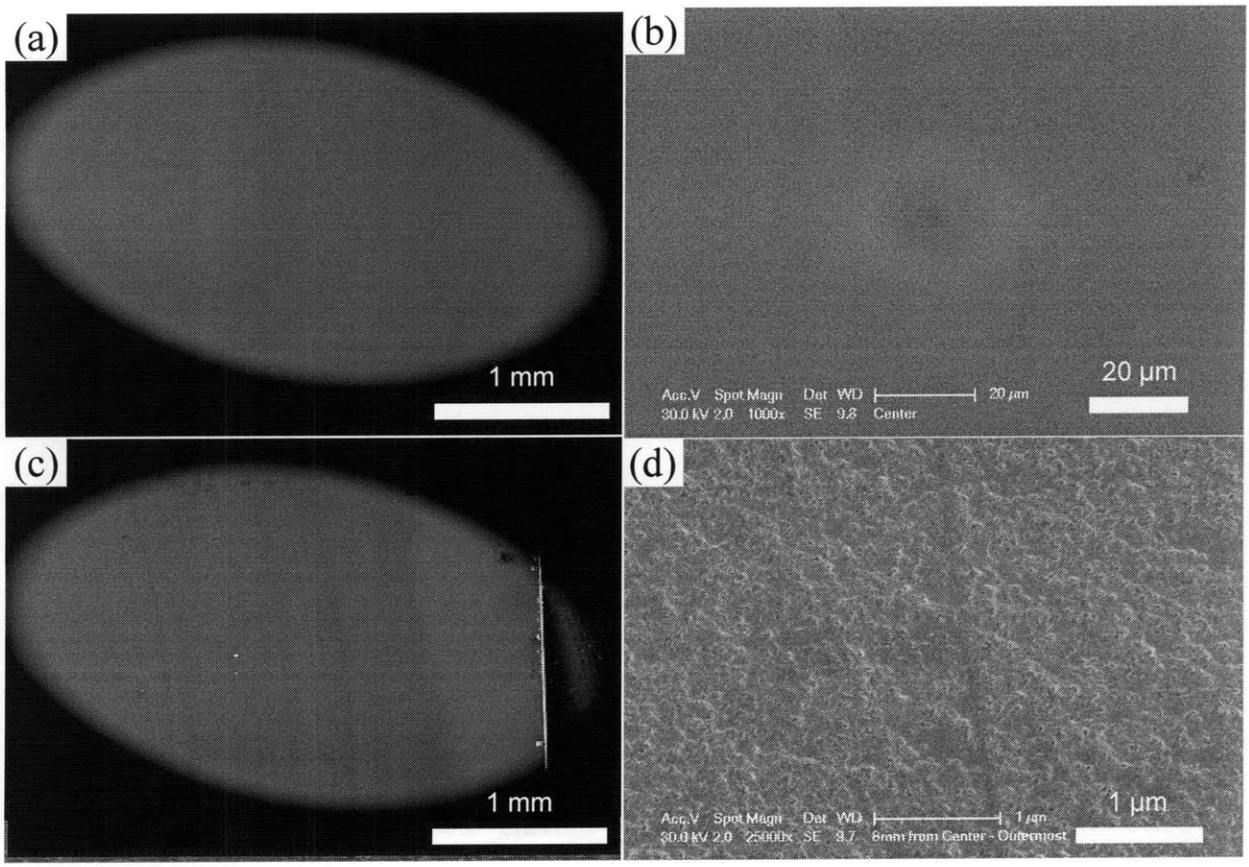

Figure 2.5. Autoclaved (124°C, 1 hour) PDAC-silica nanoparticle films after abrasion testing under a 100 kPa normal stress. (a) and (b) show the central region. Since the sample is wiped rotationally, the edge is damaged more than the center. A microscopic scratch on the edge of the sample is shown in (d), and a group of such scratches in low magnification are indicated with arrows in (c).

Chemical composition (i.e., presence of organic components) and the packing density of the films (i.e., geometric considerations and porosity) influence mechanical durability. Retention of PDAC in autoclaved PDAC-silica nanoparticle films was confirmed with X-ray photoelectron spectroscopy (XPS). A high-resolution Nitrogen (N) scan of a PDAC-silica film is presented in Figure 2.6. The high and low energy peaks correspond to quaternized and non-quaternized N signals, respectively[61]. Figure 2.7 quantifies the peaks in Figure 2.6.

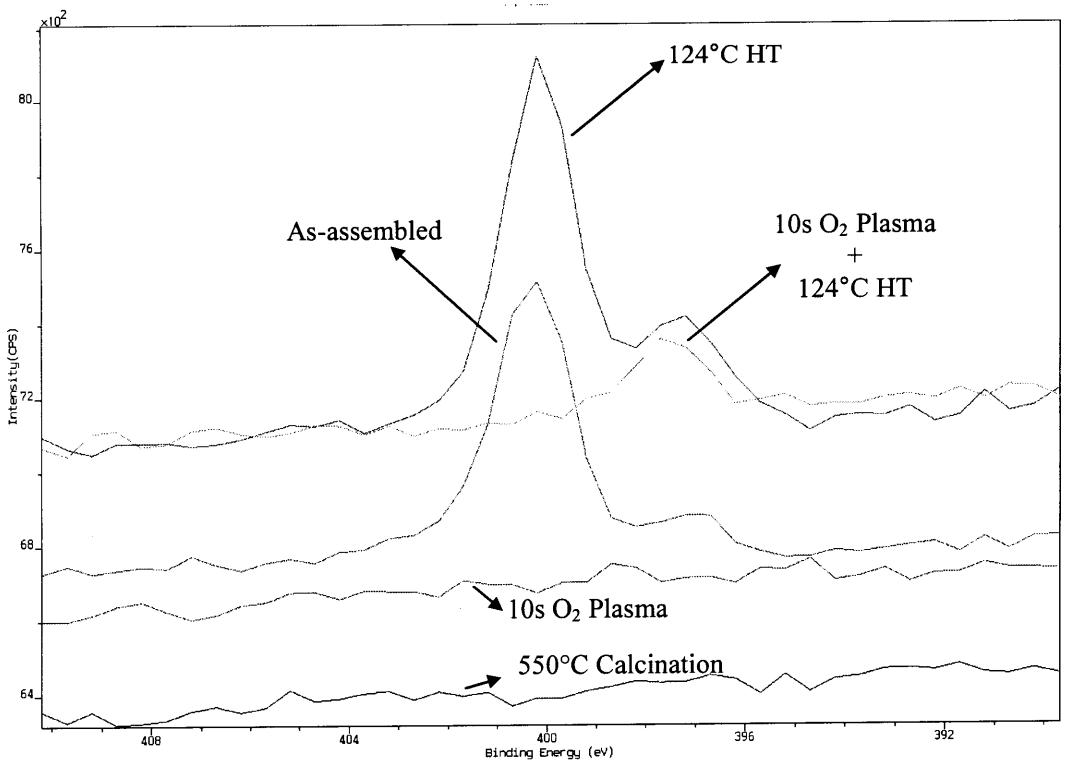

Figure 2.6. High-resolution Nitrogen (N) XPS spectra of ~100nm-thick PDAC-silica films on glass. These films are terminated with PDAC at the air interface. HT stands for hydrothermal treatment.

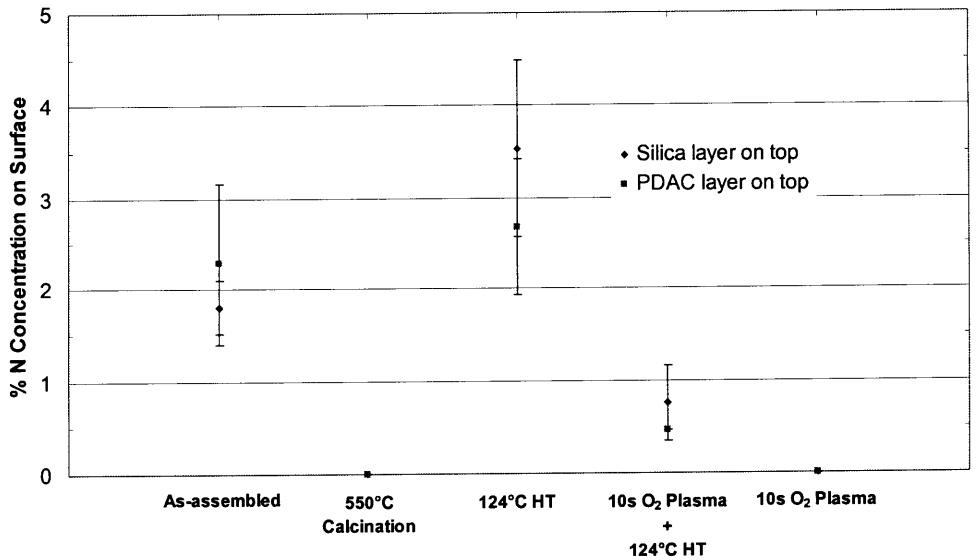

Figure 2.7. XPS results show that hydrothermal treatment does not eliminate PDAC from the surface. HT stands for hydrothermal treatment.

In addition, Fourier-transform infrared spectroscopy (FTIR) measurements indicate that hydrothermal treatment does not degrade PDAC to any significant extent. In contrast, high-temperature calcination eliminates PDAC from the film completely. 100 bilayers of PDAC-poly(styrene-4-sulfonate) (SPS) were assembled on ZnSe substrate in the presence of 0.1 M NaCl. FTIR spectra of the film was recorded in the as-assembled state, then after 10s O_2 plasma treatment (to mimic the pre-hydrothermal treatment conditioning of films assembled on soda lime glass), and finally after hydrothermal treatment at 124°C for 1 hour. The results are presented in Figure 2.8. Unlike nanoparticle-containing films, the autoclaved polymer-polymer film was hazy. Haze leads to a wavelength-dependent artificial reduction in transmittance. Therefore, the slope of the autoclaved film spectrum in the range of 2500-2800 cm^{-1} was different from those of as-assembled and only plasma-treated film spectra. In order to allow for an easier comparison, both the plasma-treated and autoclaved film spectra were re-scaled to match the slope of the as-assembled film spectrum in the 2500-2800 cm^{-1} range. An offset has been introduced to match the levels of transmittance in the 2500-2800 cm^{-1} region. Hence, the % transmittance is presented in arbitrary units.

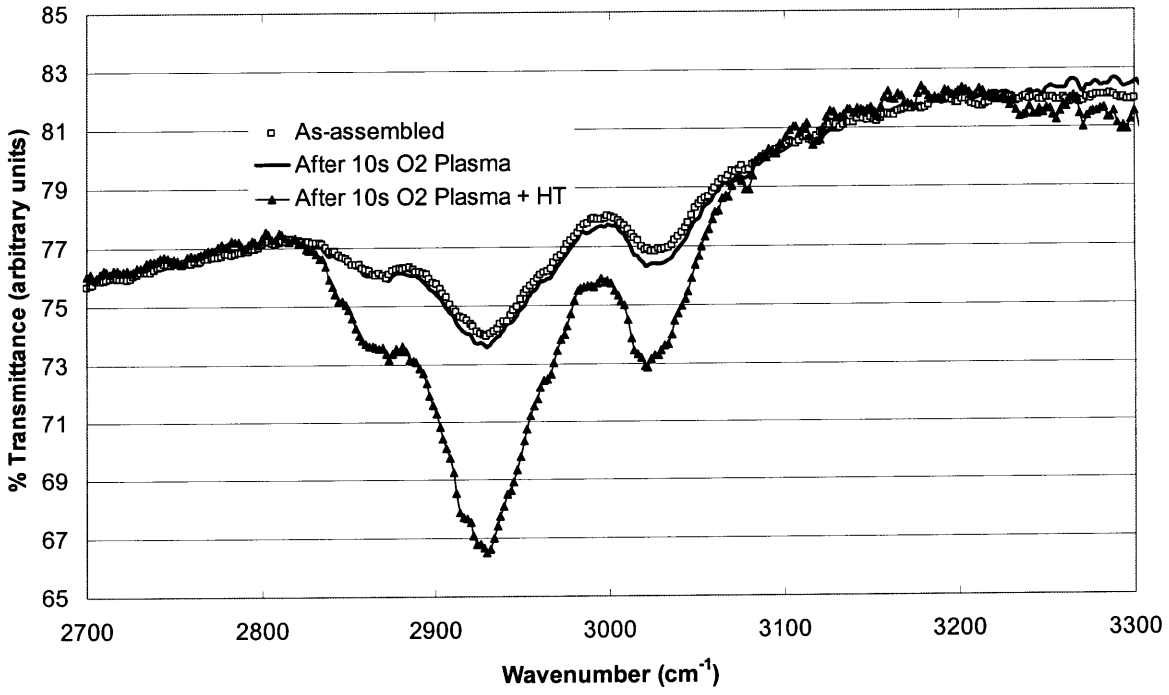

Figure 2.8. FTIR spectrum of 100 bilayers of PDAC-SPS assembled on ZnSe substrate in the presence of 0.1 M NaCl. HT stands for hydrothermal treatment.

Autoclaved PDAC-silica nanoparticle films are more durable than both calcinated PDAC-silica nanoparticle films and autoclaved all-silica nanoparticle films. As discussed earlier, the presence of PDAC enhances particle necking upon hydrothermal treatment. It is worth noting, however, that the refractive indices of both PDAC-silica and all-silica nanoparticle films remain essentially unchanged upon hydrothermal treatment at 124°C for 1 hour; porosity is not reduced significantly.

Calcinated PDAC-silica nanoparticle films are more durable than calcinated all-silica nanoparticle films. Hence, the polymer component appears to play a role even in the high-temperature process, where it is degraded. Simulations by Jeon et al[62] suggest that the polymer component in polymer-nanoparticle films provides sufficient mobility and room for rearrangement during film assembly to form more complete and cohesive layers at each step, as compared to all-nanoparticle films. Morphological differences between all-nanoparticle and nanoparticle-polymer systems may distinguish calcinated PDAC-silica nanoparticle films from calcinated all-silica nanoparticle films.

Up to this point we have presented in detail all-nanoparticle and polymer-nanoparticle LbL films with remarkably enhanced mechanical properties on glass substrates. Focusing on the films themselves and ignoring any substrate effects we have concluded that polymer-nanoparticle films are more durable than all-nanoparticle films. The potential of a low-temperature, hydrothermal process as a versatile means of nanoparticle thin film reinforcement has been demonstrated. The major advantage of a low-temperature process, however, is its applicability on plastic substrates of industrial importance, such as polycarbonate. Indeed, as will become apparent, hydrothermal treatment enhances mechanical durability of both polymer-nanoparticle and all-nanoparticle films on polycarbonate. Since the thermal and chemical properties of a substrate can affect both the calcination and hydrothermal treatment processes, it is worthwhile to discuss the role of the substrate before proceeding to our results on polycarbonate.

Soda lime glass contains a significant amount of sodium; Na^+ ions decrease the annealing temperature of soda lime glass from ~1000°C to 547°C and also cause corrosion under hydrothermal environments[30] by increasing the solubility of silica. We hypothesize that enhanced thermal and chemical mobility of soda lime glass under calcination and hydrothermal treatment conditions, respectively, induces mixing and improves adhesion at the glass-coating interface; treated coatings pass the crosshatch adhesion test (i.e., the scotch-tape test). In addition to improving adhesion of the film to the underlying substrate, Na^+ ions that corrode away from soda lime glass during

hydrothermal treatment can also accelerate the dissolution/redeposition mechanism that necks neighboring particles within the film. Thus, both thermal and hydrothermal treatments successfully impart mechanical robustness to films on soda lime glass. Quartz and silicon wafers do not contain Na^+ ions and have high annealing temperatures (~1000°C). Particle fusion is not noticeable in all-silica nanoparticle films on quartz and silicon wafer substrates (see Figure B.3) upon hydrothermal treatment up to 134°C. In addition, neither autoclaved nor calcinated all-silica nanoparticle films are robust on quartz and silicon wafers (see Table 2.2). Thus, adhesion to the substrate upon thermal or hydrothermal treatments depends largely on the chemical and thermal properties of the substrate. Reactive and/or thermally mobile substrates are preferable. As for the film parameters that influence mechanical durability, chemical composition and nanoscale architecture of the film (e.g., surface coverage of each layer), as well as extent of particle interconnectivity and densification are important.

Table 2.2. Correlation between noticeable particle necking as observed by SEM and qualitative mechanical durability of various films on various substrates. HT stands for hydrothermal treatment.

System			Qualitative Durability		Particle Necking Noticeable Under SEM?
Film		Substrate	124°C HT	550°C Calc.	(HT Temperature)
All-nanoparticle	All-silica	Soda Lime Glass	Good		Yes (134°C)
		Polycarbonate	Good	N/A*	No
		Silicon Wafer	Poor		No
		Quartz	Poor		No
	Silica-titania	Soda Lime Glass	Good		Yes (124°C)
Polymer-nanoparticle	PDAC-silica	Soda Lime Glass	Good		Yes (124°C)

* Films on polycarbonate substrate cannot be calcinated at 550°C.

2.2.2 Films on Polycarbonate Substrate

Clearly, thermal calcination is not possible on plastic substrates. Hydrothermal treatment thereby enables significant improvements in the mechanical durability of LbL films on plastic substrates, such as polycarbonate. Polycarbonate is Na^+-free (confirmed by XPS, data not shown) and has a relatively low Tg (~140°C). Polycarbonate cannot provide supplementary Na^+ ions to promote particle necking, but is close to its Tg under the low-temperature hydrothermal treatment conditions (124°C) and therefore has a thermally mobile surface. Analogous to other Na^+-free substrates, hydrothermal treatment up to 134°C does not noticeably fuse all-silica nanoparticle films on polycarbonate (see Figure B.3). In contrast to other substrates, however, the all-silica nanoparticle films autoclaved on polycarbonate at 124°C are mechanically robust. The results suggest that

substrate properties (thermal and chemical) determine whether hydrothermal treatment of a film can result in any qualitative improvement in durability. If the substrate is compatible with hydrothermal treatment, film properties (e.g., interconnectivity, particle size distribution, porosity etc.) determine finer differences among various films.

Bare polycarbonate abrades significantly and develops substantial haze under a 25 kPa normal stress (Figure 2.9a). As shown in Figure 2.10, abrasion induces 2-6% scattering-related loss of transmittance in bare polycarbonate. Extremely thin (~100 nm-thick) all-silica and PDAC-silica nanoparticle antireflection films (autoclaved at 124°C for 1 hour) not only substantially increase the transmittance of intact, bare polycarbonate (Figure 2.10), but also successfully protect polycarbonate in abrasion testing (Figures 2.9b and 2.9c as compared to Figure 2.9a). Transmittance curves of the PDAC-silica nanoparticle film overlap in Figure 2.10 before and after abrasion testing, making the two curves indistinguishable. The all-silica nanoparticle film, on the other hand, loses 0.1-0.5% transmittance (Figure 2.10). Thus, our conclusion that the PDAC-silica nanoparticle film is more durable than the all-silica nanoparticle film based on experiments performed on glass substrate have been confirmed on polycarbonate substrate. While some scratches are observed on the periphery of the abraded all-silica nanoparticle film (Figure 2.9b), the abraded PDAC-silica nanoparticle film (Figure 2.9c) appears completely intact. The peak transmittance level of PDAC-silica nanoparticle films (~94%) autoclaved on polycarbonate is significantly lower than that of autoclaved all-silica nanoparticle films (~99%). The reduction in AR performance is due to a densification-induced increase in refractive index. Interestingly, hydrothermal treatment does not densify polymer-nanoparticle or all-nanoparticle films on glass to such a significant extent. This difference is most likely related to the chemical activity of soda lime glass, as discussed earlier, and is under investigation.

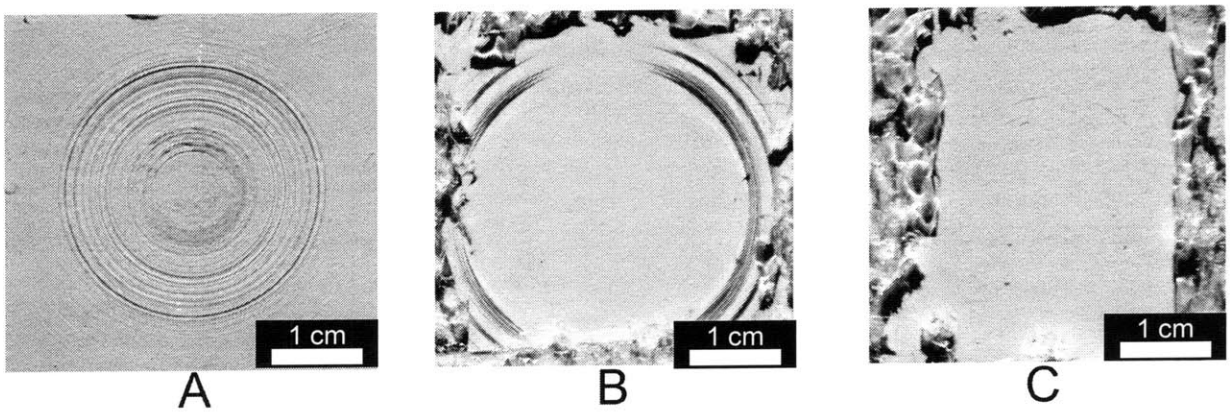

Figure 2.9. After abrasion testing under a 25 kPa normal stress, photographs of (a) bare polycarbonate, (b) bare polycarbonate coated with ~100 nm-thick, autoclaved (124°C, 1 hour) all-silica nanoparticle film, (c) bare polycarbonate coated with ~100 nm-thick, autoclaved (124°C, 1 hour) PDAC-silica nanoparticle film. Adhesive residue is observed on the peripheries; double-sided tape was used to attach specimens onto sample holders during abrasion testing (see Section 2.4.6 for more details).

2.2.3 Wear Mechanisms

Abrasive and tribochemical wear appear to be the two most relevant wear mechanisms common to both all-nanoparticle and polymer-nanoparticle films. Scratches generated in abrasion testing are not regions of complete delamination (Figure 2.11). Even macroscopically large scratches are delaminated only at their centers, suggesting that coating delamination does not occur easily but is instead the result of continual abrasive wear. Third bodies are generated upon film delamination in the form of silica aggregates, and are also introduced from the testing environment in the form of dust. Third bodies can scrape coating off the substrate and generate more third bodies to facilitate a runaway delamination process. For example, bare and coated soda lime glass (as-assembled) abrade differently. While the 100 kPa test does not damage bare glass, as-assembled all-silica nanoparticle films delaminate within 10 seconds and the resulting debris scores and scratches the underlying glass substrate during an hour-long abrasion test (Figure 2.12). Considering the hardness of glass, this result suggests an abrasive mode of wear[63] and highlights the effect of loosely bound asperities on the coating surface. Abrasive wear is illustrated in Figure 2.13 on an autoclaved (124°C, 1 hour) all-silica film on glass under a 25 kPa normal stress. The involvement of a third body is clear,

resembling a growing snowball. Another microscopic scratch on an autoclaved (124°C, 1 hour) all-silica film tested under a 100 kPa normal stress is shown in Figure 2.14. The film inside these wear tracks has not delaminated, demonstrating good adhesion to the substrate.

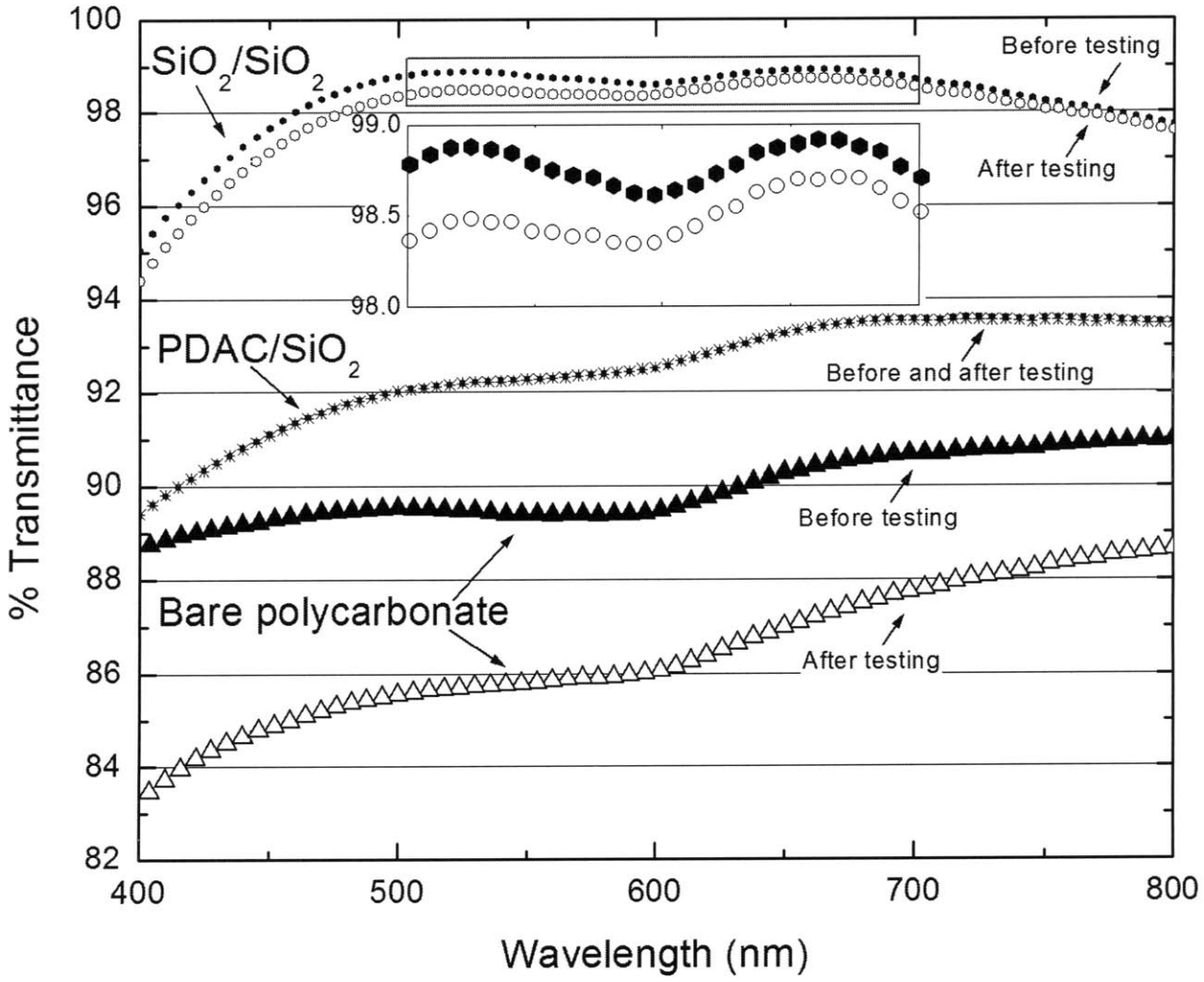

Figure 2.10. Transmittance curves of bare and coated (~100 nm all-silica and PDAC-silica nanoparticle films autoclaved at 124°C for 1 hour) polycarbonate substrates before and after abrasion testing under a 25 kPa normal stress. Transmittance curves of PDAC-silica nanoparticle films before and after abrasion testing overlap and are therefore indistinguishable. All-silica nanoparticle films are damaged minimally, as detailed in the inset.

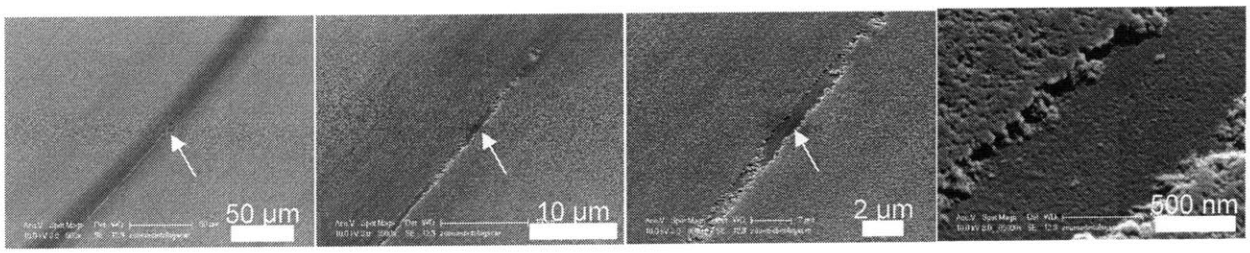

Figure 2.11. A macroscopic scratch on an autoclaved (124°C, 1 hour) all-silica nanoparticle film on glass substrate, abraded under a 100 kPa normal stress. Note that the scratch is wide (darker region), but only a small portion of it has delaminated. The periphery has thinned down, yet remains adherent to the substrate.

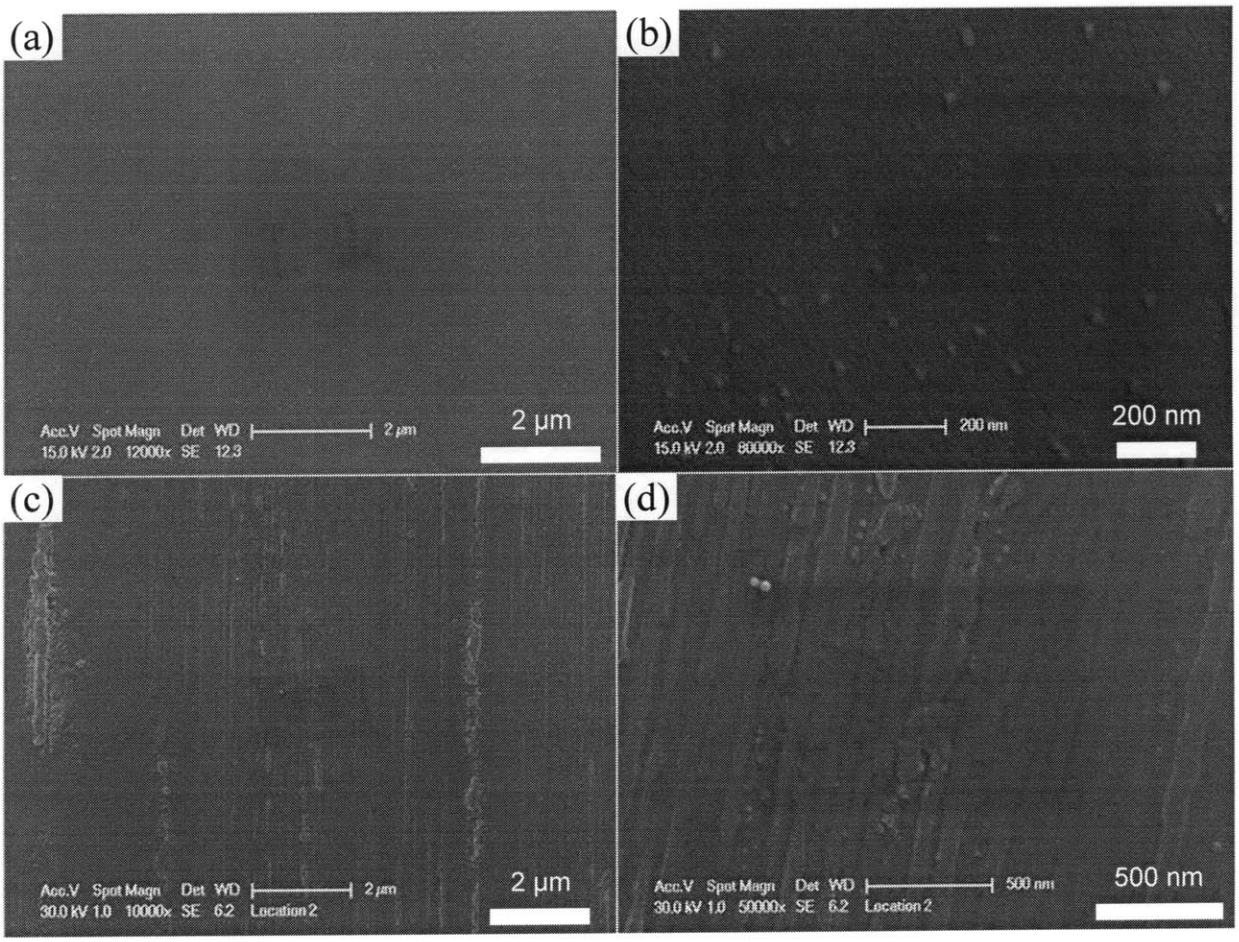

Figure 2.12. (a,b) Bare and (c,d) coated soda lime glass with an all-silica nanoparticle film in its as-assembled state after abrasion testing under a 100 kPa normal stress.

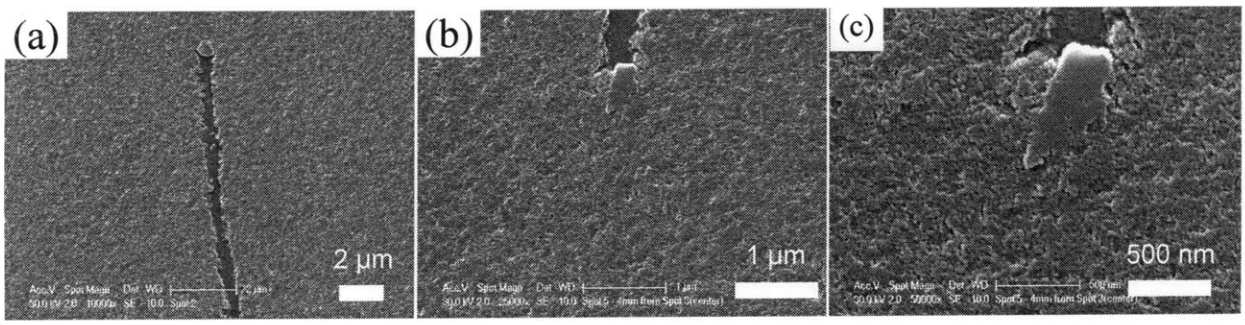

Figure 2.13. Third bodies play an important role in abrasive wear. (a) and (b) show two different locations of autoclaved (124°C, 1 hour) all-silica nanoparticle films on glass, tested under a 25 kPa normal stress. Micrographs (b) and (c) differ only in magnification.

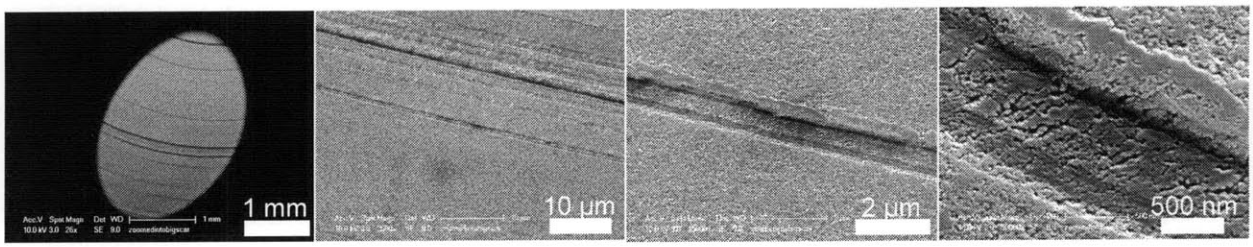

Figure 2.14. A microscopic scratch on an autoclaved (124°C, 1 hour) all-silica nanoparticle film on glass substrate, abraded under a 100 kPa normal stress. The coating has not delaminated, and wear tracks are visible.

None of the films discussed are "scratch-resistant." Pencils of all hardnesses scratch the surface, but the depth of the scratch ranges from only 10% to 40% of the original coating thickness, as determined using profilometry on glass substrates (see Supporting Information). The results suggest good adhesion to the substrate. Extreme thinness (only ~100 nm) and high porosity (~45%) of these nanoparticle-containing films are most likely parameters that limit scratch resistance.

Scratch-free regions of both all-silica and PDAC-silica nanoparticle films are smoothed out and flattened upon abrasion testing (Figures 2.15 and B.4). Nanoscale roughness on the nanoparticle-decorated surface is replaced by caked regions. Plastic deformation of the surface under the influence of frictional heating may account for some of the flattening. However, we believe tribochemical wear contributes to flattening as well. Fischer and Mullins[64] explain the ability of humidity to reduce wear of Si_3N_4 by tribochemical surface oxidation of Si_3N_4 to silica, followed by the formation of water-soluble silicic acid. Silica surfaces are known to release silicic acid during chemo-mechanical

polishing as well[65]. The resulting smooth surfaces accomodate hydrodynamic lubrication. Alumina behaves similarly[66]. Kato[67] suggests that such a reaction layer acts as a soft coating, such as MoS_2, in terms of its wear mechanism.

Surface roughness and morphology are critical for both superhydrophilic and superhydrophobic surfaces; it has been pointed out previously[68] that preservation of surface nanotexture is a major bottleneck in developing practical applications. The few studies[69] that have addressed this issue have placed much emphasis on hardness and/or scratch-resistance. However, the nanostructured textures typically used to create surfaces with extreme wetting behavior can be easily planarized by tribochemical wear.

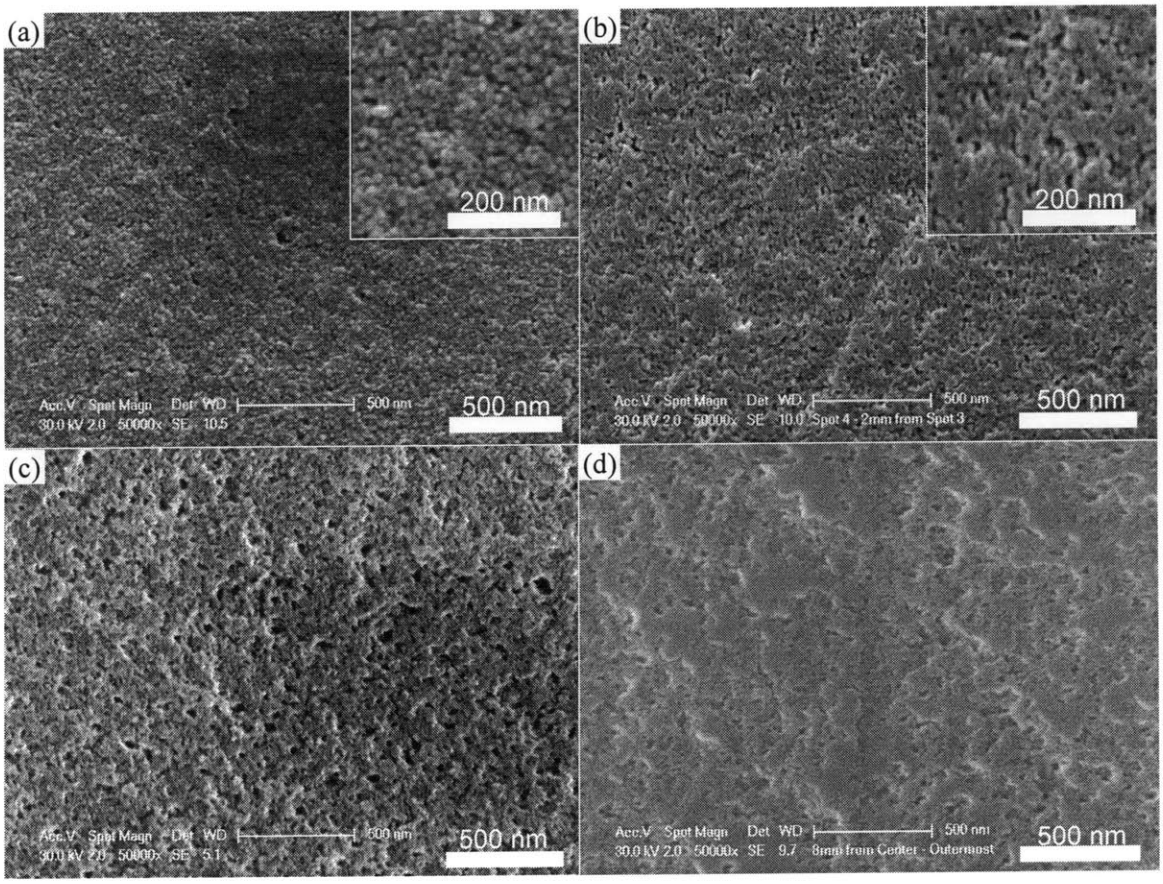

Figure 2.15. Autoclaved (124°C, 1 hour) all-silica nanoparticle film (a) before and (b) after abrasion testing under a 25 kPa normal stress. (c) and (d) are autoclaved (124°C, 1 hour) PDAC-silica nanoparticle films before and after testing under a 100 kPa normal stress, respectively. Micrographs (a) and (b) have been digitally magnified in their corresponding insets.

2.3 Conclusions

The mechanical durability of all-nanoparticle and polymer-nanoparticle LbL films, which in the as-assembled form can be readily damaged by gentle rubbing, has been substantially improved using a low-temperature process on both glass and polycarbonate substrates. Polymer-nanoparticle composites were found to be more durable than all-nanoparticle films. The presence of a polymer appears to enhance particle necking on glass and film densification on polycarbonate substrates, which may be correlated to an increase in durability. However, both necking and densification phenomena show substrate dependence. Thus, enhancement of durability requires attention to both substrate and film properties.

Future studies relating wear to porosity, composition, particle size, Young's modulus, friction coefficient, etc. should provide useful engineering design guidelines and extend attainable functionalities beyond suppression of light reflection. In particular, tribochemically inert surfaces may preserve nanoscale surface texture more effectively than surfaces made of silica nanoparticles. The SIEBIMM technique[70] has been used to further detail mechanical properties of interest (Chapter 4). A durable multilayer, broadband AR design has also been implemented (Chapter 6).

The historical application of hydrothermal treatment to sol-gel materials has thus been extended in scope to potentially encompass delicate and diverse nanoparticle assemblies for modern applications. In the LbL field, hydrothermal treatment may help enable commercialization efforts.

2.4 Materials and Methods

2.4.1 Materials

Anatase titanium oxide nanoparticles (1.37 g/L suspension in water, average particle size of 5-6 nm) were synthesized as described elsewhere[71]. Silica nanoparticles with native negative surface charge, Ludox® HS-40 (40 wt.% SiO_2 dispersion in water, average particle size of 15 nm, and specific surface area of ~220 m^2/g), 3-aminopropylsilane-modified silica nanoparticle preparation (3 wt.% SiO_2 suspension in ethanol, average particle size of 15 nm) with positive surface charge, and poly(diallyldimethylammonium chloride) (PDAC, 20 wt.% aqueous solution, average molecular weight of 200,000-300,000 g/mol) were purchased from Sigma-Aldrich (St. Louis, MO). The

average size of modified silica nanoparticles was provided by the suppliers, and the average sizes of silica and titania nanoparticles were determined by dynamic light scattering (DLS). 3″x1″ and 3″x2″ glass slides were purchased from VWR International and Erie Scientific, respectively. Both suppliers use Electroverre® glass manufactured by Erie Scientific (Switzerland). Bare polycarbonate was kindly provided by Teijin-Kasei Corporation. Polycarbonate was pre-treated with 400 mTorr oxygen plasma (PDC-32G, Harrick Scientific Products, Inc.) for 10 s on both sides. Polishing cloth (DP-NAP) with adhesive backing was purchased from Struers Inc.

2.4.2 Film Assembly

Sequential adsorption of polymers and nanoparticles was performed using an automated dipping machine. PDAC-silica and silica-titania films were dipped in a StratoSequence VI spin dipper (nanoStrata Inc.), controlled by StratoSmart v6.2 software, at 120-130 rpm. All-silica films were dipped in an HMS Series Programmable Slide Stainer (Carl Zeiss, Inc.) controlled by a software developed in-house. The concentration of polymers and nanoparticles were 0.01 M and 0.03 wt.%, respectively; as an exception, Ludox® particles were used at 0.023 wt.% concentration and filtered through a 0.20 μm cellulose acetate filter prior to dilution. Titania particles were filtered through a 0.02 μm aluminum oxide (Anotop®, Whatman International Ltd., England) filter prior to dilution. Distilled water (> 18 MΩ·m, Millipore Milli-Q) water (MQ water) was used to dilute the nanoparticle suspensions to the desired concentration. Glass substrates were degreased using Alconox® (Alconox, Inc.) detergent powder under sonication for 15 min, and then cleaned with 1.0 M NaOH solution under sonication for another 15 min. Finally, the substrates were sonicated in MQ water for 5 min and blow-dried with dry air. The dipping time in each polymer or nanoparticle solution was 10 min followed by three rinse steps (2, 1, and 1 min) in deionized water. All-silica and silica-titania films were dipped at pH 4.5 and pH 3.0, respectively, and rinse water was adjusted to the same pH as deposition solutions. PDAC-silica films were dipped from pH 4.0 and pH 9.0 PDAC and silica solutions, respectively. Hazy films were obtained when the films were rinsed at pH 4.0 and 9.0 after dipping in PDAC and silica solutions, respectively. Therefore, rinse water pH was not adjusted when assembling transparent PDAC-silica films. All films were 80-150 nm thick. Thickness and refractive index were measured using a Woollam Co. VASE spectroscopic ellipsometer; the data

analysis was done using the WVASE32 software package. The ellipsometry technique is described in Section 2.4.5.

2.4.3 High-Temperature Calcination and Hydrothermal Treatment

A Barnstead Thermolyne 47900 furnace was used to calcinate the films at 550°C for 4 h. The films were placed into the furnace slightly tilted against an aluminum foil support. A Tuttnauer-Brinkmann model 2340M autoclave was used for hydrothermal treatment. ~350 mL fresh MQ water was placed into the autoclave chamber manually in every cycle. The slides were placed onto the autoclave tray vertically using clamp holders. Films on glass slides were treated with oxygen plasma (PDC-32G, Harrick Scientific Products, Inc.) for 10 s on both sides at 400 mTorr prior to hydrothermal treatment. While the effect of plasma pre-treatment is not clear, it prohibits formation of water marks on glass substrates after autoclaving. Films on polycarbonate substrates were autoclaved without any pre-treatment.

2.4.4 Dynamic Light Scattering (DLS) Measurements

DLS was performed at an angle of 90° using a Brookhaven BI-200SM light scattering system (Brookhaven Instruments Corporation). A 3 min integration time was used. The autocorrelation function was fit using the cumulant method and CONTIN algorithms in the software provided by the instrument manufacturer, and intensity-averaged size distributions were recorded. 12x75 mm borosilicate test tubes (VWR Cat# 47729-570) were used after overnight washing in concentrated sulfuric acid, followed by thorough deionized water (> 18 MΩ·m, Millipore Milli-Q (MQ)) and methanol rinses and a drying step.

2.4.5 Ellipsometry Measurements

Thickness and refractive index were measured using a Woollam Co. VASE spectroscopic ellipsometer; the data analysis was done using the WVASE32 software package. Measurements were done using 250 to 900 nm light at a 70° angle of incidence. Measurements were fit to a Cauchy model, which assumes that the real part of refractive index (n_f) can be modeled as $n_f(\lambda) = A_n + \frac{B_n}{\lambda^2} + \frac{C_n}{\lambda^4}$, where A_n, B_n, and C_n are constants and λ is the wavelength of incident light.

In our experiments, C_n was set to 0 and refractive index values were determined at 632 nm. Uncoated substrates were first scanned and their properties were saved. It was necessary to roughen the back sides of transparent substrates in order to eliminate reflections from the transmittance side and to collect reflections only from the incidence side. A stack of two Cauchy layers was used to model coated slides.

2.4.6 Abrasion Testing

The quantitative abrasion test was adapted from the Taber abrasion test (ASTM D 1044) and the Cleaning Cloth Abrasion Test of Colts Laboratories, a widely accepted testing laboratory serving the ophthalmic industry[72]. The cleaning cloth abrasion test by Colts Laboratories[73] involves rubbing a lens with a soft cloth for 4000 cycles, where one cycle consists of one back-and-forth motion. The motion range of the testing instrument (i.e., the distance traveled by the cloth in each back or forth motion) is ~0.5 in. Then, the total path length the cloth travels on the lens is $0.5\times 2\times 2.55\times 10^{-3}\times 4000 = 102m \simeq 100m$. The lens diameter is 4.5 cm, and 10 lb (44.5 N) force is applied. Thus, the normal stress is ~28 kPa. In this study, abrasion testing was performed using a Struers Rotopol 1 polishing machine equipped with a Pedemat automatic specimen mover (Figure 2.16), operated at 150 rpm against a dry Struers DP-NAP polishing cloth. The Pedemat specimen mover can apply a minimum of 30 N force in the single sample mode. Therefore, the polishing cloth was cut into 2 and 4 cm circles to achieve approximately 25 kPa and 100 kPa normal stresses, respectively. Since the samples were abraded with rotational motion, the edges of the samples travel the longest distance while the centers of the samples should – in theory – remain stationary. The spectrophotometer beam spot is an 8 mm-long, thin line. Therefore, if the beam is aligned at the center of an abraded sample, the measured transmittance samples the film from the center to a 4 mm radius. Assuming $abrasion \propto (pressure)\times(path\ length)$, the duration of abrasion, t, in our in-house test that would be equivalent to the industrial test can be calculated as follows:

$$P_1 \cdot l_1 = \frac{t \cdot RPM \cdot P_2 \cdot \int_0^{r_S} (2\pi r)dr}{\int_0^{r_S} dr}$$, where P_1 and l_1 are pressure and path length of the industrial test, respectively. P_2 is the pressure applied in the in-house test, r_S is the spectrophotometer beam radius

(in our case, half of beam length, or 4 mm), and *RPM* is the rate of revolution of the metal polishing disk. Using the above equation, one calculates that ~15 and ~60 minutes of testing are necessary using 100 and 25 kPa normal stresses, respectively. All abrasion tests were run for 60 minutes. Variation in relative velocity along the sample radius was ignored, although some mathematical models of wear (e.g., Preston's equation[74]) suggest shear-rate-dependence.

All samples were gently washed with a cellulose sponge (Shaw's Supermarkets, Inc.) soaked in 2% MICRO-90® solution (International Products Corporation) before and after abrasion testing. The washing step is critical, as contaminants from the cloth infiltrate the porous coatings and increase their refractive indices. Therefore, immediately after abrasion testing and before washing with soap, regions of a coating in contact with the cloth appear to have lost antireflection (AR) functionality completely. However, a simple wash cleans the coatings perfectly.

Samples were adhered to the sample holder using CRL 3M™ .020" x 1/4" Transparent Double-Sided VHB™ Tape, purchased from C.R. Laurence Co., Inc. The adhesive was cured at 50°C for 30-60 minutes, and then cured at room temperature for another 30-60 minutes to ensure good adhesion of the sample to the polisher holder. The sample was removed from the holder with a razor blade after testing.

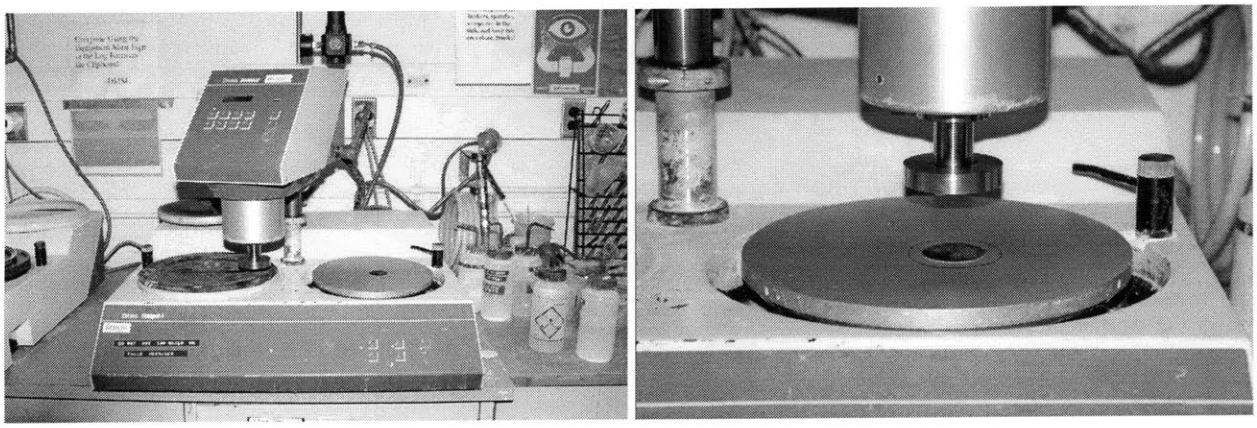

Figure 2.16. The metal polishing instrument, modified to perform the quantitative abrasion test. The bottom wheel was held stationary while the top wheel was rotated at 150 rpm.

2.4.7 UV/Visible Spectrophotometry

A Cary 5E UV-Vis-NIR spectrophotometer (Varian, Inc.) was used to record transmittance spectra.

2.4.8 Pencil Hardness Testing

Mars Lumograph® (Staedtler Mars GmbH & Co. KG, Germany) pencils ranging in hardness from 8B to 6H were used. The films were scratched manually, at an ~45° to the surface. Sufficient force was applied to crush the pencil tip. Graphite particles and dust left inside the scratches and on the film were eliminated by dipping the scratched films into Piranha solution for 15 minutes. Piranha solution was prepared by mixing equal volumes of concentrated sulfuric acid and 50% hydrogen peroxide (SAFETY NOTE: PIRANHA SOLUTION IS EXTREMELY DANGEROUS AND REACTS VIOLENTLY WITH ALL ORGANIC MATERIALS. PLEASE CONSULT THE LITERATURE[75, 76] PRIOR TO EXPERIMENTING WITH PIRANHA SOLUTION YOURSELF). The piranha solution was allowed to equilibrate for 5 minutes prior to use. Depth profiling was done using a P10 (KLA-Tencor Corporation) surface profiler. Data points were collected every 10-20 nm at a tip speed of 2 μm/s.

2.4.9 X-Ray Photoelectron Spectroscopy (XPS)

An X-ray photoelectron microscope (Kratos Axis Ultra; Kratos Analytical of Manchester, England) was operated with a monochromatic Al source at 150 W. Survey and high-resolution data were acquired with pass energies of 160 and 80 eV, respectively.

2.4.10 Fourier-Transform Infrared Spectroscopy (FTIR)

A Nicolet Magna-IR 550 Spectrometer Series II, controlled by OMNIC v.6.1a software, was used. Polished ZnSe windows (25x2 mm) were purchased from Crystran Ltd, UK. 100 bilayers of PDAC-SPS were assembled on ZnSe substrate in the presence of 0.1 M NaCl. FTIR spectra of the film was recorded in the as-assembled state, then after 10s O_2 plasma treatment (to mimic the pre-hydrothermal treatment conditioning of films assembled on soda lime glass), and finally after hydrothermal treatment at 124°C for 1 hour.

2.4.11 Scanning Electron Microscopy (SEM)

A Philips XL-30 environmental SEM was used in high-vacuum mode for imaging. All samples were sputter-coated with 10 nm Au/Pd prior to imaging, and were mounted onto SEM stubs using carbon paste.

Chapter 3
Chemical Modification via Capillary Condensation

3.1 Introduction

Modification of nanoporous materials can be used to tune their surface interactions or to make organic-inorganic composites[77, 78]. Nanoparticle thin films, nanotube forests[79], membranes[80], and catalyst supports[81] are porous materials of particular interest. Successful surface functionalization methods have included the formation of self-assembled monolayers on surfaces[82, 83], grafting and chemical coupling[84], conformal coating strategies[85, 86], and the use of block copolymers or surfactants[87, 88]. The versatility of these chemical functionalization methods, however, has been limited by requirements for particular substrate surface chemistries, compatible solvents, and concerns over uncontrolled extents of reaction. Here we describe the advantageous use of capillary condensation, a well-known natural phenomenon in nanoporous materials, as a more universal functionalization strategy[89].

3.1.1 Background and Motivation

Capillaries in porous materials facilitate the condensation of sub-saturated vapors, because the condensate vapor pressure is depressed inside capillaries according to the Kelvin equation[6]. Capillary condensation is responsible for the infamous sensitivity of nanoporous materials to water vapor (humidity) and other adventitious vapors. While many of the past efforts have been focused on protecting nanoporous media from the negative consequences of naturally occurring capillary condensation[77, 90], we exploit capillary condensation of carefully chosen solvents, oligomers and monomers to impart desirable mechanical and optical characteristics to nanoparticle thin films. The thermodynamic nature of capillary condensation allows the use of hydrophilic, hydrophobic, reactive, or inert chemical vapors with equal facility to functionalize nanoporous thin films. We first present a theoretical analysis of how treatment conditions (e.g., temperature) can be adjusted to target films composed of nanoparticles of a certain size range. We then exploit the particle (or pore) size dependency of capillary condensation in conjunction with the morphological control inherent in the LbL assembly technique[38, 44, 59, 91] to generate chemical and physical gradients through the coating

thickness. Finally, we demonstrate *in situ* UV-crosslinking of capillary-condensed monomers in comparison with stitching together of neighboring nanoparticles through a dissolution-redeposition mechanism facilitated by the condensation of solvents.

As explained in Section 1.3, the vapor pressure of a liquid confined in a capillary between to spherical nanoparticles ($P_0^{Capillary}$) is lower than the standard vapor pressure (P_0) of the same liquid[6]:

$$RT \ln\left(\frac{P_0^{Capillary}}{P_0}\right) = \gamma^{L-V} V_m \left(\frac{1}{x} - \frac{1}{r_C}\right), \tag{3.1}$$

where γ^{L-V} and V_m are the surface tension and the molar volume of the liquid condensate, respectively. R, T, x, and r_C are the universal gas constant, the absolute temperature, and the two principal radii characterizing the saddle-shaped L-V interface, respectively (see Figure 1.1). Assuming a 0° contact angle between the condensate and the nanoparticle surface, the case of $x = r_C = 2r/3$ represents the theoretical maximum extent of capillary condensation at saturation (see Section 1.3 for derivation). Note that equation (1) balances two energy terms: (i) the demand for stabilization on the left hand side, dictated by thermodynamic parameters temperature and vapor pressure, and (ii) the supply of stabilization on the right hand side, dictated by interfacial curvature (geometry) for a specified liquid. On the x-axis of Figure 3.1 is plotted the geometric supply term, and on the y-axis is shown what fraction of the maximum theoretical condensation can ensue for a given extent of stabilization and particle size (Figure 3.1 inset).

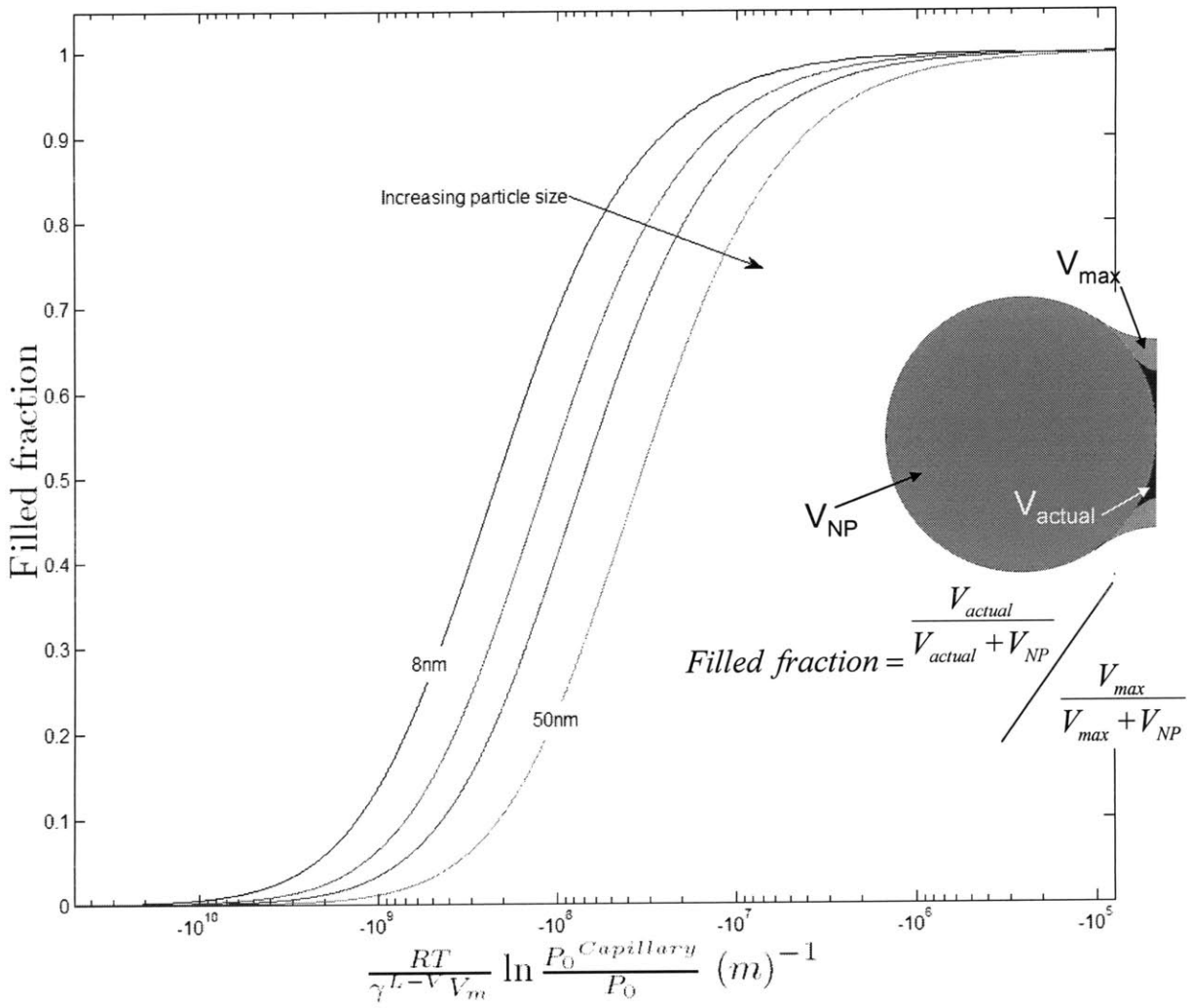

Figure 3.1. The fractions of condensate in nanoparticle-condensate mixtures with various nanoparticle sizes are plotted as functions of the interfacial curvature at the L-V interfaces, which provide the thermodynamic stabilization necessary for capillary condensation. The condensation temperature and the material properties of the condensate determine the point of interest on the x-axis. The y-axis is normalized against the maximum possible fraction of condensate, and the normalization procedure is shown in the inset.

The extent of capillary condensation in thin films has a particle size-dependence under certain treatment conditions. A high-temperature process pushes the energy demand for capillary condensation to the far left of the x-axis. Only the very close vicinity of the interparticle contact point can afford such a high demand for stabilization, and almost no condensation occurs for any particle

size. At low temperatures (far right on the x-axis), an almost negligible interfacial curvature is sufficient to induce capillary condensation and the theoretical maximum for condensation is achieved ($x = r_C = 2r/3$) for any particle size. Notice that no particle-size dependence is observed in either limiting case. However, between the two extremes, the volume fraction of the condensate in a film shows strong particle size-dependence. The refractive index of a dielectric thin film can be approximated as the volume-weighted average index of its constituents[92]. Thus, capillary condensation in a porous film can be monitored by the refractive index increase.

3.2 Results and Discussion

LbL-assembled films (100-160 nm in thickness) composed of a polycation, poly(allylamine hydrochloride) (PAH), paired with negatively charged SiO_2 nanoparticles of various sizes (8 nm, 24 nm, or 50 nm in diameter)[12] were exposed to vapors of water (n~1.33), poly(dimethylsiloxane) (PDMS, MW ~ 700-800 g/mol, n ~ 1.40), or tri(ethyleneglycol) dimethacrylate (TEGDMA, n ~ 1.46) (see Supporting Information for experimental details). The two vapors at the opposite extremes of the hydrophilicity scale (namely, PDMS and water) capillary-condensed readily in the films composed of various particle sizes. As expected, film refractive index is inversely correlated to the particle size and directly correlated to the condensate refractive index (Figure 3.2), although the difference between PAH/8 nm SiO_2 and PAH/24 nm SiO_2 films was not as stark as predicted in Figure 3.1. Particle size polydispersity in the 24 nm SiO_2 nanoparticle dispersion may contribute to this effect. Nevertheless, a PAH/8 nm SiO_2 and PAH/50 nm SiO_2 films are indeed very different in terms of their capillary condensation characteristics. We took advantage of this particle size-dependence to produce refractive index gradients through the film thickness. 2-stack PAH/8 nm SiO_2 + PAH/50 nm SiO_2 films were functionalized with PDMS and TEGDMA vapors at 100°C (Figure 3.3a). The bottom and top stacks are composed of 8 nm and 50 nm SiO_2 nanoparticles, respectively. Capillary condensation into the entire 2-stack structure enhances the index contrast between the top and bottom stacks, because the refractive index of the bottom stack is much more sensitive to capillary condensation. The volume fraction of condensate in the top layer is almost negligible, as indicated by an invariant refractive index. If the stack thicknesses are selected appropriately, the resulting structures serve as very effective graded-index, broadband antireflection coatings (Figure 3.3b) on soda lime glass (n ~ 1.52) substrate. The average reflectances of PDMS-functionalized and

TEGDMA-functionalized 2-stack films over the entire visible wavelength range (400-800 nm) are 0.4% and 0.6%, respectively. TEGDMA-functionalized films have a 7-10° contact angle with water, compared to 130-150° in the case of PDMS-functionalized films.

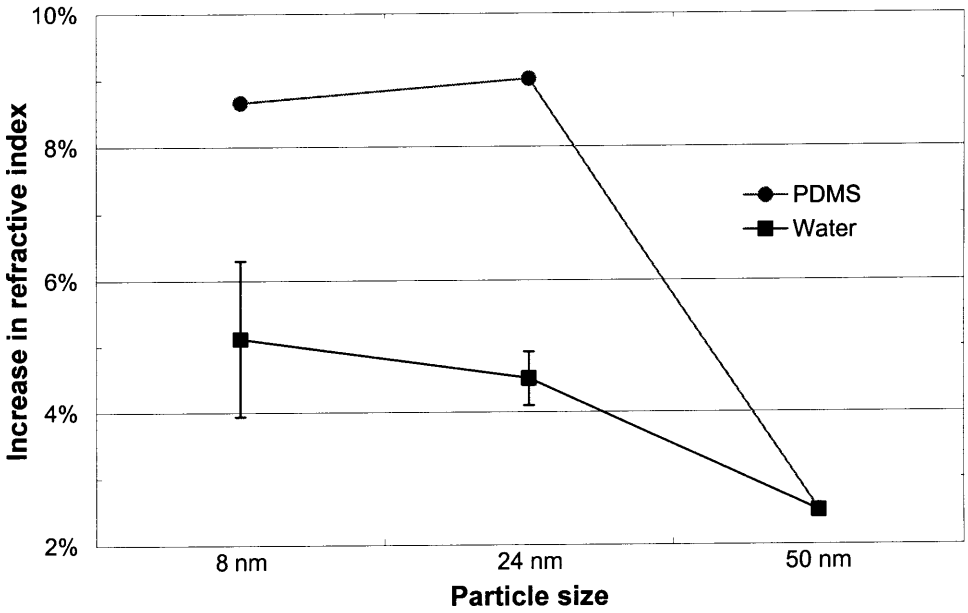

Figure 3.2. Capillary condensation of water (37°C, 80% r.h.) and PDMS (100°C) in PAH/SiO_2 nanoparticle films results in a particle size-dependent increase in film refractive index.

The selected treatment conditions determine the sensitivity of the capillary condensation process to particle size. The condensation experiments discussed above were performed using saturated chemical vapors at 100°C. When the TEGDMA-functionalized 2-stack film is subsequently heated to 85°C in air, with negligible TEGDMA partial pressure, some of the TEGDMA evaporates away from the bottom stack (Figure 3.4a). This heat treatment is equivalent to sliding the energy demand significantly to the left on the x-axis of Figure 3.1. Thus, the corresponding condensate fraction on the y-axis of Figure 3.1 decreases and the bottom stack refractive index declines from $n \sim 1.45$ to $n \sim 1.33$. Nevertheless, the activation energy for further evaporation of the condensate is sufficiently large so that heating the film for either 22 hours or 44 hours does not restore the original refractive index of the bottom stack ($n \sim 1.27$). Instead, a pseudo-equilibrium is reached at 85°C. The retained TEGDMA is presumably stabilized in the close vicinity of nanoparticle contact points, where interfacial curvature is most significant. It is known that capillary condensation-desorption cycles can show hysteresis[93].

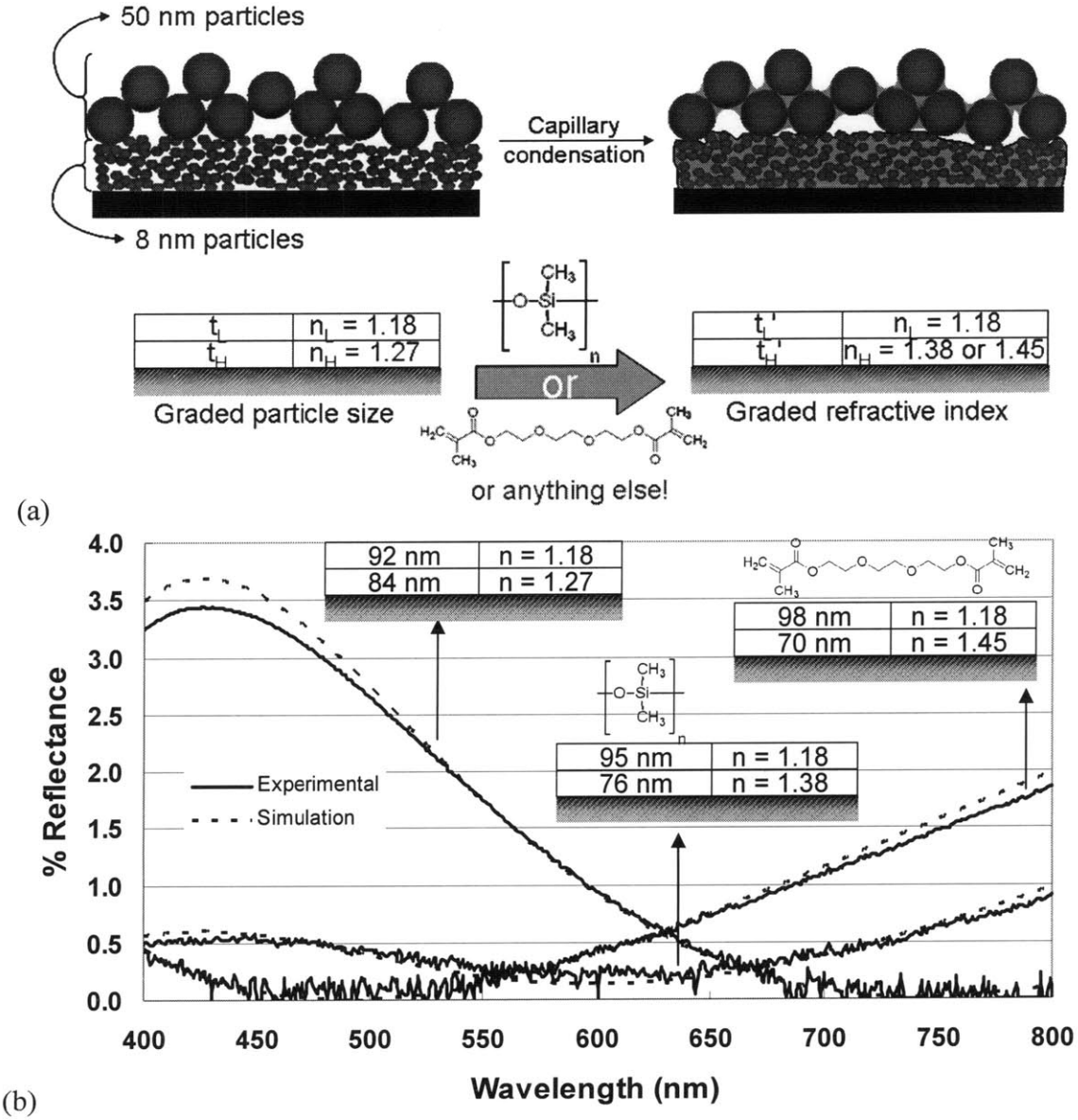

Figure 3.3. (a) Illustrations and refractive index profiles of 2-stack, graded-index coatings before and after PDMS- and TEGDMA-functionalization. (b) Reflectance profiles of the corresponding films in (a).

In situ UV-crosslinking of TEGDMA halts temperature-induced desorption, since crosslinking increases the molecular weight and reduces the vapor pressure of the condensate. TEGDMA consists of a short poly(ethylene glycol) (PEG) chain, bracketed by two UV-sensitive dimethacrylate groups

(Figure 3.4b). TEGDMA-functionalized and subsequently UV-crosslinked films do not change their spectral responses upon prolonged heating at 85°C (Figure 3.4b).

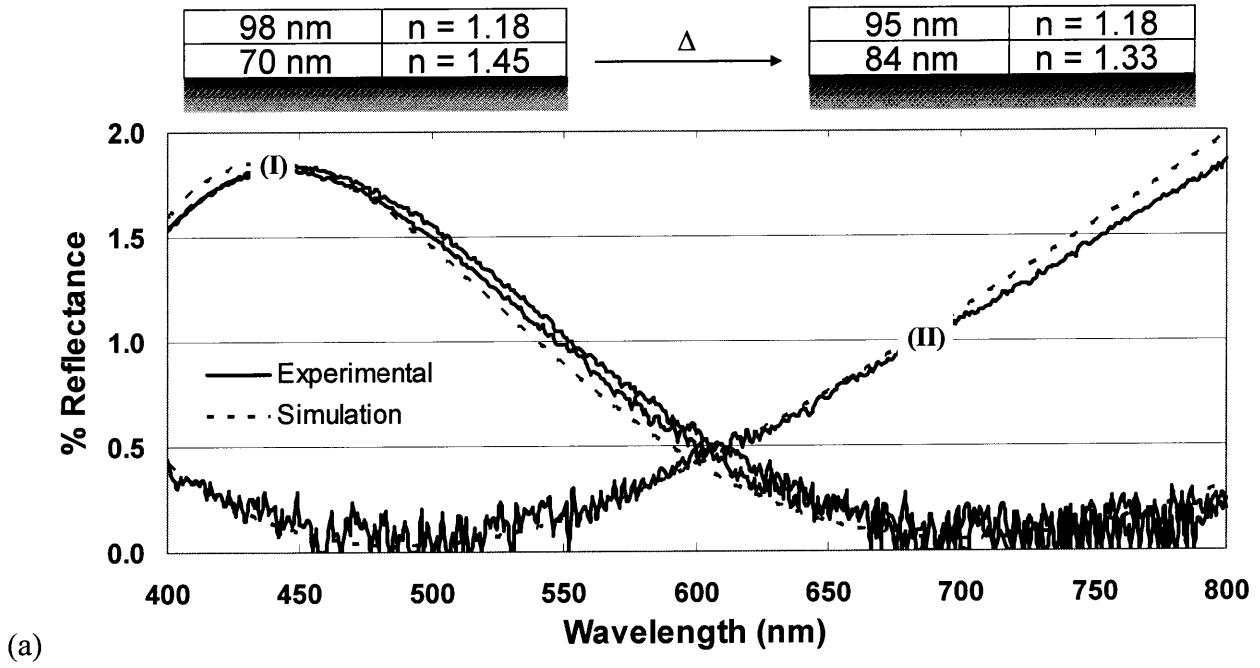

(a)

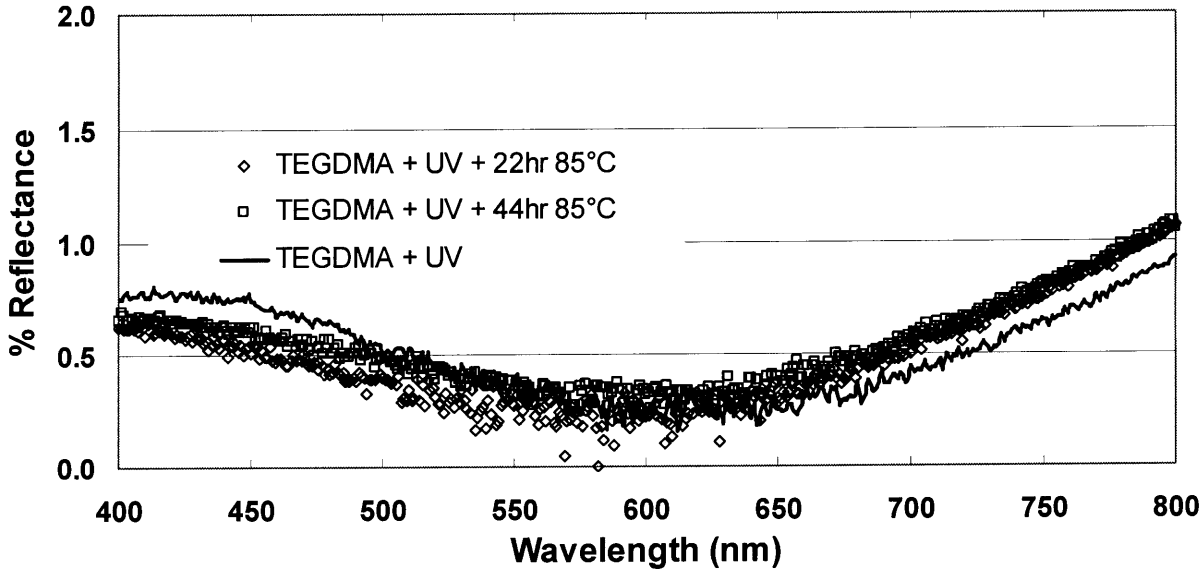

(b)

Figure 3.4. (a) Refractive index and reflectance profile of the TEGDMA-functionalized 2-stack film before (curve I) and after (curve II) prolonged heating at 85°C. (b) Reflectance profile of the UV-

crosslinked, TEGDMA-functionalized 2-stack film before and after prolonged heating at 85°C. The UV-sensitive side chains of TEGDMA are circled in red. Heating does not drive the crosslinked condensate out of the capillaries.

Although UV-crosslinked TEGDMA molecules form a crosslinked network among themselves, neither the SiO_2 nanoparticle surface nor the substrate glass surface is reactive with TEGDMA. Therefore, TEGDMA cannot be used to establish covalent linkages between nanoparticles in the host thin film. Instead, neighboring nanoparticles can be physically stitched together by capillary condensation of saturated steam at 124°C. Pressure difference across the curved S-L interface (ΔP^{S-L}, Figure 1.1) increases the solubilities of neighboring SiO_2 nanoparticles in water[30]. Upon evaporation of the condensed steam, a solid bridge between neighboring particles is deposited. A higher process temperature increases the solubility of SiO_2 nanoparticles, and promotes dissolution-redeposition. While the untreated, delicate nanoparticle thin films are readily damaged by gentle manual rubbing, 124°C steam-treated films offer rotary wear-resistance at 100kPa normal stress for one hour[94] (see Section 2.4.6 for testing method). Capillary condensation of 124°C steam in a given film requires much larger curvature-induced energetic stabilization than water vapor at 37°C. The extent of water condensation at 124°C is insufficient to cause an appreciable refractive index increase, and is therefore difficult to measure. The correlation between capillary condensation capacity as measured at 37°C and enhancement in mechanical durability upon steam treatment at 124°C is shown in Figure 3.5. The case of PAH/(5 0nm + 8 nm) SiO_2 nanoparticle films is noteworthy. Silica gels with polydisperse particle size distributions are known to have a greater number of nanoparticle contact points[30]. More effective capillary condensation translates to enhanced mechanical durability.

Despite the highly active surfaces of SiO_2 nanoparticles[64, 95, 96], capillary condensation of a hydrophobic material such as PDMS protects nanoparticle assemblies from the physical-chemical action of humidity. Such passivation may be desired to preserve the surface texture or spectral response of a carefully optimized nanoparticle thin film. The reflectance profiles of a PDMS-functionalized 2-stack broadband AR coating before and after humidity-aging at 37°C and 80% relative humidity (r.h.) for 3 days are plotted in Figure 3.6. Unlike an as-assembled film, the PDMS-functionalized film resists capillary condensation of water vapor.

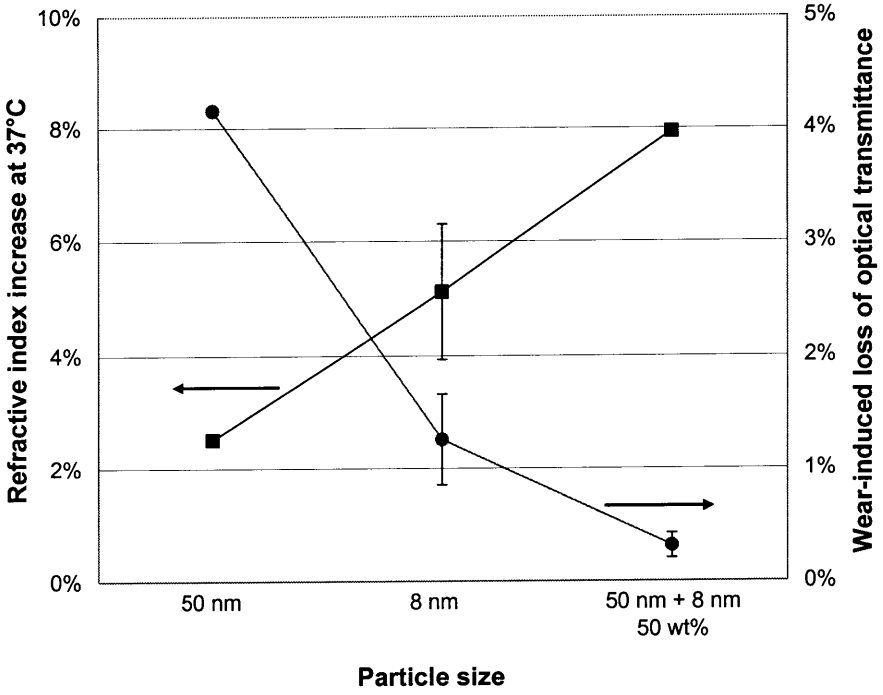

Figure 3.5. Capillary condensation of water vapor in nanoparticle thin films with various particle size distributions upon storage for 3 days at 37°C and 80% r.h. (blue squares) are correlated to wear resistance (red circles) of the same films upon steam-reinforcement for 1 hour at 124°C. Wear testing is performed for one hour under a 100kPa normal stress.

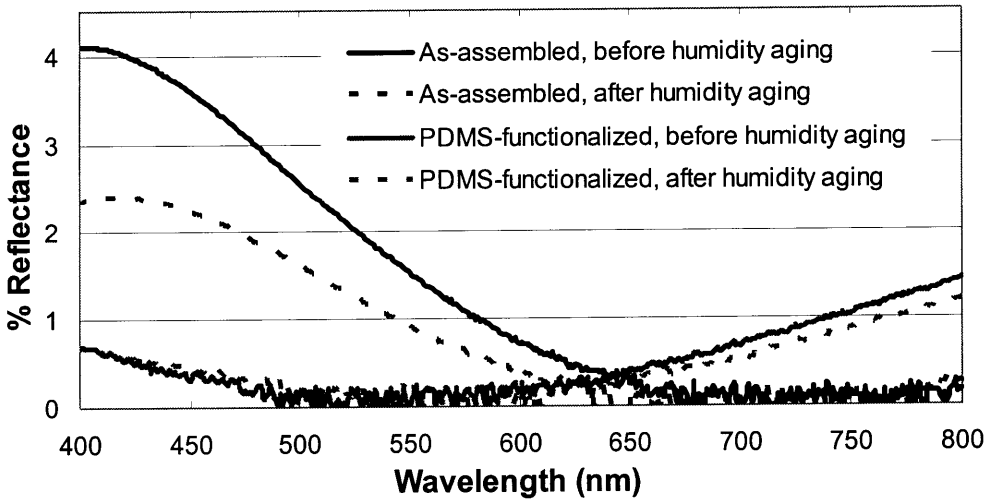

Figure 3.6. As-assembled and PDMS-functionalized, 2-stack AR films before and after aging in a humidity chamber (37°C, 80% r.h.) for 60 hours. The capillary-condensed PDMS protects the nanoporous coating from humidity aging.

3.3 Conclusions

Capillary condensation in nanoporous materials is an inevitable phenomenon with a strong thermodynamic driving force. Instead of abandoning these highly sought-after materials to the mercy of adventitious vapors, appropriate selection of operating parameters (e.g., T), particle size distribution, and condensate liquid makes capillary condensation a versatile tool to functionalize nanoporous thin films. We have studied particle size-dependence of capillary condensation in nanoparticle thin films, and have functionalized nanoparticle thin films to achieve desirable, long-lasting optical and mechanical properties. Our work can be readily extended to other nanoporous materials with appropriate pore geometries. Among a plethora of interesting molecules to choose as the vapor-phase material, non-linear optical materials (see Section 7.2.3), antifouling agents, molecules that impart valuable wetting (see Section 7.2.2) or stimuli-responsive characteristics are some first examples that come to mind.

3.4 Materials and Methods

3.4.1 Materials

Ludox® SM-30 (30 wt.% SiO_2 nanoparticle dispersion in water, average particle size of 8 nm, and specific surface area of ~345 m^2/g), PAH (average molecular weight of 56,000 g/mol), Boric acid (BDH) and KCl (Mallinckrodt) were purchased from Sigma-Aldrich (St. Louis, MO). 50 nm SiO_2 nanoparticles (5.73% wt.% dispersion in water) were purchased from Polysciences, Inc. The average sizes of silica nanoparticles were provided by the suppliers. 3″x1″ glass slides were purchased from VWR International. The supplier uses Electroverre® glass manufactured by Erie Scientific (Switzerland). Polishing cloth (DP-NAP) with adhesive backing was purchased from Struers Inc.

3.4.2 Film Assembly

Sequential adsorption of polymers and nanoparticles was performed using a StratoSequence VI spin dipper (nanoStrata Inc.), controlled by StratoSmart v6.2 software, at 120-130 rpm. The concentrations of the PAH and SiO_2 nanoparticle solutions were 0.01 M and 0.023 wt.%, respectively. Ludox® particles were filtered through a 0.20 μm cellulose acetate filter prior to dilution in a pH 9.0 boric acid buffer solution (3.1 g/L Boric acid, 3.7 g/L KCl, and 0.86 g/L NaOH

in water). Distilled water (> 18 MΩ·m, Millipore Milli-Q) water (MQ water) was used to prepare the buffer, PAH, and rinse solutions. PAH solution was adjusted to pH 7.5 by dropwise addition of a 1.0 M NaOH solution. Rinse solutions were not adjusted for pH. Glass substrates were degreased using Alconox® (Alconox, Inc.) detergent powder under sonication for 15 min, and then cleaned with 1.0 M NaOH solution under sonication for another 15 min. Finally, the substrates were sonicated in MQ water for 5 min and blow-dried with dry air. The dipping time in each polymer or nanoparticle solution was 10 min followed by three rinse steps (2, 1, and 1 min) in deionized water. Thickness and refractive index were measured using a Woollam Co. VASE spectroscopic ellipsometer; the data analysis was done using the WVASE32 software package. The ellipsometry technique is described in Section 2.4.5.

3.4.3 Capillary Condensation Experiments

Capillary condensation experiments were performed in KIMAX® glass weighing bottles (VWR Catalog# 16713-182). Each weighing bottle can accommodate up to two substrates. Prior to use, the bottles were first rinsed with toluene thrice. The same weighing bottles were subsequently rinsed with MilliQ water until toluene odor could no longer be detected. The bottles were then dried in an oven at 80°C for 15 minutes and left to equilibrate at room temperature. After the bottles cooled down, a 2 mL glass vial (VWR Catalog# 66011-020) was placed inside a larger, 20 mL glass vial (VWR Catalog# 66022-106). One 20 mL vial (containing a smaller vial inside) was placed in each weighing bottle. Neither the 20 mL nor the 2 mL vials were capped. The substrates (e.g., glass slides) to be functionalized via capillary condensation were placed in between the walls of the 20 mL vial and the weighing bottle. Using Pasteur pipettes, the 2 mL vials were filled up to approximately ¾ of their height with the chemicals to be condensed into the substrate capillaries. Finally, the weighing bottle was capped (Figure 3.7). Avoiding filmwise condensation is critically important. If chemical vapors in the weighing bottle condense filmwise either on the bottle walls or on the substrate (due to temperature differentials, for example), the ability to target condensation at nanoparticle interstices is lost and a multi-micron thick condensate covers the nanoparticle thin film. Special measures were taken in order to avoid temperature gradients at any point of the condensation experiment. An oven was positioned underneath a Snorkel, and the oven was cooled to room temperature prior to operation. The capped weighing bottle at room temperature was then placed into the oven. The oven

was then switched on and adjusted to the desired treatment temperature. The experiment was terminated by opening the weighing bottle cap while the bottle was still in the hot oven, removing the substrates using tweezers, then removing the weighing bottle from the oven. This sequence of operation ensures that the walls of the weighing boat containing hot chemical vapors do not cool down rapidly and cause filmwise condensation.

3.4.4 Optical and Mechanical Characterization

The 124°C steam treatment (hydrothermal treatment) procedure, abrasion testing procedure, and UV/Visible spectrophotometry procedure are described in detail in Sections 2.4.3, 2.4.6, and 2.4.7, respectively.

Chapter 4
Strain-Induced Elastic Buckling Instability for Mechanical Measurements on Nanoparticle Thin Films

4.1 Introduction

Nanoscale colloidal assemblies and thin films have attracted much attention due to their novel dielectric, wetting, and optical properties to name a few. The mechanical properties of such ultrathin assemblies are of great interest as well. However, the extreme thinness of these materials has limited the applicability of traditional testing methods (e.g., nanoindentation) and has underscored undesired substrate effects in such measurements[97].

Strain-induced elastic buckling instability for mechanical measurements (SIEBIMM) and nanoindentation measurements of polymeric and sol-gel ultrathin films yield essentially identical Young's moduli[98], except SIEBIMM come at a fraction of the cost and effort required by nanoindentation experiments[99]. SIEBIMM of colloidal assemblies has not been explored heavily.

We have assembled LbL ultrathin colloidal films on PDMS, whereby multiple conformal layers of positively and negatively charged polymers or nanoparticles were electrostatically adsorbed on a substrate. Chemical and mechanical substrate-film interactions were studied. Unfavorable colloidal film-substrate interactions were eliminated to a large extent using barrier layers between the colloidal films and the PDMS substrates. Young's moduli are reported as a function of humidity.

4.1.1 SIEBIMM Theory and Methodology

When a thin, higher-modulus film is adhered on a lower-modulus bulk substrate, the thin film responds to compressive planar stresses on the substrate by buckling. Buckling reduces the strain energy of the system, and occurs at a particular wavelength (λ) characteristic of the thin film mechanical properties:

$$\lambda = 2\pi d\left(\frac{E_f(1-\nu_s^2)}{3E_s(1-\nu_f^2)}\right)^{1/3}, \tag{4.1}$$

where d is the film thickness, and E_f, ν_f, E_s, and ν_s are Young's moduli and Poisson's ratios of the film and substrate, respectively. The substrate properties can be readily characterized using uniaxial compression testing. Provided a refractive index difference between the substrate and the film, the film thickness can be measured using ellipsometry. Finally, buckling wavelength can be measured (i) by Fourier-transforming an optical micrograph of a buckled film, or (ii) by passing a laser beam through a buckled film and analyzing the diffraction pattern. The film modulus can then be easily calculated using Equation 4.1. It is worth noting that buckling is a critical phenomenon, and λ is approximately independent of strain in the limit of small (< 10%[100]) deformations.

In some cases, it is desirable to have a barrier thin film with known properties in between the thin film of interest and the bare substrate. For example, the thin film of interest may be difficult to assemble onto the bare substrate directly, may have negligible refractive index contrast with the bare substrate (in which case ellipsometry cannot be used to measure film thickness), or the bare substrate and the overcoating film may have unwanted interactions. Nolte et al.[101] has developed the experimental and mathematical methodolgy for such a two-plate SIEBIMM application, which involves deconvoluting the mechanical properties of the measured two-plate composite film into its individual components according to:

$$\overline{E}_f = \frac{\frac{\overline{E}_{Composite}}{4} - \overline{E}_{Barrier}\left[\left(\phi_{Barrier} - \frac{\kappa}{2}\right)^3 + \left(\frac{\kappa}{2}\right)^3\right]}{\left(1-\frac{\kappa}{2}\right)^3 - \left(\phi_{Barrier} - \frac{\kappa}{2}\right)^3}, \tag{4.2}$$

$$\phi_{Barrier} = \frac{d_{Barrier}}{d_{Composite}};\ \kappa = \frac{1+\phi_{Barrier}^2\left(\frac{\overline{E}_{Barrier}}{\overline{E}_f}-1\right)}{1+\phi_{Barrier}\left(\frac{\overline{E}_{Barrier}}{\overline{E}_f}-1\right)};\ \overline{E}_{Composite} = 3\overline{E}_s\left(\frac{\lambda}{2\pi d_{Composite}}\right)^3;\ \overline{E} = \frac{E}{(1-\nu^2)}, \tag{4.3}$$

where $\overline{E}_{Composite}$, $\overline{E}_{Barrier}$, and $\overline{E}_f$ are the reduced Young moduli of the two-plate composite film, the barrier film, and the film of interest, respectively. The "reduced" Young's modulus, $\overline{E}$, is defined in Equation 4.3 as a function of the Young's modulus and Poisson's ratio. The experimental scheme

and flow of information in the two-plate SIEBIMM we performed on colloidal thin films are summarized in Figure 4.1.

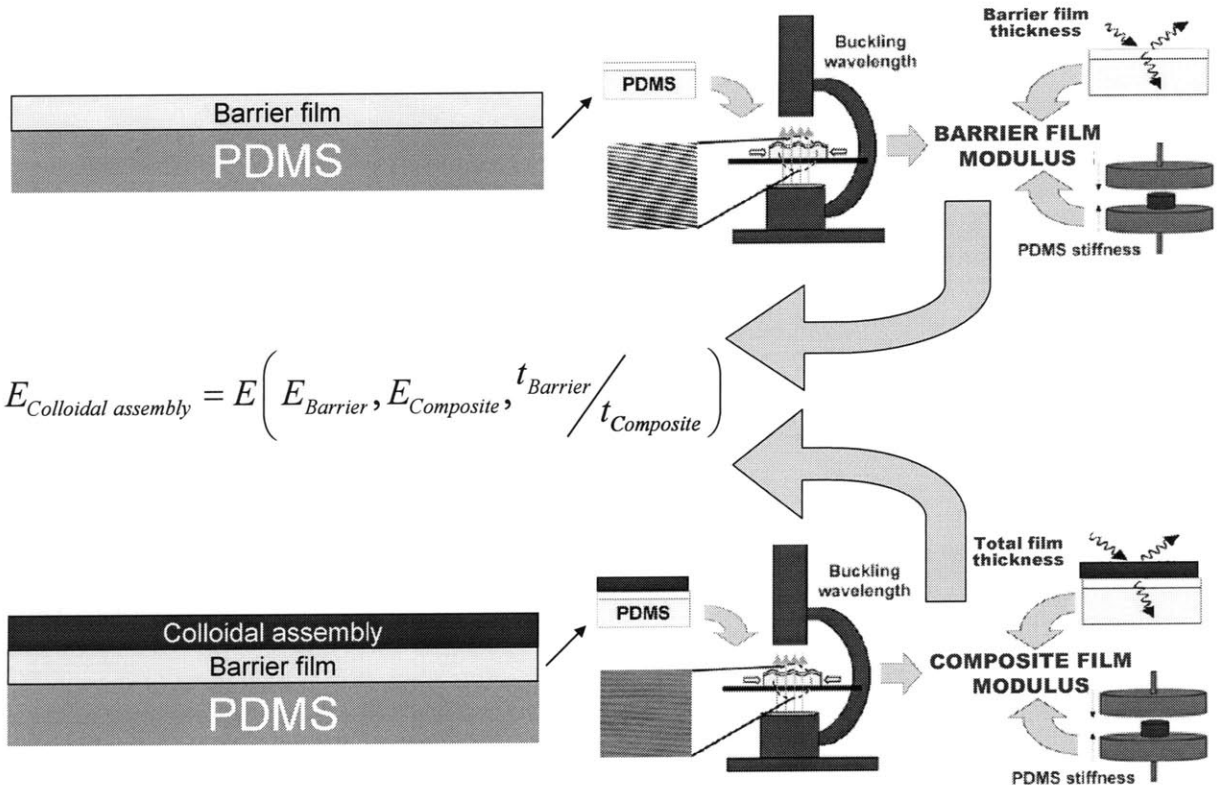

Figure 4.1. Experimental scheme for two-plate buckling experiments on colloidal thin films. Figure modified from work of Nolte et al.[102]

4.1.2 Prior SIEBIMM Work on LbL and Sol-Gel Films

SIEBIMM on thin films was developed by Stafford et al.[98], who applied SIEBIMM on sol-gel organosilicate films made nanoporous by virtue of a sacrificial organic component. Young's modulus was studied as a function of porosity using both SIEBIMM and nanoindentation, and an excellent correlation between the results obtained using the two different measurement techniques was demonstrated.

Nolte et al.[70, 101] were the first to establish the applicability of SIEBIMM on LbL films. Their studies provided valuable insights to how assembly conditions (e.g., charge density on film components), ambient humidity, solvent effects (e.g., swelling), and ionic strength affect the Young's

moduli of LbL polyelectrolyte complexes. The two-plate technique was also developed and used by Nolte et al. to study LbL films which do not readily assemble on the bare substrate.

The only study of SIEBIMM on colloidal thin films we are aware of has been reported by Lu et al[103]. The authors assembled gold nanoparticles and a photosensitive polycation LbL, and studied the Young's modulus of the assembly before and after photocrosslinking.

4.2 Results and Discussion

4.2.1 Stability of Nanoparticle Thin Films on PDMS

Two types of colloidal assemblies were studied: (1) all-nanoparticle films assembled from negatively charged native SiO_2 nanoparticles (15 nm) and positively charged 3-aminopropylsilane-modified SiO_2 nanoparticles ($APSiO_2$, 15 nm), and (2) polymer-nanoparticle films assembled from negatively charged native SiO_2 nanoparticles (15 nm) and poly(diallyldimethylammonium chloride) (PDAC), a polycation. Both films have very low refractive indices of ~1.25 on most substrates, owing to their nanoporous structures (~40-50% porosity). Surface profile of a typical film assembled on glass is shown in Figure 4.2. Note that peak-to-valley distances on the order of the total film thickness is consistent with a corrugated surface texture. The films of interest happen to be anti-fogging (i.e., superwetting) by virtue of such rough and porous surface features. Interestingly, these same films, when assembled on PDMS, exhibit significantly larger refractive indicex values of ~1.41-1.45. SEM images (Figure 4.3). Ellipsometry results confirm the presence of a film of the expected thickness, albeit of an unexpectedly high refractive index.

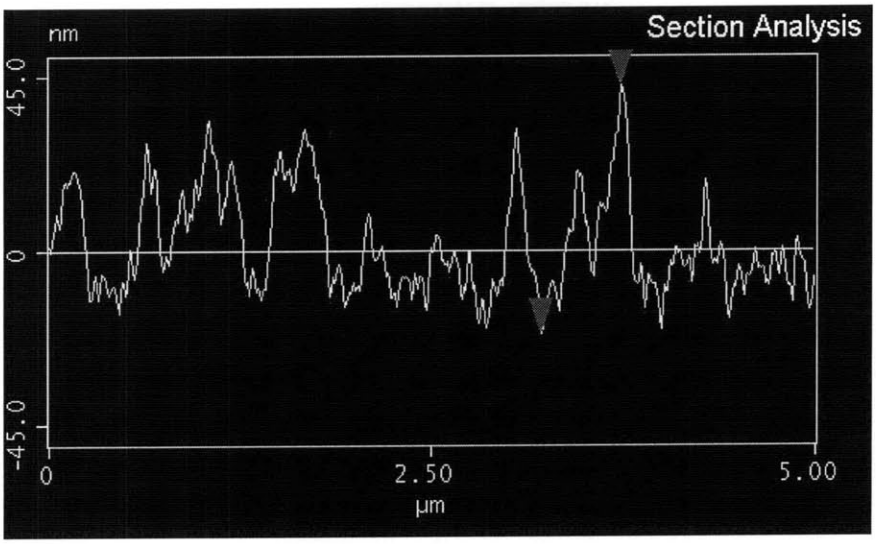

Figure 4.2. Cross-sectional height profile of an ~100 nm-thick PDAC/SiO_2 assembly on glass substrate. Peak-to-valley distance is on the order of film thickness.

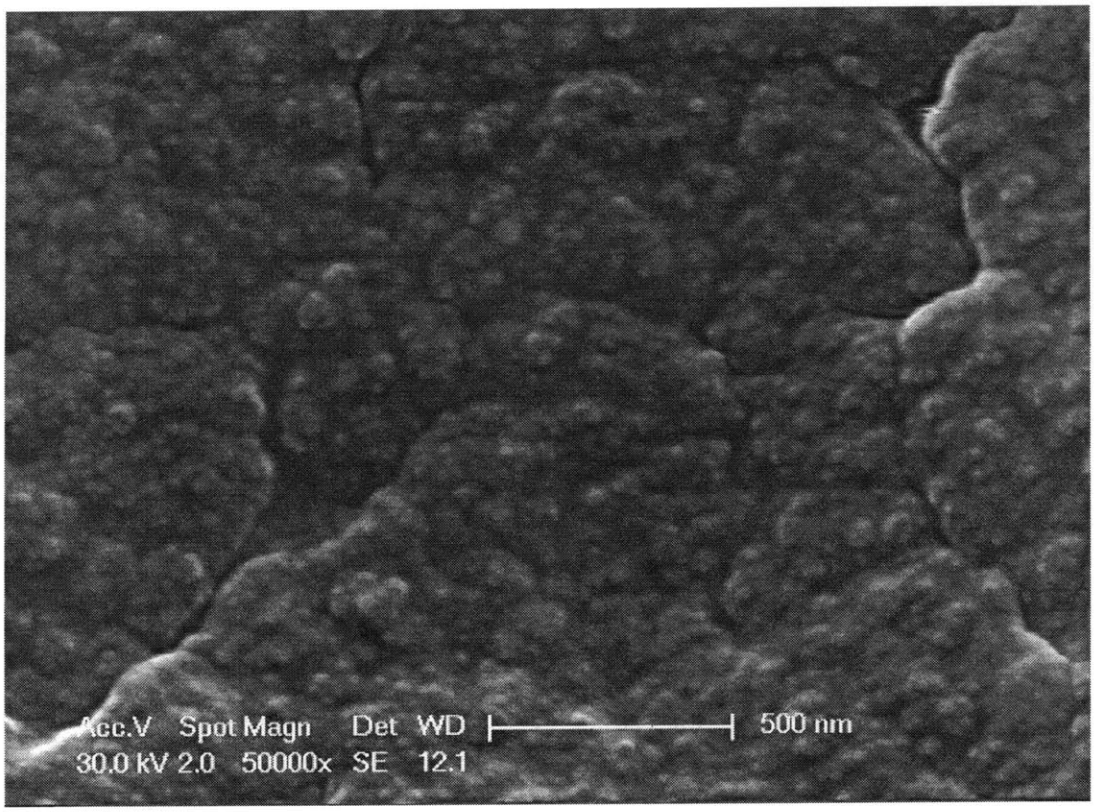

Figure 4.3. SEM micrograph of an APSiO_2/SiO_2 film on PDMS.

These films, which are superhydrophilic and anti-fogging on glass, had water contact angles of ~100° on when assembled on PDMS and fit ellipsometric models where the anticipated void fraction (40-50%) was replaced with PDMS. We hypthothesize that soluble, non-crosslinked PDMS oligomers imbibe into the overlying film. This imbibition is most likely driven by (i) the extreme energy difference between PDMS oligomers and the hydrophilic SiO_2 nanoparticle surface, and (ii) the favorable thermodynamic environment provided by capillaries of nanoporous films as described in Section 1.3. In order to test this hypothesis, we placed three different kinds of barrier layers in between the bare PDMS surface and the nanoparticle assembly: a polystyrene film, a polycarbonate film, and a polyelectrolyte multilayer film made of positively charged PAH and negatively charged SPS ionomers. We also tested the effect of extracting the soluble fraction of the PDMS substrate using a Soxhlet apparatus. The results are summarized in Table 4.1.

Films assembled on tack-free PDMS (row 1, from which free oligomers were extracted) had significantly lower refractive indices (n ~ 1.29) than those assembled on regular PDMS (n~1.43, row 2). However, colloidal films assembled directly on PDMS (row 1) crack extensively upon straining (Figure 4.4c). As the crack density increased upon repeated buckling-relaxation cycles, the films stopped buckling due to extensive stress relaxation. Insertion of a ~100nm thick polycarbonate barrier layer underneath a ~70 nm thick $APSiO_2/SiO_2$ film (n ~ 1.28) eliminated cracking (Figure 4.4a). Polymeric barrier layers with Young's moduli on the order of GPa (as opposed to MPa for PDMS) presumably accomodate the modulus contrast at the PDMS interface more easily than colloidal films do. Moreover, the increase in refractive index from row 6 (n ~ 1.29) to row 7 (n ~ 1.32) over 2 days suggests that some free PDMS oligomers are retained even in tack-free PDMS substrates, and that these free oligomers can diffuse through a sufficiently thin (~75 nm) polycarbonate barrier. Therefore, it is desirable to use a barrier layer for two reasons: (1) to prevent cracking, and (2) to block diffusion of residual PDMS oligomers.

Table 4.1. Chemical and mechanical stability of colloidal assemblies on various substrates.

Row #	Barrier layer	Barrier thickness (nm)	Colloidal assembly	Assembly thickness (nm)	R.I. @ 632 nm	Tack-free?	Buckling delamination?	Age (days)
1	None	0	$SiO_2/APSiO_2$	164	1.43	No	No (Cracks)	1
2	None	0	$SiO_2/APSiO_2$	124	1.29	Yes	No (Cracks)	1
3	PAH/SPS	90-95	$SiO_2/APSiO_2$	85-90	1.42	No	No	1
4	PAH/SPS	90-95	$PDAC/SiO_2$	80-85	1.47	No	No	1
5	Polystyrene	550-570	$SiO_2/APSiO_2$	85-100	1.41	No	Yes	1
6	Polycarbonate	76	$SiO_2/APSiO_2$	105	1.29	Yes	No	1
7	Polycarbonate	76	$SiO_2/APSiO_2$	105	1.32	Yes	No	3
8	Polycarbonate	76	$PDAC/SiO_2$	120	1.3	Yes	No	1
9	Polycarbonate	45-50	$SiO_2/APSiO_2$	310-320	1.46	No	No	1
10	Polycarbonate	85	$SiO_2/APSiO_2$	310-320	1.4	No	No	1
11	Polycarbonate	205-210	$SiO_2/APSiO_2$	310-320	1.29	No	Yes	1

Rows 9-11 show that the effectiveness of a barrier layer increases with its thickness. A sufficiently thick polycarbonate barrier (~210 nm) support porous colloidal films even on regular (i.e., non-tack-free) PDMS substrates. However, thicker films have a greater tendency to buckle in a 'buckle delamination' mode of buckling, as opposed to a 'wrinkling' mode of buckling[104]; only the wrinkling mode of buckling yields useful information on mechanical properties of thin films. Buckling delamination in the film corresponding to row 5 of Table 4.1 (~600 nm thick) is shown in Figure 4.4b, to be contrasted with wrinkling shown in Figure 4.4a. Therefore, design of an optimal barrier layer involves balancing transport properties (e.g., diffusion coefficients) with mechanical properties.

Finally, the chemical identity of the barrier layer is important. Inserting a polystyrene or polyelectrolyte multilayer barrier layer makes no difference in the temporal stability of the overcoating nanoporous colloidal assembly, as apparent from high refractive index values reported in rows 3-5.

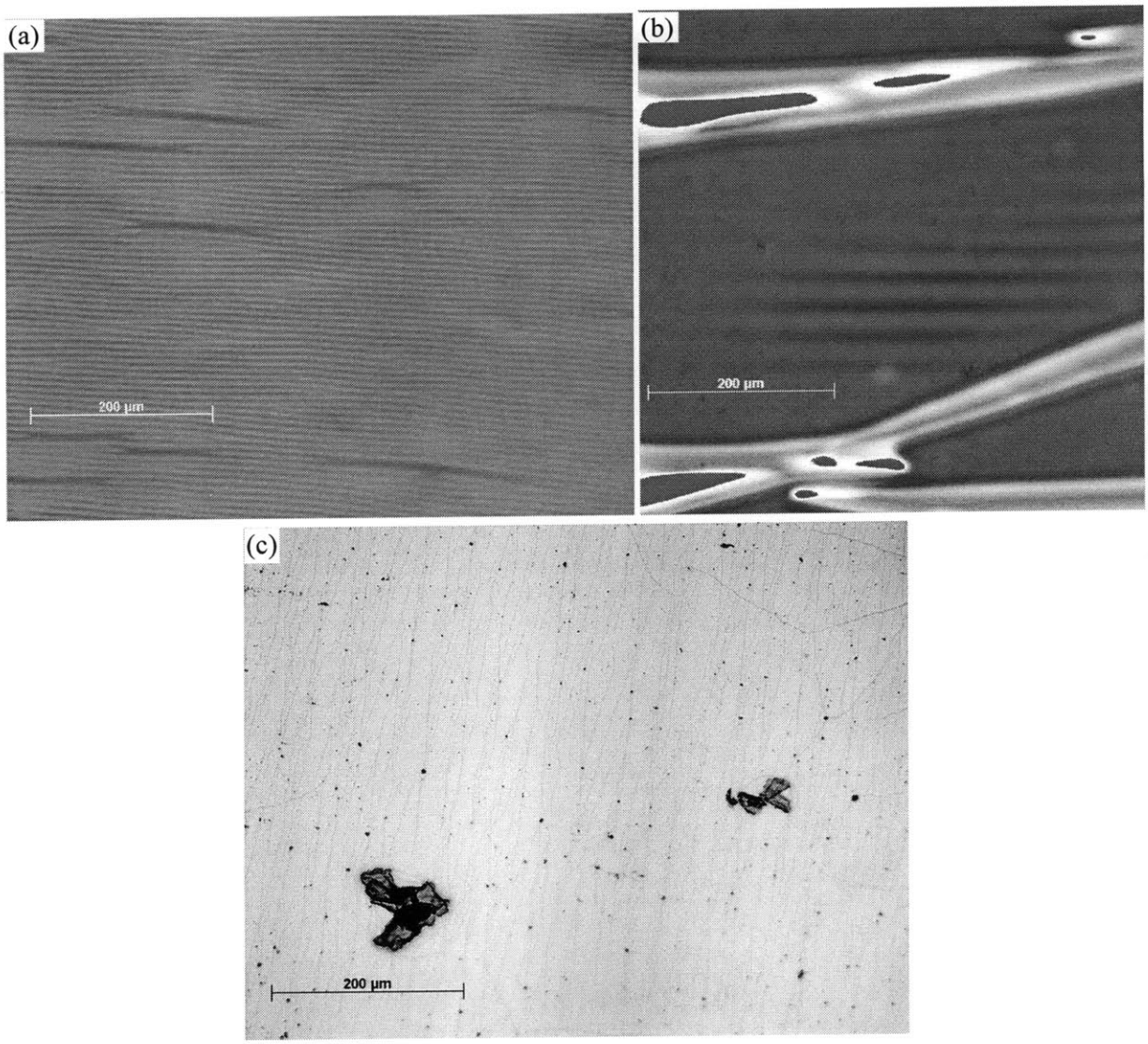

Figure 4.4. Films can (a) wrinkle, (b) delaminate, or (c) crack upon straining on elastic substrates. Wrinking is the desired mode of deformation.

4.2.2 Modulus Measurements

Young's moduli of both the $APSiO_2/SiO_2$ and $PDAC/SiO_2$ assemblies corresponding to rows 6 and 8, respectively, of Table 4.1 were measured as a function of humidity (Figures 4.5a and 4.5b). Contrary to polyelectrolyte multilayer films studied by Nolte et al.[105], the moduli of both colloidal assemblies investigated were independent of humidity. This result is not surprising, since colloidal films are much less mobile than ionomer chains. Ionomers can rearrange their conformations and ionic crosslinks with varying levels of water activity within the film. Moreover, the measured moduli (1-2

GPa) are in excellent agreement with those of 40-50% porous organosilicate films as reported by Stafford et al.[98] in their pioneering SIEBIMM study. Interestingly, the original organosilicate films were prepared using sol-gel methods and are therefore continuous, cohesive structures as opposed to assemblies of discrete colloids under investigation. The remarkable agreement in moduli suggest that void fraction contributes more to small-strain mechanical properties than does particle interconnectivity among individual colloids.

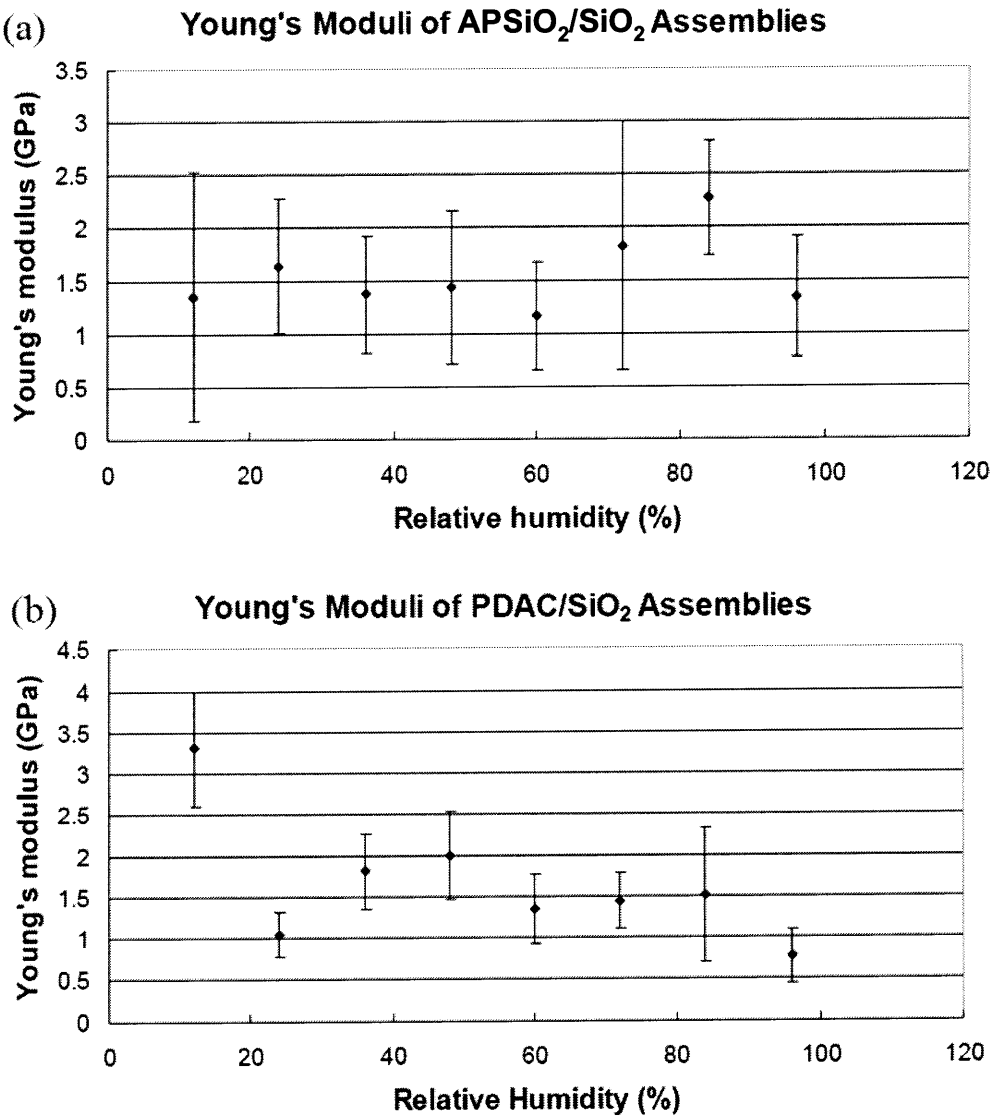

Figure 4.5. Young's moduli of $APSiO_2/SiO_2$ and $PDAC/SiO_2$ assemblies as a function of relative humidity, measured via SIEBIMM. A polycarbonate barrier layer is present between the underlying PDMS substrates and the colloidal assemblies.

4.3 Conclusions

Compositional (e.g., porosity) and mechanical (e.g., cracking, delamination) stability of nanoporous colloidal assemblies on PDMS was studied as a function of interfacial surface energy and modulus differentials, respectively. A barrier layer of an optimized thickness and material choice is proposed for use in SIEBIMM of colloidal assemblies. Moduli of all-nanoparticle and polymer-nanoparticle assemblies have been measured in good agreement with films of similar chemistry and composition (yet different interconnectivity among constitutive elements – i.e., individual nanoparticles) reported earlier. The measured moduli were also relatively independent of humidity.

4.4 Materials and Methods

4.4.1 Materials

Silica nanoparticles with native negative surface charge, Ludox® HS-40 (40 wt.% SiO_2 suspension in water, average particle size of 15 nm, and specific surface area of ~220 m^2/g), 3-aminopropylsilane-modified silica nanoparticle preparation ($APSiO_2$, 3 wt.% SiO_2 suspension in ethanol, average particle size of 15 nm) with positive surface charge, poly(diallyldimethylammonium chloride) (PDAC, 20 wt.% aqueous solution, Mw = 200,000-300,000 g/mol), poly(allylamine hydrochloride) (PAH, powder form, Mw = 56,000 g/mol), poly(styrene-4-sulfonate) (SPS, powder form, Mw = 70,000 g/mol), toluene, and chlorobenzene were purchased from Sigma-Aldrich (St. Louis, MO). Poly(dimethylsiloxane) (PDMS, Sylgard 184) was purchased from Dow Corning Corporation. Polystyrene (PS, Sytron 663 W) was purchased from Dow Chemical Company, and polycarbonate (PC) was kindly provided by Bayer Corporation.

4.4.2 PDMS Synthesis

The crosslinker and the base compound were mixed in a 1:10 w/w ratio and cast into a tray (~3 mm thickness), allowed to de-gas for 1 hour, and cured in an oven at 80°C for 45 min. The PDMS was then cut into 2 cm x 6 cm substrates. Tack-free PDMS was prepared by extracting crosslinked PDMS with toluene in a Soxhlet extractor for 3 days, and dried in a vacuum oven overnight at 60°C.

4.4.3 Film Assembly and Characterization

Sequential adsorption of polymers and nanoparticles was performed using an automated dipping machine. PDAC/SiO_2[57] films were dipped in a StratoSequence VI spin dipper (nanoStrata Inc.), controlled by StratoSmart v6.2 software, at 120-130 rpm. PDMS substrates with polycarbonate or polystyrene barrier layers (see Section 4.2.4) were O_2-plasma treated for 10 s (Harrick Scientific PDC-32G plasma cleaner/sterilizer, 100 W, 400 mTorr) immediately prior to film assembly. The plasma treatment utilized was confirmed not to decrease barrier film thickness significantly (data not shown). SiO_2/$APSiO_2$[3] films were dipped in an HMS Series Programmable Slide Stainer (Carl Zeiss, Inc.) controlled by a software developed in-house. The concentration of polymers and nanoparticles were 0.01 M and 0.023 wt.%, respectively. Nanoparticles were filtered through a 0.20 μm cellulose acetate filter prior to dilution. Solutions were prepared in deionized water (> 18 MΩ·m, Millipore Milli-Q), and solution pHs were adjusted using either 1.0 M HCl or 1.0 M NaOH. The dipping time in each polymer or nanoparticle solution was 10 min followed by three rinse steps (2, 1, and 1 min) in deionized water. SiO_2/$APSiO_2$ films were dipped at pH 4.5, and rinse water was adjusted to the same pH as deposition solutions. PDAC/SiO_2 films were dipped from pH 4.0 and pH 9.0 PDAC and SiO_2 solutions, respectively. Rinse water pH was not adjusted in this case.

4.4.4 Barrier Film Deposition

The PAH/SPS polyelectrolyte multilayer film was assembled directly on PDMS at pH 4.0 using the general film assembly procedure outlined above. In contrast to the colloidal assemblies, the polyelectrolyte solutions contained 0.1 M NaCl. Polystyrene and polycarbonate barriers were spin-coated (PWM32 Headway Research) on silicon wafers (2 cm x 3 cm pieces, p-type, WaferNet Inc.) cleaned for 5 minutes in an air-plasma. Solvent was spun onto each wafer immediately prior to spinning the polymer solutions. Spin coating parameters for various barrier films in Table 4.1 are listed below in Table 4.2. Ramp was 300 rpm/s for all films. Polystyrene and polycarbonate films were annealed at 70°C and 135°C, respectively, for 1 hour. After cooling the substrates to room temperatures, the films were transferred onto PDMS substrates as described elsewhere[98].

Table 4.2. Spin-coating parameters for various barrier layers.

Row # in Table 1	Barrier layer	Barrier layer thickness (nm)	Solvent	Concentration (g/L)	Program
5	Polystyrene	550-570	Toluene	44	2000 rpm, 20 s
6	Polycarbonate	76	1:1 Chloroform:Chlorobenzene	40	1800 rpm, 20 s
7	Polycarbonate	76	1:1 Chloroform:Chlorobenzene	40	1800 rpm, 20 s
8	Polycarbonate	76	1:1 Chloroform:Chlorobenzene	40	1800 rpm, 20 s
9	Polycarbonate	45-50	Chloroform	10	2000 rpm, 20 s
10	Polycarbonate	85	Chloroform	20	2000 rpm, 20 s
11	Polycarbonate	205-210	Chloroform	40	2000 rpm, 20 s

4.4.5 Buckling Experiments

Calculation of Young's moduli in SIEBIMM requires knowledge of the modulus and Poisson's ratio of PDMS, the Poisson's ratios and thicknesses of all thin films, and buckling wavelengths. We assumed a modulus of 1.7 MPa for all PDMS substrates and Poisson's ratios of 0.5 and 0.33 for PDMS and all thin films, respectively. Film thicknesses were measured ellipsometrically. Buckling wavelengths of barrier layers were measured using optical microscopy. The buckling wavelengths of polystyrene and polycarbonate barriers were measured immediately after plasma treatment, and just before film assembly. Buckling wavelengths of the two-plate films were measured using laser diffraction. Laser diffraction experiments were performed in a controlled-humidity glove box (Model 506A Humidity Control Chamber, Electro-Tech Systems, Inc., Glenside, PA), whereas optical microscopy could only be done under ambient conditions. The detailed experimental procedures for measuring buckling wavelengths and calculating Young's moduli are described elsewhere[70, 102, 105, 106].

The humidity chamber was 9 cubic feet in volume, made of 0.25 inches-thick PMMA sheets. Humidity and temperature in the humidity chamber were controlled to ±2% of the setpoint using a microprocessor controller (Model 5200, Electro-Tech Systems, Inc., Glenside, PA). Humidity was controlled using an ultrasonic humidification system (Electro-Tech Systems, Inc., Glenside, PA) and a pair of desiccating columns. Temperature could only be increased using a 500 W heating system; no cooling system was installed. The chamber had a 12-square-inch door, through which the samples could be placed into and removed from the chamber.

4.4.6 AFM Measurements

AFM measurements were done on a NanoScope IIIa (Digital Instruments Inc., Santa Barbara, CA) tapping-mode scanning probe microscope controlled by Nanoscope v5.30r3sr3 software. Arrow NC-20 (Nanoandmore USA Inc., Lady's Island, SC) tapping-mode Silicon tips were used.

4.4.7 SEM and Ellipsometry Measurements

SEM and ellipsometry methods are described in Sections 2.4.11 and 2.4.5, respectively.

Chapter 5
Wetting Properties of Nanoparticle Thin Films

5.1 Introduction

Wetting characteristics of a surface can often be critical or enabling for particular applications. For example, successful bonding of two surfaces requires good wetting of both surfaces with the cement. Formation of uniform, defect free coatings on industrial substrates and successful application of pesticides on plant leaves also require excellent wetting of the substrate[68].

Apart from intentional wetting of surfaces, the interaction of surfaces with ambient water in the form of humidity or rain droplets can significantly harm the aesthetics and success of commercial products. Fogging of eyeglasses, endoscopic lenses, car windshields, greenhouse windows, and food packaging are examples of major unresolved wetting-related problems. Fogging is a result of water droplets large enough to scatter light nucleating on surfaces, and extremely hydrophilic (i.e., superhydrophilic) substrates which merge and spread condensate water droplets into a thin, uniform sheet of water do not fog[11, 107]. Superhydrophobicity[12], on the other hand, is at the opposite extreme of the wettability spectrum. Water droplets never wet superhydrophobic surfaces; rather they roll over them like marbles. For example, a superhydrophobic windshield would not require wipers to maintain visibility under rain. Superoleophobicity[108] is a recent achievement which allows not only prohibits water droplets, but also oil droplets from wetting a surface.

Nanoparticle thin films have been used to achieve both superhydrophilicity and superhydrophobicity. However, most fundamental understanding of wettability originates from studies on micron-scale, lithographically textured surfaces[109-111]. The theoretical foundations of superhydrophilicity and superhydrophobicity in nanoparticle thin films are still lacking, and the available studies are highly empirical in nature. In this chapter, we apply standard wettability analyses developed for micron-scale systems to nanoparticle thin films. Our work demonstrates that carefully designed contact angle studies can reveal topographical and structural information. We then report on the important environmental stresses on and ageing characteristics of nanoparticle thin

films. Finally, we demonstrate that nanoparticles thin films may provide a suitable platform to develop transparent superoleophobic coatings.

5.1.1 Effect of Surface Roughness on Wettability

Condensation of light-scattering water droplets on otherwise transparent surfaces results in fogging. While condensation is required by thermodynamics, the kinetics of spreading of condensate water droplets can be controlled; extremely fast-spreading droplets rapidly coalesce into a thin, transparent sheet of water on the substrate. Two particularly interesting wetting regimes[112] (the Wenzel and superwetting regimes) are illustrated in Figure 5.1. In the Wenzel regime, roughness, r (i.e., surface area/projected area), enhances the hydrophilicity and hydrophobicity of hydrophilic ($\theta < 90°$) and hydrophobic ($\theta > 90°$) surfaces, respectively:

$$\cos\theta^* = r\cos\theta, \tag{5.1}$$

where θ^* is the contact angle on a rough surface and θ is the contact angle on a *smooth* chemical replica of the rough surface. In the superwetting regime, the liquid droplet sits on top of a wet surface, which is a mixture of solid and liquid surfaces. The roughness (r) is washed away by the liquid already occupying the surface features, such as vallies. ϕ_s is the solid fraction of a super-wetted surface (e.g., top parts of very tall needles on a surface), and determines topography-induced enhancement of hydrophilicity. The contact angle on a mixed solid-liquid surface tends to 0° as the solid fraction of the surface tends to 0, since the contact angle of the liquid with itself 0°:

$$\cos\theta^* = 1 - \phi_S(1-\cos\theta) \tag{5.2}$$

A wetting diagram (Figure 5.2), where $\cos(\theta^*)$ is plotted against $\cos(\theta)$, contains topographical information. A larger r in the Wenzel regime and a smaller ϕ_s in the superwetting regime are desirable for antifogging applications. The transition between two wetting regimes occurs at θ_c, the critical flat-surface contact angle necessary to achieve superwetting.

Cebeci et al.[11] have made self-assembled silica nanoparticle thin films which mimic the surface morphology shown in Figure 5.1[113]. There is an inverse correlation between film thickness and refractive index in these films. Refractive index is lowered by the presence of pores, suggesting that the assembly process increases the aspect ratio of topographical features with increasing film

thickness (Figure 5.3a). A larger aspect ratio at greater film thickness reduces ϕ_S and contact angle (Figure 5.3b). Water droplets spread rapidly on films composed of 14 or more bilayers. Such thick films achieve 0° contact angle with water within 0.5 seconds of contact with a water droplet, and are antifogging. Thinner films have finite equilibrium contact angles (~10°) with water, and they fog. However, root-mean-square (RMS) surface roughness, measured using atomic force microscopy (AFM), does not confirm the inferred evolution of topography with film growth, and does not correlate with the observed wetting behavior. As shown in Figure 5.3c, RMS roughness is approximately constant across a wide thickness range. However, a wetting diagram analysis presented in Section 5.2.1 revealed structural differences among the same films.

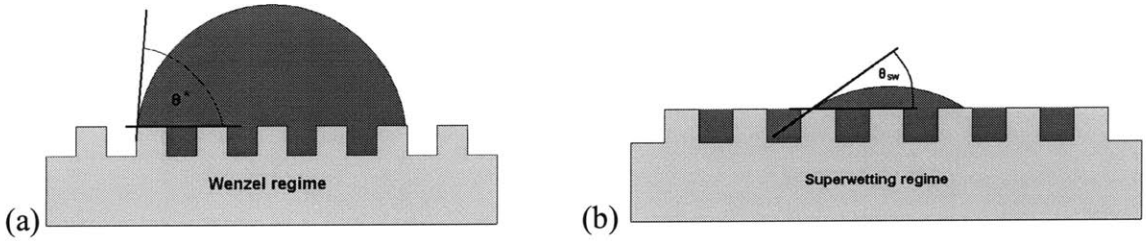

Figure 5.1. Illustration of the Wenzel and superwetting regimes. The figure has been reproduced from the work of Schwachulla[113].

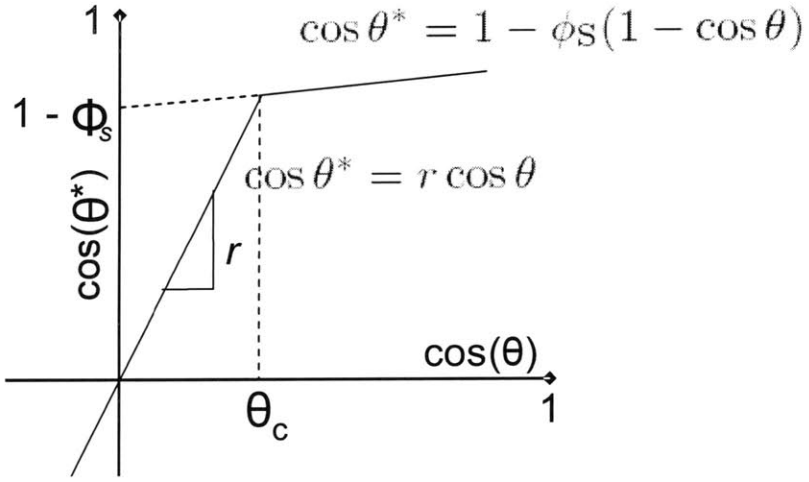

Figure 5.2. An illustrative wetting diagram of a conceptual hydrophilic surface. θ and θ^* are contact angles on chemically identical smooth and rough surfaces, respectively. r stands for surface roughness (i.e., actual surface area/projected area), and ϕ_s stands for solid fraction that remains dry in a superwetted state[112].

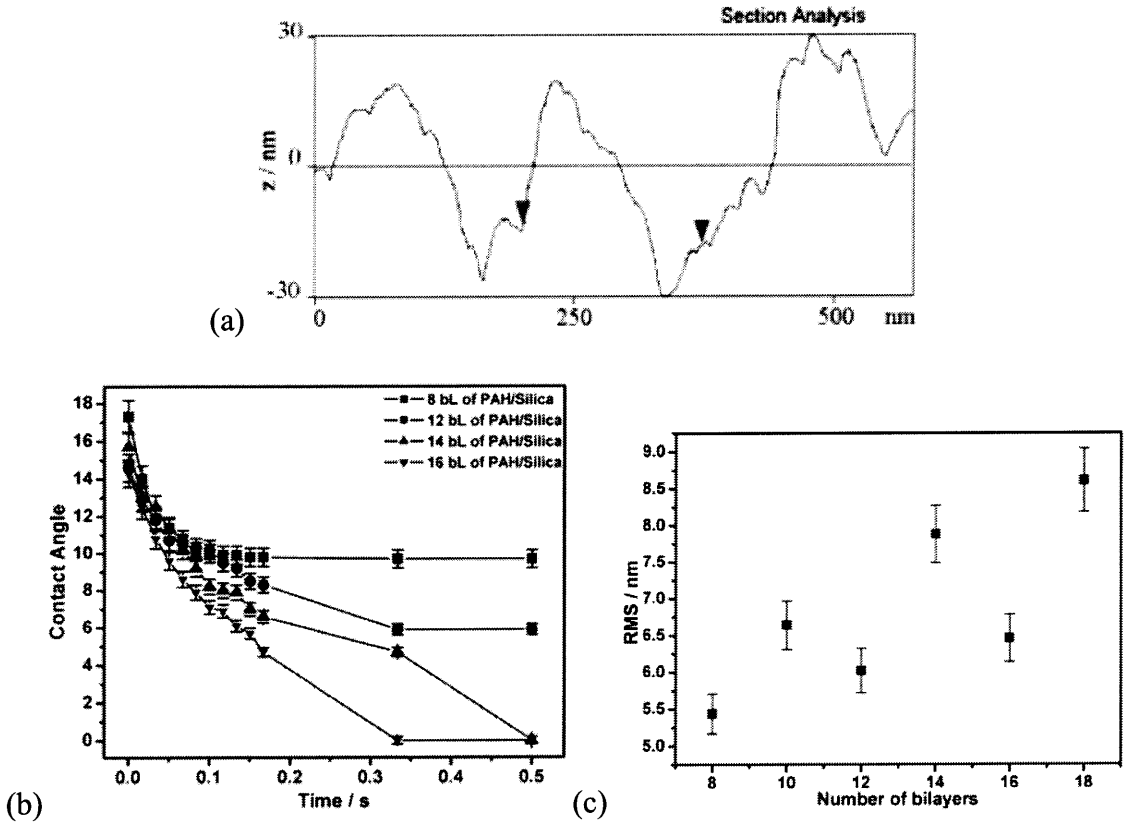

Figure 5.3. (a) Cross-sectional height profile, (b) kinetic of water droplet contact angle evolution on LbL films of various thicknesses, and (c) RMS roughnesses of LbL films of various thicknesses. The figures have been reproduced from the original antifog study by Cebeci et al[11].

5.1.2 Significance of Capillary Shape

Beyond the hills, valleys, and other relatively large-scale topographical features composed of nanoparticles, the nanoscale capillaries that form in between nanoparticles also influence the wetting characteristics of nanoparticle thin films. Structural and chemical changes that ensue upon capillary condensation in interparticle capillaries were discussed in detail in Chapters 2 and 3. As will be discussed in Section 5.2.2, the susceptibility of nanoparticle thin films to capillary condensation of adventitious vapors provides an aging mechanism by which antifog properties can be compromised over time.

However, the shape of interparticle capillaries can influence wetting characteristics even in the absence of (or prior to the onset of) capillary condensation. Equation 5.1, which describes the

classical Wenzel theory of wetting, predicts that surface roughness can only enhance the innate hydrophilicity ($\theta < 90°$) or hydrophobicity ($\theta > 90°$) of a surface. In other words, from a classical standpoint, it is impossible to convert a hydrophilic surface into a hydrophobic surface simply by roughening it. Tuteja et al.[108] recently showed that re-entrant surface features, such as those presented by the lower hemispheres of nanoparticles on surfaces, can defy Equation 5.1 and convert a smooth, hydrophilic surface into a rough, hydrophobic surface. The droplets with $\theta < 90°$ and $\theta^* > 90°$ on surfaces with re-entrant roughness features are in a metastable state. If pressure is exerted on the droplets, the metastable droplets can be forced to transition to their equilibrium states, in which case their contact angles are accurately predicted by Equation 5.1. The authors used their findings to design precise lithographic superoleophobic surfaces on which oil droplets with equilibrium contact angles $\theta << 90°$ bead up on to attain $\theta^* > 90°$. Since lithography provides a coarse spatial resolution, the structures made by Tuteja et al.[108] are not transparent. Nanoparticle thin films are transparent materials with tunable particle sizes and topographies. Many superhydrophobic films have been fabricated using nanoparticles, including a transparent superhydrophobic LbL film by Bravo et al.[12] The LbL assembly technique allowed the authors to tune surface roughness and strike a balance between desirable non-wetting properties and optical transparency. In Section 5.2.4, we present a wetting diagram analysis of the same transparent superhydrophobic film. Our analysis revealed that the superhydrophobic nanoparticle thin film under study indeed has re-entrant surface features, and can support metastable liquid droplets at contact angles > 90° even though the equilibrium contact angles of the droplets with the underlying rough surface is < 90°. Nevertheless, the droplets under study were all in the Wenzel regime and therefore contact angle hysteresis was high and superoleophobicity could not be achieved.

5.2 Results and Discussion

5.2.1 Wetting Diagram Analysis of Highly Porous Antifogging Films

A wetting diagram analysis was done for antifogging PAH/8 nm SiO_2 nanoparticle films reported by Cebeci et al.[11] (Figure 5.4). An ~20 nm thick PAH/SPS primer layer was assembled underneath the nanoparticle films as a primer layer. The standard method to prepare a wetting diagram is to measure the contact angles of various alkanes with a (typically) hydrophobic surface. However, even water (γ

= 72 mN/m) has almost 0° contact angle with some of the superhydrophilic films of interest. Therefore, it is impossible to measure finite contact angles using alkanes. Instead, we chose to generate the wetting diagram by first fluorinating the surface using a fluorinated silane reagent (see Section 5.4.3) and subsequently measuring contact angles of various water-ethanol mixtures on the hydrophobized surface. We assume that the fluorosilane treatment forms a negligibly thin monolayer on the surface and that it does not significantly alter the parameters of interest, r and ϕ_s.

Coatings of different thicknesses behave differently on the wetting diagram (Figure 5.4), as opposed to the RMS roughness study (Figure 5.3c). In order to estimate ϕ_s, the point (1,1) has been connected to the closest data point of a particular film thickness using a dashed line. The dashed line was then extrapolated to intersect the y-axis. The intersection of the dashed line with the y-axis marks $1-\phi_s$. As the film thickness increases, ϕ_s decreases. In other words, the solid fraction of a wet surface decreases as the film thickness increases. There are indeed structural differences between films of different thicknesses.

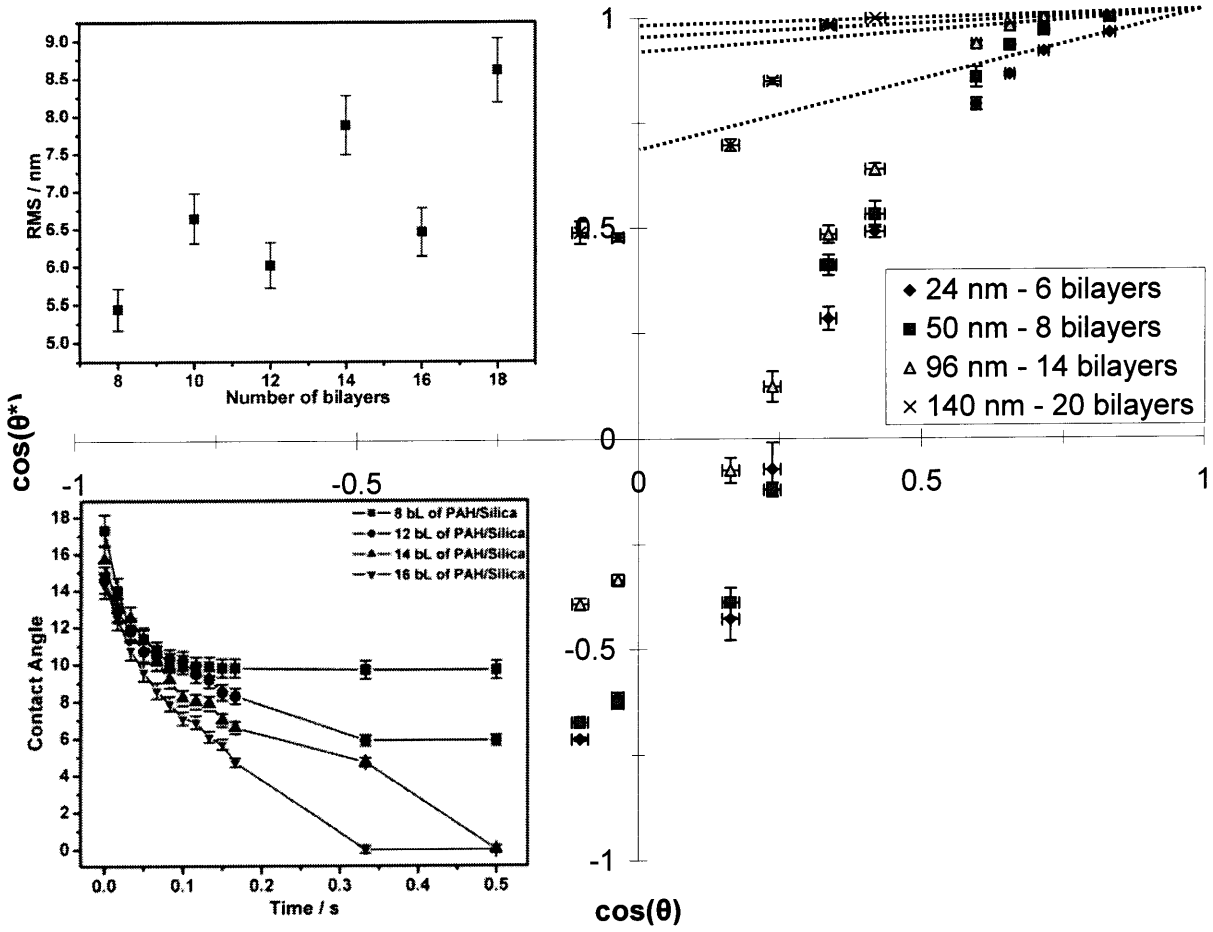

Figure 5.4. Wetting diagrams for fluorinated LbL films of various thicknesses listed in the legend. Contact angles and RMS-roughnesses of as-assembled films (i.e., prior to fluorination) as a function of thickness are plotted in the insets[11]. The points of intersection of the dashed lines with the y-axis provide structural information on the thin films (i.e., ϕ_s).

Interestingly, highly porous antifogging films lose their antifog properties in a matter of days upon storage under high levels of humidity (e.g., 80% r.h. at 37°C). Capillary condensation in porous nanoparticle thin films was described previously in Sections 1.3 and 3.1.1. The impact of capillary condensation of water vapor on the contact angles of nanoporous films (Figure 5.5) is inversely proportional to the constituent particle size. Films made of smaller particles lose their antifog properties faster than films made of larger particles. Interestingly, the equilibrium contact angles of 3-day-old films composed of various particle sizes are approximately equal to each other. The loss of wettability upon condensation of water in the nanopores is a highly unintuitive outcome. However,

the chemical-physical action of capillary-condensed water should be taken into consideration. Condensed water does not remain pure and slowly dissolves away surrounding SiO_2 nanoparticles. Depending on relative abundances of its native surface functional groups, an SiO_2 surface can have water contact angles ranging from 0° to 60°[30]. The nanoporous morphology of the coating also becomes questionable upon prolonged incubation of condensed water in the nanopores.

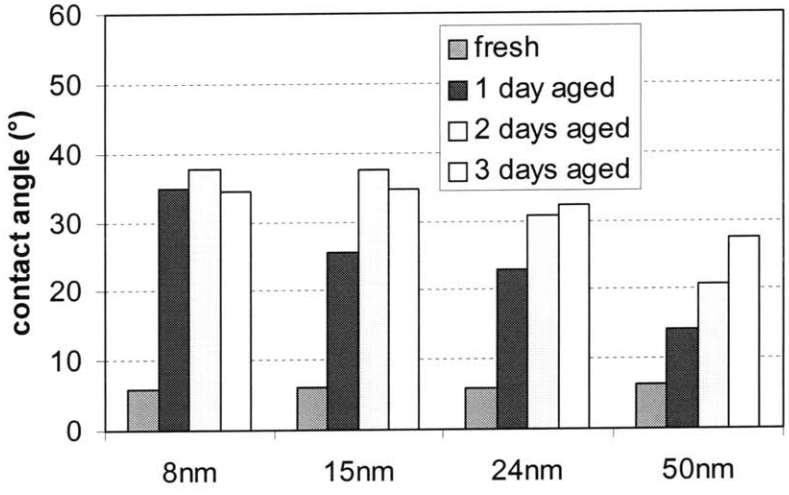

Figure 5.5. The influence of capillary condensation of water (i.e., humidity aging) on the contact angles of porous nanoparticle thin films composed of various particle sizes. The films were stored at 80% r.h. at 37°C for various durations.

5.2.2 Influence of Capillary Condensation of Water Vapor on Wettability and Possible Recovery Treatments

Various recovery treatments were attempted to desorb capillary-condensed water from 1-day-old films aged at 37°C and 80% r.h. (Table 5.1). Humidity aging increases the refractive index of a fresh PAH/8 nm SiO_2 film from 1.27 to 1.30 over one day. We measured water contact angles and the minimum volume fractions of ethanol (EtOH) required to achieve 0° contact angles on various aged films. Recovery of wettability parallels recovery of refractive index, but the extent of recovery upon most treatments is not sufficient to rejuvenate antifog property. As an exception, plasma treatment decreases the aged film index to a value below the fresh film index, most likely by burning away some of the PAH in the film, and fully recovers antifog property. Plasma treatment is sufficient to

impart a transient antifog property to even a bare glass substrate. However, repeated aging/plasma treatment experiments on aged PAH/8 nm SiO_2 films (Table 5.2) revealed that the favorable action of plasma treatment is more long-lived on coated substrates than on bare glass substrates. When a plasma-recovered 1-day-old film is further aged for one more day at 37°C and 80% r.h., it does not lose wettability (Table 5.2, row 4). The difference in antifog properties of coated and bare sections of this particular sample is shown in Figure 5.6. Upon prolonged post-recovery storage for 2.5 days at 37°C and 80% r.h., antifog property starts deteriorating as refractive index gradually increases. A second cycle of recovery was attempted (Table 5.2, row 6). Although the antifog property was recovered, the extent of recovery in refractive index and water contact angle did not match the original extent of recovery upon the first plasma treatment cycle. This result is consistent with our observation of hysteresis in temperature-induced desorption of organic capillary-condensates from highly porous films discussed earlier.

Table 5.1. The outcomes of various recovery treatments to rejuvenate antifog functionality of humidity-aged PAH/8 nm SiO_2 films. The films were aged for one day at 37°C and 80% r.h.

#	PAH/8nm SiO_2	Refractive index	Water contact angle	EtOH vol% to achieve 0° contact angle	Antifog properties
1	Fresh	1.27	6	10%	very good
2	Aged	1.30	30	50%	bad
3	Aged + 10s O_2 plasma	1.25	0	0%	very good
4	Aged + pH10 wash + 1 hr 120°C	1.28	16	20%	middle
5	Aged + 3 hr 120°C	1.28	24	20%	bad
6	Aged + Ethanol wash	1.28	24	40%	bad
7	Aged + Ethanol wash + 1 hr 120°C	1.28	21	50%	bad
8	Aged + 3 hr UV	1.30	20	50%	bad
9	Aged + 2 days dessication	1.31	20	50%	bad
10	Aged + 2 days dessication + 3 hr vacuum	1.29	28	30%	bad

Table 5.2. The effect of repeated aging/recovery cycles to rejuvenate antifog functionality of humidity-aged PAH/8 nm SiO_2 films using O_2-plasma treatment as the recovery treatment. The films were aged for the specified durations at 37°C and 80% r.h.

#	PAH/8nm SiO_2	Refractive index	Water contact angle	Antifog properties
1	Fresh	1.27	6	very good
2	Aged (24hr)	1.30	30	bad
3	Aged (24hr) + 10s O_2 plasma	1.25	0	very good
4	Aged (24hr) + 10s O_2 plasma + Aged (24hr)	1.28	0	very good
5	Aged (24hr) + 10s O_2 plasma + Aged (60hr)	1.31	8	good
6	Aged (24hr) + 10s O_2 plasma + Aged (60hr) + 10s O_2 plasma	1.29	5	very good
7	Aged (24hr) + 10s O_2 plasma + Aged (60hr) + 10s O_2 plasma + Aged (24hr)	1.29	9	very good

Figure 5.6. Photograph of film #4 in Table 5.2 during antifog testing. The uncoated part of the slide fogs, whereas the coated part is antifogging.

5.2.3 Influence of Film Porosity and Substrate Choice on Wettability

Unlike the PAH/SiO_2 films, APSiO_2/PAA films are not porous. For reasons that are not fully understood, positively charged nanoparticles (i) constitute a lower volume fraction of LbL films than negatively charged particles, and (ii) result in polymer-rich, relatively dense films when assembled LbL with polyanion counterparts. Porosities and the antifog property longevities of APSiO_2/PAA films assembled on various substrates are listed in Table 5.3. On soda lime glass, the films are remarkably non-porous, and retain their antifog properties upon storage at 37°C and 80% r.h. for three days. The same material system assembles into a more porous structure on silicon wafer,

quartz, and polycarbonate substrates. On these substrates, antifog property is lost within a day of humidity aging. The gradual increase in refractive index and loss of antifog property upon storing $APSiO_2$/PAA films assembled on polycarbonate substrate at 37°C and 80% r.h. is shown in Table 5.4. Similar to previously studied highly porous PAH/SiO_2 films, porous $APSiO_2$/PAA films lose their antifog properties upon what appears to be capillary condensation of water vapor.

Table 5.3. Thicknesses, refractive indices, porosities, and the lifetime of antifog properties of $APSiO_2$/PAA films assembled on soda lime glass, silicon wafer, quartz, and polycarbonate substrates.

Substrate	Ellipsometry Results			AF Longevity @ 80% r.h., 37°C
	Thickness (nm)	Refractive index	Porosity (%)	
Soda lime glass	92	1.43	4%	Retained over 3 days
Silicon wafer	115	1.42	11%	Lost in 1 day
Quartz	87	1.43	11%	Lost in 1 day
Polycarbonate	125	1.39	21%	Lost in 1 day

Table 5.4. Evolution of porosity, refractive index, and antifog property of an $APSiO_2$/PAA film assembled on polycarbonate. The films were aged for the specified durations at 37°C and 80% r.h.

$APSiO_2$/PAA on Polycarbonate		Refractive index	Porosity	Antifogging property
Fresh		1.39	21%	very good
Stored at 37°C 80% r.h.	**1-day-old**	1.46	5%	middle
	3-day-old	1.47	0.1%	bad

The hydrophilicity and charge density of the substrate surface influence the procession of multilayer growth. Soda lime glass becomes negatively charged and very hydrophilic upon cleaning with sodium hydroxide (see Section 5.4). Quartz, silicon wafer, and polycarbonate surfaces are not readily hydrophilized to the same extent. Clean polycarbonate substrates dewet as they are being withdrawn from water, while clean quartz and silicon wafer dewet within several seconds of withdrawal. In contrast, clean soda lime glass substrates withdrawn from water sustain a uniform sheet of water on their surfaces until the water eventually evaporates. Just like water, polyelectrolyte molecules "wet" and cover the soda lime glass surface more uniformly than they cover other substrate surfaces during the onset of multilayer growth. As a result, uniform and smooth multilayers grow on soda lime glass, compared to what is referred to as "island growth" in LbL literature. Island

growth involves establishment and growth of sparse nuclei on the substrate surface. Growing islands eventually merge and form a uniform film, which then continues its growth uniformly. Nevertheless, island growth results in rougher and more porous films. AFM micrographs of PAH/SPS and PEI/SPS films grown on soda lime glass, silicon wafer, and quartz are shown in Figure 5.7. Films on soda lime glass are consistently smooth and uniform, whereas films on quartz and silicon wafer are rough or disjoined.

Not surprisingly, assembly of hydrophilic primer films did not eliminate the substrate-dependence of $APSiO_2$/PAA films. CHI/CMC and PAH/SPS films were tested as primer coatings on quartz (Table 5.5). The antifog property lifetime on primed substrates was at best identical to that on bare substrates.

Table 5.5a. Humidity aging-dependent antifog properties of $APSiO_2$/PAA films assembled on soda lime glass and quartz substrates with or without primer CHI/CMC layers. The films were aged for the specified durations at 37°C and 80% r.h.

Substrate	Underlayer	Antifog film	Antifog property	Stability in 37°C and 80% r.h.	
				1 day	3 days
Glass		$APSiO_2$/PAA	very good	very good	very good
Glass	CHI/CMC		good	middle	middle
Glass	CHI/CMC	$APSiO_2$/PAA	very good	middle	middle
Quartz		$APSiO_2$/PAA	very good	bad	bad
Quartz	CHI/CMC		middle	bad	bad
Quartz	CHI/CMC	$APSiO_2$/PAA	good	bad	bad

Table 5.5b. Humidity aging-dependent antifog properties of $APSiO_2$/PAA films assembled on quartz substrates with or without primer PAH/SPS layers. The films were aged for the specified durations at 37°C and 80% r.h.

Substrate	Underlayer	Antifog film	Antifog property	Stability in 37°C and 80% r.h.	
				1 day	3 days
Quartz	(None)	$APSiO_2$/PAA	very good	middle	bad
Quartz	PAH/SPS	$APSiO_2$/PAA	very good	middle	bad
Quartz	PAH/SPS	$APSiO_2$/PAA	very good	middle	bad

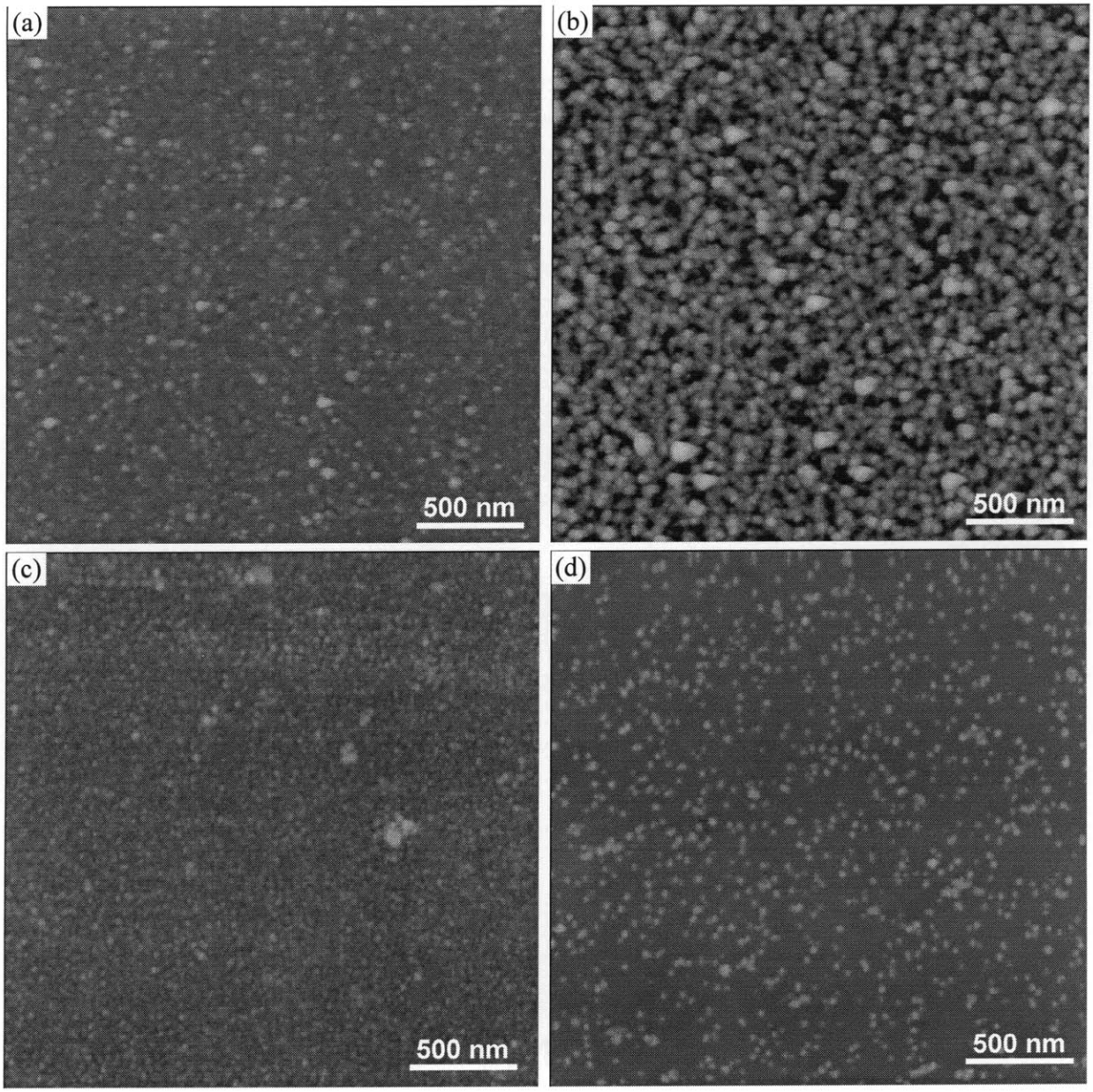

Figure 5.7. 21 layers (10.5 bilayers) of (a) PAH/SPS on soda lime glass, (b) PAH/SPS on silicon wafer, (c) PEI/SPS on soda lime glass, and (d) PEI/SPS on quartz. Despite the large number of layers that have been assembled, the films on silicon wafer and quartz substrates are significantly rougher than those on soda lime glass and non-coherent, respectively.

5.2.4 Wetting Diagram Analysis of Transparent Superhydrophobic Films

A wetting diagram analysis was done on the transparent superhydrophobic film reported by Bravo et al.[12] (Figure 5.8). This 2-stack film is composed of a 20 bilayer bottom stack made of a 50 wt.% mixture of 24 nm and 50 nm SiO_2 nanoparticles, and a 3 bilayer top stack made of 8 nm SiO_2 nanoparticles. PAH was used as the positively charged counterpart to the negatively charged SiO_2 nanoparticles in both stacks (see Section 5.2). The 2-stack construct was fluorinated using a fluorosilane (see Section 5.4.3) before measuring contact angles of various water-ethanol mixtures on the hydrophobized surface. We assume that the fluorosilane treatment forms a negligibly thin monolayer on the surface and that it does not significantly alter the parameters of interest, r and ϕ_s.

Data points in the quadrant IV of the wetting diagram (Figure 5.8) is a signature of metastable droplets. Droplets in quadrant IV have contact angles $\theta^* > 90°$ on the nanoparticle film, although their contact angles on a chemically equivalent smooth surface (i.e., a fluorosilane-treated glass slide) is $\theta < 90°$. When metastable droplets are pressured from the top, so that they are provided with sufficient energy to overcome any energy barriers and reach their equilibrium states, their new contact angles are predicted well by Equation 5.1; the data points in quadrant IV jump to quadrant I. A metastable droplet in quadrant IV is shown in Figure 5.9a. Figures 5.9b and 5.9c show the transition of the metastable droplet from quadrant IV ($\theta^* > 90°$) to quadrant I ($\theta^* < 90°$) upon pressuring the droplet from the top with an identical surface to the one on the bottom. When the two identical surfaces are finally separated (Figure 5.9d), the droplets remaining on both surfaces are clearly in quadrant I ($\theta^* < 90°$).

These experiments demonstrate that nanoparticle thin films have re-entrant surface features which can be potentially useful for making transparent superoleophobic surfaces. Unfortunately, the metastable droplets observed in our study were in the Wenzel regime and all had receding contact angles < 90°. This may be due to incomplete or non-homogeneous fluorination of the sophisticated surface texture.

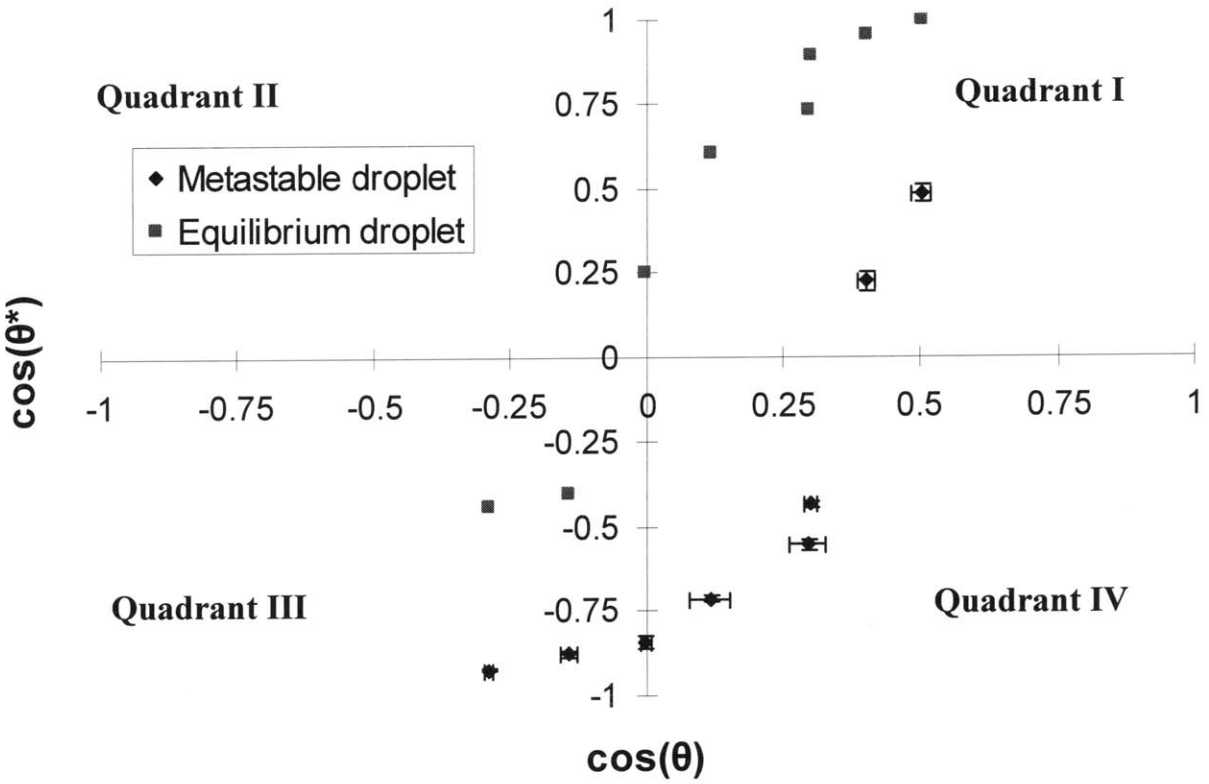

Figure 5.8. Wetting diagram of metastable and equilibrium-state droplets on a transparent superhydrophobic surface.

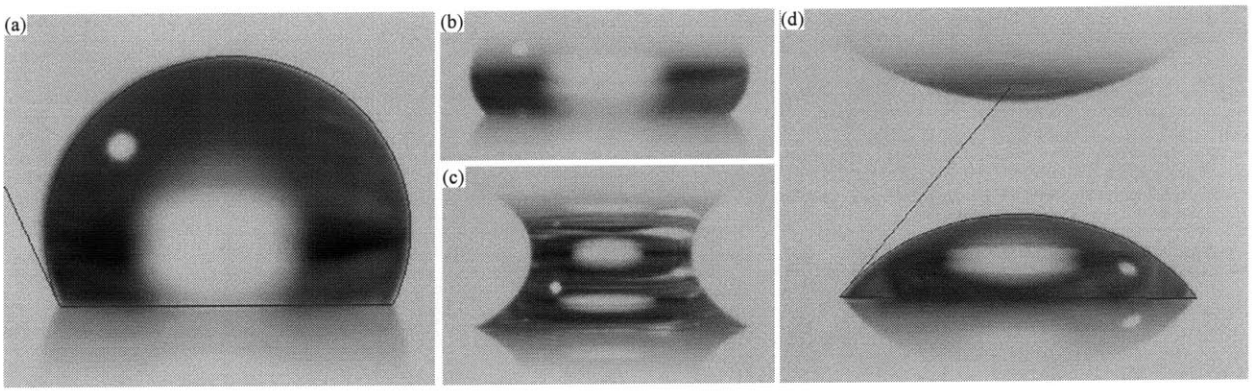

Figure 5.9. (a-d) Evolution of a 40 vol.% ethanol-water mixture droplet pressured between two identical superhydrophobic surfaces.

5.3 Conclusions

A wetting diagram analysis was applied to nanoparticle thin film assemblies, to our knowledge, for the first time. ϕ_s was confirmed as an important parameter that influences the wetting state (Wenzel versus superwetting) of a surface, and morphological features that appear almost identical under AFM were successfully discerned using the wetting diagram analysis.

Capillary condensation of water vapor and the subsequent physical-chemical action of the water condensate, such as dissolution-redeposition of neighboring nanoparticles, was claimed to affect the wettability and antifog property of highly porous nanoparticle thin films in a particle size-dependent manner. Films composed of smaller particles show better antifog properties initially, possibly due to their larger surface area. However, since films composed of smaller particles are also more susceptible to capillary condensation, these films have the shortest-lived antifog properties.

A relatively dense, non-porous nanoparticle thin film, $APSiO_2$/PAA, was investigated as assembled on soda lime glass substrate. The interstitial volumes between nanoparticles are filled with PAA in $APSiO_2$/PAA films, and therefore there is not much volume available for capillary condensation of ambient humidity. These denser films were shown to retain their antifog properties over at least three days of storage under 37°C and 80% r.h. However, the $APSiO_2$/PAA films assemble into more porous films on substrates less hydrophilic than soda lime glass, such as quartz, silicon wafer, and polycarbonate. The difference in porosity on different substrates is most likely due to an alteration to the film growth mechanism, as suggested by past[3] and recent AFM studies. The more porous $APSiO_2$/PAA films on polycarbonate substrates were shown to lose their antifog properties as capillary condensation of water vapor ensued. Extent of capillary condensation was monitored using the refractive index increase. Application of hydrophilic underlayers (e.g., CHI/CMC or PAH/SPS) prior to assembly of $APSiO_2$/PAA did not extend antifog longevity. Assembling hydrophilic underlayers is not an effective method to eliminate substrate-dependence, since the underlayers themselves assemble differently on different substrates (e.g., soda-lime glass vs. quartz and polycarbonate). Therefore, substrate properties should be investigated not in and of themselves, but rather in the context of their influence on nanoparticle self-assembly.

5.4 Materials and Methods

5.4.1 Materials

Ludox® SM-30, HS-40, TM-40 (30 wt.%, 40 wt.%, and 40 wt.% SiO_2 nanoparticle dispersions in water, average particle sizes of 8 nm, 15 nm, and 24 nm and specific surface areas of ~345 m^2/g, ~220 m^2/g, and ~140 m^2/g, respectively), $APSiO_2$ (3 wt.% SiO_2 suspension in ethanol, average particle size of 15 nm) PAH (Mw ~ 56,000 g/mol), SPS (Mw ~ 70,000 g/mol), CHI, CMC, and PEI (Mw ~ 750,000 g/mol), Boric acid (BDH), KCl (Mallinckrodt), and heptadecafluoro-1,1,2,2-tetrahydrodecyl triethoxysilane were purchased from Sigma-Aldrich (St. Louis, MO). 50 nm SiO_2 nanoparticles (5.73% wt.% dispersion in water) and PAA (Mw ~ 250,000 g/mol) were purchased from Polysciences, Inc. The average sizes of silica nanoparticles were provided by the suppliers. 3″x1″ glass slides were purchased from VWR International. The supplier uses Electroverre® glass manufactured by Erie Scientific (Switzerland). Bare polycarbonate was kindly provided by Teijin-Kasei Corporation.

5.4.2 Film Assembly

Sequential adsorption of polymers and nanoparticles was performed using a StratoSequence VI spin dipper (nanoStrata Inc.), controlled by StratoSmart v6.2 software, at 120-130 rpm. The concentrations of polymer solutions, SiO_2 nanoparticle solutions, and $APSiO_2$ nanoparticle solutions were 0.01 M, 0.023 wt.%, and 0.03 wt.%, respectively. MQ water was used to prepare the buffer, polymer, and rinse solutions. Ludox® particles were filtered through a 0.20 μm cellulose acetate filter prior to dilution in a pH 9.0 boric acid buffer solution (3.1 g/L Boric acid, 3.7 g/L KCl, and 0.86 g/L NaOH in MQ water). $APSiO_2$ particles were sonicated for 15 min and filtered through a 0.20 μm cellulose acetate filter prior to dilution in MQ water at pH 3.0. CHI was dissolved in a 0.1 M acetic acid solution. CMC, SPS, and PAA were diluted in regular MQ water. CHI/CMC and $APSiO_2$/PAA films were assembled at pH 3.0, including rinse solutions. PAH/SPS films were assembled at pH 4.0, including rinse solutions. PAH and SPS solutions contained 0.1 M NaCl for faster film growth. PAH/SiO_2 films were assembled at pH 7.5 and 9.0, respectively, for the polymer and nanoparticle solutions. Rinse solutions were not adjusted for pH in PAH/SiO_2 assemblies. Only superhydrophobic films were assembled using a different recipe. In the case of superhydrophobic 2-stack films, the

bottom stack was dipped from PAH and a 50 wt.% mixture of Ludox® TM-40 and 50 nm SiO_2 particles diluted in a pH 9.0 buffer made by titrating an aqueous 0.05M sodium tetraborate solution with HCl. The top stack was dipped from PAH and an aqueous solution of Ludox® SM-30 nanoparticles at their native pH. Rinse solutions were not adjusted for pH. Glass and quartz substrates were degreased using Alconox® (Alconox, Inc.) detergent powder under sonication for 15 min, and then cleaned with 1.0 M NaOH solution under sonication for another 15 min. Finally, the substrates were sonicated in MQ water for 5 min and blow-dried with dry air. Polycarbonate samples were O_2-plasma treated for 10 s (see Section 2.4.3). Silicon wafer substrates were used as received. The dipping time in each polymer or nanoparticle solution was 10 min followed by three rinse steps (2, 1, and 1 min).

5.4.3 Film Hydrophobization

An open vial of 0.5 mL heptadecafluoro-1,1,2,2-tetrahydrodecyl triethoxysilane was placed in a sealed Teflon container (BrandTech Inc., Essex, CT). The Teflon container was then heated to 140°C in an oven for 30 minutes. The substrates to be hydrophobized were then placed into the Teflon container and kept in the oven at 140°C for another 30 minutes. The container was opened immediately upon removal from the oven and the hydrophobized substrates were taken out. The substrates were stored under ambient conditions overnight prior to contact angle measurement.

5.4.4 Antifog Property Characterization

The humidity chamber described in Section 4.4.5 was set to 80% r.h. at 37°C. The samples to be tested were placed in a closed transparent box under ambient conditions, and the box was then moved into the humidity chamber. The box featured a background text behind the transparent sample to be tested for its antifog properties, such that the background text could only be read if the sample did not fog. The first photograph of the background text behind the sample was taken immediately upon opening the box inside the humidity chamber. Two more photographs were taken after 10 s and 20 s of opening the box. The antifog property was evaluated based on the 10 s data point. The films were rated very good, good, middle, or bad for antifog applications (Figure 5.10).

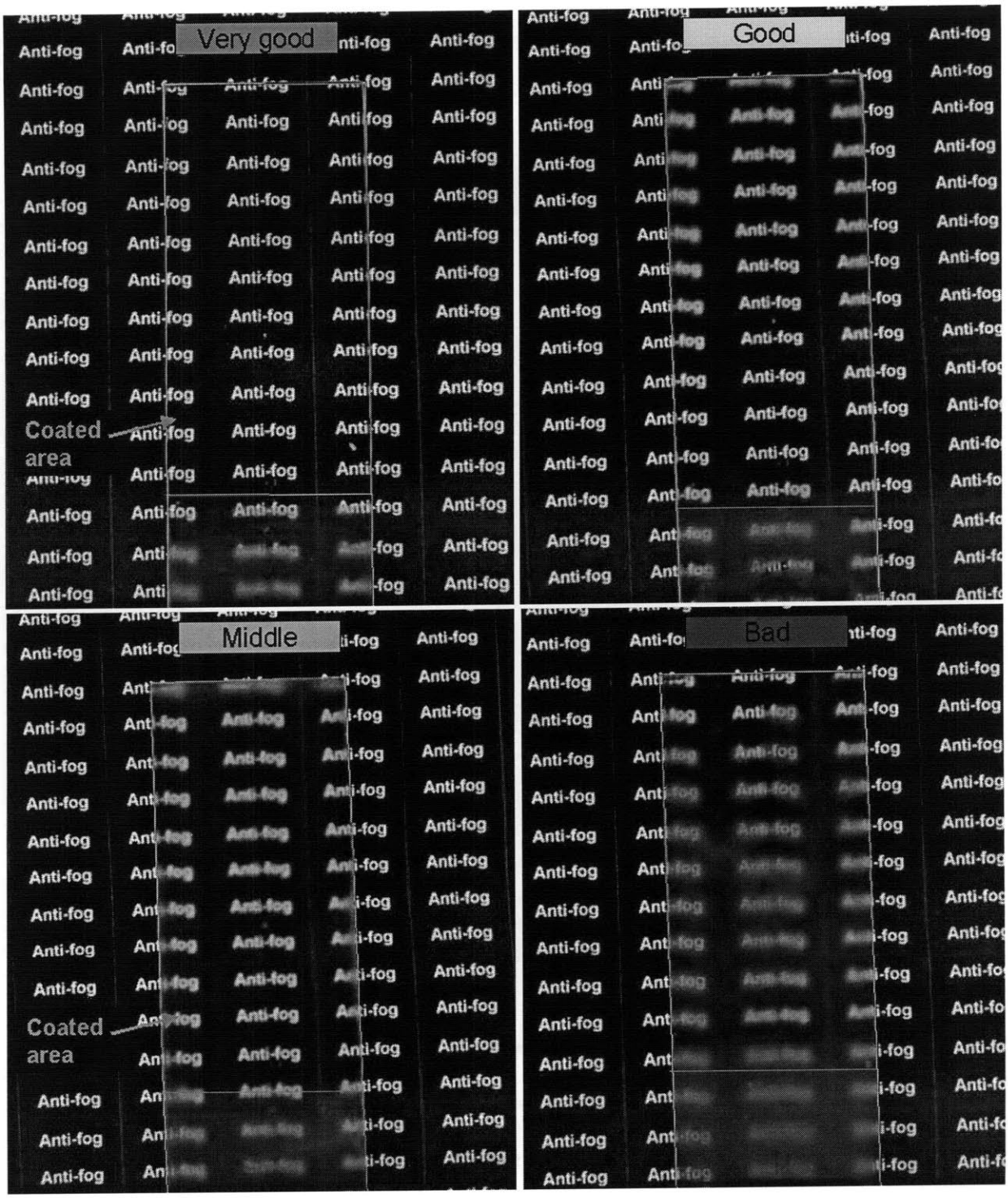

Figure 5.10. Evaluation and rating of antifog property.

5.4.5 Contact Angle Measurements

Sessile drop advancing contact angles of approximately 0.5 μl MQ water droplets were measured using a VCA-2000 contact angle measurement system (AST Products, Inc., MA).

5.4.6 AFM and Ellipsometry Measurements

AFM and ellipsometry methods are described in Sections 4.4.6 and 2.4.5, respectively.

5.4.7 Porosity Measurements

Porosity was inferred from the difference between dry-state and wet-state (submerged in ethanol) refractive indices of porous nanoparticle thin films, assuming that all pores are interconnected and accessible by ambient liquids. The detailed experimental and mathematical procedure outlined by Lee et al.[1] was followed without modification.

Chapter 6
High-Performance Optical Films From Aqueous Solution

6.1 Introduction

6.1.1 Multi-Stack Broadband Antireflection Coatings

AR coatings are among the most comprehensively studied optical coatings. AR coatings are widely used in eyewear, imaging devices, lasers, etc. Sol-gel and vacuum deposition techniques have been adopted as industrial manufacturing routes. Solution techniques (e.g., sol-gel) are preferable over vacuum techniques from an economic perspective. Vacuum systems involve significantly higher capital and maintenance costs. While vacuum processes provide line-of-sight deposition, solution techniques coat both sides of the substrate simultaneously. Recent technological trends require high-throughput application of conformal, high-performance multi-stack broadband AR coatings on very small and very large substrates with equal facility. For example, optical coatings on microlenses for cellular telephone cameras, ever-expanding flat-panel television screens, and large glass panes for solar cell and energy-efficient architectural applications are in demand. Vacuum processes stop short of meeting the scale, speed, cost, and quality requirements simultaneously. While single-layer quarter-wave AR coatings can be easily applied onto flat substrates using sol-gel techniques, more complicated multi-stack broadband AR coatings require vacuum deposition techniques to meet stringent thickness control requirements. A most ambitious 4-stack sol-gel AR coating is found on the dashboard covers of Toyota Prius cars[114]. However, the coating has a haze value of 2-4%. While a relatively high level of haze is advantageous for antiglare functionality, it is not generally acceptable. Moreover, sol-gel films cannot be applied conformally and uniformly to curved substrates, due to surface tension effects.

The LbL assembly technique is a promising method to achieve high-quality, solution-based optical coatings[59]. A great virtue of the LbL assembly technique is its capability to produce uniform, conformal thin film coatings of virtually any charged polymer or nanoparticle species, with precise morphological, compositional, and thickness control over the resultant multi-stack assembly from aqueous solution (see Section 1.2). An overview of the assembly process is presented in Figure 1.1.

A charged surface is dipped into alternating aqueous solutions of oppositely charged polyelectrolytes or nanoparticles, with thorough rinse steps in between. Each cycle of alternating dipping grows a "bilayer" on the surface. It is important to note that the charged species do not deposit onto the substrate; instead, polyelectrolytes and/or charged nanoparticles electrostatically assemble on the substrate. Therefore, surface tension effects are minimized and remarkably uniform films are obtained even on highly curved substrates. Film properties can be tuned by changing assembly pH (charge density on constituent materials), ionic strength, particle size distribution, etc. Many "bilayers" assembled on top of one another constitute a stack, and multiple stacks can be assembled to produce sophisticated optical coatings.

Indeed, many LbL high-performance optical coatings have been reported. Nolte et al.[115] has made digital rugate filters using in situ synthesis of silver nanoparticles in certain layers of polymeric LbL assemblies, demonstrating exquisite thickness control and film uniformity using very simple experimental methods. Hiller et al.[116] made graded-index AR coatings from polymeric LbL assemblies which can undergo pH-responsive porosity transitions to vary the refractive index.

A major drawback of polymeric films is their lack of mechanical durability, particularly in the case of porous polymeric films. The incorporation of inorganic nanoparticles greatly enhances mechanical durability of thin films if a post-assembly curing step is utilized. High-temperature calcination processes can be used to sacrifice the polymeric components all-together and to sinter the nanoparticles in the film to enhance mechanical durability. Alternative, low-temperature methods of enhancing mechanical durabilities of LbL nanoparticle thin films have also been reported.

Tikhonravov[117] established the "maximum principle," according to which two materials of greatest index contrast are sufficient to provide optimal optical performance at normal angles of incidence for any multilayer film. We present our high- and low-index materials of choice for a broadband AR application, followed by a discussion of optical film design using the two materials of choice. How material choice affects inter-stack roughness and optical properties of resultant multilayer structures is discussed in fair detail.

6.1.2 Multi-Stack Highly Reflective Coatings

In addition to AR application, multi-stack optical films have received attention for structural color applications. A butterfly wing, for example, is a perfect example of a natural object which owes its brilliant colors not to pigmentation, but to the highly sophisticated multi-stack optical film that covers its surface[118]. Mimicking such biological structures to achieve such successful coloration in industrial applications (e.g., cars) is an attractive thought.

Wu et al.[57] recently studied structural color using high-temperature (550°C) calcinated, durable LbL nanoparticle assemblies. The authors successfully achieve > 90% reflectance at certain tunable wavelengths using alternating high- and low-index stacks (Figure 6.1).

The width and intensity of the reflectance peak, as well as the intensities of the sidebands, depends on the refractive index contrast between high- and low-index stacks. Therefore, experimental limitations exist to attaining ideal structurally-colored materials. Using the same mathematical techniques that will be presented in Section 6.4.3 of this chapter, theoretical studies to approximate the optical responses of conceptual, very high-index stacks using multiple physically achievable stacks have been performed. These early results will be presented in Section 7.2.4 as a suggested direction for future research.

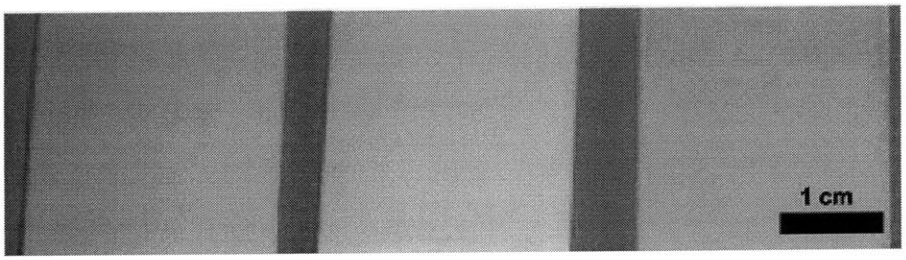

Figure 6.1. Structurally-colored glass substrates. Figure reproduced from work of Wu et al.[57]

6.2 Results and Discussion

6.2.1 High- and Low-Index Material Selection

Low-index nanoparticle films are typically highly (~50%) porous. In this study, we used all-silica nanoparticle thin films, comprised of negatively charged native 15 nm silica (SiO_2) nanoparticles paired with positively charged 3-aminopropyl-modified 15 nm silica ($APSiO_2$) nanoparticles. The

high-index material of choice was a polymer-nanoparticle film, comprised of a polyanion, poly(vinyl sulfate) (PVS), and positively charged 7 nm TiO_2 nanoparticles. Controlling stack thicknesses is critically important in multilayer AR coating design. In particular, thicknesses of low-index stacks must be on target; a sensitivity analysis reveals that a 5% thickness variation in the low-index stacks substantially worsens coating performance (see Figure C.2). The growth curves and refractive indices of the low- and high-index stacks are shown in Figure 6.2. The assembly and growth of multilayers are somewhat substrate-dependent. Low- and high-index films have therefore been assembled on top of their high- and low-index counterparts, respectively, rather than on top of bare glass substrates. Thus, the growth curves shown in Figure 6.2 describe the growth of constitutive stack elements within a multi-stack structure. The growth rate of the 7 nm TiO_2/PVS film (~2.2 nm/bilayer) is much lower than that of the $APSiO_2/SiO_2$ film (~7.5 nm/bilayer). Notice in Figure 6.2b that the ~40 nm thickness point of the 7 nm TiO_2/PVS film marks a transition in growth regimes, possibly due to incomplete surface coverage prior to reaching a critical thickness.

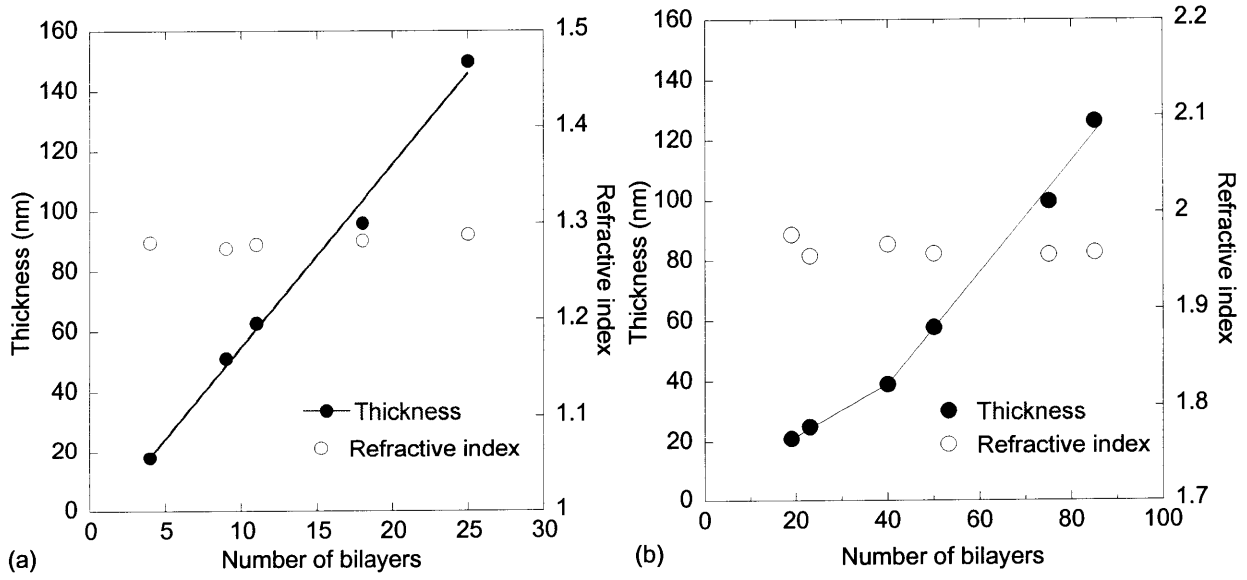

Figure 6.2. Thickness and refractive indices of (a) calcinated $APSiO_2/SiO_2$ films on calcinated TiO_2/PVS films, and of (b) calcinated TiO_2/PVS films on calcinated $APSiO_2/SiO_2$ films as functions of number of deposited bilayers.

Optimizing a sufficiently transparent high-index material was significantly more involved than the choice of the low-index material. While some haze can be accommodated in highly reflective films,

AR applications demand extremely transparent films with less than 0.5% scattering. Kim and Shiratori[119] have studied how the negatively charged polymer affects TiO_2 loading and surface roughness in TiO_2/polymer LbL films. The PVS-TiO_2 pair is reported to have the lowest root-mean-square (RMS) roughness values (σ > 15 nm). As a first-order approximation, haze scales with roughness. Kim and Shiratori's study provided a good initial guess for our material search. We investigated the influence of roughness on transparency of both single-stack high-index and multi-stack broadband AR coatings. Unfortunately, previously reported high-index layers are too rough to meet the high transparency demands of a multilayer broadband AR coating.

In search of a more suitable high-index material, we varied the TiO_2 particle size and the negatively charged polymer counterpart. The use of small, monodisperse nanoparticles provides superior transparency. Commercially available TiO_2 nanoparticles (Ishihara STS-100) were compared to nanoparticles synthesized in-house. The synthesized TiO_2 naoparticles are relatively monodisperse (5 to 11 nm in diameter; see Table 6.1) compared to STS-100 (9 to 77 nm in diameter, used previously by Kim and Shiratori). STS-100/PVS films contain large aggregates, are relatively hazy (1.5%) and rough $\sigma \sim 10$ nm (Figure 6.3a). The synthesized TiO_2 sol resulted in much smaller aggregates and a much smoother and transparent film (σ < 4nm and haze < 0.26%, respectively) with either PVS or poly(styrene-4-sulfonate) (SPS) as the negatively charged counterpart (Figures 6.3b and 6.3c). Although the refractive indices of the three films were approximately the same before calcination ($n \sim 1.8$), the 7 nm TiO_2 nanoparticle films densified to a greater extent ($n \sim 2.1$) and their surface roughness relaxed down to ~2 nm. The refractive index and σ of the calcinated STS-100 films were 1.9 nm and 9 nm, respectively.

Table 6.1. Thicknesses, refractive indices, RMS roughnesses, and haze values of various coatings (as-assembled and calcinated) composed of 7 nm or 25 nm TiO_2 nanoparticles.

Post-treatment		Sample	TiO_2 diameter (nm)	Thickness (nm)	Refractive index at 632 nm	Values of RMS Roughnesses (nm)				Haze (%)
						σ_l	σ_s	σ_i	σ	
As-assembled	Glass	TiO_2/SPS	25 ± 5	126	1.88	6.2 ± 0.7	4.1 ± 0.1	6.6 ± 0.4	10 ± 0.6	1.50%
			7 ± 1	128	1.81	1.2 ± 0.1	2.9 ± 0.03	2.1 ± 0.2	3.8 ± 0.1	0.26%
	Glass	TiO_2/PVS	7 ± 1	120	1.84	0.9 ± 0.1	2.0 ± 0.1	1.7 ± 0.2	2.7 ± 0.2	0.21%
Calcinated (550°C for 4 hours)	Glass	TiO_2/SPS	25 ± 5	91	1.91	6.9	3.6	5.4	9.4	-
			7 ± 1	70	2.06	0.6 ± 0.1	1.6 ± 0.5	1.2 ± 0.4	2.1 ± 0.6	-
	Glass	TiO_2/PVS	7 ± 1	78	2.10	0.6 ± 0.1	1.4 ± 0.2	1.1 ± 0.2	1.9 ± 0.05	-
	Glass	4-stack AR coating	7 ± 1	129	1.28	4.2 ± 1.2	4.3 ± 1.0	3.2 ± 1.2	6.9 ± 0.4	0.16%

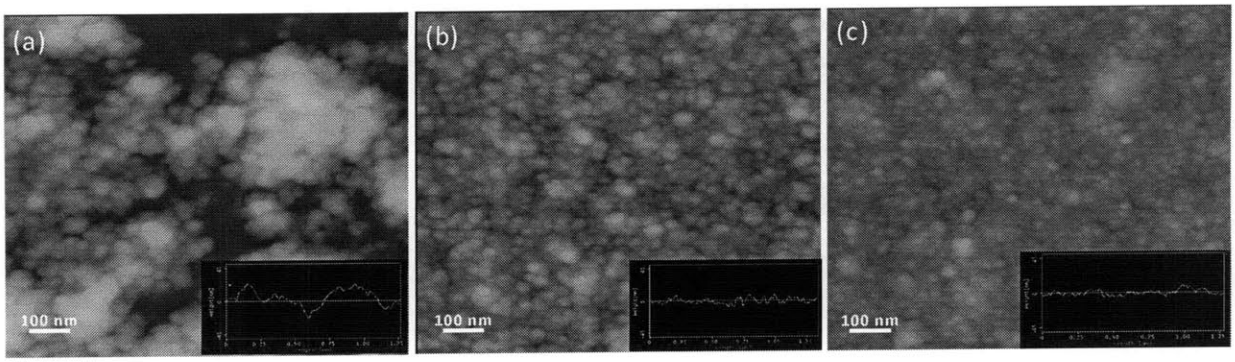

Figure 6.3. AFM height images and cross section thickness traces of as-assembled (a) 25 nm TiO_2/SPS, (b) 7 nm TiO_2/SPS, and (c) 7 nm TiO_2/PVS films on glass substrate. Film thicknesses are 126 nm, 128 nm, and 120 nm, respectively. Haze values are 1.5%, 0.26%, and 0.21%, respectively.

6.2.2 Optical Film Design

Having identified sufficiently transparent materials for the low- and high-index stacks, we proceeded to design a broadband AR film. Two alternative 4-stack films were designed using the Needle algorithm[120] and the equivalent layers method[121, 122]. The Needle algorithm recursively inserts an infinitesimally thin stack (a "needle") at an optimal position in a multi-stack film. The inserted stack thickness is then optimized while keeping all other stack thicknesses constant. The thicknesses of all the stacks are then optimized collectively before proceeding to the next "needle" insertion. Thus, the Needle algorithm has a maximum of four parameters to vary at any optimization step of a two-component, 4-stack AR design. No physical heuristics are utilized in the optimization procedure. Inevitably, the designs consist of two relatively thick high- and low-index stacks, with thinner high- and low-index stacks elsewhere in the multi-stack structure (Figure 6.4d). This is because the most beneficial addition (i.e., steepest gradient) to the original starting point (i.e., a single stack) is a needle of opposite index, which then inflates in thickness until the 2-stack structure is optimized. This 2-stack starting point dominates the optimization procedure, and as we will show shortly, hinders access to more optimal solutions.

In contrast, the Southwell[123] flip-flop algorithm slices a pre-determined total coating thickness into many decades of thin sections and flip-flops the refractive indices of these sections between high and low values. In our study, a 500 nm-thick coating was divided into 100 stacks (5 nm/stack). Initially, all 100 stacks were high-index. After flip-flopping the stack indices between n_{high} = 1.99 and n_{low} =

1.28, the design shown in Figure 6.4a was achieved. Due to the experimental difficulty of making a 100-stack coating, the spectral response of the first 98 stacks (bracketed between dashed lines in Figure 6.4a) to incident light at 600 nm was approximated using a 3-stack Herpin-equivalent, as outlined by Skettrup[121] (Figure 6.4b; see Section 6.4.3). The topmost high-index layer of 5 nm thickness was omitted. Gradient-based numerical optimization was performed on this approximate to obtain the refractive index profile shown in Figure 6.4c. The optimization objective was to minimize reflectance throughout the visible spectrum, rather than to match the 100-stack flip-flop design reflectance profile. Notice that although only four parameters (the stack thicknesses) were varied going from Figure 6.4b to 6.4c, the overall design procedure utilized a much larger parameter space than the Needle algorithm. In addition, the use of Herpin-equivalent stacks introduced a physical heuristic to the search algorithm.

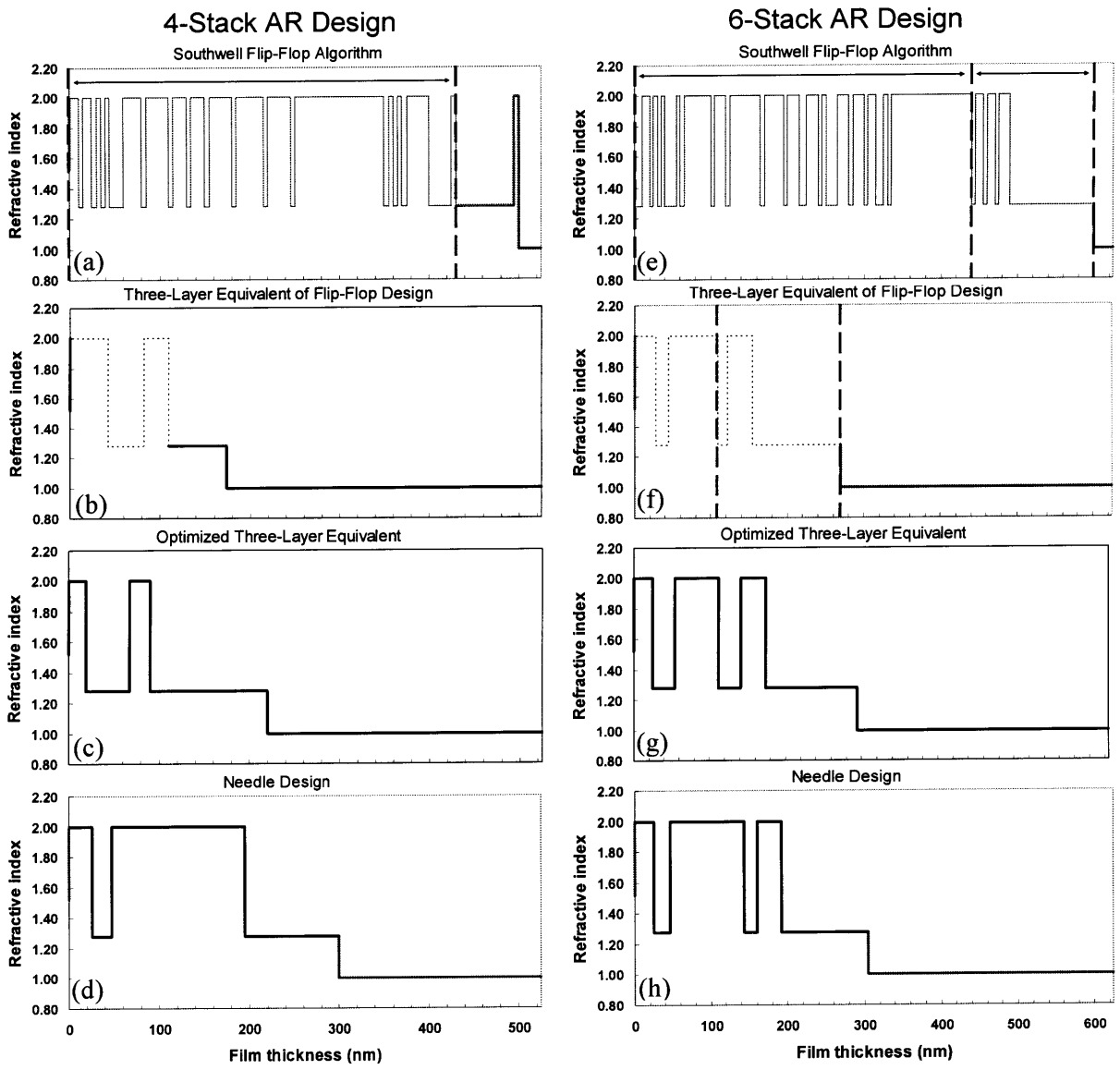

Figure 6.4. Refractive index profiles at various design stages of (a-c) a 4-stack AR coating design using equivalent layers, (d) a 4-stack AR coating design using the Needle algorithm, (e-g) a 6-stack AR coating design using equivalent layers, and (h) a 6-stack AR coating design using the Needle algorithm.

AR performances of the coatings at various design stages are plotted in Figure 6.5. The 4-stack AR coating designed using the equivalent-stacks method has been synthesized, and its optical properties are shown in Figure 6.6. The average reflectance in the visible range (400-800 nm) is < 0.5%, and the reflectance is < 1% from 400-700 nm. The stark contrast between a bare glass substrate, a single-

stack AR coating, and a 4-stack AR coating is photographed in Figure 6.6b. The single-stack coating appears bright blue, whereas the broadband AR coating reflects a barely noticeable, faint green color.

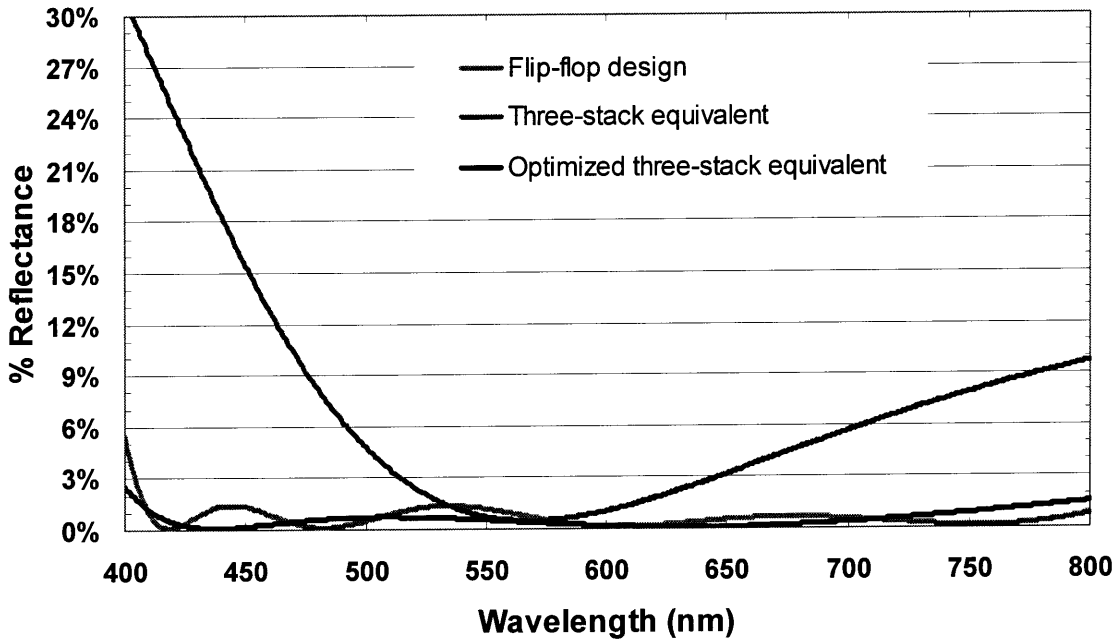

Figure 6.5. Reflectance profiles at various stages of a 4-stack AR coating design process using the equivalent-stack method.

As the number of stacks (and hence the number of variables) in the AR design increase, the difference between the two design methods should diminish. 6-stack AR coatings were designed (Figure 6.4e-h). The simulated reflectance profiles of 4- and 6-stack coatings are plotted in Figure 6.7. Using our material system, the equivalent-stack designs outperform the 4-stack Needle design and match the 6-stack Needle design in terms of AR performance. The equivalent-stack designs provide additional advantages for LbL film processing. As discussed earlier, thick high-index layers may pose a light scattering (i.e., haze) problem. The total thicknesses of the high- and low-index components in equivalent-stack and Needle designs are contrasted in Table 6.2. The equivalent-stack designs achieve excellent AR performance using much less high-index material than the Needle design.

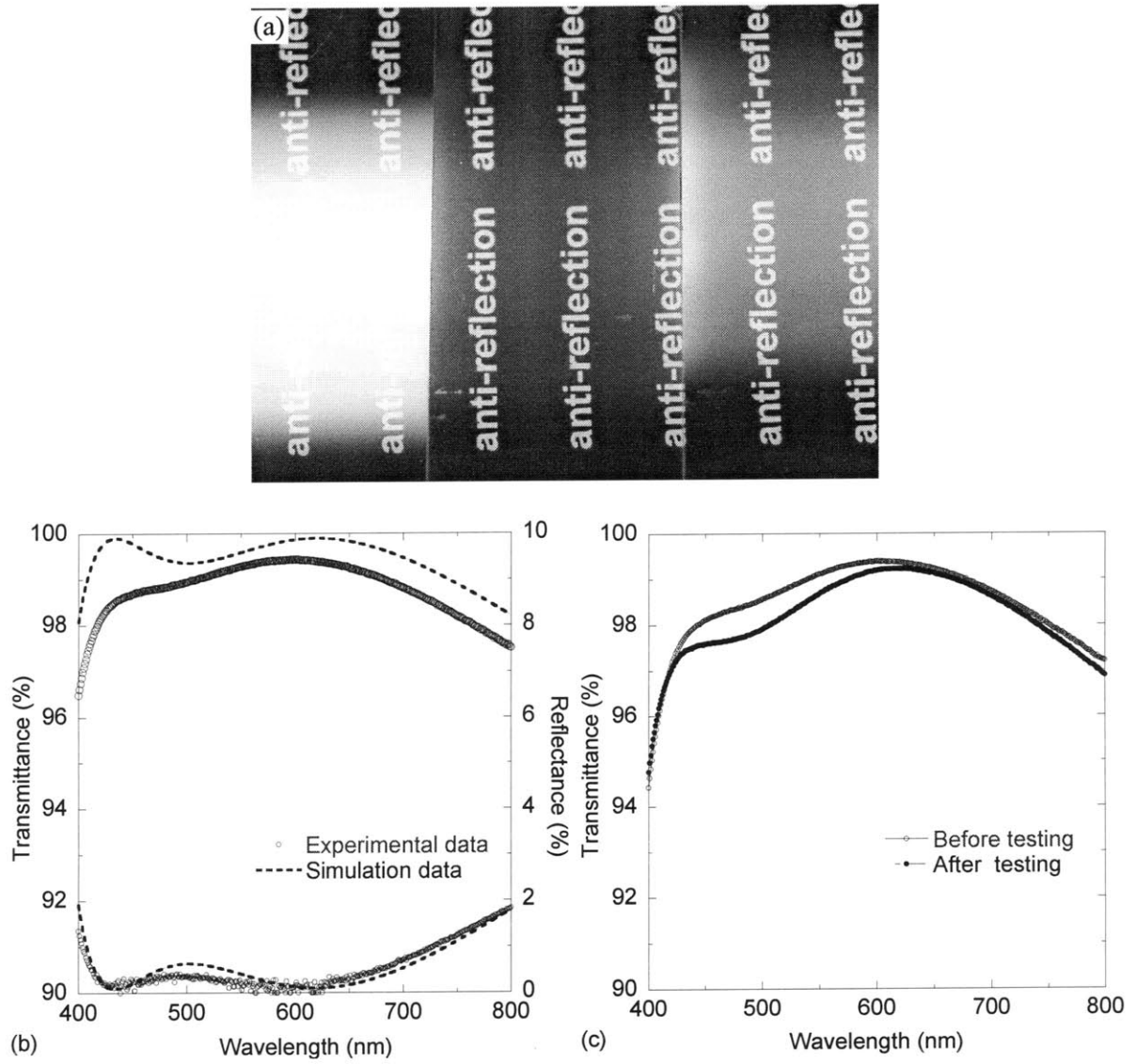

Figure 6.6. (a) Photographs of the 4-stack broadband AR coating (0.16% haze), a single-stack AR coating (0.20% haze), and bare glass substrate (0.16% haze). (b) Transmittance and reflectance spectra of the 4-stack AR coating. (c) Transmittance spectra of the 4-stack AR coating before and after abrasion testing.

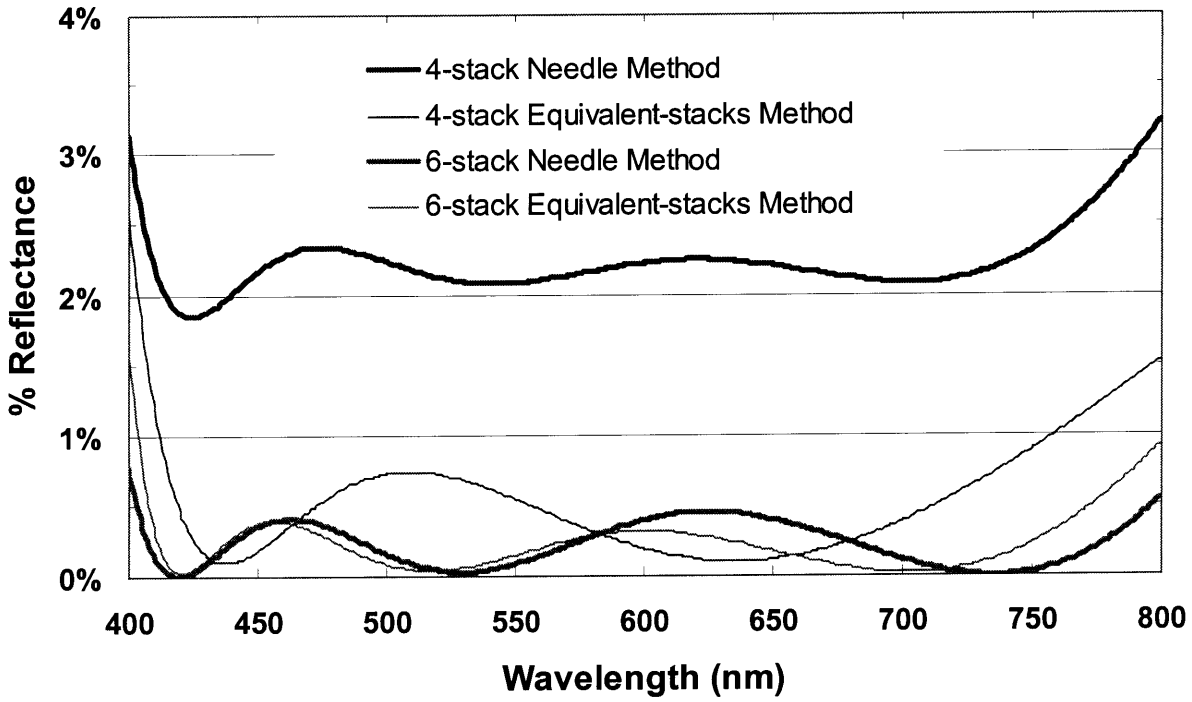

Figure 6.7. A comparison of 4- and 6-stack AR coatings designed using the Needle and equivalent-stack methods.

Table 6.2. The total thicknesses of the high- and low-index components in the 4- and 6-stack designs calculated using Needle and equivalent-stack methods.

	4-Stack Coating Design Method		6-Stack Coating Design Method	
	Needle	Equivalent-stacks	Needle	Equivalent-stacks
Total high-index stack thickness (nm)	174	42	154	116
Total low-index stack thickness (nm)	126	178	151	178
Total film thickness (nm)	300	220	305	294

6.2.3 Surface Roughness, Inter-Stack Roughness, and Transparency

Roughness is the principal cause of scattering in optical thin films[124]. Atomic force microscopy (AFM) is commonly used to characterize surface roughness. The most commonly reported parameter, σ, characterizes roughness to a first approximation. It may appear from the discussion above that < 3 nm roughness is necessary for film transparency. However, low-index films have σ > 7 nm, and are very transparent. Moreover, the undulations of a relatively rough low-index stack are readily conducted to a highly conformal overlying high-index stack, and elevate the σ of the

overlying, otherwise smooth high-index stack. Nevertheless, as we will show shortly, extremely transparent multilayer broadband AR coatings can be made using these two stacks. Clearly, the correlation between σ and haze is not a simple inverse proportionality.

Light scattering is induced primarily by surface features of length scales greater than the optical wavelength of incident light[125]:

$$\lambda_{surface} > n_{surface} \cdot \lambda_{incident}, \tag{6.1}$$

where $\lambda_{surface}$ is related to the spatial frequency of surface features, $n_{surface}$ is the refractive index of the surface, and $\lambda_{incident}$ is the wavelength of incident light in vacuum. On the other hand, surface features with smaller optical wavelength than the wavelength of incident light do not make any significant contribution to light scattering[125]:

$$\lambda_{surface} \cdot n_{surface} < \lambda_{incident}. \tag{6.2}$$

σ does not discriminate between small and large spatial frequencies of surface texture. A Fourier transform of an AFM image can be used to deconvolute the lumped-sum roughness (σ) into its small-, large-, and intermediate-scale roughness components (σ_S, σ_L, and σ_i, respectively) such that[125]:

$$\sigma^2 = {\sigma_S}^2 + {\sigma_L}^2 + {\sigma_i}^2. \tag{6.3}$$

The frequencies of interest are bounded by the image scan size (longest possible wavelength) and the digital image resolution (shortest possible wavelength). σ_L is calculated by integrating over surface spatial wavelengths between the image scan size and $n_{surface} \cdot \lambda_{incident}$. σ_S embodies wavelengths between $\lambda_{surface} \cdot n_{surface}$ and digital image resolution (see Section 6.4.4). σ_S does not decrease specular transmittance to any appreciable extent, and the principal contribution to haze can be attributed to ${\sigma_L}$[125]:

$$\frac{r}{r_0} = \left(1 - 2\left(\frac{2\pi}{\lambda_{incident}}\right)^2 n^2 {\sigma_L}^2\right), \text{ and} \tag{6.4}$$

$$\frac{t}{t_0} = \left(1 - \frac{1}{2}\left(\frac{2\pi}{\lambda_{incident}}\right)^2 (n - n')^2 \sigma_L{}^2\right), \tag{6.5}$$

where r/r_0 and t/t_0 are the ratios of roughness-corrected Fresnel coefficients for use in a recursive spectral simulation algorithm (e.g., Ábeles matrix algorithm[9]). n and n' are the refractive indices of the stack of interest and of the overlying stack, respectively. Note that σ_L reduces reflectance of a particular stack in proportion to its refractive index. In contrast, the transmittance is reduced in proportion to the refractive index contrast with the overlying stack. In either case, high-index stacks have a greater tendency to scatter light. While light scattering by internal (i.e., bounded) high-index stacks is mitigated by a smaller index contrast, high index materials scatter much more effectively across air interfaces (pores within the high-index stacks and possibly the final film-air interface). The 4-stack broadband AR coating in Section 6.2.2 terminates at the air interface with a low-index stack. Comparing this low-index stack with the high-index stack composed of 25 nm TiO_2 nanoparticles, the combination of a lower σ_L (4.2 nm versus 6.9 nm) and lower refractive index (1.28 versus 1.91) results in a haze level equal to that of the underlying glass substrate (0.16%). To our knowledge, this material system provides the greatest transparency among alternative solution-based films, and is on par with vacuum-deposited films.

We have studied the correlation between various components of σ and haze values (Table 6.1). Both σ and σ_L/σ of the high-index layer decrease with decreasing particle size. Haze values correlate with the σ_L values of high-index stacks. We used σ_L and σ values to simulate roughness-corrected spectral properties of the 4-stack AR coating we prepared. Both σ_L and σ are on the same order of magnitude, but σ grossly overestimates scattering loss in transmittance. Neither measure of surface roughness has a significant impact on the previously simulated reflectance profile (data not shown). Although σ_L accurately estimates average transmittance (see Figure 6.8 inset) and predicts light scattering, successful simulation of intricate spectral features await the development of more detailed optical models. Accounting for intra-stack index variations, scattering losses due to internal pores, and effects of "inclusion" (e.g., pore or nanoparticle) shapes[126] on refractive index models would assist the development of sophisticated solution-based optical coatings.

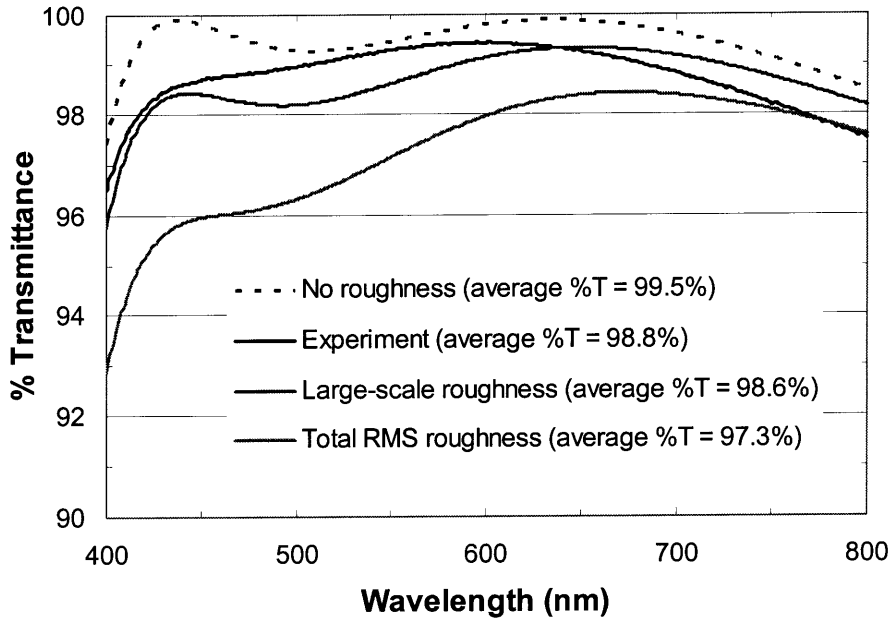

Figure 6.8. Roughness-corrected (red and blue curves) and zero-roughness (dashed) simulations of the 4-stack AR coating transmittance, compared to the experimental result (solid black curve).

6.3 Conclusions

A highly transparent, durable, 4-stack broadband AR coating with 0.2% haze and < 0.5% reflectance over the entire visible range (400 – 800 nm) has been made on soda lime glass substrate from aqueous solution. A four-stack approximation of a 100-stack flip-flop AR coating design was implemented using LbL films composed of $APSiO_2/SiO_2$ and 7 nm TiO_2/PVS nanoparticles as high-index (n ~ 2.1) and low-index (n ~ 1.3) materials, respectively. The effect of inter-stack and surface roughness on light scattering (i.e., haze) has been investigated using AFM measurements and optical simulations. Using the smallest possible high-index nanoparticles and achieving low large-scale surface roughness values (σ_L, particularly in the high-index stacks) were found to be critical for success. To our knowledge, the uniform, conformal coating we made matches the optical specifications of its vacuum-deposited equivalents, and thus exceeds those of previously reported solution-based AR coatings.

6.4 Materials and Methods

6.4.1 Materials

7 nm anatase TiO_2 nanoparticles (1.37 g/L dispersion in water) were synthesized as described elsewhere[71]. 20-25 nm anatase TiO_2 nanoparticles STS-100 (18 wt% dispersion in water) were kindly provided by Ishihara Sangyo Kaisha. Ludox® HS-40 (40 wt.% SiO_2 dispersion in water, average particle size of 15 nm, and specific surface area of ~220 m^2/g), $APSiO_2$ (3 wt.% dispersion in ethanol, average particle size of 15 nm), SPS (Mw=70,000 g/mol), and PVS (25 wt% in water, Mw = 4,000-5,000 g/mol) were purchased from Sigma-Aldrich (St. Louis, MO). The average size of $APSiO_2$ nanoparticles was provided by the suppliers, and the average sizes of SiO_2 and TiO_2 nanoparticles were determined by DLS (see Section 2.4.4). 3″x1″ glass slides were purchased from VWR International. The supplier uses Electroverre® glass manufactured by Erie Scientific (Switzerland).

6.4.2 Film Assembly

Sequential adsorption of polymers and nanoparticles was performed using a StratoSequence VI spin dipper (nanoStrata Inc.), controlled by StratoSmart v6.2 software, at 120-130 rpm. The polymer, TiO_2, $APSiO_2$, and SiO_2 concentrations in the dipping solutions were 0.01 M, 0.015 wt.%, 0.03 wt.%, and 0.023 wt.%, respectively. Ludox®, $APSiO_2$, and STS-100 particles were sonicated for 20 minutes and filtered through a 0.20 μm cellulose acetate filter prior to dilution. Synthesized 7 nm TiO_2 nanoparticles were filtered through a 0.02 μm aluminum oxide (Anotop®, Whatman International Ltd., England) filter prior to dilution. Distilled water (> 18 MΩ·m, Millipore Milli-Q) water (MQ water) was used to dilute the nanoparticle suspensions to the desired concentration. The dipping time in SiO_2 and $APSiO_2$ solutions were 10 min followed by three rinse steps (2, 1, and 1 min). The SiO_2 and $APSiO_2$ solutions and their respective rinse solutions were adjusted to pH 4.5 with HCl. The dipping time in TiO_2 and polymer solutions were 1 min followed by three rinse steps (1 min each). The 7 nm TiO_2, STS-100, SPS, PVS solutions and their respective rinse solutions were adjusted to pH 2.0 with HNO_3. The SPS and PVS solutions were filtered through 0.20 μm polyether sulfone (PES) filters (VWR International) prior to dipping.

Glass substrates were degreased using Alconox® (Alconox, Inc.) detergent powder under sonication for 15 min, and then cleaned with 1.0 M NaOH solution under sonication for another 15 min. Finally, the substrates were sonicated in MQ water for 5 min and blow-dried with dry air. After assembly of each stack (e.g., a 7 nm TiO_2/PVS stack or an $APSiO_2/SiO_2$ stack), the coated substrate was calcinated for 2 hours at 550°C (see Section 2.4.3) prior to assembly of another stack on top. No detergent- or NaOH-cleaning processes were applied to calcinated stacks prior to subsequent film assembly.

6.4.3 Southwell Flip-Flop Design and Herpin Equivalent-Stack Calculations

The general procedure outlined by Skettrup[121] was followed. The flip-flop method of Southwell[123] was used to design AR coatings with a large number of 5nm-thick stacks, starting from an all-high-index initial condition. The characteristic matrix of this flip-flop design was calculated according to Equation 6.6:

$$M(\lambda) = \prod_{i=1}^{number\ of\ layers} M_i(\lambda) = \prod_{i=1}^{number\ of\ layers} \begin{bmatrix} \cos\phi_i & \frac{i}{n_i}\sin\phi_i \\ i \cdot n_i \cdot \sin\phi_i & \cos\phi_i \end{bmatrix}, \text{ where } \phi_i = \frac{2\pi}{\lambda} n_i d_i \qquad (6.6)$$

Then, the challenge became distilling this complicated stack of very thin films into a physically realizable, easy-to-synthesize coating. Two coatings with identical characteristic matrices have identical optical properties. By equating all four elements of two characteristic matrices evaluated at an arbitrary reference wavelength, λ_0, we would like to design the simplest multi-stack coating that has an identical characteristic matrix to that of the original flip-flop design. The determinant of any characteristic matrix must be unity. Thus, there are three degrees of freedom remaining and a three-stack coating is equivalent to the flip-flop design at wavelength λ_0. At all wavelengths other than λ_0, the equivalency is only approximate. Nevertheless, the three-stack equivalent design provides a useful initial guess for a gradient-based, nonlinear optimization routine which finally optimizes the AR coating for the desired wavelength range.

There are typically two physical solutions to the equivalent-stack problem, before numerical optimization: a high-low-high index (HLH) equivalent, and a low-high-low (LHL) index equivalent. The solution which best approximates the target spectrum at wavelengths other than λ_0 is optimal. The index profile bracketed between dashed lines in Figure 6.4a is replaced with its three-stack

equivalent in Figure 6.4b. Among the two physical solutions obtained for a HLH and a LHL three-stack equivalent, the HLH stack better approximates the flip-flop stack (Figure 6.9a). As expected, both the HLH and the LHL approximation match the flip-flop reflectance profile exactly at 600 nm, the reference wavelength at which the three-layer equivalents were calculated. A 600 nm-thick flip-flop design developed for the 6-stack AR coating was approximated using two three-layer equivalents. The upper and lower sections of the coating (indicated with dashed lines in Figure 6.9e) were best approximated using LHL and HLH three-stack equivalents, respectively (Figures 6.9b and 6.9c).

6.4.4 AFM Analysis

1 μm x 1 μm AFM scans were done as described in Section 4.4.6. Quantitative image analysis was done using the 1-D Power Spectral Density (PSD) function in the x-axis using Nanoscope v5.30r3sr3 (Digital Instruments Inc., Santa Barbara, CA) software. A 0th order Flatten algorithm was applied to all images prior to analysis. $\lambda_{incident}$ was taken to be 400 nm; thus, surface features with wavelengths between 1 μm (image size) and $400\,nm \cdot n_{surface}$ were reverse-transformed to calculate the corresponding σ_L. Surface features with wavelengths between $1\,\mu m/128$ (image resolution) and $400\,nm/n_{surface}$ were reverse-transformed to calculate the corresponding σ_S.

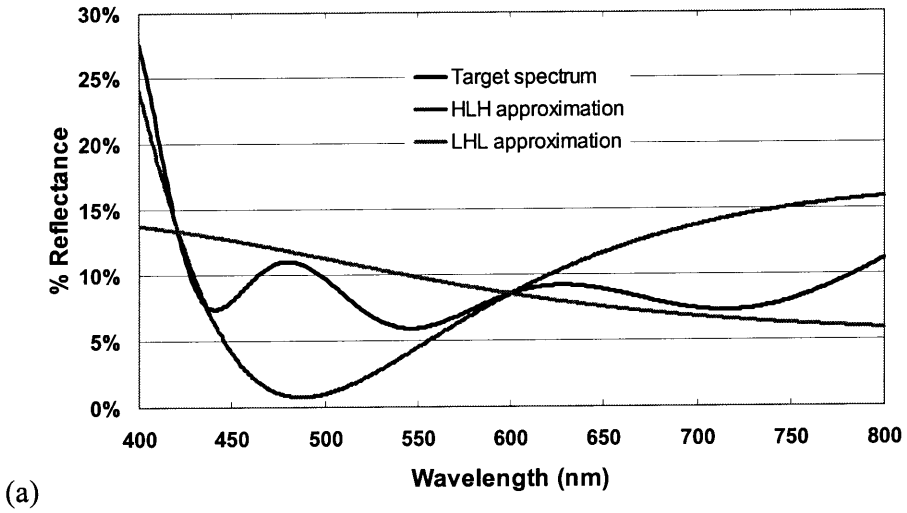

(a)

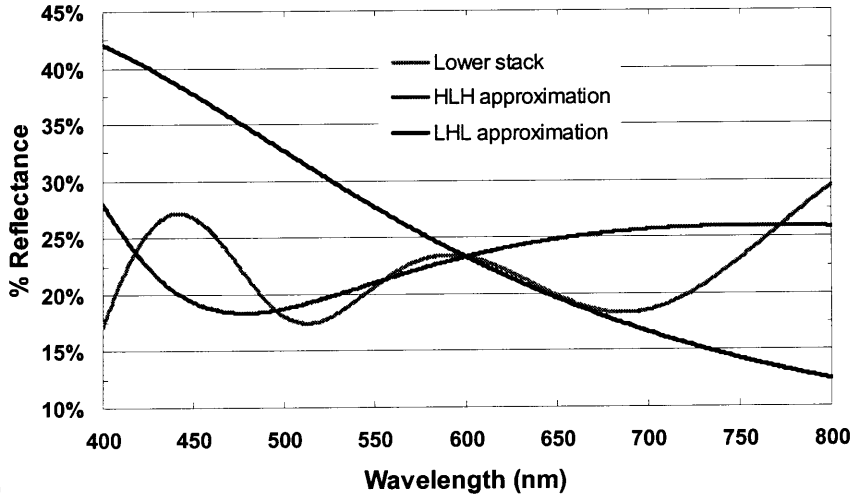

(b)

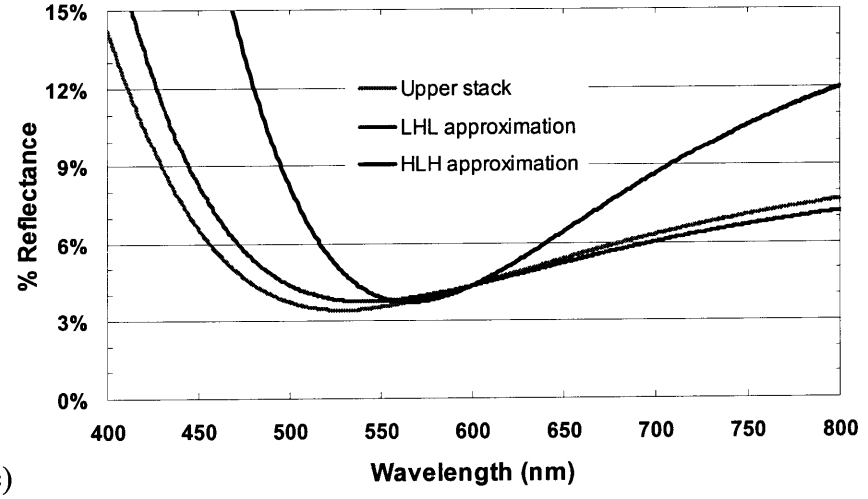

(c)

Figure 6.9. HLH and LHL three-stack approximations to the multi-stack original film sections bracketed within dashed lines in (a) Figure 6.4a and (b,c) Figure 6.4e, respectively.

Chapter 7
Conclusions and Directions for Future Research

7.1 Thesis Summary

This thesis has focused on the influence of interfacial curvature, pore geometry, and surface roughness on the thermodynamics and optical, mechanical, and wetting properties of nanoparticle thin films.

In Chapter 1, basics of the LbL assembly method were introduced as a means of assembling nanoparticles into functional thin films with precise morphological, compositional, and thickness control from aqueous solution. The elementary thermodynamic relationships between interfacial curvature and free energy, as well as basics of AR coating optics, have also been established in this introductory chapter.

Chapter 2 focused on the capillary condensation of saturated steam in between nanoparticles in an LbL thin film to promote fusion (or bridging) of neighboring nanoparticles to impart mechanical durability to the otherwise extremely delicate film. The mechanical durability of nanoporous all-nanoparticle and polymer-nanoparticle films (80-150 nm thick) on both glass and polycarbonate substrates has been greatly enhanced by hydrothermal treatment (124-134°C). Polymer-nanoparticle composite films were found to be more durable than all-nanoparticle films after hydrothermal treatment. The optical properties of the single-stack nanoporous AR films were exploited in an abrasion test (25-100 kPa normal stress) to quantify the extent of abrasive wear observed qualitatively by SEM. Marginal damage was observed under optimal reinforcement conditions. Untreated films not only delaminated from the surface completely, but also damaged their underlying glass and polycarbonate substrates during testing. The nature of the substrate was found to play an important role in determining abrasion resistance, regardless of the level of particle fusion in the film. The relatively low-temperature process enables *in situ* mechanical reinforcement of otherwise delicate nanoparticle assemblies on plastic substrates. Tribochemical wear was found to planarize the nanoscale surface texture of these films, similar to what is observed in CMP. This finding is useful for anyone trying to make robust superhydrophobic or superhydrophilic coatings. To our knowledge, this is the first report on hydrothermal reinforcement of LbL films.

Chapter 3 took a more general approach to the utilization of capillary condensation to functionalize nanoparticle thin films. First, a calculation was done to show the particle-size and temperature dependence of the volume fraction of capillary condensate in a thin film. Particle size-dependence of mechanical durability enhancement via hydrothermal treatment was also established and positioned in the more general context of capillary condensation. Next, PDMS, TEGDMA, and water vapor were condensed in films composed of various particle size distributions, and theoretical predictions we made earlier were qualitatively confirmed. The particle-size dependence was used to modulate refractive index in films where particle size varies over film thickness from 50 nm to 8 nm. Graded-index, broadband AR coatings with < 0.6% average reflectance in the visible range were prepared in this manner. In situ UV-crosslinking ability was demonstrated for TEGDMA-functionalized films.

SIEBIMM on nanoparticle thin films was reported in Chapter 4. The favorable thermodynamic habitat in pores of nanoparticle thin films and the high-energy surface of hydrophilic silica nanoparticles were hypothesized to attract soluble PDMS oligomers from the underlying PDMS substrate into the porous coating. The strongest indication of such contamination was the much elevated refractive index of the films assembled on PDMS ($n \sim 1.4$), compared to those assembled on inert substrates such as glass or Silicon wafer ($n \sim 1.3$). The use of a 100-150 nm-thick polycarbonate barrier layer in between the porous nanoparticle film and the PDMS substrate was shown to eliminate most of the oligomer migration. Polystyrene or PAH/SPS LbL films were shown to be ineffective barriers to oligomer migration. The Young's moduli of both $APSiO_2/SiO_2$ and $PDAC/SiO_2$ films were measured to be 1-2 GPa, and showed no humidity dependence. The modulus values matched literature values for organosilicate sol-gel films of comparable porosity, suggesting that porosity is the key parameter that determines Young's modulus in nanoparticle thin films.

Chapter 5 focused on the wetting properties of nanoparticle thin films for antifog, superhydrophobic, and superoleophobic film applications. A wetting diagram analysis commonly applied to micron-scale structures was, to our knowledge, applied to a nanoparticle thin film for the first time. The wetting diagram analysis revealed structural differences between films that appeared identical under the AFM, and demonstrated the ability of nanoparticle thin films to support metastable liquid droplets. The latter observation qualifies nanoparticle thin films as a potentially useful material platform to develop transparent superoleophobic films. Capillary condensation of adventitious water vapor (humidity) was shown to be a principal cause of ageing and loss of

desirable wetting characteristics of nanoparticle thin films. Recovery treatments were attempted to reverse the effects of unwanted capillary condensation.

The design and fabrication of sophisticated, high-performance, multi-component optical coatings from aqueous solution was the central theme of Chapter 6. A 4-stack AR coating was designed and fabricated using alternating high-index ($n \sim 2.1$) and low-index ($n \sim 1.3$) films. The effects of inter-stack and surface roughness on coating transparency and light scattering properties (i.e., haze) were studied quantitatively by extracting structural parameters from AFM measurements and subsequently using them in optical simulations. The optimized aqueous solution-based 4-stack AR coating had < 0.5% reflectance and ~0.2% haze in the visible range, and endured a one-hour-long cloth cleaning test under 100 kPa normal stress. An emphasis was put on the enabling aspect of the equivalent-stack approximation for solution-based optical coatings; this theoretical technique allows approximation of conceptual multi-stack structures with experimentally inaccessible thickness/refractive index combinations using readily available materials.

Beyond the scientific implications of this thesis, the presented work addresses some of the critical issues of solution-based nanoparticle thin films, and has been incorporated in two US patent applications[127, 128]. Our work has attracted support from multiple leading international companies. Such concerted and sectorally comprehensive industrial commitment is particularly exciting for the LbL assembly arena, where many commercially desirable functionalities achieved and accumulated over the last 16 years may finally enjoy procession to the marketplace.

7.2 Suggestions for Future Research

7.2.1 Low-Temperature Enhancement of Mechanical Durability via Capillary Condensation

In Chapter 2, we discussed hydrothermal treatment as a method of connecting neighboring nanoparticles via a dissolution-redeposition mechanism. In Chapter 3, we put hydrothermal treatment in the more universal context of capillary condensation of a solvent in nanoparticle thin films. We also presented results on capillary condensation of other functional materials (e.g., PDMS and TEGDMA) into nanoparticle thin films to achieve desirable optical properties by modulating refractive index. However, molecules such as TEGDMA, which can crosslink in situ can also

enhance the mechanical properties of nanoparticle thin films by linking neighboring nanoparticles at even lower temperatures than hydrothermal treatment. While TEGDMA-functionalized and UV-crosslinked 96 nm-thick PAH/8 nm SiO_2 films (see Section 3.4) on glass are not mechanically durable, TEGDMA does impart qualitative mechanical durability to films assembled on polycarbonate. As discussed in Chapter 2, adhesion to the substrate is an important element of wear-resistance, and the polycarbonate surface can react with UV-activated TEGDMA, whereas the glass surface remains inert.

Another approach we have taken is to capillary-condense a moisture-sensitive compound, tetraethylorthosilicate (TEOS) into the films and to subsequently expose the films to ambient moisture for 2 days to cure (i.e., polymerize) the condensate and link the neighboring particles. Since TEOS is a moisture-sensitive compound, it cannot be capillary-condensed into the films under ambient conditions[89]. Therefore, a moisture-free flow chamber was constructed (Figure 7.1). Argon was used as the carrier gas. The bubbler and the sample chamber were kept at the same temperature using a single piece of heating tape to heat both elements. Temperature was measured using a thermocouple (77 ± 3°C), and flow rate at the entrance and exit were measured using two flowmeters (50 ± 2 cm^3/min). TEOS treatment elevated the refractive index of the nanoparticle thin film from $n \sim 1.30$ to $n \sim 1.36$. The coated and bare polycarbonate substrates were then tested under a 25 kPa normal stress for one hour. While the bare polycarbonate (Figure 7.2a, similar to Figure 2.13a) has macroscopic grooves and scratches which scatter much of the reflections, the coated and TEOS-reinforced film on polycarbonate (Figure 7.2b) is mostly retained upon wear-testing. The color of the reflection demonstrates the retention of an AR coating, and no light scattering is evident.

Urethanes, urethane acrylates, epoxies, cyanoacrylates, and silanes are examples of functional groups that may enhance the mechanical durability of their host nanoparticle thin film matrices upon capillary condensation and *in situ* curing. The focus of future work, however, should be on anchoring the films of interest on hard-coated polycarbonate. Without an underlying hard coat, the bare polycarbonate surface is too compliant to support even a relatively tough optical thin film suitable for commercial applications.

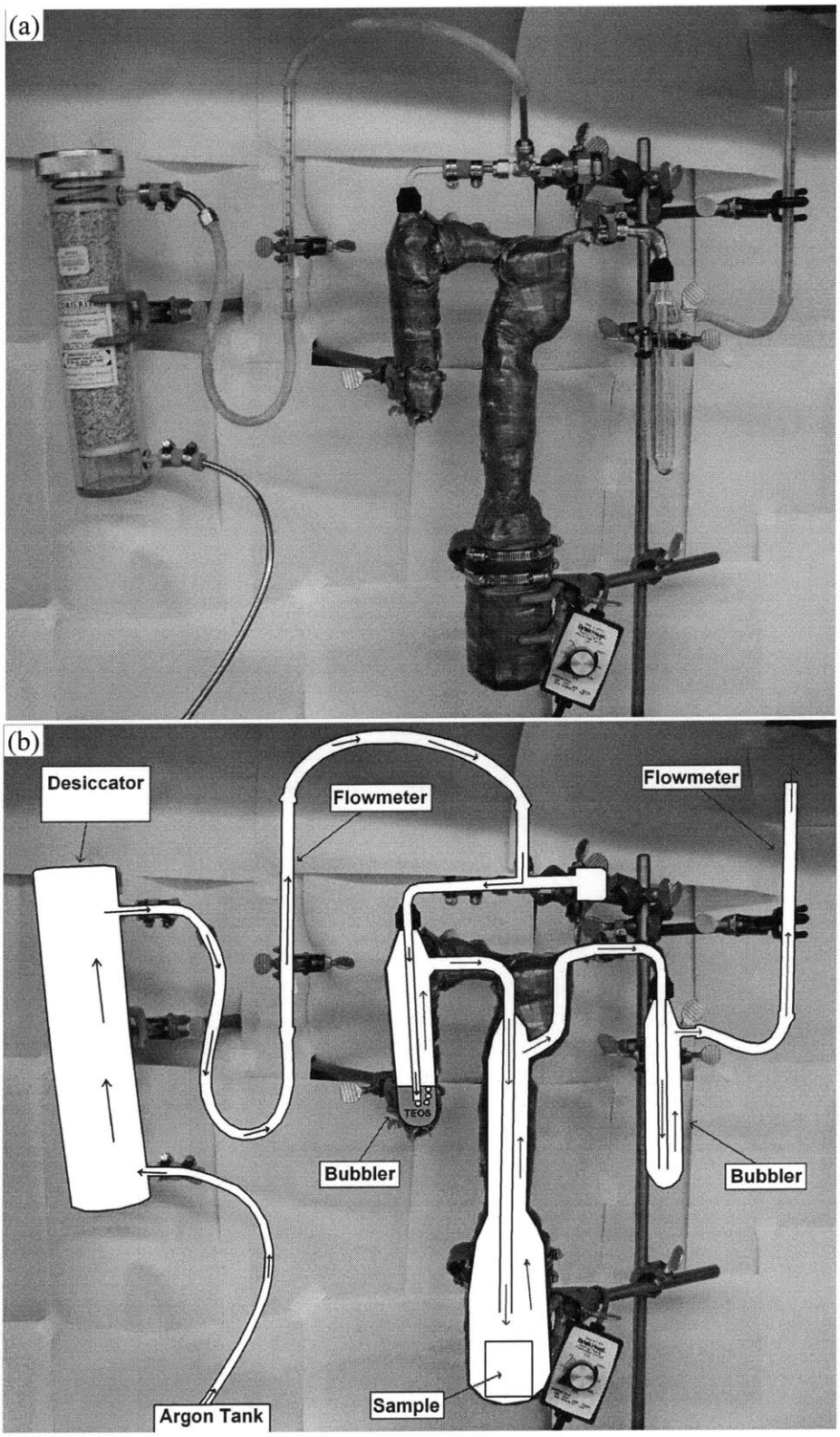

Figure 7.1. Flow chamber for capillary condensation of moisture-sensitive compounds.

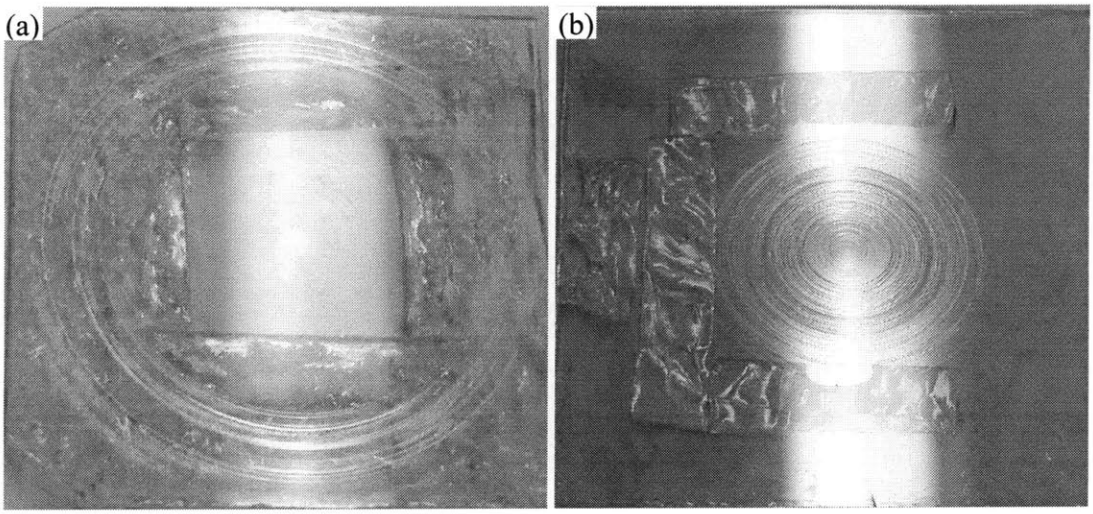

Figure 7.2. (a) Bare polycarbonate and (b) a 96 nm-thick, TEOS-reinforced PAH/8 nm SiO_2 nanoparticle coating after abrasion testing under a 25 kPa normal stress. Adhesive residue is observed on the peripheries; double-sided tape was used to attach specimens onto sample holders during abrasion testing (see Section 2.4.6 for more details).

7.2.2 Protection of Wetting Properties via Capillary Condensation

In Chapter 5, capillary condensation and subsequent solvent action of water vapor was argued to be the principal stress factor that causes ageing-related loss of antifog properties in hydrophilic nanoparticle thin films. In Chapter 3, capillary condensation of a hydrophilic material, TEGDMA, into nanoparticle thin films was presented. If TEGDMA is not a good solvent for SiO_2 nanoparticles, we would expect it to then improve the longevity of antifog property of its host matrix. Indeed, ageing-dependent antifog measurements on 2-stack PAH/8 nm SiO_2 + PAH/50 nm SiO_2 films presented in Chapter 3 indicate that TEGDMA-functionalization improves antifog longevity on glass substrates (Table 7.1). However, the antifog property of TEGDMA-functionalized 2-stack films on polycarbonate substrate are actually worsened (Table 7.1). The reasons for this inconsistency should be investigated further. One possibility is that small hydrophobic molecules migrate from the polycarbonate substrate into the overlying nanoparticle coating and contaminate it. Nevertheless, our most recent results show that capillary condensation of hydrophilic non-solvents for SiO_2 nanoparticles may prove useful in making long-lasting antifog coatings.

Table 7.1. Humidity aging-dependent antifog properties of 2-stack films presented in Chapter 3 assembled on soda lime glass and polycarbonate substrates with or without primer TEGDMA treatment and UV-crosslinking. The films were aged for the specified durations at 37°C and 80% r.h.

Substrate	TEOS Treatment?	Fresh	1 day old	3 day old
Glass	No	Very Good	Bad	Bad
	Yes	Very Good	Very Good	Very Good
	Yes (UV-crosslinked)	Very Good	Very Good	Very Good
Polycarbonate	No	Very Good	Good	Good
	Yes	Middle	Middle	Middle

7.2.3 High-Index, Ultra-Transparent Non-Linear Optical Materials via Capillary Condensation

Materials with non-linear optical (NLO) properties have long been investigated as enabling materials for the potential replacement of electro-magnetic data storage and data processing devices with photonic ones. NLO materials have an intensity-dependent refractive index[129, 130]. A subset of NLO materials show the photorefractive (PR) effect, whereby refractive index of a material can be spatially modulated under non-uniform illumination. PR materials are highly sought after for data storage applications, as they can be fabricated into erasable holograms. The intensity-dependent spatial modulation of refractive index in PR materials scales with the third power of the refractive index in the absence of illumination[130]. However, as discussed in Chapter 6, obtaining very transparent high-index thin films is a significant challenge. Similar to AR coating performance, PR performance is also highly sensitive to scattering effects. Suzuki et al.[131] recently studied polymer-nanoparticle composite composed of ZrO_2 nanoparticles and a PR polymer. They showed that incorporation of high-index ($n \sim 2.2$) ZrO_2 nanoparticles significantly improved PR performance.

LbL assembly of high-index nanoparticles into porous thin films, and functionalization of the resulting nanoporous assemblies with PR materials via capillary condensation can provide an unmatched tool to fabricate complicated holograms. Multiple highly transparent high- and low-index stacks can be built on top of each other, as studied in Chapter 6. Varying particle size distribution through the coating thickness can provide an additional means to target capillary condensation of PR materials to certain regions of multi-stack films.

7.2.4 Sophisticated Highly Reflective Film Designs using Equivalent-Stack Calculations

As discussed in Chapter 6, the equivalent-stack approach can assist the development of sophisticated optical coatings from aqueous solution. Although we have used this approach to make an excellent broadband AR coating, highly reflective coatings are gaining importance and attracting much attention recently for structural color applications (Section 6.1.2). The requirements on optical materials to achieve high reflectivity are even more rigorous than those to achieve AR functionality. Extremely high refractive index values are typically desired. For example, to achieve the reflectance spectrum shown in Figure 7.3b, materials of 2.89 and 2.50 index need to be used (Figure 7.3a). Such high index values push the limits of transparent coating materials available by any deposition method. We have followed a method outlined by Tikhonravov et al.[132] to calculate three-stack approximations to the 2.89- and 2.50-index stacks shown in Figure 7.3a, respectively (see Section A.2.3), at a reference wavelength of 525 nm. The three-stack approximations make use of two materials whose refractive indices (2.00 and 1.28) do not bracket the target indices of 2.89 and 2.50. Nevertheless, as can be seen in Figure 7.3c, the approximate structure can reproduce some of the original spectral features. Further numerical optimization of the approximate structure (similar to that applied in the design of AR coatings) using carefully chosen objective functions and optimization constraints can bring significant improvements.

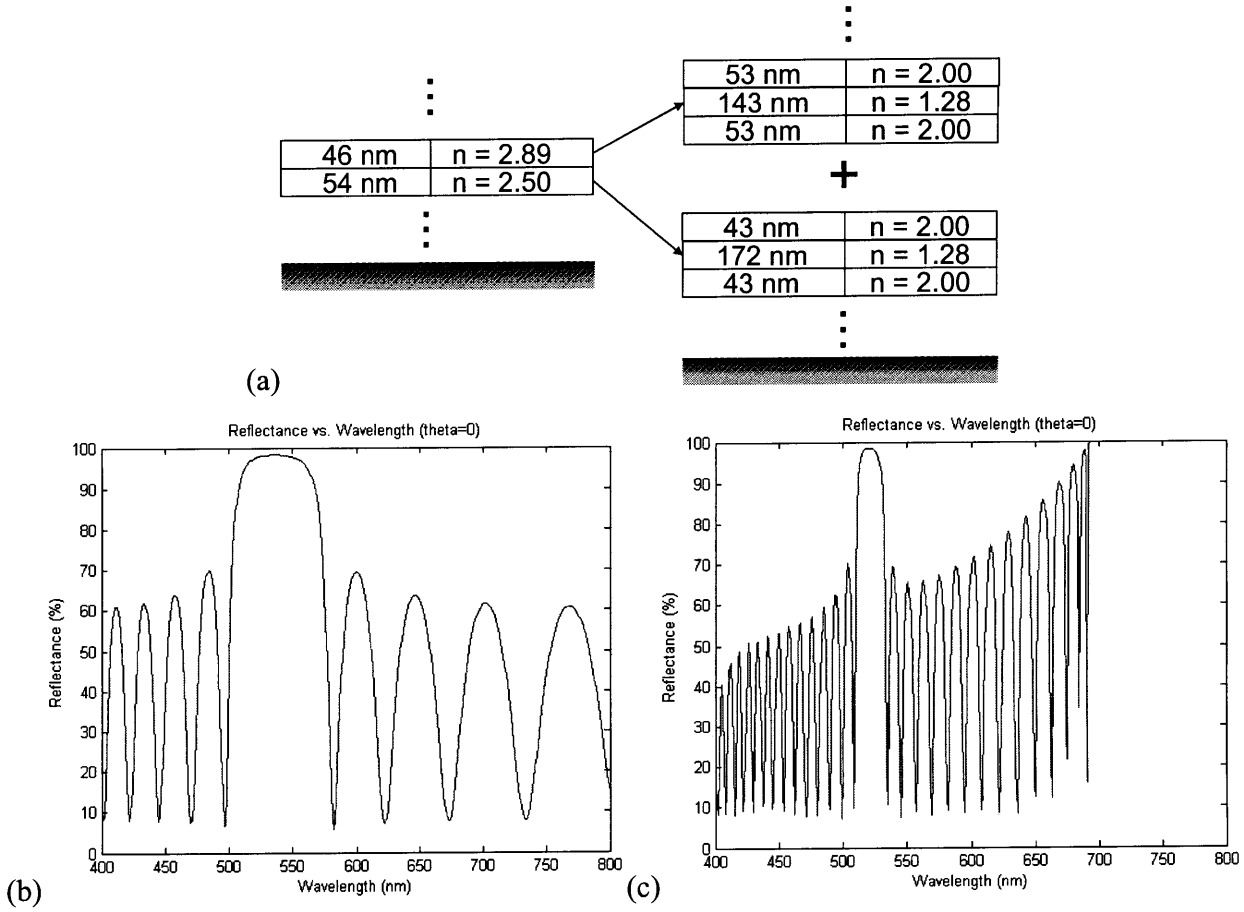

Figure 7.3. (a) Three-stack approximations to conceptual 2.89- and 2.50-index stacks using experimentally available 2.00- and 1.28-index materials. The reflectance curve shown in (b) has been simulated by placing 15 pairs of the original 2-stack structure in (a) on a glass substrate to achieve structural coloration. The reflectance curve in (c) is a simulation of the approximate structure shown in (a).

Chapter 8
PhD in Chemical Engineering Practice
Integrative Research Paper

8.1 Introduction

One of the degree requirements for the PhD in Chemical Engineering Practice is an integrative research paper on the commercial prospects of technical research, and the work presented in this thesis lends itself ideally to a licensing model of commercialization. This capstone chapter is on the financial valuation of a potential patent licensing agreement for the graded-index AR coating technology presented in Chapter 3.

We first introduce the wafer-level optics market, where the AR technology presented in Chapter 3 can add substantial value. Then, we develop a duopoly competition model in this market, where two firms, firm A and firm B, compete.

Neither, both, or only one of the firms in the duopoly competition model may choose to enter a licensing agreement with the patentee (i.e. MIT). In the Results and Discussion section, we analyze the three different licensing scenarios in terms of each company's market share, profitability, and net present value (NPV). In the Methods section we present the market data and assumptions used to construct the duopoly competition model. We conclude with a licensing strategy recommendation to the MIT Technology Licensing Office (TLO).

8.1.1 Wafer-Level Optics

Mobile camera modules can be manufactured either by chip-on-board or surface-mount technology (SMT)[133]. Developed in the 1960s, surface-mount technology has become the dominant electronics manufacturing methodology. Cell phone manufacturers would like to adopt surface-mount technology for their camera modules as well in order to achieve thinner, more reliable and cheaper phones. However, traditional plastic lenses cannot support the standard high-temperature SMT "lead-free reflow" process used in assembling the printed circuit boards for mobile phones, since surface-mount components need to be reflow-soldered by heating the entire circuit board up to 260°C in a

reflow oven. Therefore, the lens systems of the cameras must be mounted separately in an extra assembly step onto dedicated sockets (chip-on-board assembly). Chip-on-board assembly adds to the height, footprint and cost of the overall camera solution. Surface-mount components can be one-quarter to one-tenth the size and weight of their chip-on-board substitutes, and are also less expensive to manufacture[133-135].

Recently, wafer-scale lens technologies have been developed which cut through these problems by allowing high-performance lenses to be integrated directly through the standard SMT lead-free reflow process with no additional holders. Also, because lens wafers are in the same 8" and 12" formats as CMOS sensor wafers, it is possible to assemble the lens-and-sensor modules directly at the wafer scale, producing thousands of complete camera modules in one wafer-scale assembly step.

Antireflection (AR) coatings are key auxiliary components of high-end mobile cameras for several reasons. Such cameras are composed of a system of several lenses (i.e. an "optical train"), rather than a single lens. A typical optical train consists of four lenses in tandem. Ghost images are inevitable without broadband antireflection coatings that can suppress internal reflections among the lenses over the entire visible spectrum to a level below 0.5%. Moreover, as the pixel sizes of the CMOS sensors continue to shrink, light transmission becomes an issue. The CMOS sensor performs much better with increased light transmittance through AR-coated lenses. Image quality suffers in the absence of an outstanding AR coating.

The lack of an appropriate AR coating has become a limiting factor in the market expansion of wafer-scale optics. Just like traditional plastic lenses, traditional AR coatings cannot support the standard high-temperature SMT lead-free reflow process used in assembling the printed circuit boards.

Fortunately, the broadband AR coating presented in Chapter 3 is reflow-compatible, and can enable surface-mount manufacturing of mobile cameras.

8.1.2 Duopoly Competition Model

Suppose two firms, A and B, compete in the market for wafer-level optics. Thus, we assume that no firm except A and B can supply optical components to wafer-level camera manufacturers (i.e. no

supply substitutability) and that A and B can only sell their products to wafer-level camera manufacturers (i.e. no demand substitutability).

We model our invention as a cost-reducing invention, as opposed to a product-enabling invention[136-138]. In reality, AR coatings are necessary on wafer-level optics for high-end cameras and we are not aware of an alternative reflow-compatible AR coating. However, if we were to model our invention as a unique product-enabling solution, we would obtain the trivial solution that both A and B should surrender all their profits to MIT in exchange for access to our AR coating technology. This trivial solution is unrealistic, since both A and B would rather invest in R&D and eventually develop their own AR coatings than surrender all of their profits. Thus, we assume that both A and B are capable of making alternative R&D investments in order to develop suitable AR coatings for their wafer-level optics products while remaining cost-competitive with conventional optics products readily available on the market. Since virtually all commercial broadband AR coatings are vacuum-processed, we assume the AR coating developed by firms A and B in the baseline scenario would also be vacuum-processed. In contrast, the MIT AR coating is solution-processed, and in our model this difference enables cost savings for licensees.

Suppose that the marginal cost of producing a complete wafer-level optical train is c for a non-licensee. This baseline marginal cost, c, includes the vacuum-processed AR coating cost on each of the four lenses in the optical train. A licensee of the solution-based MIT AR coating reduces its marginal cost from c to $c-(\varepsilon-r)$, where ε is the cost reduction enabled by the solution-based MIT AR coating technology and r is the royalty charged by MIT per optical train. Thus, the profits of a licensee (L) and a non-licensee (NL) are:

$$\Pi_L = \left(P^{optics} - \left(c-(\varepsilon-r)\right)\right)\left(Q_L^{optics}\right) \tag{8.1}$$

and

$$\Pi_{NL} = \left(P^{optics} - c\right)\left(Q_{NL}^{optics}\right) \tag{8.2}$$

where P^{optics} is the market price of a wafer-level optical train, and Q_L^{optics} and Q_{NL}^{optics} are the quantities which the licensee and the non-licensee sell at price point P^{optics}, respectively. Neither, both, or only one of the firms A and B may choose to license the MIT AR technology. Q^{optics} is the

total number of wafer-scale optical trains sold in the industry, and therefore $Q^{optics} = Q_A^{optics} + Q_B^{optics}$. The number of licensees in the industry is a strategic decision which will be investigated in the Results and Discussion section. P^{optics} and Q^{optics} are related through the market demand curve. We did a linear demand approximation[139] for wafer-level optics, such that:

$$P^{optics} = P_{\max}^{optics} + \frac{P_{\max}^{optics}}{Q_{\max}^{optics}} Q^{optics} \tag{8.3}$$

and

$$P^{optics} = P_{\max}^{optics} + \frac{P_{\max}^{optics}}{Q_{\max}^{optics}} \left(Q_A^{optics} + Q_B^{optics} \right) \tag{8.4}$$

or equivalently,

$$\left(\frac{P^{optics}}{P_{\max}^{optics}} \right) = 1 + \left(\frac{Q_A^{optics}}{Q_{\max}^{optics}} \right) + \left(\frac{Q_B^{optics}}{Q_{\max}^{optics}} \right) \tag{8.5}$$

where $P_{\max}^{optics}$ is the maximum price any camera manufacturer would be willing to pay for a wafer-scale optical train and $Q_{\max}^{optics}$ is the market capacity for zero-cost wafer-scale optical trains.

The two competing firms need to choose a strategic variable to compete on. If the firms compete on price (Bertrand competition), then we would need to express Q^{optics} as a function of P^{optics} in Eqs. (8.1) and (8.2). The profit-maximizing strategies would be obtained by simultaneously solving $\left(\frac{\partial \Pi_A}{\partial P_A^{optics}} = 0 \right)$ and $\left(\frac{\partial \Pi_B}{\partial P_B^{optics}} = 0 \right)$ for P_A^{optics} and P_B^{optics}. If the firms compete on quantity (Cournot competition), then we would need to express P^{optics} as a function of Q^{optics} in Eqs. (8.1) and (8.2). The profit-maximizing strategies would be obtained by simultaneously solving $\left(\frac{\partial \Pi_A}{\partial Q_A^{optics}} = 0 \right)$ and $\left(\frac{\partial \Pi_B}{\partial Q_B^{optics}} = 0 \right)$ for Q_A^{optics} and Q_B^{optics} [139].

Price competition can substantially hurt both competitors, since a price war can drive prices toward marginal cost of production, thereby eroding profit margins in the industry. Whether firms compete on price or on quantity depends partly on the managers' skills and partly on the industry structure. Industries with high sunk costs and low marginal costs are particularly prone to intense price competition. For example, airlines often compete on price in order to fill their planes. In the case of firms A and B, Cournot competition (competition on quantity) is more likely, because managers of both firms are trying to decide how much *manufacturing capacity* they should build, rather than how to *price* their products. Thus, we assume Cournot competition between A and B, and calculate their profit-maximizing production strategies under the various licensing scenarios in Table 8.1.

In order to proceed with the model and to simulate the profit-maximizing strategies of the two competitors under the various licensing possibilities, we need to estimate the numerical values of key constants introduced so far – namely, $Q_{\max}^{optics}$, $P_{\max}^{optics}$, c, and ε. These numerical estimates are summarized below in Table 8.2. The market data and assumptions which were used to arrive at the values in Table 8.2 are described in the Methods section.

Table 8.1. Optimal outputs of two firms engaged in Cournot competition under various licensing scenarios, and the resulting market price and firm profits. Tax effects are omitted (see Table 8.3).

	Optimal Quantity	**Market Price**	**Resulting Profits**
Neither firm licenses	$Q_A^{optics} = Q_B^{optics} = \ldots$ $\ldots \frac{P_{\max}^{optics} - c}{3\left(P_{\max}^{optics} / Q_{\max}^{optics}\right)}$	$P^{optics} = \ldots$ $\ldots \frac{P_{\max}^{optics} + 2c}{3}$	$\Pi_A = \Pi_B = \frac{Q_{\max}^{optics}}{P_{\max}^{optics}} \left(\frac{P_{\max}^{optics} - c}{3} \right)^2$
Both firms license	$Q_A^{optics} = Q_B^{optics} = \ldots$ $\ldots \frac{P_{\max}^{optics} - \left(c - (\varepsilon - r)\right)}{3\left(P_{\max}^{optics} / Q_{\max}^{optics}\right)}$	$P^{optics} = \ldots$ $\ldots \frac{P_{\max}^{optics} + 2c - 2(\varepsilon - r)}{3}$	$\Pi_A = \Pi_B = \ldots$ $\ldots \frac{Q_{\max}^{optics}}{P_{\max}^{optics}} \left(\frac{P_{\max}^{optics} - c + (\varepsilon - r)}{3} \right)^2$
Only firm A licenses	$Q_A^{optics} = \frac{P_{\max}^{optics} - \left(c - 2(\varepsilon - r)\right)}{3\left(P_{\max}^{optics} / Q_{\max}^{optics}\right)}$ $Q_B^{optics} = \frac{P_{\max}^{optics} - \left(c + (\varepsilon - r)\right)}{3\left(P_{\max}^{optics} / Q_{\max}^{optics}\right)}$	$P^{optics} = \ldots$ $\ldots \frac{P_{\max}^{optics} + 2c - (\varepsilon - r)}{3}$	$\Pi_A = \frac{Q_{\max}^{optics}}{P_{\max}^{optics}} \left(\frac{P_{\max}^{optics} - c + 2(\varepsilon - r)}{3} \right)^2$ $\Pi_B = \frac{Q_{\max}^{optics}}{P_{\max}^{optics}} \left(\frac{P_{\max}^{optics} - c - (\varepsilon - r)}{3} \right)^2$

Using the numerical constants in Table 8.2 and an arbitrary choice of the royalty rate, r, we can evaluate the optimal outputs and corresponding profits of firms A and B using the formulae in Table 8.1. In order to calculate the NPV of the MIT AR coating license to the licensee(s), we also assumed a licensing period and a discount rate.

We assumed a licensing period of four years, beginning in 2011. Although a US patent is valid for 17 years, we assumed that the licensee(s) will become independent after the first four years of licensing either by developing their own cost-competitive AR coating technologies or by adopting alternative, state-of-the-art innovations available in the market after year 2014. At that time, the marginal cost of production of both A and B would reduce to $c-\varepsilon$ and neither firm would pay royalties to MIT beyond 2014, regardless of their original licensing decisions. However, we assumed that the two firms' market shares will not change after 2014. Thus, a licensee may gain a substantial advantage over a non-licensee by capturing a larger market share in the period 2011-2014, even though both firms gain access to a cost-effective AR coating technology beyond 2014.

Table 8.2. Demand curve constants to be used in Eqs. (8.3) and (8.5), as well as marginal cost estimations. $\overline{P}$ is the estimated average market price of an optical train without an AR coating[140].

		2010	2011	2012	2013	2014
Total wafer-scale optical train demand $\left(Q_{\max}^{optics}\right)$ (in millions of units)		50	275	875	2,125	2,500
Maximum market price of a wafer-scale optical train $\left(P_{\max}^{optics}\right)$ (under three different scenarios)	$P_{\max}^{optics}=1.1\times\overline{P}$	\$0.68	\$0.65	\$0.63	\$0.60	\$0.57
	$P_{\max}^{optics}=1.5\times\overline{P}$	\$0.93	\$0.89	\$0.85	\$0.82	\$0.78
	$P_{\max}^{optics}=2\times\overline{P}$	\$1.24	\$1.19	\$1.14	\$1.09	\$1.04
Marginal cost of producing a wafer-level optical train	With vacuum AR coating (c)	\$0.54	\$0.52	\$0.50	\$0.48	\$0.47
	With MIT AR coating $(c-\varepsilon)$ (under two different scenarios)	\$0.43-\$0.48	\$0.41-\$0.46	\$0.40-\$0.44	\$0.38-\$0.42	\$0.37-\$0.41

Due to systemic risks inherent in any particular industry, as well as the time value of money, future profits of firms A and B must be discounted to present terms. We used the discount rate of Tessera Inc., a publicly-traded wafer-scale optics manufacturer (NASDAQ: TSRA), to do the NPV calculations. Using the Capital Asset Pricing Model (CAPM), we found the appropriate discount rate for Tessera Inc. to be 12.5%. In other words, $112.50 of expected profits one year from today for a wafer-scale optics manufacturer is worth $100 today. The NPV of a licensing decision is the difference between the NPVs of all future profits of a firm with versus without the licensing agreement. The modeling assumptions we used to estimate all future profits of the two competing firms are shown in Table 8.3.

Table 8.3. Modeling assumptions used to estimate future cash flows and calculate NPVs of firms A and B under various licensing arrangements.

<table>
<tr><th></th><th>2011-2014</th><th>2015 onwards</th></tr>
<tr><td>Licensee assumptions</td><td>• Marginal cost = $c-(\varepsilon-r)$
• Pays royalties</td><td rowspan="2">• Marginal cost = $c-\varepsilon$
• Do not pay royalties
• Annual profits = (Total industry profits in 2014 under the double-licensee scenario) x (Market share in 2014)</td></tr>
<tr><td>Non-licensee assumptions</td><td>• Marginal cost = c
• Does not pay royalties</td></tr>
<tr><td>Industry assumptions</td><td colspan="2">• Corporate tax rate = 40%
• Discount rate = 12.5%
• Average retail price of complete CMOS cameras drop at 4.3% per year, 2011-2014</td></tr>
</table>

8.2 Results and Discussion

The payoff diagram in Figure 8.1 shows the NPV of various licensing decisions to firms A and B in the duopoly competition model. In the baseline scenario, neither firm licenses the MIT AR coating technology, and the payoff is $0 to each firm by definition. If exactly one firm licenses the technology, the licensee receives a net benefit (NPV) of $89.4M and the non-licensee loses $63.7M. If both firms license the technology, both licensees receive a net benefit of $17M. Under these conditions, licensing is said to be the "dominant strategy" for both firms, since each firm has an incentive to license the technology, regardless of its competitor's decision. Therefore, at Nash equilibrium, both firms would license the technology.

If both firms were to license the technology, the industry (consisting of two firms) would receive a total benefit of $34.0M. If the MIT TLO issued two licenses and was able to extract all the value generated by this AR coating technology, the payoff to MIT would be $34.0M. In comparison, the payoff of an exclusive license to MIT could be up to $89.4M. Therefore, the MIT TLO should license this technology exclusively.

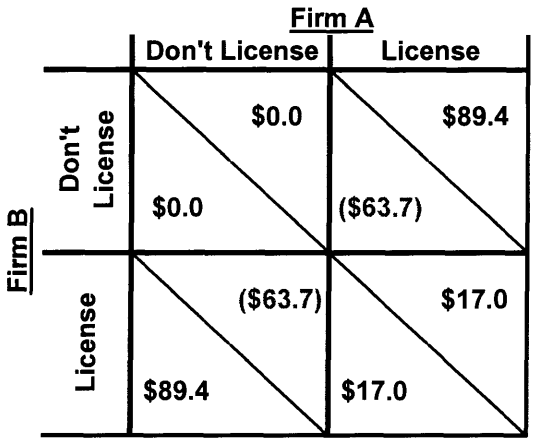

Figure 8.1. Payoff diagram with respect to licensing options of firms A and B in the duopoly competition model. All values are in millions. Since the focus is on the gross impact of their licensing decisions on the licensee(s) and the non-licensee(s), the royalty rate (r) was assumed to be zero in this calculation.

Ultimately, the question we are trying to answer is how much the MIT AR technology is worth. If the payoff matrix in Figure 8.1 had no uncertainty, we would have already arrived at the final answer. However, the NPVs presented in Figure 8.1 are averages over three uncertain variables which impact the value of the licensing agreement: $P_{\max}^{optics}$, ε, and r. Therefore, the negotiation and the final agreement between MIT and the exclusive licensee will depend on the negotiating parties' private estimates of $P_{\max}^{optics}$, ε, and r. In this context, we investigated how sensitive the value of a licensing agreement is to these three parameters. After prioritizing the three parameters from a strategic perspective, we also present how various scenarios for $P_{\max}^{optics}$, ε, and r affect the NPV of a licensing agreement.

8.2.1 The Case of an Exclusive Licensee

As mentioned earlier, an exclusive license is worth more to its single licensee ($89.4M, Figure 8.1) than a non-exclusive license is to both of its licensees combined (2*$17M = $34M, Figure 8.1). This is because an exclusive license can leverage its cost advantage to earn market share and decrease competition in the industry, whereas non-exclusive licensees benefit solely from the cost savings enabled by the new technology. In our model, both non-exclusive licensees retain 50% market share, while an exclusive licensee increases its market share due to its competitive cost position. Once one of the competitors captures the great majority of the market, there is effectively less competition among the two firms, and therefore the *effective* number of competing firms in the industry decreases. This effect can be calculated using the Herfindahl-Hirschman Index (HHI, see Methods for details). Under certain conditions, an exclusive licensee may even manage to monopolize the industry. Table 8.4 shows the effective number of equal-sized firms in the wafer-level optics market under various scenarios for $P_{\max}^{optics}$, ε, and r. Clearly, market size ($P_{\max}^{optics}$) is the most important factor which determines the strategic advantage an exclusive licensee enjoys. In a small market, there are 1.0-1.5 effective firms in competition, whereas in a large market, there are at least 1.9 firms. Intuitively, a small market can become crowded easily, even with two competing firms. Therefore, if one of the competitors can gain a slight competitive advantage by reducing its costs, it can push the non-licensee out of the market. In contrast, it is much more difficult to monopolize a large market using a relatively small (10-20%) cost advantage. The next important factor is the invention quality (ε). As shown in Table 8.4, a 21% cost reduction provides greater competitive advantage than a 12% cost reduction. However, the range of possible values for ε is not large enough to compensate for market size effects, and therefore invention quality is less important than market size from a strategic perspective. Finally, the royalty rate (r) does not have a substantial effect on the competitive ability of the exclusive licensee. The strategic advantage which an exclusive licensee enjoys is not substantially reduced with a higher r.

Table 8.4. Intensity of competition in the wafer-scale optics industry, as a function of market size, invention quality and royalty rate.

Market Size	21% Cost Reduction Due to MIT Technology		12% Cost Reduction Due to MIT Technology	
	Effective Number of Equal-Sized Competitors Under Various Royalty Schemes ($/wafer)		Effective Number of Equal-Sized Competitors Under Various Royalty Schemes ($/wafer)	
	$1	$3	$1	$3
Small	1.0 (Monopoly)	1.1	1.4	1.5
Medium	1.7	1.7	1.9	1.9
Large	1.9	1.9	2.0	2.0 (Duopoly)

A greater strategic advantage does not necessarily mean greater profits for an exclusive licensee. For instance, becoming a monopoly in a small market may be less profitable than having a 50% market share in a large market. Similarly, a higher royalty rate would certainly impact the profitability of a licensee, even though it does not adversely affect its strategic business position. NPV data with various $P_{\max}^{optics}$ values, ε values, and royalty rates (r) ranging from \$0/wafer to \$3/wafer are listed in Tables 8.5 and 8.6 for the case of an exclusive licensee. Table 8.5 presents the benefit of the exclusive licensing agreement to the licensee (firm A), as well as to the non-licensee (firm B) in dollar terms (i.e. NPV of the exclusive licensing agreement). The average payoff to the exclusive licensee in Figure 8.1, \$89.4M, is the average of the six NPVs listed under the zero-royalty column of Table 8.5 for the exclusive licensee (Firm A). Similarly, the average payoff to the non-licensee in Figure 8.1, -\$63.7M, is the average of the six NPVs listed in red color under the zero-royalty column of Table 8.5 for the non-licensee (Firm B). Table 8.6 presents the benefit of the exclusive licensing agreement as a percentage of the base value of the licensee firm without the agreement (i.e. NPV of the licensing agreement divided by NPV of the licensee firm, had MIT never developed the AR coating technology).

Table 8.5. NPV of an exclusive licensing agreement to the licensee (in black color) and to the non-licensee (in red color) under various market sizes, invention qualities, and royalty rates. Firm value without license refers to the NPV of each firm in the industry, had the MIT invention not been made. All values are in millions.

Market Size	A / B	12% Cost Reduction Due to MIT Technology: Change in Firm Values Under Various Royalty Schemes ($/wafer) $0	$1	$2	$3	Firm Value w/o License	21% Cost Reduction Due to MIT Technology: Change in Firm Values Under Various Royalty Schemes ($/wafer) $0	$1	$2	$3	Firm Value w/o License
Small		$39.7 / ($27.2)	$37.0 / ($25.8)	$34.3 / ($24.3)	$31.7 / ($22.8)	$39.7	$91.4 / ($60.6)	$87.9 / ($59.2)	$84.5 / ($57.6)	$81.0 / ($56.0)	$60.7
Medium		$61.5 / ($44.8)	$57.4 / ($42.1)	$53.2 / ($39.3)	$49.0 / ($36.5)	$162.4	$122.4 / ($86.8)	$117.6 / ($83.9)	$112.8 / ($81.0)	$108.0 / ($78.1)	$195.2
Large		$76.8 / ($57.2)	$71.6 / ($53.6)	$66.5 / ($49.9)	$61.3 / ($46.2)	$362.0	$144.7 / ($105.7)	$139.1 / ($102.0)	$133.4 / ($98.3)	$127.8 / ($94.5)	$402.8

Table 8.6. Percent increase in firm values of the licensee (in black color) and the non-licensee (in red color) due to an exclusive licensing agreement under various market sizes, invention qualities, and royalty rates.

Market Size	A / B	12% Cost Reduction Due to MIT Technology: % Change in Firm Values Under Various Royalty Schemes ($/wafer) $0	$1	$2	$3	21% Cost Reduction Due to MIT Technology: % Change in Firm Values Under Various Royalty Schemes ($/wafer) $0	$1	$2	$3
Small		100% / -68%	93% / -65%	87% / -61%	80% / -58%	150% / -100%	145% / -97%	139% / -95%	133% / -92%
Medium		38% / -28%	35% / -26%	33% / -24%	30% / -22%	63% / -44%	60% / -43%	58% / -42%	55% / -40%
Large		21% / -16%	20% / -15%	18% / -14%	17% / -13%	36% / -26%	35% / -25%	33% / -24%	32% / -23%

We generated three different scenarios for $P_{\max}^{optics}$ in Table 8.2, where $P_{\max}^{optics}$ is 10%, 50%, or 100% higher than the average market price of a conventional optical train without an AR coating, $\overline{P}$ (see Methods section for details of how $\overline{P}$ was estimated). Since $P_{\max}^{optics}$ is the maximum price which any customer is willing to pay for wafer-level optics, a higher $P_{\max}^{optics}$ implies a larger market for wafer-level optics. The three scenarios we considered simulate a small, medium, and large market for wafer-scale optics. As expected, the NPV of the license increases with increasing market size (compare the different rows of Table 8.5). However, the percent contribution of the license to the firm value of the exclusive licensee is larger in a small market (see Table 8.6). In other words, the competitive advantage that the MIT technology provides to the exclusive licensee is of greater significance in a small market. Intuitively, this is due to more intense competition in a smaller market. Hence, even a small competitive advantage can add substantial value to the exclusive licensee competing in a small market.

We generated two different scenarios for ε in Table 8.2, where marginal cost of manufacturing an AR-coated wafer-level optical train is either 12% or 21% cheaper with the MIT technology. ε represents the cost savings made possible by the MIT invention, or the quality of the invention. A higher-quality invention is worth more to a licensee than a lower-quality invention, because a higher-quality invention enables greater cost savings (see Tables 8.5 and 8.6). Note that the invention quality affects the firm value even without licensing (i.e. had MIT never developed the AR coating technology) in Table 8.5, since we assume that both competitors would have independently developed a similar cost-saving technology by 2015 (see "2015 onwards" column in Table 8.3).

Finally, we considered four different royalty rates, r, ranging from \$0/wafer to \$3/wafer in \$1/wafer increments. The NPV of a licensing agreement, calculated assuming a royalty of \$0/wafer, reflects the full economic potential of the MIT AR coating technology. A finite royalty rate increases marginal cost of production, and therefore effectively reduces the cost-reducing ability (i.e. "quality") of the invention. Therefore, the licensee cannot capitalize the full economic benefit of the technology and the NPV of the licensing agreement is inversely related to the royalty rate (see Tables 8.5 and 8.6). A portion of the value lost by the licensee is transferred to the patentee (MIT) in the form of royalty payments. The NPVs of all the royalty payments in the period 2011-2014 at various royalty rates are listed in Table 8.7. Note that typical range of royalty payments are 0% to 3% of

product revenues in industry. Table 8.7 also lists the magnitude of royalty payments as a fraction of licensee revenues, and the scenarios under consideration are within industry norms.

Table 8.7. NPV of royalty payments (above diagonal) and annual royalty payments as a percentage of licensee revenues (below diagonal) received by MIT under various market sizes, invention qualities, and royalty rates. All NPV values are in millions.

		12% Cost Reduction Due to MIT Technology			21% Cost Reduction Due to MIT Technology		
		Royalty Payments to MIT (NPV / % of Revenues)			Royalty Payments to MIT (NPV / % of Revenues)		
		$1/wafer	$2/wafer	$3/wafer	$1/wafer	$2/wafer	$3/wafer
Market Size	Small	$2.0 / 0.8%	$3.9 / 1.5%	$5.6 / 2.3%	$2.8 / 0.8%	$5.4 / 1.6%	$7.9 / 2.3%
	Medium	$2.9 / 0.7%	$5.7 / 1.3%	$8.4 / 2.0%	$3.5 / 0.7%	$6.8 / 1.4%	$10.1 / 2.0%
	Large	$3.5 / 0.6%	$6.9 / 1.2%	$10.3 / 1.7%	$3.9 / 0.6%	$7.8 / 1.2%	$11.5 / 1.8%

Interestingly, the royalties cost more to the licensee than they add value to MIT. For example, consider the case of a small market where the MIT technology reduces cost by 12%. According to Table 8.5 (upper left corner), if MIT does not charge a royalty, the NPV of the exclusive license is \$39.7M. If MIT charges \$1/wafer, the value of the license reduces by \$2.7M to \$37.0M. However, according to Table 8.7 (upper left corner), the NPV of the royalty payments is only \$2M, implying that \$0.7M of value is destroyed in the value transfer process. This economic inefficiency arises due to the artificial reduction in invention "quality," which effectively reduces from ε to $\varepsilon - r$. Therefore, the licensee not only bears the cost of cash payments to MIT, but also the economic cost of lowered invention quality. The extents of value destruction for various r, averaged over the three market sizes ($P_{\max}^{optics}$) and two invention qualities (ε) under consideration, are shown in Table 8.8. As expected, value destruction increases with r.

8.2.2 The Case of Two Licencees

An industry with two non-exclusive licensees benefits only from the cost-savings enabled by the MIT AR coating technology in the period 2011-2014. We assume that the two licensees split the market for wafer-level optics equally with 50% market share each, and that they both develop

equally cost-effective AR coating technologies independently by year 2015. Therefore the two licensees pay royalties to MIT only in the period 2011-2014.

Table 8.8. Value destruction due to royalty charges. All values are in millions.

	Royalty ($/wafer)			
	$0	$1	$2	$3
NPV of royalty payments to patentee (P)	$0.0	$3.1	$6.1	$9.0
Total economic cost of royalty payments to licensee (L)	$0.0	$4.3	$8.6	$12.9
Value destruction due to royalty payments (L-P)	$0.0	$1.2	$2.6	$4.0

Tables 8.9 and 8.10 are analogous to Tables 8.5 and 8.6. Table 8.9 presents the benefit of the non-exclusive licensing agreement to one of the licensees in dollar terms (i.e. NPV of the non-exclusive licensing agreement). The average payoff to each of the non-exclusive licensees in Figure 8.1, $17.0M, is the average of the six NPVs listed under the zero-royalty column of Table 8.9. Table 8.10 presents the benefit of the non-exclusive licensing agreement as a percentage of the base value of each licensee firm without the agreement (i.e. NPV of the licensing agreement divided by NPV of the licensee firm, had MIT never developed the AR coating technology). As expected, the firm values without licensing (base value) are the same as in the exclusive licensee case.

Similar conclusions can be drawn from Table 8.9 as were drawn from Table 8.5 for the exclusive licensee. Larger market size, higher invention quality, and lower royalty rate increase the expected profits of either licensee. However, note that the NPVs of the non-exclusive licensing agreements in Table 8.9 are much lower than the NPVs of the exclusive licensing agreements in Table 8.5. Also, note that both firms benefit from the non-exclusive licensing structure, whereas a non-exclusive licensing agreement had a negative NPV for the non-licensee (firm B) in Table 8.5.

Table 8.10 shows the same trends as Table 8.6 does for the exclusive licensee. The MIT AR technology becomes a more important contribution to the licensee's business as the market size gets smaller. However, in comparison to the case of an exclusive licensee analyzed in Table 8.6, the MIT technology is much more important (and therefore much more valuable) to an exclusive licensee. The maximum percentage contribution of the MIT technology to a non-exclusive licensee is 22.4% of the licensee's base firm value (Table 8.10), whereas the MIT technology can more than double a non-

exclusive licensee's base firm value (150%, Table 8.6). Therefore, an exclusive licensee is willing to pay more than the sum of two non-exclusive licensees for the MIT technology, and the MIT TLO should issue a single license for this technology.

Table 8.9. NPV of a non-exclusive licensing agreement to the either licensee under various market sizes, invention qualities, and royalty rates. Firm value without licensing refers to the NPV of each firm in the industry, had the MIT invention not been made. All values are in millions.

		12% Cost Reduction Due to MIT Technology					21% Cost Reduction Due to MIT Technology				
		Change in Value of Each Firm Under Various Royalty Schemes ($/wafer)				Firm Value w/o Licensing	Change in Value of Each Firm Under Various Royalty Schemes ($/wafer)				Firm Value w/o Licensing
		$0	$1	$2	$3		$0	$1	$2	$3	
Market Size	Small	$6.8	$6.3	$5.7	$5.2	$39.7	$13.6	$12.9	$12.2	$11.6	$60.7
	Medium	$12.5	$11.6	$10.8	$9.9	$162.4	$23.1	$22.1	$21.1	$20.1	$195.2
	Large	$16.5	$15.3	$14.2	$13.1	$362.0	$29.6	$28.4	$27.1	$25.9	$402.8

Table 8.10. Percent increase in the value of either firm due to a non-exclusive licensing agreement under various market sizes, invention qualities, and royalty rates.

		12% Cost Reduction Due to MIT Technology				21% Cost Reduction Due to MIT Technology			
		% Change in Value of Each Firm Under Various Royalty Schemes ($/wafer)				% Change in Value of Each Firm Under Various Royalty Schemes ($/wafer)			
		$0	$1	$2	$3	$0	$1	$2	$3
Market Size	Small	17.1%	15.8%	14.4%	13.1%	22.4%	21.3%	20.2%	19.1%
	Medium	7.7%	7.2%	6.6%	6.1%	11.8%	11.3%	10.8%	10.3%
	Large	4.6%	4.2%	3.9%	3.6%	7.3%	7.0%	6.7%	6.4%

8.2.3 Licensing Strategy Recommendation to the MIT TLO

MIT TLO should issue an exclusive license for the technology, and should frontload the licensing fees as much as possible because large royalty payments destroy value by effectively reducing the invention quality. On average, every additional dollar of royalties per wafer has a marginal benefit of approximately $3.0M to MIT, and a marginal cost of approximately -$4.3M to the licensee (see Table 8.8). On average, the technology is expected to add $89.4M to the licensee's firm value. A fraction (ϕ) of this $89.4M should be paid to MIT as part of the licensing agreement. The licensee can split this total cost into an upfront component and an annual royalty stream in the period 2011-2014. This arrangement can be formulated as follows:

$$Cost\ to\ licensee = (\phi) \times (\$89.4M) = Upfront\ fee + (r) \times (\$4.3M) \quad (8.6)$$

The licensee is indifferent to any combination of an upfront fee and a royalty rate (r) which satisfies Eq. (8.6). For a constant ϕ, MIT TLO is best off with no royalty and only an upfront payment, because the marginal benefit of royalties to MIT is lower than the marginal cost of royalties to the licensee. Specifically:

$$Benefit\ to\ MIT = Upfront\ fee + (r) \times (\$3.0M) \quad (8.7)$$

For example, if $\phi = 10\%$, the total cost of the licensing agreement to the licensee is \$8.9M. If the licensee pays \$1/wafer royalty, the upfront fee should be \$8.9M - \$4.3M = \$4.6M, where \$4.3M is the total economic cost of a \$1/wafer royalty to the licensee. However, the benefit of this agreement to MIT is less than \$8.9M; MIT gets paid \$3.0M + \$4.6M = \$7.7M, because the royalty payment destroys, on average, \$1.2M by reducing the invention quality.

Finally, it is worth highlighting the assumption that these numerical values assume 1,000 lenses per wafer and 4 lenses per optical train. While upfront fees are insensitive to these assumptions, the royalty rate can be adjusted in proportion to the number of optical trains per wafer.

8.3 Methods

8.3.1 Estimation of the Market Demand Curve Parameters

$Q_{\max}^{optics}$ is bounded by the total wafer-scale mobile camera manufacturing capacity worldwide, and can be estimated by the total demand for mobile cameras, Q^{camera}, multiplied by the fraction of this manufacturing capacity compatible with wafer-scale manufacturing, f. Even if the wafer-scale optical trains of mobile cameras were available at zero cost, the market price and market demand of complete mobile devices (e.g. cell phones) would remain virtually unchanged. Thus, $Q_{\max}^{optics} = f \times Q^{camera}$, as shown in Table 8.11. Mobile device shipments are expected to grow rapidly from approximately 1 billion units in 2010 and reach 2.5 billion units[140]. We estimated that only 5% of camera manufacturing facilities worldwide can accommodate wafer-scale optical trains in 2010.

However, this fraction is expected to increase rapidly over the next 5 years until all camera manufacturing is compatible with SMT, similar to other electronic components today.

Table 8.11. Numerical estimation of $Q_{\max}^{optics}$.

	2010	2011	2012	2013	2014
Demand for mobile cameras (in millions) $\left(Q^{camera}\right)$	1,000	1,375	1,750	2,125	2,500
Fraction of wafer-scale manufacturing (f)	5%	20%	50%	100%	100%
Total wafer-scale optical train demand (in millions) $\left(Q_{\max}^{optics}\right)$	50	275	875	2,125	2,500

The second constant that needs to be estimated to construct a linear demand curve is $P_{\max}^{optics}$. If wafer-scale optics were to be sold for $P_{\max}^{optics}$, there would be exactly one mobile product line (e.g. a very high-end mobile phone or laptop computer) which could afford to use wafer-scale manufacturing technology. We assumed that $P_{\max}^{optics}$ is 10% to 100% higher than the market price of an average (not necessarily wafer-scale) optical train on the market. However, the market price of an average optical train is not readily observable and therefore we estimate it in Table 8.12 based on the market price of a complete CMOS camera (including the CMOS image sensor, optical train and housing) and typical profit margins in the consumer electronics manufacturing industry. The retail price of an average CMOS camera dropped by 4.3% per year, from $10.60 in 2002 to $8.50 in 2007[141]. As shown in the first row of Table 8.12, we assumed that the prices will continue to drop at this rate. The average trade margin of CMOS camera retailers was 17% in 2008, which we assumed will remain constant through 2014[141]. Thus, the wholesale prices of CMOS cameras are shown in the second row of Table 8.12. A CMOS camera has many components, including the CMOS image sensor, the optical train, and the camera housing. The CMOS image sensor constitutes 5-20% of the complete CMOS camera manufacturing cost. Similarly, we assume that the bare optical train (without AR coating) constitutes 10% of the complete CMOS camera manufacturing cost. Average prices of bare optical trains ($\overline{P}$) were thus estimated in the third row of Table 8.12. Once $\overline{P}$ is known, $P_{\max}^{optics}$ can be calculated. Three different possibilities we considered for $P_{\max}^{optics}$ are outlined in the fourth row of Table 8.12.

Table 8.12. Demand curve constants to be used in Eqs. (8.3) and (8.5), as well as marginal cost estimations.

		2010	2011	2012	2013	2014
Average retail price of a CMOS camera (including image sensor, optical train, and housing)		$7.45	$7.12	$6.68	$6.52	$6.24
Average wholesale price of a CMOS camera (assuming 17% trade margin)		$6.22	$5.95	$5.69	$5.45	$5.21
Average price of an optical train without AR coating $(\bar{P})$ (assuming 10% of price of complete CMOS camera)		$0.62	$0.59	$0.57	$0.54	$0.52
Maximum market price of a wafer-scale optical train (P_{max}) (under three different scenarios)	$P_{max} = \bar{P} \cdot (1+10\%)$	$0.68	$0.65	$0.63	$0.60	$0.57
	$P_{max} = \bar{P} \cdot (1+50\%)$	$0.93	$0.89	$0.85	$0.82	$0.78
	$P_{max} = \bar{P} \cdot (1+100\%)$	$1.24	$1.19	$1.14	$1.09	$1.04
Marginal cost of producing a wafer-level optical train (assuming 33% operating margin)	Without AR coating	$0.42	$0.40	$0.38	$0.36	$0.35
	With vacuum AR coating (c)	$0.54	$0.52	$0.50	$0.48	$0.47
	With MIT AR coating $(c-\varepsilon)$	$0.43-$0.48	$0.41-$0.46	$0.40-$0.44	$0.38-$0.42	$0.37-$0.41

8.3.2 Estimation of Marginal Costs

The marginal cost of producing a bare optical train, without an AR coating, can be estimated using typical operating margins of publicly traded wafer-scale optics manufacturers. For instance, Tessera Inc. had an operating margin of 33% in the second half of 2009[142]. As shown in the last row of Table 8.12, we estimated that a bare optical train can be manufactured for approximately $0.42 in 2010. As mentioned earlier, the additional cost of AR-coating all four lenses in the optical train depends on the coating technology used. A typical vacuum coating process costs $30 per 8" wafer. Assuming that a typical wafer can accommodate 1,000 lenses and that a typical optical train has four lenses in tandem, the cost of conventional vacuum AR coating on an optical train is $0.12. We estimated that the cost of our solution-based AR coating procedure is between $0.02 and $0.06. The marginal cost of producing a vacuum AR-coated optical train, c, is $0.54 in 2010. The cost-saving enabled by

licensing the MIT AR coating technology is ε, which ranges between \$0.06 and \$0.10. Thus, $c-\varepsilon$ is between \$0.43 and \$0.48 in 2010. As shown in the last row of Table 8.12, the marginal cost of producing an optical train in the baseline scenario (with a vacuum coating) in 2010 is \$0.54 while the bare optical train can be produced for \$0.42.

8.3.3 Calculation of the Herfindahl-Hirschman Index (HHI)

The HHI is a measure of the size of the firms in an industry compared to the size of the industry itself[143]. The HHI is also an indicator of the amount of competition among industry participants. The HHI is calculated as:

$$HHI = \sum_{i=1}^{N} s_i^2 \tag{8.7}$$

where s_i are the market shares of each of the N firms in the industry. We define market share on an ouput basis:

$$s_A = \frac{Q_A^{optics}}{Q_A^{optics} + Q_B^{optics}} \tag{8.8}$$

and

$$s_B = \frac{Q_B^{optics}}{Q_A^{optics} + Q_B^{optics}} \tag{8.9}$$

The HHI, as defined in Eq. (8.7), ranges in numerical value from $1/N$ to 1, where a larger numerical value implies that the market is dominated by a few large players and that there is less competition in the market. The reciprocal of the HHI, $(1/HHI)$, is the effective number of equal-sized firms competing in the industry.

8.3.4 Calculation of the Discount Rate

According to the capital asset pricing model (CAPM)[144], the appropriate discount rate (r_E) for a publicly traded company can be calculated as follows:

$$r_E = r_f + \beta\left(r_M - r_f\right) \tag{8.10}$$

where r_f is the risk-free interest rate, r_M is the expected annual return of the entire market, and β is the sensitivity of the particular company's returns to the expected market returns. In this study, r_f was assumed to be the yield on 5-year US T-bonds (2.6%). $\left(r_M - r_f\right)$, the market risk premium, has historically been 7-8%, and we assumed 7.5%. Finally, we used the β of Tessera Inc., which is 1.33. Thus, Eq. (8.10) yields 12.5% for the discount rate, r_E.

8.4 Conclusions

The MIT AR coating technology will add, on average, \$89.4M to the firm value of an exclusive licensee and \$17M to the firm value of either non-exclusive in a duopoly. Market size is the most important parameter which will determine the strength of the MIT technology as a strategic weapon. Other important factors are invention quality and royalty rate.

The MIT TLO should license this technology exclusively, and should bargain for as high an upfront fee as possible in return for a low royalty rate. An upfront fee of \$4.6M and a royalty rate of \$1/wafer, or an upfront fee of \$0.3M and a royalty rate of \$2/wafer are reasonable options, assuming that there are 1,000 lenses per wafer and each optical train contains 4 lenses in tandem.

Appendix A

MATLAB® Source Codes

A.1 Capillary Condensation Calculations

A.1.1 Calculation of Figure 3.1 Parameters

```
% This routine does the necessary calculations and plots
% Figure 3.1.

clear all

% Calculate radii
r = [8;15;24;50];
r = r.*0.5E-9;

% Calculate maximum "x" to which capillary condensation
% can occur (see Figure 1.2)
x_upper = 2/3.*r;

% Calculate maximum volume fraction of capillary condensate
alphamax = (asin(2/3))^4;
maxratio = 0.25*alphamax/(0.25*alphamax + 4/3);

% Calculate nanoparticle volumes
Vnp = 4/3.*pi.*r.^3;

% Create an array of "x" values
xvals8 = 0:0.001E-9:x_upper(1);
xvals15 = 0:0.001E-9:x_upper(2);
xvals24 = 0:0.001E-9:x_upper(3);
xvals50 = 0:0.001E-9:x_upper(4);

% Calculate corresponding "Rc" values (by Pythagorean Theorem)
Rcvals8 = (xvals8.^2)./(2*(r(1)-xvals8));
Rcvals15 = (xvals15.^2)./(2*(r(2)-xvals15));
Rcvals24 = (xvals24.^2)./(2*(r(3)-xvals24));
Rcvals50 = (xvals50.^2)./(2*(r(4)-xvals50));

%Calculate condensate volume in each case
Vcondensate8 = 0.5.*pi.*r(1)^3.*(asin(Rcvals8./r(1).*(-1 + sqrt(1 +
2*r(1)./Rcvals8)))).^4;
```

```
Vcondensate15 = 0.5.*pi.*r(2)^3.*(asin(Rcvals15./r(2).*(-1 + sqrt(1 +
2*r(2)./Rcvals15)))).^4;
Vcondensate24 = 0.5.*pi.*r(3)^3.*(asin(Rcvals24./r(3).*(-1 + sqrt(1 +
2*r(3)./Rcvals24)))).^4;
Vcondensate50 = 0.5.*pi.*r(4)^3.*(asin(Rcvals50./r(4).*(-1 + sqrt(1 +
2*r(4)./Rcvals50)))).^4;

% Calculate the volume fraction of condensate in each case
ratio8 = (Vcondensate8./2)./(Vcondensate8./2 + Vnp(1));
ratio15 = (Vcondensate15./2)./(Vcondensate15./2 + Vnp(2));
ratio24 = (Vcondensate24./2)./(Vcondensate24./2 + Vnp(3));
ratio50 = (Vcondensate50./2)./(Vcondensate50./2 + Vnp(4));

ratio8 = ratio8'./maxratio;
ratio15 = ratio15'./maxratio;
ratio24 = ratio24'./maxratio;
ratio50 = ratio50'./maxratio;

% Calculate the X-AXIS values (thermodynamic "demand")
pdiff8 = - 1./Rcvals8 + 1./xvals8;
pdiff15 = - 1./Rcvals15 + 1./xvals15;
pdiff24 = - 1./Rcvals24 + 1./xvals24;
pdiff50 = - 1./Rcvals50 + 1./xvals50;

%Plot
cap_cond_makefig(pdiff8,ratio8,pdiff15,ratio15,pdiff24,ratio24,pdiff50
,ratio50);
```

A.1.2 Plotting of Figure 3.1 Parameters

```
function cap_cond_makefig(X1, Y1, X2, Y2, X3, Y3, X4, Y4)
%CREATEFIGURE(X1,Y1,X2,Y2,X3,Y3,X4,Y4)

%  Auto-generated by MATLAB on 11-Jun-2008 19:48:17

% Create figure
figure1 = figure;

% Create axes
axes('Parent',figure1,'XScale','log','XMinorTick','on',...
    'Position',[0.1515 0.1341 0.7638 0.815],...
    'FontSize',12);
% Uncomment the following line to preserve the X-limits of the axes
% xlim([-2e+010 -1e+005]);
% Uncomment the following line to preserve the Y-limits of the axes
% ylim([0 0.06]);
box('on');
hold('all');
```

```
% Create semilogx
semilogx(X1,Y1);

% Create semilogx
semilogx(X2,Y2);

% Create semilogx
semilogx(X3,Y3);

% Create semilogx
semilogx(X4,Y4);

% Create xlabel
%xlabel('$\frac{1}{x}-\frac{1}{r_C}$ ${(nm)}^{-
1}$','Interpreter','latex',...
 %   'FontSize',24);

xlabel('$\frac{RT}{\gamma^{L-
V}{V_m}}\ln{\frac{{P_0}^{Capillary}}{P_0}}$ ${(m)}^{-
1}$','Interpreter','latex',...
    'FontSize',24);
% Create ylabel
%ylabel('$\frac{V_{cond}}{V_{cond}+V_{NP}}$','Interpreter','latex',...
 %   'FontSize',24);

ylabel('${Filled fraction}$','Interpreter','latex',...
    'FontSize',24);
% Create textarrow
annotation(figure1,'textarrow',[0.4904 0.7702],[0.7993 0.6997],...
    'TextEdgeColor','none',...
    'FontSize',12,...
    'FontName','Arial',...
    'String',{'Increasing particle size'});
% Create textbox
annotation(figure1,'textbox','String',{'8nm'},'FontSize',12,...
    'FontName','Arial',...
    'FitHeightToText','off',...
    'EdgeColor',[1 1 1],...
    'BackgroundColor',[1 1 1],...
    'Position',[0.363 0.3338 0.05292 0.04424]);
% Create textbox
annotation(figure1,'textbox','String',{'50nm'},'FontSize',12,...
    'FontName','Arial',...
    'FitHeightToText','off',...
    'EdgeColor',[1 1 1],...
    'BackgroundColor',[1 1 1],...
    'Position',[0.4562 0.2682 0.05292 0.04424]);
```

A.2 Optical Calculations

A.2.1 Broadband AR Coating Design Software

Table A.1. Input parameters used with the MATLAB function AR() in order to achieve the 4-stack and 6-stack AR coating designs discussed in Chapter 6.

	4-Stack Design	6-Stack Design
Wavelengths of interest	[400, 450, ..., 750, 800]	
Total film thickness	500 nm	600 nm
Low-index material	A = 1.2699 B = 0.00237	
High-index material	A = 1.9068 B = 0.03427	
Substrate	A = 1.51 B = 0.001	
Slices to be approximated	Stacks [3-33] (Ignore Stack 1)	Stacks [1-7] Stacks [8-40]
Reference wavelength	600 nm	

```
%***      BROADBAND AR DESIGN SOFTWARE v 1.0      ***
%***        Zekeriyya Gemici, August 2008         ***

% This function designs a multi-stack, broadband AR coating from
% two materials with different refractive indices. The method
% outlined by Skettrup (Applied Optics 28(14):2860, 1989) has
% been followed. First, a flip-flop design is done using AR().
% Then 3-stack equivalent stack approximations are used to
% diminish the number of stacks, using findEQ(). Finally, the
% design is numerically optimized using Toptim().

clear all

% Collect the necessary input data
disp('Welcome to the film design routine!');

% The wavelength range in which the AR coating is expected to
% operate in.
lambda = input('Wavelengths of interest = ');

% The sum of the thicknesses of all stacks
total_T = input('Approximate total film thickness = ');

% The reference wavelength at which 3-stack approximations should
```

```
% be done.
eq_lambda = input('Reference wavelength to use in the equivalent-3-
stack approximation = ');

% Refractive indices of non-absorbing Cauchy layers (k = 0)
lowA = input('Low refractive index component A = ');
lowB = input('Low refractive index component B = ');
highA = input('High refractive index component A = ');
highB = input('High refractive index component B = ');
subA = input('Substrate index component A = ');
subB = input('Substrate index component B = ');

% Calculate indices at 632 nm
low632 = lowA + lowB/(0.632)^2;
high632 = highA + highB/(0.632)^2;
sub632 = subA + subB/(0.632)^2;

% Calculate indices at the reference wavelength
low_eq = lowA + lowB/(eq_lambda/1000)^2;
high_eq = highA + highB/(eq_lambda/1000)^2;
sub_eq = subA + subB/(eq_lambda/1000)^2;

% Calculate indices at all wavelengths of interest
long_lambda = lambda(1):lambda(length(lambda));
params.nL = lowA + lowB./(long_lambda./1000).^2;
params.nH = highA + highB./(long_lambda./1000).^2;
params.nS = subA + subB./(long_lambda./1000).^2;
params.nL = params.nL';
params.nH = params.nH';
params.nS = params.nS';
params.lambda = lambda;
params.isMean = 0;
params.min_T = 5;

% Make the Southwell flip-flop design
% Notice reference to function BRBAR()
first_design = BRBAR(lambda, total_T, params.min_T, high632, low632,
sub632);
disp('1 = Low index component');
disp('2 = High index component');
disp('AIR');
disp(first_design);
disp('SUBSTRATE');

% Ask the user how he would like to partition the flip-flop
% design, so that each partition will be approximated with a
% three-stack equivalent. Note that any (min_T) nm-thick stacks
% left isolated will be removed and ignored later on.
```

```
disp('Starting from the AIR side, please indicate BEFORE which rows
you would like to place dividers that flag STARTING POINTS for
equivalent-3-layer calculation.');
disp('Please type your choices within brackets, separated with
commas(e.g., [3,5,10]). Please type "1" to include the first row in a
division.');
start_dividers = input('');
disp('Starting from the AIR side, please indicate AFTER which rows you
would like to place dividers that flag ENDING POINTS for equivalent-3-
layer calculation.');
disp('Please type your choices within brackets, separated with
commas(e.g., [3,5,10]). Please type "0" to include the first row in a
division.');
end_dividers = input('');
num_stacks = length(start_dividers);
second_design = [];
counter = 1;

% Do three-stack approximations
% Notice reference to findEQ()
for i = 1:num_stacks
    stack = first_design(start_dividers(i):end_dividers(i),:);
    [eq_stack,rank] = findEQ(stack, eq_lambda, high_eq, low_eq,
sub_eq);
    second_design =
[second_design;first_design(counter:start_dividers(i) - 1,:)];
    second_design = [second_design;eq_stack];
    counter = end_dividers(i) + 1;
end

if(counter < size(first_design,1))
    second_design =
[second_design;first_design(counter:size(first_design,1),:)];
end

i = 1;

% Remove remaining (min_T) nm-thick stacks
while (i < size(second_design,1))
    if (second_design(i,1) == params.min_T)
        second_design = [second_design(1:i-
1,:);second_design(i+1:size(second_design,1),:)];
    end
    i = i + 1;
end

% Tie up some loose ends
```

```
disp(second_design);
    type_A = second_design(1,2);
    type_B = type_A;
    layer_T = 0;
    counter_2 = 1;
    for counter = 1:length(second_design)
        type_B = second_design(counter,2);
        if type_A == type_B
            layer_T = layer_T + second_design(counter,1);
        else
            third_design(counter_2,1) = layer_T;
            third_design(counter_2,2) = type_A;
            type_A = type_B;
            counter_2 = counter_2 + 1;
            layer_T = second_design(counter,1);
        end
        if counter == length(second_design)
            third_design(counter_2,1) = layer_T;
            third_design(counter_2,2) = type_B;
        end
    end
disp(third_design);

% Numerically optimize the approximated design
% Notice reference to Toptim()
final_design = Toptim(third_design,params);

% Show the final design
disp(final_design);

% The user can copy-past the following lines into MATLAB if he
% would like to plot the reflectances, transmittances, or
% absorbances corresponding to the Southwell, 3-stack-equivalent,
% or final designs. Notice reference to photonic_calc60()

%[R1,T1,A1] =
photonic_calc60(0,0.5,[lambda(1):lambda(length(lambda))]',first_design
,[params.nL,params.nH],1,params.nS,1,0,0,1,2,[lambda(1)
lambda(length(lambda))],[0 0]);
%[R2,T2,A2] =
photonic_calc60(0,0.5,[lambda(1):lambda(length(lambda))]',second_desig
n,[params.nL,params.nH],1,params.nS,1,0,0,1,2,[lambda(1)
lambda(length(lambda))],[0 0]);
%[R3,T3,A3] =
photonic_calc60(0,0.5,[lambda(1):lambda(length(lambda))]',final_design
,[params.nL,params.nH],1,params.nS,1,0,0,1,2,[lambda(1)
lambda(length(lambda))],[0 0]);
```

A.2.1.1 Southwell Flip-Flop Design Function

```
% This function assists the function AR() by providing the
% Southwell flip-flop design.

function result = BRBAR(lambda, T, min_T, nH, nL, nS)

% lambda: a column vector with the wavelengths at which the
% reflectance of the desired AR coating should perform best at.
%
% T: total film thickness (scalar)
%
% min_T: thickness of each "slice" of the total film thickness.
% The slices are either high- or low-index, and they will be
% flip-flopped between the two index values to achieve a good AR
% coating. (scalar)
%
% nH: the high-index value (scalar)
%
% nL: the low-index value (scalar)
%
% nS: the substrate refractive index (scalar)

%Refractive index of the incident medium.
nA = 1;

%Number of layers used to model the entire film.
num_layers = ceil(T/min_T);

best_design = zeros(num_layers,2);
index = [nL,nH];
best_design(:,1) = min_T;

% 'OF' stands for 'objective function'
% The lower the objective function, the better the AR
% performance.
best_OF = inf;

% Set the initial state (starting point) to all-high-index
% stacks. If the '= 2' is replaced with '= 1' the initial state
% would be all-low-index stacks. Alternative, more complicated
% initial states can be provided.
best_design(:,2) = 2;

% Cycle through the initial design 5 (determined by j) to reach
% an optimum.
```

```
[OF,a,b] =
photonic_calc60(0,0.5,lambda',best_design,index,nA,nS,0,0,0,1,2,[0
0],[0 0]);
for (j = 1:5)
    for (i = 1:length(best_design(:,1)))
        design = best_design;
        % Flip!
        if (design(i,2) == 2)
            design(i,2) = 1;
        else design(i,2) = 2;
        end
        [OF,a,b] =
photonic_calc60(0,0.5,lambda',design,index,nA,nS,0,0,0,1,2,[0 0],[0
0]);
        % If the flip is useful (i.e., improves the objective
        % function, then keep it. Otherwise, flop!
        if (best_OF > sum(OF))
            best_design = design;
            best_OF = sum(OF);
        end
    end
end

% Tidy the design up by merging neighboring identical-index
% stacks into thicker stacks.
type_A = best_design(1,2);
type_B = type_A;
layer_T = 0;
counter_2 = 1;
for counter = 1:length(best_design)
    type_B = best_design(counter,2);
    if type_A == type_B
        layer_T = layer_T + best_design(counter,1);
    else
        result(counter_2,1) = layer_T;
        result(counter_2,2) = best_design(counter-1,2);
        type_A = type_B;
        counter_2 = counter_2 + 1;
        layer_T = best_design(counter,1);
    end
    if counter == length(best_design)
        result(counter_2,1) = layer_T;
        result(counter_2,2) = best_design(counter-1,2);
    end
end
```

A.2.1.2 Three-Stack Approximation Function

```
% This function assists the function AR() by providing the
% three-stack equivalent approximations

% The output is a 3x4 matrix, eq_layers, which has thicknesses of
% three stacks in each column. 2 of these columns are typically
% non-physical. The first two columns are in HLH index order. The
% last two are in LHL order. The output 'rank' makes a guess at
% which design is the best approximation. However, this judgement
% may not always be correct. The best way to tell is to actually
% plot the two approximations (see Figure 6.9).

function [eq_layers,rank] = findEQ(design,lambda,nH,nL,nS)

% design: an nx2 matrix, describing the thickness and index
% values of the multi-stack structure to be approximated with
% three stacks. The first column contains thickness values (in
% units of nm) and the second column contains the value "1" for
% low-index and "2" for high-index.
%
% lambda: the reference wavelength at which the three-stack
% approximation has exactly the same spectral properties as the
% full multi-stack original.
%
% nH: the high-index value (scalar)
%
% nL: the low-index value (scalar)
%
% nS: the substrate refractive index (scalar)

index = [nL,nH];
eq_layers = zeros(3,4);

%Find characteristic matrix of the design provided:
M = eye(2);
for i = 1:length(design(:,1))
    phi = (2*pi/lambda)*index(design(i,2))*design(i,1);
    M_temp =
[cos(phi),complex(0,sin(phi)/index(design(i,2)));complex(0,sin(phi)*in
dex(design(i,2))),cos(phi)];
    M = M*M_temp;
end
phi = 0;
M12 = imag(M(1,2));
M21 = imag(M(2,1));
M11 = real(M(1,1));
M22 = real(M(2,2));
```

```
alpha = M22-M11;

%First possibility: n1>n2
n1 = nH;
n2 = nL;

ro = n1/n2;
beta = ro*(M22-M11/ro^2);
delta = ro*n1*(M21/ro^2/n1^2-M12);
epsilon = n1*(M21/n1^2-M12);
E = ro*(M22/ro^2-M11);
F = ro*n1*(M21/n1^2-M12/ro^2);
A = beta*E + delta*F;
B = epsilon*E - alpha*F - alpha*delta + beta*epsilon;
C = alpha^2 + epsilon^2;

q1 = -B/2/A + ((B/2/A)^2-C/A)^0.5;
p1 = -(epsilon+beta*q1)/(alpha - delta*q1);
r1 = (alpha - E*p1*q1)/(alpha*p1 + beta*q1);

q2 = -B/2/A - ((B/2/A)^2-C/A)^0.5;
p2 = -(epsilon+beta*q2)/(alpha - delta*q2);
r2 = (alpha - E*p2*q2)/(alpha*p2 + beta*q2);

% HLH possibilities. p,q,r are thickness values.
eq_layers(:,1) = [p1;q1;r1];
eq_layers(:,2) = [p2;q2;r2];

%Second possibility: n1<n2
n1 = nL;
n2 = nH;

ro = n1/n2;
beta = ro*(M22-M11/ro^2);
delta = ro*n1*(M21/ro^2/n1^2-M12);
epsilon = n1*(M21/n1^2-M12);
E = ro*(M22/ro^2-M11);
F = ro*n1*(M21/n1^2-M12/ro^2);
A = beta*E + delta*F;
B = epsilon*E - alpha*F - alpha*delta + beta*epsilon;
C = alpha^2 + epsilon^2;

q3 = -B/2/A + ((B/2/A)^2-C/A)^0.5;
p3 = -(epsilon+beta*q3)/(alpha - delta*q3);
r3 = (alpha - E*p3*q3)/(alpha*p3 + beta*q3);

q4 = -B/2/A - ((B/2/A)^2-C/A)^0.5;
p4 = -(epsilon+beta*q4)/(alpha - delta*q4);
```

```
r4 = (alpha - E*p4*q4)/(alpha*p4 + beta*q4);

eq_layers(:,3) = [p3;q3;r3];
eq_layers(:,4) = [p4;q4;r4];

eq_layers = atan(eq_layers)/2/pi*lambda;
eq_layers(:,1) = eq_layers(:,1)./[n2;n1;n2]; %[n2;n1;n2];
eq_layers(:,2) = eq_layers(:,2)./[n2;n1;n2]; %[n2;n1;n2];
eq_layers(:,3) = eq_layers(:,3)./[n1;n2;n1];
eq_layers(:,4) = eq_layers(:,4)./[n1;n2;n1];

% Display the eq_layers matrix
eq_layers

eq_layers = eq_layers(:,sum(ceil(eq_layers) >= 0) >= 2);
eq_layers(eq_layers <= 0) = 0;
eq_layers = eq_layers(eq_layers >= 0);

%Check the HLH case. Calculate the spectral properties.
[R1,T1,A1] = photonic_calc60(0,0.5,[400:800]',[eq_layers(1)
2;eq_layers(2) 1;eq_layers(3) 2],[nL,nH],1,nS,0,0,0,1,2,[400 800],[0
0]);

%Check the LHL case. Calculate the spectral properties.
[R2,T2,A2] = photonic_calc60(0,0.5,[400:800]',[eq_layers(4)
1;eq_layers(5) 2;eq_layers(6) 1],[nL,nH],1,nS,0,0,0,1,2,[400 800],[0
0]);

%Check the reference case (i.e., no approximation).
[R,T,A] =
photonic_calc60(0,0.5,[400:800]',[design],[nL,nH],1,nS,0,0,0,1,2,[400
800],[0 0]);

%How bad is the HLH case? Check against reference case (original)
rank = sum(abs(R-R1));

%How bad is the LHL case? Check against reference case (original)
rank2 = sum(abs(R-R2));

% If LHL is better than HLH, pick LHL (output of '2').
% Otherwise, pick HLH (output of '1').
if (rank2 < rank)
    rank = 2;
    eq_layers = [eq_layers(4:6),[1 2 1]'];
else
    rank = 1;
    eq_layers = [eq_layers(1:3),[2 1 2]'];
```

```
end

return;
```

A.2.1.3 Numerical Optimization Function

```
% This function assists the function AR() by numerically
% optimizing the three-stack approximation (third_design) in the
% function AR().

function ans = Toptim(design,params)

% design: Please see findEQ() header
%
% params: Defined in AR()

% Initial guess of thicknesses
x0 = design(:,1);

% Uses MATLAB's built-in constrained optimization function.
% Notice that there is no upper limit on the thickness of each
% stack, but the stacks cannot be thinner than the stack
% thickness used in the flip-flop design. This constraint is
% placed so that the optimization function cannot delete a stack
% all-together.
% Notice that OF() is used to calculate the objective function.

ans =
fmincon(@OF,x0,[],[],[],[],ones(size(design,1),1).*params.min_T,Inf(si
ze(design,1),1),[],[],design,params);

ans = [ans,design(:,2)];

return;
```

A.2.1.4 Objective Function to Evaluate AR Performance

```
% This function assists the function Toptim() by evaluating the
% objective function of the AR design at various stages of
% numerical optimization.
%
% This function is not to be used alone, but only in conjunction
% with (or as referred to by) Toptim().

function ans = OF(T,design,params)

% T: a column vector of stack thicknesses (to be optimized)
%
```

```
% design: Please see findEQ() header
%
% params: Defined in AR().
% The most important element of params, with special relevance to
% OF() is the variable "isMean"
% isMean = 0 ==> sum of %R will be minimized, and a coating with
% minimum total reflectance will be favored.
% isMean = 1 ==> average of %R will be minimized, and a coating
% with a flat reflectance profile will be favored.

lambda_begin = params.lambda(1);
lambda_end = params.lambda(length(params.lambda));

[R,T,A] =
photonic_calc60(0,0.5,[lambda_begin:lambda_end]',[T,design(:,2)],[para
ms.nL,params.nH],1,params.nS,0,0,0,1,2,[400 800],[90 100]);

if params.isMean
    ans = mean(R);
else ans = sum(R);
end

return;
```

A.2.2 Roughness-Corrected Thin Film Optics Simulation Software

```
%***       1-D PHOTONIC CALCULATOR version 7.0        ***
%***            Adam Nolte, February 2002             ***
%*** Roughness Feature, August 2008, Zekeriyya Gemici ***

%This function uses the matrix method to calculate the
%reflectivity, transmission, and absorptance of a 1-D optically
%stratified medium.

%USAGE:  "[R,T,A] = photonic_calc70(lambda,d,n,n0,ns,Rplot,Tplot,...
%...Aplot,plot_choice,substrate_a ccount,xlimits,ylimits)"

%Version 7.0 incorporated the effect of small-scale and large-scale
%inter-stack and surface roughness into the spectral
%calculations, as described by Tikhonravov et al. (Applied Optics
%42(25) : 5140, 2003). The simulation (with roughness effects) is
%only valid for normal incidence. Therefore, parameters theta0
%and P in version 6.02, describing the angle of (theta0)
%incidence and polarity of light (P), respectively, have been
%removed.

%This function [photonic_calc70()] takes as inputs the following
%entries in this particular order:
```

```
% 1. A column vector (lambda) containing the wavelengths of
% interest, measured
%    in nm (i.e. approx [400:700] for the visible spectrum).

% 2. A # by 2 matrix containing in the first column the
% thicknesses
% of each layer from incidence to transmission side, measured
%    in nm. The second column should contain a number for each
%    respective layer which tells the program which column of the
%    index of refraction matrix contains the lambda dependent
%    index of refraction data for that layer.

% 3. The index of refraction matrix, a matrix containing as
%    columns the lambda dependent index of refraction data.  It
%    should have as many rows as there are elements in the lambda
%    vector, and as many columns as there are different materials
%    in the photonic stack.
%
%    v 1.0 and above incorporate an option whereas if a row
%    vector of refractive indices is given in place of a full
%    matrix, the program will assume the given refractive index
%    is constant over all wavelengths

% 4. The refractive index of the incidence medium, a column
%    vector with wavelength dependence.  (if v 1.0 or above, a
%    constant value assumes constant refractive index over all
%    wavelengths)

% 5. The refractive index of the transmission medium, a column
%    vector with wavelength dependence.  (if v 1.0 or above, a
%    constant value assumes constant refractive index over all
%    wavelengths)

% 6. A "1" if a plot of the %Reflectance is desired, a "0" if
% not.

% 7. A "1" if a plot of the %Transmission is desired, a "0" if
% not.

% 8. A "1" if a plot of the %Absorbance is desired, a "0" if not.

% 9. A "1" if a plots should be versus wavelength, a "0" if
% versus angular frequency.

% 10. A "1" if the plot should take substrate back-reflectance
% into account, a "0" if not.  New to version 6.0 is the option
```

```
% of putting a "2".  This calculates the spectral response
% assuming a filter on each side of the substrate.  It assumes
% mirror symmetry through a plane cutting the substrate in half.

% 11. The abscissa limits expressed as a two-element vector [xlow
% xhigh]. An entry of "[0 0]" specifies auto-set limits.

% 12. The ordinate limits expressed as a two-element vector [ylow
% yhigh]. An entry of "[0 0]" specifies auto-set limits.

% 13. A row vector of large-scale roughness values (in units of
% nm) corresponding to stacks from the incidence to transmittance
% side. Substrate roughness is not entered, and is assumed to be
% 0.

% 14. A row vector of small-scale roughness values (in units of
% nm) corresponding to stacks from the incidence to transmittance
% side. Substrate roughness is not entered, and is assumed to be
% 0.

% This function returns as output a column vector of associated %
% reflectance, a column vector of associated % transmittance, and
% a column vector of associated % absorptance.

function [R,T,A] =
photonic_calc70(lambda,d,n,n0,ns,Rplot,Tplot,Aplot,plot_choice,substra
te_account,xlimits,ylimits,roughness,srough);

%Using x and y graph limits?
graph_limitx = 0;
graph_limity = 0;

if xlimits(1) | xlimits(2)
    graph_limitx = 1;
end

if ylimits(1) | ylimits(2)
    graph_limity = 1;
end

%Convert roughness from units of nm to units of m
roughness = roughness.*10^-9;
srough = srough.*10^-9;

%Set Substrate Thickness (mm)
sub_thick = 1.09; %units of mm.  glass substrate usually ~1.09mm
sub_thick = sub_thick*10^-3;  %convert to m
```

```
% Calculate angular frequency vector
omega0 = (2 * pi * 3.00E8)./(lambda*10^-9);
central_wavelength = 1000; %Set central wavelength for k/k0 plots
(units of nm)
omega0_center = (2 * pi * 3.00E8)/(central_wavelength*10^-9);

%ditto for central wavelength
cen_wave = num2str(central_wavelength);

%define needed constant of the square root of epsilon 0 over mu 0
emu = 2.65442E-3;

%convert "lambda" and "d" vectors to meters
lambda = lambda*10^-9;
d(:,1) = d(:,1)*10^-9;

% Find the number of layers we're dealing with
numlayers = size(d);
numlayers = numlayers(1);

% Find the number of wavelengths we're scanning
numwaves = size(lambda);
numwaves = numwaves(1);

% Find min and max lambda

lami = lambda(1);
lamf = lambda(numwaves);

%this section converts constant entries (for the refractive
%indices) into vectors
size_n0 = size(n0);
size_n0 = size_n0(1);
if size_n0 == 1
    n0 = n0 * ones(numwaves,1);
end

size_ns = size(ns);
size_ns = size_ns(1);
if size_ns == 1
    ns = ns * ones(numwaves,1);
end

size_n = size(n);
dec_n = size_n(1);
num_n = size_n(2);
```

```
if dec_n == 1
    for I = 1 : num_n,
        new_n(:,I) = n(1,I) * ones(numwaves,1);
    end
    n = new_n;
end

% Loop over wavelengths and create and multiply transfer matrices
% for TE polarization case

% Different from version 6.01, the transfer matrices for each
% stack are deconvoluted into the interfacial
% reflection/transmission contribution (as described by Fresnel
% coefficients), and the phase shift that occurs during light's
% passage through the bulk of the film (related to film
% thickness).

for I = 1 : numwaves,
   % Create unity matrix M1
   M1 = [1 0;0 1];
   k0 = 2*pi/lambda(I);

   if (numlayers > 1)
       for J = 2 : numlayers
           h = n(I,d(J,2))*d(J,1);

           % Calculate Fresnel coefficients assuming normal
           % incidence and no roughness
           r0 = (n(I,d(J-1,2)) - n(I,d(J,2)))/(n(I,d(J-1,2)) +
n(I,d(J,2)));
           t0 = 2*n(I,d(J-1,2))/(n(I,d(J-1,2)) + n(I,d(J,2)));

           % Calculate correction coefficients for large-scale
           % roughness
           rcoeff = 1 - 2*k0^2*n(I,d(J,2))^2*roughness(J)^2;
           tcoeff = 1 - 0.5*k0^2*(n(I,d(J-1,2)) -
n(I,d(J,2)))^2*roughness(J)^2;

           % Calculate correction coefficients for small-scale
           % roughness
           rcoeff_small = 1 - 2*k0^2*n(I,d(J,2))*n(I,d(J-
1,2))*srough(J)^2;
           tcoeff_small = 1 + 0.5*k0^2*(n(I,d(J-1,2)) -
n(I,d(J,2)))^2*srough(J)^2;

           % Correct Fresnel coefficients to take roughness into
           % account
           rfinal = r0*rcoeff*rcoeff_small;
```

```
            tfinal = t0*tcoeff*tcoeff_small;

            % M2 is the interfacial contribution to the transfer
            % matrix
            M2 = M1 * [1/tfinal,rfinal/tfinal;rfinal/tfinal,1/tfinal];

            % Multiply M2 with the bulk contribution to the
            % transfer matrix
            M1 = M2 *
[complex(cos(k0*h),sin(k0*h)),0;0,complex(cos(k0*h),-sin(k0*h))];
        end
    end

    % Factor in the substrate-film interface. Assume 0 roughness
    % here.
    r0sub = (n(I,d(numlayers,2)) - ns(I))/(ns(I) +
n(I,d(numlayers,2)));
    t0sub = 2*n(I,d(numlayers,2))/(ns(I) + n(I,d(numlayers,2)));

    B0 = [1/t0sub,r0sub/t0sub;r0sub/t0sub,1/t0sub];
    M1 = M1 * B0;

    % Factor in the top layer, at the air interface.
    h4 = n(I,d(1,2))*d(1,1);
    C4 = [complex(cos(k0*h4),sin(k0*h4)),0;0,complex(cos(k0*h4),-
sin(k0*h4))];
    M1 = C4 * M1;

    r4 = (n0(I) - n(I,d(1,2)))/(n0(I) + n(I,d(1,2)));
    t4 = 2*n0(I)/(n0(I) + n(I,d(1,2)));

    rcoeff4 = 1 - 2*k0^2*n(I,d(1,2))^2*roughness(1)^2;
    tcoeff4 = 1 - 0.5*k0^2*(n0(I) - n(I,d(1,2)))^2*roughness(1)^2;

    rcoeff_small4 = 1 - 2*k0^2*n(I,d(1,2))*n0(I)*srough(1)^2;
    tcoeff_small4 = 1 + 0.5*k0^2*(n0(I) - n(I,d(1,2)))^2*srough(1)^2;

    rfinal4 = r4*rcoeff4*rcoeff_small4;
    tfinal4 = t4*tcoeff4*tcoeff_small4;

    B4 = [1/tfinal4,rfinal4/tfinal4;rfinal4/tfinal4,1/tfinal4];

    M1 = B4 * M1;

    %Calculate amplitude reflection and transmission coefficients

    t_TE(I,1) = 1/M1(1,1);
```

```
    r_TE(I,1) = t_TE(I,1)*(M1(2,1));

    if substrate_account
        %Calculate reverse amplitude reflection and transmission
        %coefficients (M1(1,1)-> M1(2,2) and vice versa for
        %reverse stack)
        tRev_TE(I,1) = ns(I)/M1(2,2);
        rRev_TE(I,1) = -(M1(1,2))/M1(1,1);
    end
end

% Find reflectance (R), transmittance (T), and absorptance (A)
R_TE = r_TE .* conj(r_TE);
T_TE = ((real(ns))./(real(n0))) .* t_TE .* conj(t_TE);
A_TE = 1 - R_TE - T_TE;
if substrate_account
    % Find rev reflectance/transmittance
    Rrev_TE = rRev_TE .* conj(rRev_TE);
    Trev_TE = ((n0)./(ns)) .* tRev_TE .* conj(tRev_TE);
    Arev_TE =  1 - Rrev_TE - Trev_TE;

    % Find Reflectance of back-surface interface with Fresnel
    % equations-- either air or reverse film
    if substrate_account == 1;
        psi_TE = ((ns-n0)./(ns+n0)) .* conj((ns-n0)./(ns+n0));
        phi_TE = 1 - psi_TE;
        abs_TE = phi_TE * 0;
    elseif substrate_account == 2;
        psi_TE = Rrev_TE;
        phi_TE = Trev_TE;
        abs_TE = Arev_TE;
    end

    % Recalculate reflectance/transmittance/absorptance with
    % substrate effect.  R+T+A no longer = 1 with absorbing
    % substrate! This assumes imaginary RI, no matter what the
    % sign convention, are meant to assume absorption.

    for I = 1 : numwaves,
        R_TEn(I,1) = R_TE(I,1) + (T_TE(I,1) * Trev_TE(I,1) *
psi_TE(I,1) * exp(-2*4*pi*abs(imag(ns(I,1)))*sub_thick/lambda(I)))/(1-
Rrev_TE(I,1)*psi_TE(I,1)*exp(-
2*4*pi*abs(imag(ns(I,1)))*sub_thick/lambda(I)));
        T_TEn(I,1) = (phi_TE(I,1) * T_TE(I,1) * exp(-
4*pi*abs(imag(ns(I,1)))*sub_thick/lambda(I)))/(1-
Rrev_TE(I,1)*psi_TE(I,1)*exp(-
2*4*pi*abs(imag(ns(I,1)))*sub_thick/lambda(I)));
```

```
        A_TEn(I,1) = A_TE(I,1) + (T_TE(I,1) * exp(-
4*pi*abs(imag(ns(I,1)))*sub_thick/lambda(I)) * (abs_TE(I,1) +
psi_TE(I,1) * exp(-4*pi*abs(imag(ns(I,1)))*sub_thick/lambda(I)) *
Arev_TE(I,1))/(1-Rrev_TE(I,1)*psi_TE(I,1)*exp(-
2*4*pi*abs(imag(ns(I,1)))*sub_thick/lambda(I))));
    end
    R_TE = R_TEn;
    T_TE = T_TEn;
    A_TE = A_TEn;
end
% Create R, T, and A
R = R_TE;
T = T_TE;
A = A_TE;

R = real(R);
T = real(T);
A = real(A);

%Convert lambda back to nm
lambda = lambda * 10^9;

% Plot R, T, and A
if plot_choice
if Rplot == 1
   figure('color','white');
   plot(lambda,100*R);
   title(strcat('Reflectance vs. Wavelength'));
   xlabel('Wavelength (nm)');
   ylabel('Reflectance (%)');
   if graph_limitx
       xlim(xlimits);
   end
   if graph_limity
       ylim(ylimits);
   end
end
if Tplot == 1
   figure('color','white');
   plot(lambda,100*T);
   title(strcat('Transmittance vs. Wavelength'));
   xlabel('Wavelength (nm)');
   ylabel('Transmission (%)')
   if graph_limitx
       xlim(xlimits);
   end
   if graph_limity
       ylim(ylimits);
```

```
   end
end
if Aplot == 1
   figure('color','white');
   plot(lambda,100*A);
   title(strcat('Absorptance vs. Wavelength'));
   xlabel('Wavelength (nm)');
   ylabel('Absorbance (%)');

   if graph_limitx
       xlim(xlimits);
   end
   if graph_limity
       ylim(ylimits);
   end
  end
else
   if Rplot == 1
   figure('color','white');
   plot(omega0/omega0_center,100*R);
   title(strcat('Reflectance vs. Dimensionless Wavenumber'));
   xlabel(strcat('k/k0, lambda0=',cen_wave,' nm'));
   ylabel('Reflectance (%)');

   if graph_limitx
       xlim(xlimits);
   end

   if graph_limity
       ylim(ylimits);
   end
end
if Tplot == 1
   figure('color','white');
   plot(omega0/omega0_center,100*T);
   title(strcat('Transmittance vs. vs. Dimensionless Wavenumber'));
   xlabel(strcat('k/k0, lambda0=',cen_wave,' nm'));
   ylabel('Transmission (%)');
   if graph_limitx
       xlim(xlimits);
   end
   if graph_limity
       ylim(ylimits);
   end
end
if Aplot == 1
   figure('color','white');
   plot(omega0/omega0_center,100*A);
```

```
    title(strcat('Absorptance vs. vs. Dimensionless Wavenumber'));
    xlabel(strcat('k/k0, lambda0=',cen_wave,' nm'));
    ylabel('Absorbance (%)');

    if graph_limitx
        xlim(xlimits);
    end

    if graph_limity
        ylim(ylimits);
    end

end

end
```

A.2.3 Alternative Three-Stack Approximation Function

```
% This function can be used to do equivalent-stack calculations
% using a different method, outlined by Tikhanravov et al.
% (Applied Optics 45(7): 1530, 2006). The major differences
% between this routine and the earlier one used for AR design are
% that this routine (i) gives a symmetrical 3-stack structure,
% (ii) can be used when the original stack to be approximated has
% an index value outside the bounds of the two experimentally
% available materials, and (iii) would never output an unphysical
% result (e.g., a negative thickness).

function [eq_layers] = findEQ_gen(D,N,L,n1,n2)

% D: Original film thickness (in nm)
%
% N: Original film index (need not be within [n1,n2]
%
% L: Reference wavelength at which the approximation is exact.
%
% n1: Refractive index of material 1
%
% n2: Refractive index of material 2
%
% NOTE: PLEASE REPEAT YOUR CALCULATION BY SWITCHING THE POSITIONS
% OF n1 AND n2. YOU WILL GET LHL or HLH FILMS, DEPENDING ON THE
% ORDER OF n1 AND n2.

syms d1 d2;

p = 0.5*(n1/n2 + n2/n1);
```

```
q = 0.5*(n1/n2 - n2/n1);
phi1 = 2*pi/L*n1*d1;
phi2 = 2*pi/L*n2*d2;
phi = 2*pi/L*N*D;

[d1,d2] = solve(cos(phi)-
cos(2*phi1)*cos(2*phi2)+p*sin(2*phi1)*sin(2*phi2), N-
n1*sqrt((sin(2*phi1)*cos(2*phi2)+p*cos(2*phi1)*sin(2*phi2)-
q*sin(2*phi2))/(sin(2*phi1)*cos(2*phi2)+p*cos(2*phi1)*sin(2*phi2)+q*si
n(2*phi2))));

d1s = eval(d1);
d2s = eval(d2);

d1_positive = d1s > 0;
d2_positive = d2s > 0;
both_positive = d1_positive.*d2_positive;

disp(['-----------------------------------------------------------------
-----']);

for (i = 1:4)
    if (both_positive(i))
        disp(['Top layer = ',num2str(d1s(i)),' nm thick
',num2str(n1),' index']);
        disp(['Middle layer = ',num2str(2*d2s(i)),' nm thick
',num2str(n2),' index']);
        disp(['Bottom layer = ',num2str(d1s(i)),' nm thick
',num2str(n1),' index']);
        disp(['-----------------------------------------------------
-------------']);
    end
end

return;
```

Appendix B
Supporting SEM Micrographs

SEM micrographs of an all-silica nanoparticle film assembled on glass and calcinated in air at 550°C for 4 hours are shown in Figure B.1. The film has been scratched after calcination, and the scratch cross-section (45° tilt) has been visualized to analyze the film-substrate interface.

TiO2/SiO2 nanoparticle films assembled on glass are shown in Figure B.2, before and after autoclaving at 124°C for 1 hour. Particle necking is apparent in autoclaved films (see Table 2.2). All-silica (APSiO2/SiO2) nanoparticle films assembled on soda lime glass, polycarbonate, quartz, Silicon wafer substrates and autoclaved at 134°C for 1 hour are shown in Figure B.3. Particle necking is apparent only in films assembled on glass (Table 2.2).

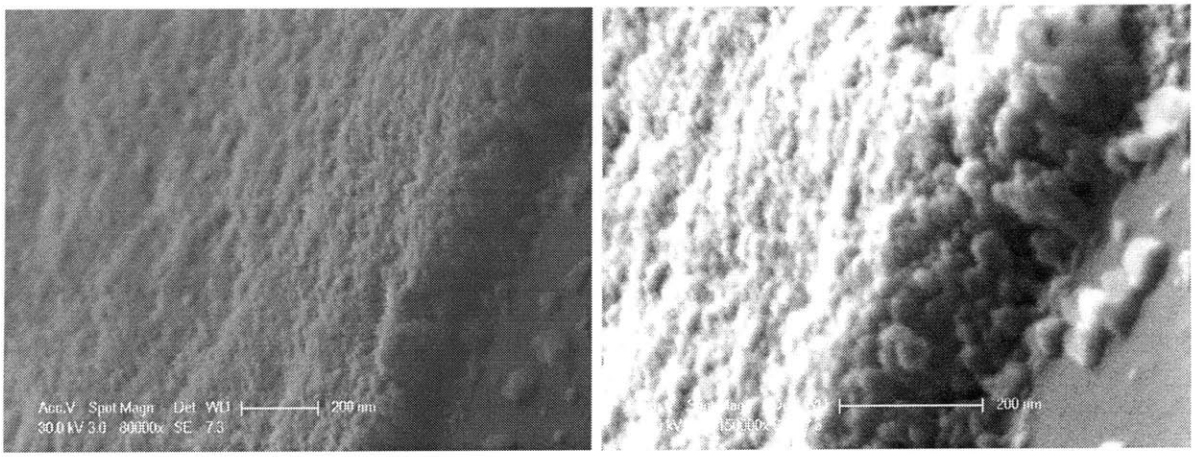

Figure B.1. Tilted view of a razor blade scratch on a calcinated (550°C, 4 hours) all-silica nanoparticle film on glass.

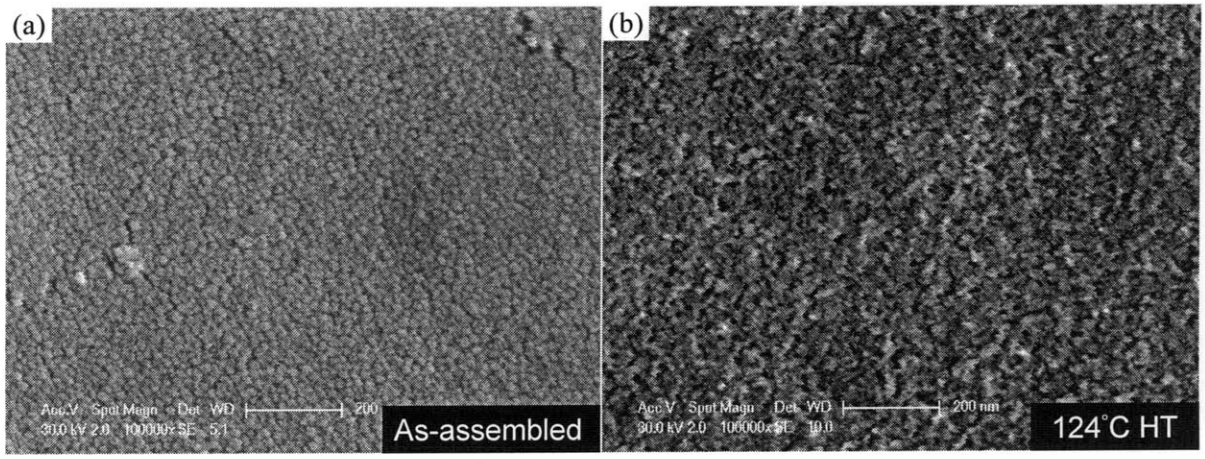

Figure B.2. (a) As-assembled and (b) autoclaved (124°C, 1 hour) TiO_2/SiO_2 film on glass. HT stands for hydrothermal treatment.

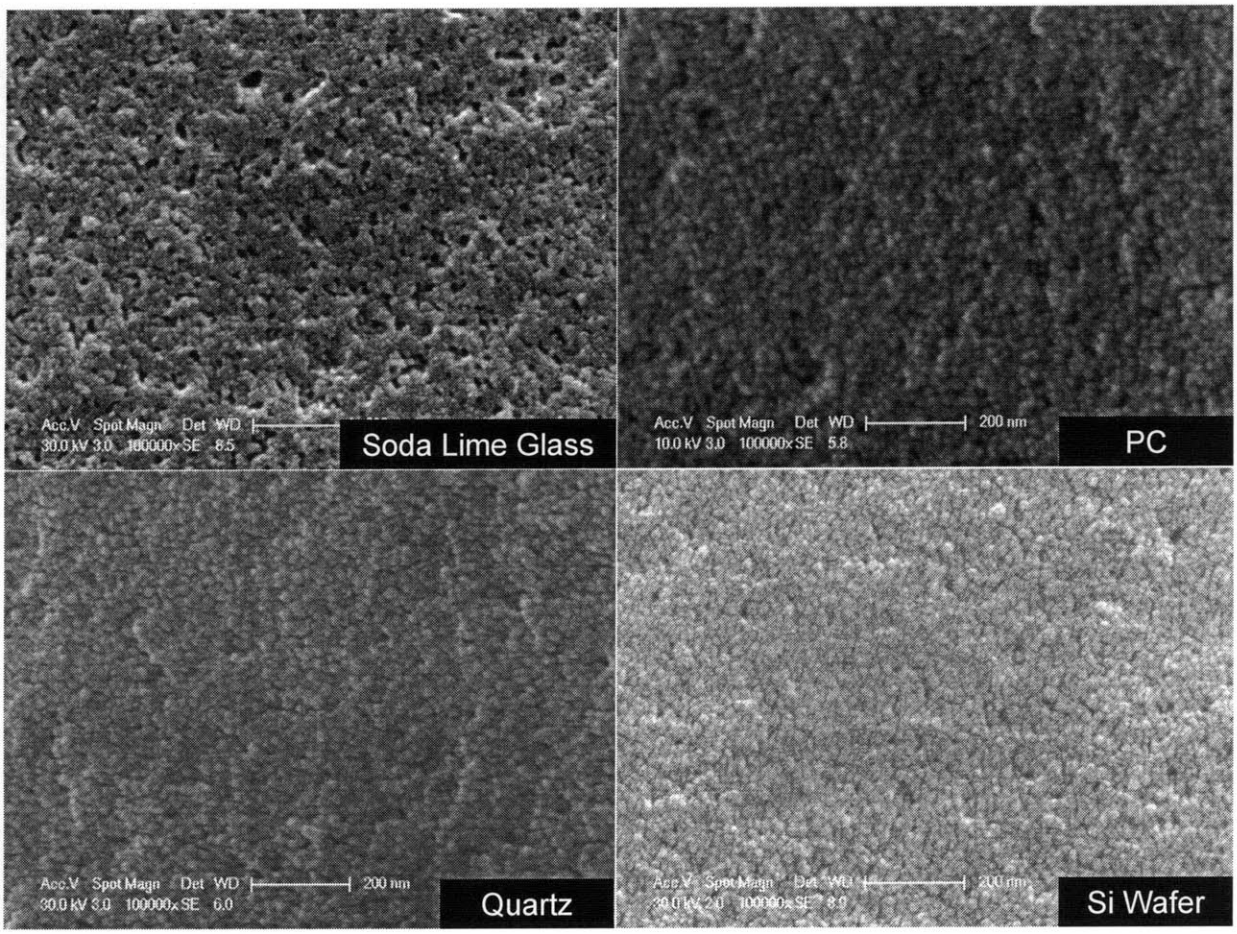

Figure B.3. An $APSiO_2/SiO_2$ film on various substrates after hydrothermal treatment (134°C, 1 hour).

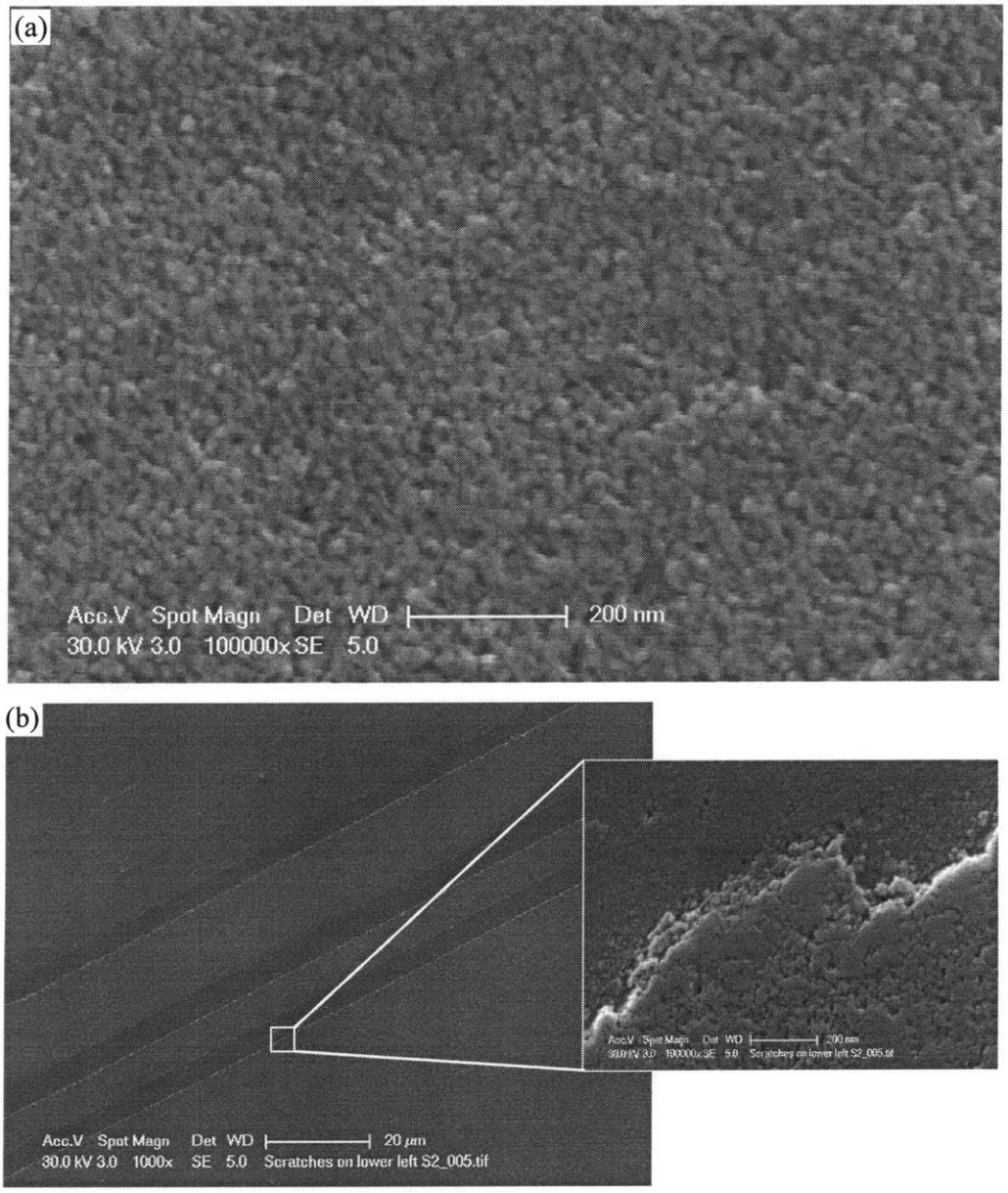

Figure B.4. An $APSiO_2/SiO_2$ film on glass, after (a) hydrothermal treatment (124°C, 1 hour) and (b) subsequent abrasion testing under a 100 MPa normal stress for 10 s. Tribochemical wear is evident even at early stages of wear testing.

Appendix C
Supporting Tables and Figures

The surface height profiles of an autoclaved (124°C, 1 hour) all-silica nanoparticle film on glass (see Chapter 2), scratched with 5B and 6H pencils are shown in Figures C.1a and C.1b, respectively. Due to low signal-to-noise ratio and height non-uniformities across the width of the scratches, it is difficult to determine unequivocally the scratch depth. In order to make a conservative estimate while omitting outlying data points, the height data was sorted in ascending order and the 100th data point was reported as the scratch depth. This algorithm suggests scratch depths of 81 and 400 Å in Figures C.1a and C.2b, which are reasonable estimates. Interestingly, pencils softer than 5B damaged the films almost as much as the hardest pencils and did not fit into the trend presented in Figure C.2, where scratch depth is plotted as a function of pencil hardness in various film constructs.

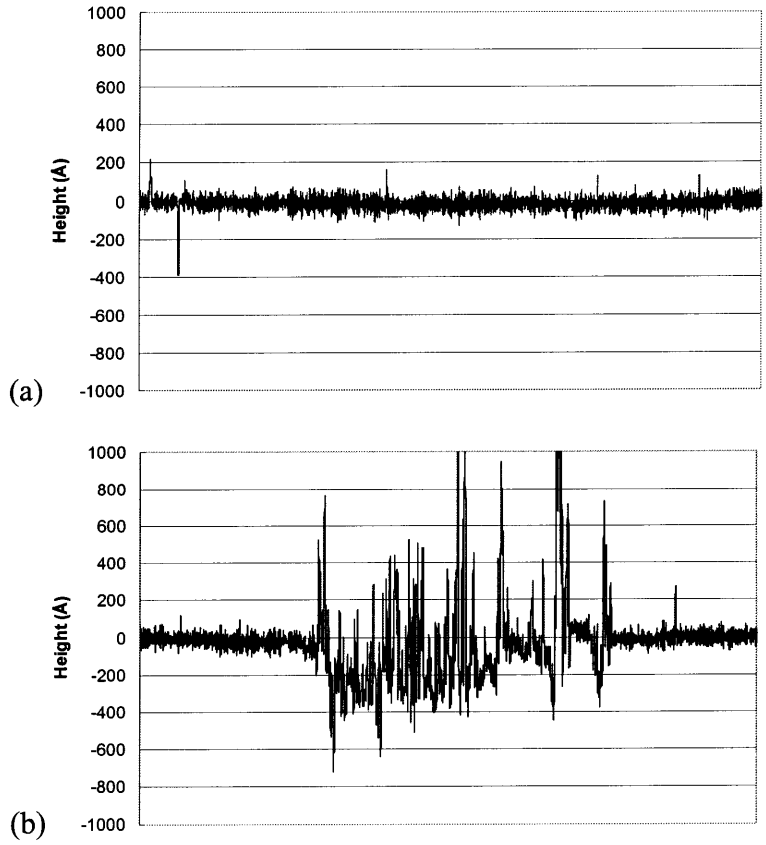

Figure C.1. Surface height profiles of an autoclaved (124°C, 1 hour) ~100nm-thick all-silica nanoparticle film on glass scratched with (a) 5B and (b) 6H pencils.

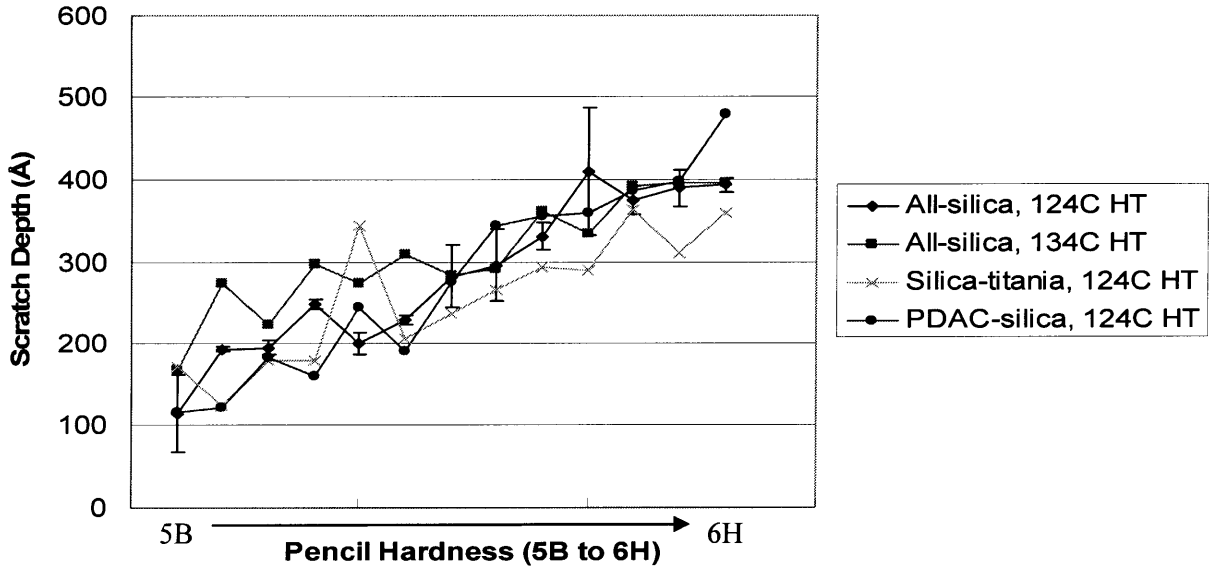

Figure C.2. Scratch depths of various ~1000Å-thick films on glass as functions of pencil hardness. HT stands for hydrothermal treatment.

Table C.1. Repeated ageing-recovery cycles using UV light exposure (λ = 302 nm, 3 hours) as the recovery tool on 100 nm-thick 7 nm TiO_2/24 nm SiO_2 nanoparticle films assembled on glass in Chapter 5. N/A indicates that a measurement was not done.

#	7 nm TiO_2/24 nm SiO_2	Refractive index	Porosity	Contact angle
1	Fresh	1.28	41%	5°
2	Aged (4 days)	1.31	34%	10°
3	Aged (4 days) + 3 hr UV	1.29	38%	6°
4	Aged (4 days) + 3 hr UV + Aged (1 day)	1.31	N/A	9°
5	Aged (4 days) + 3 hr UV + Aged (1 day) + 3 hr UV	1.31	N/A	10°

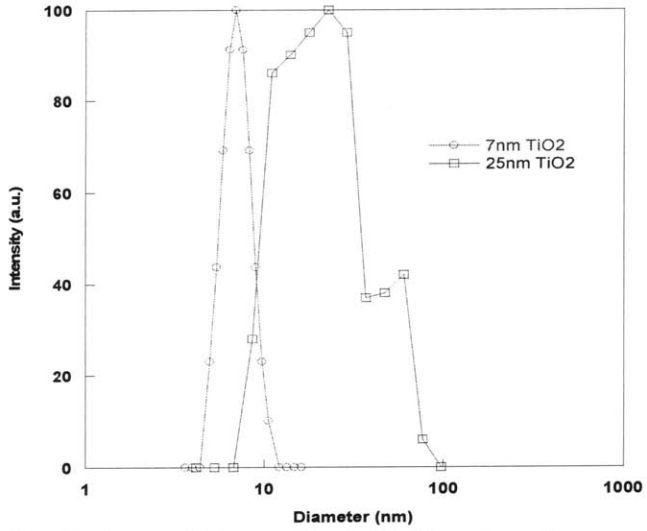

Figure C.3. Particle size distributions of the synthesized (7 nm) and commercially available (STS-100, 25 nm) TiO_2 nanoparticles measured using DLS in Chapter 6.

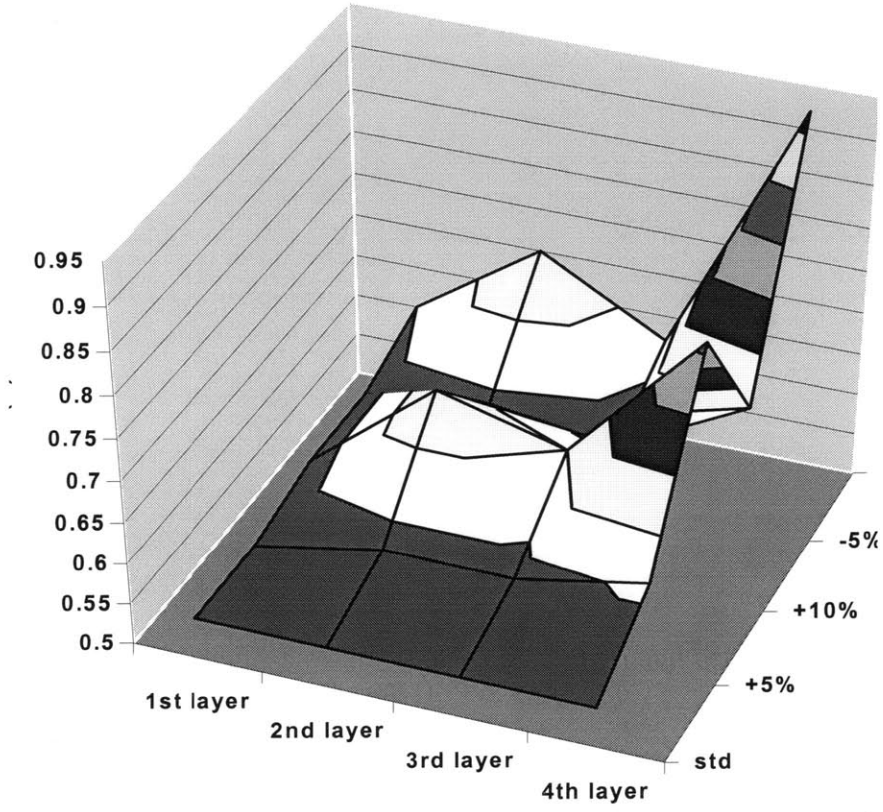

Figure C.4. A sensitivity analysis of average reflectance of the 4-stack AR coating presented in Chapter 6 to various thickness variations (+5%, +10%, or -5%) of the four different stacks. The average reflectance shows particular sensitivity to thickness changes in the 2nd and 4th stacks, which correspond to the low-index stacks.

References

1. Lee, D.; Rubner, M. F.; Cohen, R. E. *Nano Lett.* **2006,** 6, (10), 2305-2312.
2. Iler, R. K. *J. Colloid Interface Sci.* **1966,** 21, 569-594.
3. Lee, D.; Gemici, Z.; Rubner, M. F.; Cohen, R. E. *Langmuir* **2007,** 23, (17), 8833-8837.
4. Lee, D.; Omolade, D.; Cohen, R. E.; Rubner, M. F. *Chem. Mater.* **2007,** 19, (9), 2382-2382.
5. Tester, J. W.; Modell, M., *Thermodynamics and Its Applications*. Prentice Hall PTR: Upper Saddle River, 1997.
6. Butt, H.-J.; Graf, K.; Kappl, M., In *Physics and Chemistry of Interfaces*, Wiley-VCH Verlag GmbH: Weinheim, 2006; pp 16-22.
7. Dobrowolski, J. A. *SPIE* **2005,** 5963, 596303.
8. Pulker, H. K., *Coatings on Glass*. 2nd, revised ed.; Elsevier: Amsterdam, 1999.
9. Furman, S.; Tikhonravov, A. A., *Basics of Optics of Multilayer Systems*. Edition Frontieres, Gif-sur-Yvette: France, 1992.
10. Southwell, W. H. *Optics Letters* **1983,** 8, (11), 584-586.
11. Cebeci, F. Ç.; Wu, Z.; Zhai, L.; Cohen, R. E.; Rubner, M. F. *Langmuir* **2006,** 22, 2856-2862.
12. Bravo, J.; Zhai, L.; Wu, Z.; Cohen, R. E.; Rubner, M. F. *Langmuir* **2007,** 23, 7293-7298.
13. Smith, G. B. *Proc. SPIE* **2002,** 4806, 207-221.
14. Hodes, G. *Adv. Mater.* **2007,** 19, 639-655.
15. Chen, W.; Joly, A. G.; Morgan, N. Y., Optical physics and applications of luminescent nanoparticles. In *Handbook of Semiconductor Nanostructures and Nanodevices*, American Scientific Publishers: Valencia, 2006; Vol. 2, pp 295-334.
16. Schmidt, H.; Oliveira, P. W.; Mennig, M. *Proc. SPIE* **2003,** 5061, 24-33.
17. Yan, W.; Mahurin, S. M.; Overbury, S. H.; Dai, S. *Topics in Catalysis* **2006,** 39, 199-212.
18. Zou, M.; Yang, D. *Tribology Letters* **2006,** 22, (2), 189-196.
19. Wenzler, L. A.; Moyes, G. L.; Olson, L. G.; Harris, J. M.; Beebe Jr., T. P. *Anal. Chem.* **1997,** 69, 2855-2861.
20. Batteas, J. D.; Quan, X.; Weldon, M. K. *Tribology Letters* **1999,** 7, 121-128.
21. Zhang, S.-w.; Feng, D.; Wang, D. *Tribology International* **2006,** 38, (11-12), 959-965.
22. Donnet, J. B. *Composites Science and Technology* **2003,** 63, (8), 1085-1088.
23. Fan, H. Y.; Wright, A.; Gabaldon, J.; Rodriguez, A.; Brinker, C. J.; Jiang, Y. B. *Adv. Funct. Mater.* **2006,** 16, 891-895.

24. Brust, M.; Stuhr-Hansen, N.; Norgaard, K.; Christensen, J. B.; Nielsen, L. K.; Bjornholm, T. *Nano Lett.* **2001,** 1, 189-191.

25. Paul, S.; Pearson, C.; Molloy, A.; Cousins, M. A.; Green, M.; Kolliopoulou, S.; Dimitrakis, P.; Normand, P.; Tsoukalas, D.; Petty, M. C. *Nano Lett.* **2003,** 3, (533-536).

26. Boontongkong, Y.; Cohen, R. E. *Macromolecules* **2002,** 35, 3647-3652.

27. Whitesides, G. M.; Kriebel, J. K.; Mayers, B. T., Self-assembly and nanostructured materials. In *Nanoscale Assembly*, Springer US: New York, 2005; pp 217-239.

28. Rouse, J. H.; MacNeill, B. A.; Ferguson, G. S. *Chem. Mater.* **2000,** 12, 2502-2507.

29. Miguez, H.; Tetreault, N.; Hatton, B.; Yang, S. M.; Perovic, D.; Ozin, G. A. *Chem. Commun.* **2002,** (22), 2736-2737.

30. Iler, R. K., *The Chemistry of Silica: Solubility, Polymerization, Colloid and Surface Properties, and Biochemistry*. 2nd ed.; Wiley-Interscience: New York, 1979.

31. Imai, H.; Hirashima, H. *J. Am. Ceram. Soc.* **1999,** 82, (9), 2301-2304.

32. Liau, L. C.; Chang, H.; Yang, T. C.; Huang, C. *J. Chem. Eng. Jap.* **2005,** 38, (10), 813-817.

33. Decher, G.; Hong, J. D. *Makromol. Chem., Macromol. Symp.* **1991,** 46, 321-327.

34. Lvov, Y.; Ariga, K.; Onda, M.; Ichinose, I.; Kunitake, T. *Langmuir* **1997,** 13, (23), 6195-6203.

35. Marston, N.; Vincent, B. *Langmuir* **1997,** 13, (1), 14-22.

36. Kovtyukhova, N.; Ollivier, P. J.; Chizhik, S.; Dubravin, A.; Buzaneva, E.; Gorchinskiy, A.; Marchenko, A.; Smirnova, N. *Thin Solid Films* **1999,** 337, (1-2), 166-170.

37. Gao, M.; Lesser, C.; Kirstein, S.; Möhwald, H.; Rogach, A. L.; Weller, H. *J. Appl. Phys.* **2000,** 87, 2297-2302.

38. Caruso, R. A.; Susha, A.; Caruso, F. *Chem. Mater.* **2001,** 13, 400-409.

39. Ostrander, J. W.; Mamedov, A. A.; Kotov, N. A. *J. Am. Chem. Soc.* **2001,** 123, (1101-1110).

40. Cho, J.; Char, K.; Hong, J. D.; Lee, K. B. *Adv. Mater.* **2001,** 13, 1076-1078.

41. Kovtyukhova, N. I.; Martin, B. R.; Mbindyo, J. K. N.; Smith, P. A.; Razavi, B.; Mayer, T. S.; Mallouk, T. E. *J. Phys. Chem. B* **2001,** 105, (37), 8762-8769.

42. Hattori, H. *Adv. Mater.* **2001,** 13, (1), 51-54.

43. Sennerfors, T.; Bogdanovic, G.; Tiberg, F. *Langmuir* **2002,** 18, (16), 6410-6415.

44. Bogdanovic, G.; Sennerfors, T.; Zhmud, B.; Tiberg, F. *Journal of Colloid and Interface Science* **2002,** 255, (1), 44-51.

45. Krasteva, N.; Besnard, I.; Guse, B.; Bauer, R. E.; Mullen, K.; Yasuda, A.; Vossmeyer, T. *Nano Lett.* **2002,** 2, 551-555.

46. Rouse, J. H.; Ferguson, G. S. *J. Am. Chem. Soc.* **2003,** 125, (50), 15529-15536.

47. He, J. A.; Mosurkal, R.; Samuelson, L. A.; Li, L.; Kumar, J. *Langmuir* **2003,** 19, (6), 2169-2174.

48. Cant, N. E.; Zhang, H. L.; Critchley, K.; Mykhalyk, T. A.; Davies, G. R.; Evans, S. D. *J. Phys. Chem. B* **2003,** 107, 13557-13562.

49. Nolte, A. J.; Rubner, M. F.; Cohen, R. E. *Langmuir* **2004,** 20, (8), 3304-3310.

50. Tian, S. J.; Liu, J. Y.; Zhu, T.; Knoll, W. *Chem. Mater.* **2004,** 16, 4103-4108.

51. Pavoor, P. V.; Gearing, B. P.; Bellare, A.; Cohen, R. E. *Wear* **2004,** 256, (11-12), 1196-1207.

52. DeLongchamp, D. M.; Hammond, P. T. *Chem. Mater.* **2004,** 16, (23), 4799-4805.

53. Koo, H. Y.; Yi, D. K.; Yoo, S. J.; Kim, D. Y. *Advanced Materials* **2004,** 16, (3), 274-277.

54. Park, J.; Fouche, L. D.; Hammond, P. T. *Adv. Mater.* **2005,** 13, 1076-1078.

55. Ahn, J. S.; Hammond, P. T.; Rubner, M. F.; Lee, I. *Colloids and Surfaces A: Physicochemical and Engineering Aspects* **2005,** 259, (1-3), 45-53.

56. Zhou, D.; Bruckbauer, A.; Abell, C.; Klenerman, D.; Kang, D. *Adv. Mater.* **2005,** 17, 1243-1248.

57. Wu, Z.; Lee, D.; Rubner, M. F.; Cohen, R. E. *Small* **2007,** 3, (8), 1445-1451.

58. Yang, G.; Hongxia, M.; Wu, Z.; Zhang, P. *Wear* **2007,** 262, 471-476.

59. Decher, G.; Schlenoff, J. B., *Multilayer Thin Films: Sequential Assembly of Nanocomposite Materials*. Wiley-VCH Verlag GmbH & Co.: Weinheim, Germany, 2003.

60. While the transmittance would decrease ~4% upon complete antireflection film removal (due to emergent reflective losses), greater decrease in transmittance can be observed if the substrate itself is damaged and develops haze.

61. Beamson, G.; Briggs, D., *High Resolution XPS of Organic Polymers*. Wiley: Chichester, UK, 1992.

62. Jeon, J.; Panchagnula, V.; Pan, J.; Dobrynin, A. V. *Langmuir* **2006,** 22, 4629-4637.

63. Bhushan, B., *Handbook of tribology: materials, coatings, and surface treatments*. McGraw-Hill: New York, 1991.

64. Fischer, T. E.; Mullins, W. M. *J. Phys. Chem.* **1992,** 96, 5690-5701.

65. Osseo-Asare, K. *Journal of The Electrochemical Society* **2002,** 149, (12), G651-G655.

66. Kato, K.; Adachi, K. *Wear* **2002,** 253, 1097-1104.

67. Kato, K. *Wear* **2000,** 241, 151-157.

68. Feng, X. J.; Jiang, L. *Advanced Materials* **2006,** 18, (23), 3063-3078.

69. Nakajima, A.; Abe, K.; Hashimoto, K.; Watanabe, T. *Thin Solid Films* **2000,** 376, (1-2), 140-143.

70. Nolte, A. J.; Rubner, M. F.; Cohen, R. E. *Macromolecules* **2005,** 38, (13), 5367-5370.

71. Choi, W.; Termin, A.; Hoffmann, M. R. *J. Phys. Chem.* **1994,** 98, (51), 13669-13679.

72. Personal communication, Meredith, P. 2006.

73. COLTS Laboratories. www.colts-laboratories.com

74. Preston, F. W. *J. Soc. Glass Technol.* **1927,** 11, 214-256.

75. Piranha solution. http://en.wikipedia.org/wiki/Piranha_solution

76. Erickson, C. V. *C&E News* **1990,** 68, (33), 2.

77. Choi, M.; Ryoo, R. *Nature Materials* **2003,** 2, (7), 473-476.

78. Liang, C.; Li, Z.; Dai, S. *Angewandte Chemie-International Edition* **2008,** 47, (20), 3696-3717.

79. Lau, K. K. S.; Bico, J.; Teo, K. B. K.; Chhowalla, M.; Amaratunga, G. A. J.; Milne, W. I.; McKinley, G. H.; Gleason, K. K. *Nano Letters* **2003,** 3, (12), 1701-1705.

80. van Rijn, C. J. M., *Nano and Micro Engineered Membrane Technology*. Elsevier B.V.: Amsterdam, 2004.

81. Kresge, C. T.; Leonowicz, M. E.; Roth, W. J.; Vartuli, J. C.; Beck, J. S. *Nature* **1992,** 359, (6397), 710-712.

82. Lee, H.; Dellatore, S. M.; Miller, W. M.; Messersmith, P. B. *Science* **2007,** 318, (5849), 426-430.

83. Jiang, Y. G.; Wang, Z. Q.; Yu, X.; Shi, F.; Xu, H. P.; Zhang, X. *Langmuir* **2005,** 21, (5), 1986-1990.

84. Zhao, X. S.; Lu, G. Q. *J. Phys. Chem. B* **1998,** 102, 1556-1561.

85. Lee, D.; Nolte, A. J.; Kunz, A. L.; Rubner, M. F.; Cohen, R. E. *Journal of the American Chemical Society* **2006,** 128, (26), 8521-8529.

86. Dotzauer, D. M.; Dai, J. H.; Sun, L.; Bruening, M. L. *Nano Letters* **2006,** 6, (10), 2268-2272.

87. Howarter, J. A.; Youngblood, J. P. *Advanced Materials* **2007,** 19, (22), 3838.

88. Asefa, T.; MacLachan, M. J.; Coombs, N.; Ozin, G. A. *Nature* **1999,** 402, (6764), 867-871.

89. Kim, S.; Ehrman, S. H. *Langmuir* **2007,** 23, (5), 2497-2504.

90. Kruschwitz, J. D. T.; Pawlewicz, W. T. *Appl. Optics* **1997,** 36, (10), 2157-2159.

91. Lvov, Y. M.; Rusling, J. F.; Thomsen, D. L.; Papadimitrakopoulos, F.; Kawakami, T.; Kunitake, T. *Chem. Commun.* **1998,** (11), 1229.

92. Maldovan, M.; Bockstaller, M. R.; Thomas, E. L.; Carter, W. C. *Applied Physics B-Lasers and Optics* **2003,** 76, (8), 877-884.

93. Ościk, J., Adsorption. In Ellis Horwood Ltd: Chichester (UK), 1982; pp 56-63.

94. Gemici, Z.; Shimomura, H.; Cohen, R. E.; Rubner, M. F. *Langmuir* **2008,** 24, 2168-2177.

95. Vogel, R.; Dobe, C.; Whittaker, A.; Edwards, G.; Riches, J. D.; Harvey, M.; Trau, M.; Meredith, P. *Langmuir* **2004,** 20, (7), 2908-2914.

96. Kim, S. S.; Zhang, W. Z.; Pinnavaia, T. J. *Science* **1998,** 282, (5392), 1302-1305.

97. Pavoor, P. V.; Bellare, A.; Strom, A.; Yang, D.; Cohen, R. E. *Macromolecules* **2004,** 27, (13), 4865-4871.

98. Stafford, C. M.; Harrison, C.; Beers, K. L.; Karim, A.; Amis, E. J.; Vanlandingham, M. R.; Kim, H.; Volksen, W.; Miller, R. D.; Simonyi, E. E. *Nat. Mater.* **2004,** 3, 545-550.

99. *III-Vs Review* **2004,** 17, (6), 21-21.

100. Harrison, C.; Stafford, C. M.; Zhang, W. H.; Karim, A. *Appl. Phys. Lett.* **2004,** 85, 4016-4018.

101. Nolte, A. J.; Cohen, R. E.; Rubner, M. F. *Macromolecules* **2006,** 39, (14), 4841-4847.

102. Nolte, A. J. Fundamental Studies of Polyelectrolyte Multilayer Films: Optical, Mechanical, and Lithographic Property Control. PhD Thesis, MIT, Cambridge, 2007.

103. Lu, C. H.; Donch, I.; Nolte, M.; Fery, A. *Chemistry of Materials* **2006,** 18, (26), 6204-6210.

104. Mei, H.; Huang, R.; Chung, J. Y.; Stafford, C. M.; Yu, H. *App. Phys. Lett.* **2007,** 90, 151902.

105. Nolte, A. J.; Treat, N. D.; Cohen, R. E.; Rubner, M. F. *Submitted* **2007.**

106. Nolte, A. J.; Cohen, R. E.; Rubner, M. F. *Macromolecules* **2006,** 39, 4841-4847.

107. Howarter, J. A.; Youngblood, J. P. *Macromolecular Rapid Communications* **2008,** 29, (6), 455-466.

108. Tuteja, A.; Choi, W.; Ma, M. L.; Mabry, J. M.; Mazzella, S. A.; Rutledge, G. C.; McKinley, G. H.; Cohen, R. E. *Science* **2007,** 318, 1618-1622.

109. Extrand, C. W.; Moon, S. I.; Hall, P.; Schmidt, D. *Langmuir* **2007,** 23, (17), 8882-8890.

110. Ishino, C.; Okumura, K.; Quere, D. *Europhysics Letters* **2004,** 68, (3), 419-425.

111. Ishino, C.; Okumura, K. *European Physical Journal E* **2008,** 25, (4), 415-424.

112. Bico, J.; Tordeux, C.; Quere, D. *Europhys. Lett.* **2001,** 55, (2), 214-220.

113. Schwachulla, P. Application of Functional Coatings by Means of Layer by Layer Assembly. Diplom Ingenieur Thesis, HTWG Constance, Germany, 2008.

114. Chen, D. G.; Yan, Y. G.; Westenberg, E.; Niebauer, D.; Sakaitani, N.; Chaudhuri, S. R.; Sato, Y.; Takamatsu, M. *J. Sol-Gel Sci. Technol.* **2000,** 19, (1-3), 77-82.

115. Nolte, A. J.; Rubner, M. F.; Cohen, R. E. *Langmuir* **2004,** 20, (8), 3304-3310.

116. Hiller, J.; Mendelsohn, J. D.; Rubner, M. F. *Nat. Mater.* **2002,** 1, (1), 59-63.

117. Tikhonravov, A. V. *Proc. SPIE-Int. Soc. Opt. Eng.* **1990,** 1270, 28-35.

118. Prum, R. O.; Quinn, T.; Torres, R. H. *J. Exp. Biol.* **2006,** 209, (4), 748-765.

119. Kim, J. H.; Shiratori, S. *Jpn. J. Appl. Phys. Part 1* **2005,** 44, (10), 7588-7592.

120. Tikhonravov, A. V.; Trubetskov, M. K.; DeBell, G. W. *Appl. Opt.* **1996,** 35, (28), 5493-5508.

121. Skettrup, T. *Appl. Opt.* **1989,** 28, (14), 2860-2863.

122. Schallenberg, U. B. *Appl. Opt.* **2006,** 45, (7), 1507-1514.

123. Southwell, W. H. *Appl. Opt.* **1985,** 24, (4), 457-460.

124. Jakobs, S.; Duparre, A.; Truckenbrodt, H. *Appl. Opt.* **1998,** 37, (7), 1180-1193.

125. Tikhonravov, A. V.; Trubetskov, M. K.; Tikhonravov, A. A.; Duparre, A. *Appl. Opt.* **2003,** 42, (25), 5140-5148.

126. Maldovan, M.; Bockstaller, M. R.; Thomas, E. L.; Carter, W. C. *Appl. Phys. B: Lasers Opt.* **2003,** 76, (8), 877-884.

127. Gemici, Z.; Rubner, M. F.; Cohen, R. E. Nanoparticle Coatings and Methods of Making. PCT/US2007/017669, 12.06.2008.

128. Gemici, Z.; Cohen, R. E.; Rubner, M. F. Optical Coatings. MIT Case 13155 - Application number and filing date confidential, 2008.

129. Trout, T. J.; Schmieg, J. J.; Gambogi, W. J.; Weber, A. M. *Advanced Materials* **1998,** 10, (15), 1219.

130. Ostroverkhova, O.; Moerner, W. E. *Chemical Reviews* **2004,** 104, (7), 3267-3314.

131. Suzuki, N.; Tomita, Y. *Optics Express* **2006,** 14, (26), 12712-12719.

132. Tikhonravov, A. V.; Trubetskov, M. K.; Amotchkina, T. V.; Thelen, A. *Applied Optics* **2006,** 45, (7), 1530-1538.

133. Humpston, G., Engineered to the task: why camera-phones are different. *Solid State Technology* June 2009, 52(6).

134. Humpston, G., VGA Imagers in Camera Phones. *Photonics Spectra* March 2008.

135. Humpston, G., Address image capture, processing challenges in portables. *EE Times-India* January 2009.

136. Erutku, C.; Richelle, Y. *Journal of Economics & Management Strategy* **2007,** 16, (2), 407-436.

137. Kamien, M. I.; Oren, S. S.; Tauman, Y. *Journal of Mathematical Economics* **1992,** 21, 483-508.

138. Sen, D.; Tauman, Y. *Games and Economic Behavior* **2007,** 59, (1), 163-186.

139. Pindyck, R. S.; Rubinfield, D. L., *Microeconomics*. 7th ed.; Pearson Prentice Hall: Upper Saddle River, New Jersey, 2009.

140. *Mobile Devices Annual Market Overview*; ABI Research: 2009.

141. *World Image Sensors Market*; Frost & Sullivan: 2008.

142. Google Finance. http://www.google.com/finance?q=NASDAQ:TSRA (01/10/2010).

143. Herfindahl Index. http://en.wikipedia.org/wiki/Herfindahl_index (02/22/2010).

144. Bodie, Z.; Kane, A.; Marcus, A. J., *Investments*. 8th ed.; McGraw-Hill: New York, NY, 2009.